

**Mechanisms of Chiral Features of Atomically Precise Metal Clusters and
Resonant Transition Metal Complexes: Insights from Vibrational Optical
Activity**

by

Mutasem Alshalalfeh

A thesis submitted in partial fulfillment of the requirements for the degree of
Doctor of Philosophy

Department of Chemistry

University of Alberta

© Mutasem Alshalalfeh, 2024

Abstract

My PhD thesis primarily focuses on exploring chiroptical events and to elucidate the mechanisms responsible for chiroptical signatures in various compounds. These compounds encompass several atomically precise silver and copper clusters, a europium complex, and two highly flexible monosaccharide derivatives, which will serve as prototypes for future europium sensing studies, as well as several transition metal complexes. In pursuit of these objectives, a multifaceted approach was adopted, leveraging a combination of chiroptical spectroscopic techniques, and complemented by theoretical calculations. The employed chiroptical methodologies encompass Raman optical activity (ROA), vibrational circular dichroism (VCD), and electronic circular dichroism (ECD).

More specifically, Chapter 3 describes the vibrational optical activity properties of atomically precise hexanuclear silver and copper clusters that have rarely been explored in the literature. These clusters are separately decorated with two different ligands. One main goal is to examine the effects of different metal cores on the VCD features of the ligands and the reverse chirality transfer from the metal core to chiral ligands, to complement the commonly reported transfer from the ligands to the metal cores. The second goal is to examine the deficiencies of simplified models in predicting VCD spectra of these clusters, which have been commonly applied in previous pioneering research reports, by using the experimental data and the full metal models. We highlight the critical importance of a complete model for extracting rich information hidden in the experimental VCD features, including bidirectional chirality transfer between ligands and metal cores, as well as the VCD enhancement mechanism.

Another focal point of my thesis research involves examine mechanisms of the observed $I_R - I_L$ features of some lanthanide species, often subject to (near) resonance conditions with the

excitation laser source utilized in ROA. The chemical coordination mechanism in this system was effectively eliminated through the use of a double-cell experimental ROA setup, ensuring no chemical contact between the chiral Ni molecule, the racemic europium complex, and an achiral europium salt. We unraveled the key mechanism responsible for the observed $I_R - I_L$ signals in the Eu species and coined this innovative form of chirality transfer as the “backscattering luminescence mechanism”. In Chapter 5, we conducted a thorough chiroptical analysis of two highly flexible monosaccharide derivatives, phenyl-D-glucopyranoside and 4-(hydroxymethyl)phenyl-D-glucopyranoside. This examination involved the utilization of VCD and ROA spectroscopies, complemented by advanced theoretical modeling. In our forthcoming research, we plan to explore the application of the europium complex as a sensing tool for elucidating the chirality of these biomolecules. Chapter 6 describes the significant VCD enhancement of an open-shell Co(II) transition metal complex with low-lying electronic states. Considerable theoretical modelling, coupled with symmetry consideration in vibronic coupling, was carried out to extract structural information and gain further insights into the enhancement mechanisms.

Preface

This thesis is being submitted as a partial fulfillment of the requirements for the degree of Doctor of Philosophy in Chemistry at the University of Alberta. The work present in this thesis is based on my entire PhD study in the Department of Chemistry at the University of Alberta which started from September 2018 to December 2023 under the supervision of Prof. Yunjie Xu. Some of the works in the current thesis have been published, and the details of the author's contributions are provided in the list below.

Chapter 3 of this thesis is based on a publication draft which will be submitted soon. I have conducted all experimental and theoretical measurements, data analysis, and the writing of the initial manuscript. J.R. Cheeseman made significant contributions in identifying and resolving the initial issues encountered during the theoretical calculations of the clusters. X-Y Dong assisted with the preparation and provision of the actual samples of ligands and clusters. Prof. Y. Xu was the corresponding author and was involved in the conceptualization, data analysis and the manuscript writing-reviewing.

Chapter 4 of my thesis is based on the submitted paper “Mechanisms of Chiral Signals of a Racemic Eu Complex and an Achiral Eu Salt Revealed by Two-Cell Experiments.” M. Alshalalfeh, G. Li, Y. Yang, J. Kapitán, P. Bouř, Y. Xu. In this paper, I conducted all the experimental and theoretical measurements, synthesized the metal complex, data analysis, and initial manuscript writing. G. Li assisted in confirming the results of the two-cell Eu salt experiments and data collection. Y. Yang provided the Python scripts for data analyses. Profs. P. Bouř and J. Kapitán Prof were involved in reviewing and editing of the manuscript. Prof. Y. Xu is the corresponding author who contributed to the conceptualization, data analysis, and reviewing-writing of the manuscript.

Chapter 5 of my thesis is based on the published paper “Conformational Distributions of Phenyl β -D-Glucopyranoside and Gastrodin in Solution by Vibrational Optical Activity and Theoretical Calculations.” M. Alshalafeh, N. Sun, A. H. Moraes, A. P. A. Utani, Y. Xu, *Molecules* **2023**, 28, 4013. In this published paper, I carried out all the experimental and theoretical measurements, data analysis and the initial manuscript writing. N. Sun carried out some early data collection and helped with manuscript preparation. A. H. Moraes did the CREST conformational research and DFT calculations of one molecular system. A. P. A. Utani was involved in some CREST conformational researches. Prof. Y. Xu was the corresponding author and was involved in the conceptualization, data analysis and manuscript writing-reviewing.

Chapter 6 of this thesis is based on a manuscript draft which will be submitted in the next few months. I have completed all the experimental measurements, theoretical DFT and TDDFT calculations, data analysis, and initial manuscript writing. Prof. Y. Xu was the corresponding author and was involved in the conceptualization, data analysis and manuscript writing-reviewing.

Acknowledgement

I would like to express my heartfelt gratitude to Prof. Yunjie Xu, my exceptional supervisor, for her unwavering guidance, invaluable assistance, unyielding support, and priceless mentorship throughout my research journey. Working alongside Yunjie has been an incredible opportunity, enabling me to gain invaluable insights into addressing scientific challenges with unwavering determination and steadfast consistency. I am genuinely elated to have had the privilege of collaborating with someone as compassionate and supportive as her, who wholeheartedly believed in both me and my capabilities. I would like to thank all the group members of Xu and Jäger groups: Guojie, Moe, Jiarui, Aran, Colton, Alex, Amanda, Reihaneh, Arsh, Dr. Xi-Yan Dong and everyone else.

I wish to extend my appreciation to Prof. Wolfgang Jäger for his insightful comments and questions in the group meetings. Furthermore, I would also like to thank all my supervisory committee members, Prof. Mike Serpe and Prof. Gabriel Hanna for their valuable suggestions and constructive comments during my candidacy exam and defense.

I am incredibly grateful to my parents for their unwavering support, which has made me feel like a superhero in this world. My father, Mohammad Alshalalfeh, has been a guiding light in my life, instilling in me the strength and wisdom needed to achieve yet another goal. Additionally, I want to express my deepest love and gratitude to my mother, Aziza Shalalfa. Her continuous prayers and unwavering inspiration have played a pivotal role in the successful completion of this study. I miss you both immensely and eagerly await our reunion!

I want to express my utmost gratitude and appreciation to my sweetheart wife, Islam Shalalfa, for being my other half and the beating heart that keeps me going. Your unwavering support and encouragement have been my driving force throughout my entire Ph.D. journey, particularly

during the challenging process of writing this thesis. Your constant belief in me, motivation, and words of encouragement have been paramount in helping me complete my studies and strive for even greater success. Thank you for always standing by my side and being my biggest cheerleader. Without you, I would not have the passion and energy to finish my Ph.D. Journey. I would like to extend my deepest gratitude from the bottom of my heart to my children, Elaf, and Mohammed, and my little princess, Sham. Your presence in my life has not only transformed it but has also made it immeasurably more enjoyable and fulfilling. To me, each one of you is a true hero, inspiring me with your love, resilience, and joy. My love for you and our incredible children is unwavering and will continue to grow as we build beautiful memories together. Thank you for being the light that brightens my life!

I would also like to extend my thanks to my father-in-law, Shaker, my mother-in-law, Noura, my brothers, Abdelmuneim and Moath, and my sisters, Fedaa and Ayat, for their unwavering support and encouragement. Your presence and belief in me have been a great source of strength and motivation. I am grateful for the love and support I have received from each of you. May God bless you all abundantly for your continued support. Thank you for always being there for me.

Finally, I want to convey my deep gratitude to all my friends at the University of Alberta and throughout Canada. Your presence in my life has been truly priceless. May our connection continue to flourish and strengthen.

Table of Contents

Chapter 1. Introduction.....	1
1.1 An Introduction to Molecular Chirality and Chiroptical Spectroscopy	1
1.2 Chirality Transfer Mechanisms in Chiroptical Spectroscopy	3
1.3 The Applications of Chiroptical Spectroscopy in Transition Metal Complexes	9
1.4 Outline.....	10
1.5 References	13
Chapter 2. Experimental Chiroptical Methods and DFT Calculations	16
2.1 Overview	16
2.2 Raman and ROA	17
2.2.1 Basic terms in Raman and ROA	17
2.2.2 History of ROA Instrument Development	20
2.2.3 The ROA Instrument Used in the Thesis Work	22
2.2.4 Some Tips of Raman/ROA Measurements	26
2.3 Vibrational Circular Dichroism (VCD).....	28
2.3.1 History of VCD.....	28
2.3.2 Basic Terms in VCD	29
2.3.3 The VCD Instrument Used in the Thesis Work	30
2.3.4 Some Tips of VCD Measurements	31
2.3.5 Basic Terms in ECD.....	32
2.3.6 The ECD Instrument Used in the Thesis Work.....	34
2.4 Theoretical Procedures.....	35
2.5 References	40
Chapter 3. Chirality Transfer and Enhancement in Vibrational Circular Dichroism Spectra of Atomically-Precise Metal Clusters.....	44

3.1	Introduction	44
3.2	Results and Discussion.....	47
3.2.1	VCD Studies of the Ligands	47
3.2.2	Experimental and Simulated VCD Spectra of the Ag ₆ D ₆ , Ag ₆ PD ₆ , Cu ₆ D ₆ , and Cu ₆ PD ₆ Clusters.....	52
3.2.3	Simulations of IR and VCD Spectra of Several Metal Cluster Models.....	58
3.3	Conclusion.....	62
3.4	References	64
Chapter 4. Mechanisms of Chiral Signals of a Racemic Eu Complex and an Achiral Eu Salt Revealed by Two-Cell Experiments.....		66
4.1	Introduction	67
4.2	Results and Discussion.....	69
4.2.1	One-cell Experiments.....	69
4.2.2	Two-cell Experiments	74
4.2.3	Simulations of $I_R - I_L$ Spectra	80
4.3	Conclusions	83
4.4	Experimental Section	84
4.5	References	86
Chapter 5. Conformational Distributions of Phenyl β-D Glucopyranoside and Gastrodin in Solution by Vibrational Optical Activity and Theoretical Calculations		89
5.1	Introduction	90
5.2	Results and Discussion.....	93
5.2.1	Low-Energy Conformers of Phenyl β -D-Glucopyranoside and Gastrodin	94
5.2.2	Experimental and Simulated IR and VCD Spectra of ph- β -Glu and Gastrodin ...	102
5.2.3	Experimental and Simulated Raman and ROA Spectra of ph- β -Glu and Gastrodin in Water.....	110

5.2.4	Some General Comments about the Conformational Distribution of ph- β -Glu and Gastrodin in DMSO and in Water	114
5.3	Materials and Methods	117
5.3.1	Experimental	117
5.3.2	Theoretical	118
5.4	Conclusions	119
5.5	References	121
Chapter 6. Chiroptical Spectroscopic and DFT Study of a Chiral Transition Metal Complex with Low-Lying Electronic States.....		124
6.1	Introduction	124
6.2	Experimental and Theoretical Details	127
6.2.1	Experimental Details.....	127
6.2.2	Theoretical Details	128
6.3	Results and Discussion.....	129
6.3.1	Comparison of the Experimental UV-Vis, ECD, IR and VCD Spectra of the Co(II)-salen-chxn Complex with those of its Ligand and other Related Complexes.	129
6.3.2	The most stable conformers of the Co(II)-salen-chxn complex	135
6.3.3	Simulated UV-Vis and ECD Spectra and the Experimental Results	139
6.3.4	Comparison of the Experimental and Simulated IR and VCD Spectra	142
6.3.5	Discussion on Symmetry-Dependent VCD Enhancement	150
6.4	Conclusion.....	153
6.5	References	154
Chapter 7. Conclusions and Future Work.....		156
7.1	Conclusions	156
7.2	Future Work.....	161
7.3	References	164

Bibliography	165
Appendix A: Supporting Information for Chapter 3	184
Appendix B: Supporting Information for Chapter 4	192
Appendix C: Supporting Information for Chapter 5	199
Appendix D: Supporting Information for Chapter 6	206

List of Tables

Table 5.1. The parameters of four main conformers of ph β -glu at the B3LYP-D3BJ/def2-TZVPD level in DMSO.	100
Table 5.2. The parameters of four main conformers of gastrodin at the B3LYP-D3BJ/def2-TZVPD level in DMSO.	101
Table B 1. The experimental dissymmetric $g_{\text{dis}} = (I_R - I_L) / (I_R + I_L)$ factors of the vibrational bands of <i>R</i> -Ni and Eu(FOD) ₃ in CDCl ₃ with the one-cell setup.	196
Table B2. The experimental dissymmetric $g_{\text{dis}} = (I_R - I_L) / (I_R + I_L)$ factors of the vibrational bands of <i>R</i> -Ni in CDCl ₃ (Cell 1) and Eu(FOD) ₃ and EuCl ₃ in ethanol (Cell 2) with the two-cell setup.	197
Table B3. Comparison of the experimental and simulated dissymmetric $g_{\text{dis}} = (I_R - I_L)/(I_R + I_L)$ factors of <i>R</i> -Ni and CDCl ₃ in Cell 1 and Eu(FOD) ₃ , EuCl ₃ and ethanol in Cell 2 with the two-cell experimental setup. ¹	198
Table C 1. The parameters of four main conformers of ph β -glu at the B3LYP-D3BJ/def2-TZVPD level in Water.	205
Table C2. The parameters of four main conformers of gastrodin at the B3LYP-D3BJ/def2-TZVPD level in Water.	205

List of Figures (Chapters)

Figure 2.1. Four different forms of ROA, defined with respect to the polarization states of the incident (red) and scattered (blue) light. <i>R</i> represents right circularly polarized light, <i>L</i> represents left circularly polarized light, and α represents unpolarized light.	20
Figure 2.2. A picture of Chiral Raman -2X TM spectrometer with SCP-ROA configuration.	22
Figure 2.3. Schematic of the optical components inside the Chiral-Raman 2X TM spectrometer.	23
Figure 2.4. Laser system control module. The red “ENABLE” light indicates the laser is on....	24
Figure 2.5. Sample cell holder left one cell setup, and the right double cell setup.....	25
Figure 2.6. The schematic diagram of the FTIR-VCD spectrometer used in the thesis.	30
Figure 2.7. A picture of the JASCO J-1500 circular dichroism (CD) spectrometer in our laboratory.	34
Figure 2.8. A picture of EX2-755_KOOLANCE superior liquid cooling system. F stands for the Fan mode.....	35
Figure 3.1. (a) and (b) are chemical formula of the L/D and PL/PD ligands, respectively. (c) and (d) show how the related ligands arrangements around the Ag ₆ skeleton in the metal clusters. ..	47
Figure 3.2. (a) The optimized geometries of the six low energy D ligand conformers. The relative free energies in kJ mol ⁻¹ and the Boltzmann percentage abundances at 298 K are provided in the brackets. (b) The simulated individual IR (top) and VCD (bottom) spectra of the six most stable D ligand conformers and the related Boltzmann averaged IR and VCD spectra at the wB97XD/def2-TZVPD/PCM(CDCl ₃) level of theory at 298 K. The experimental IR and VCD spectra of D ligand at two different solvents, i.e., CDCl ₃ and CCl ₄ , are also provided. The corresponding IR and VCD spectra of the L ligand are given in grey colour.....	50
Figure 3.3. (a) The two low energy PL/PD ligand conformers identified by the CREST and optimized at a high level of DFT calculations. The relative free energies in kJ/mol and the Boltzmann percentage abundances at 298 K are provided in the brackets. (b) The simulated individual IR (top) and VCD (bottom) spectra of the two most stable/D ligand conformers and the related Boltzmann averaged IR and VCD spectra at the wB97XD/def2-TZVPD/PCM(CDCl ₃) level of theory at 298 K. The experimental IR and VCD spectra (PD red trace, and PL gray trace) in CDCl ₃ are also provided.	51

Figure 3.4. Comparison of the experimental IR and VCD spectra of (a) free ligand PD versus Ag_6PD_6 and Cu_6PD_6 and (b) free ligand D versus Ag_6D_6 and Cu_6D_6 . Note that the experimental IR intensities of the metal clusters are noticeably lower and are amplified so that one can see the weak bands clearly. The corresponding IR and VCD spectra of the L and PL ligands and their metal clusters are given in grey colour. All experiments were conducted in CDCl_3 except Cu_6PD_6 whose measurements were done in CH_2Cl_2 with a much longer pathlength of 0.3 mm. Some wavenumber regions were overwhelmed by solvent bands and were removed for clarity. 53

Figure 3.5. (a) The optimized geometries of Ag_6PD_6 and Ag_6D_6 ; (b) Comparison of the simulated experimental IR and VCD spectra of Ag_6PD_6 and Ag_6D_6 . The corresponding experimental IR and VCD spectra of Ag_6PL_6 and Ag_6L_6 are given in grey colour. The geometry optimizations and the IR and VCD simulations were carried out at the B3PW91-D3BJ/6-31G(d) (LanL2DZ for Ag) level. 57

Figure 3.6. (a) The simple cluster models involve the interaction of one and/or two silver atoms with a one and/or two ligands (b) The simulated IR and VCD spectra of the simple cluster models in (a). 61

Figure 4.1. $I_R + I_L$ (top) and $I_R - I_L$ (bottom) spectra of the racemic $\text{Eu}(\text{FOD})_3$ solutions with a constant concentration of *S*- and *R*-Ni (7.6 mM) in CDCl_3 with the standard one-cell experimental setup. The concentrations of $\text{Eu}(\text{FOD})_3$ 4.9 mM (top), 9.5 mM (middle), and 19.1 mM (bottom). Asterisk * and ** indicates the sharp Eu band at $\sim 1532 \text{ cm}^{-1}$ and the broad Eu features in the 1800-2200 cm^{-1} region. 70

Figure 4.2. Schematic diagrams of a) one-cell and b) two-cell experimental setup using an ROA instrument. In the one-cell set up, both Eu and Ni complexes are dissolved in CDCl_3 and the excitation laser focal point is placed at the center of the cell. In the two-cell setup, only the Ni complex in CDCl_3 is placed in Cell 1, while $\text{Eu}(\text{FOD})_3$ in ethanol or EuCl_3 in ethanol are placed in Cell 2. The laser focal point is placed very close to the front side of Cell 2 as shown in the figure. 74

Figure 4.3. The two-cell $I_R + I_L$ (top) and $I_R - I_L$ (bottom) spectra of the racemic $\text{Eu}(\text{FOD})_3$ solutions with a constant concentration of 7.6 mM of *S*- and *R*-Ni in CDCl_3 in Cell 1. The concentrations of $\text{Eu}(\text{FOD})_3$ in ethanol in Cell 2 are 4.9 mM (top), 9.5 mM (middle), and 19.1 mM (bottom). Asterisk

* and ** indicates the sharp Eu band at $\sim 1532\text{ cm}^{-1}$ and the broad Eu features in the $1800\text{-}2200\text{ cm}^{-1}$ region. 75

Figure 4.4. Top: Experimental $I_R + I_L$ and $I_R - I_L$ spectra of ethanol solutions of racemic $\text{Eu}(\text{FOD})_3$ (9.5 mM), achiral EuCl_3 (19.1 mM) and pure ethanol. Bottom: Experimental $I_R + I_L$ and $I_R - I_L$ spectra of CDCl_3 solutions of racemic $\text{Eu}(\text{FOD})_3$ (4.8 mM) and pure CDCl_3 . These experiments were performed by using 100% left CPL at 532 nm as the excitation source. Please note that the spectra traces are shifted vertically so that they do not overlap on top of each other and the experimental of $I_R + I_L$ and $I_R - I_L$ intensities were scaled by the same factor for easy comparison among the different ethanol or CDCl_3 solutions. Please see the main text for the discussion about luminescence baseline. The inserts show the zoom-in $I_R - I_L$ features in the $1400\text{-}2200\text{ cm}^{-1}$ region. Here asterisk * and ** indicate the sharp $I_R - I_L$ Eu band at $\sim 1532\text{ cm}^{-1}$ and the broad Eu features in the $1800\text{-}2200\text{ cm}^{-1}$ region, respectively. 78

Figure 4.5. Comparison of the simulated and experimental $I_R - I_L$ spectra of (top) $R\text{-Ni}$ (7.6 mM) in CDCl_3 in Cell 1 with EuCl_3 (38.0 mM) in ethanol in Cell 2 and (bottom) $R\text{-Ni}$ (7.6 mM) in CDCl_3 in Cell 1 with $\text{Eu}(\text{FOD})_3$ (19.1mM) in ethanol in Cell 2. Please see the main text for simulation details and discussions. 82

Figure 5.1. The structural formula of (a) ph- β -glu and (b) gastrodin where both molecules are shown in the $4C_1$ chair conformations. (c) Newman projections of the plausible conformations of the hydroxymethyl group of the pyranose ring around the C5–C6 and C6–O6 bonds and the plausible conformations of the phenyl group around the C1–O1 bond. (d) Newman projections of the plausible conformations of the hydroxymethyl group of the phenyl ring around the C10–C13 and C13–O7 bonds. 95

Figure 5.2. Geometries of the 14 most stable conformers of ph- β -glu at the B3LYP-D3BJ/def2-TZVPD level with the PCM of DMSO and water. The relative free energies in kJ mol^{-1} and the percentage Boltzmann factors at 298 K are also given. 97

Figure 5.3. Geometries of the 19 most stable conformers (i.e., conformers with Boltzmann population $> 0.1\%$) of gastrodin at the B3LYP-D3BJ/def2-TZVPD level with the PCM of DMSO and Water. The relative free energies in kJ mol^{-1} and the percentage Boltzmann factors at 298 K are also listed. Note that conformer No. 6 and 10 have the same name based on the current scheme

but have different phenyl group titling positions and are differentiated by adding ‘and’ at the end.
..... 98

Figure 5.4. The simulated individual IR and VCD spectra of the ph- β -glu conformers at the B3LYP D3BJ/def2-TZVPD level with the PCM of DMSO. The conformers are shown based on their theoretical stability, with the most stable one at the top to the least stable one at the bottom.... 103

Figure 5.5. Comparison of the experimental IR and VCD spectra of ph- β -glu in DMSO with the corresponding Boltzmann averaged and re-weighted IR and VCD spectra, simulated at the B3LYP-D3BJ/def2-TZVPD level with the PCM(DMSO). The predicted Boltzmann percentage factors are listed in Figure 5.2 and the adjusted Boltzmann factors are described in the main text. The main IR and VCD features are numbered to facilitate easy comparison. 105

Figure 5.6. Comparison of the experimental IR and VCD spectra of gastrodin with the corresponding Boltzmann averaged IR and VCD spectra at the B3LYP-D3BJ/def2-TZVPD level with the PCM of DMSO theory at 298 K, and the re-weighted IR and VCD spectra. The percentage Boltzmann factors are given in Figure 5.3, while the empirical ones are provided in the main text. The main IR and VCD features are numbered to facilitate easy comparison. 107

Figure 5.7. Comparison of the experimental IR and VCD spectra of ph- β -glu and gastrodin with the corresponding re-weighted simulated IR and VCD spectra at the B3LYP-D3BJ/def2-TZVPD level with the PCM of DMSO. Several regions are shaded to draw attention to the changes in the IR and VCD features in the experiments and how well they were reproduced by the modelling.
..... 109

Figure 5.8. Comparison of the experimental Raman and ROA spectra of ph- β -glu in water with the corresponding Boltzmann averaged and re-weighted Raman and ROA spectra, simulated at the B3LYP-D3BJ/def2-TZVPD level with the PCM (water). The predicted Boltzmann percentage factors are listed in Figure 5.2 and the adjusted Boltzmann factors are described in the main text. The main Raman and ROA features are numbered to facilitate easy comparison..... 111

Figure 5.9. Comparison of the experimental Raman and ROA spectra of gastrodin in water with the corresponding Boltzmann averaged and re-weighted Raman and ROA spectra, simulated at the B3LYP-D3BJ/def2-TZVPD level with the PCM (water). The predicted Boltzmann percentage factors are listed in Figure 5.3 and the adjusted Boltzmann factors are described in the main text. The main ROA and the corresponding Raman features are numbered for easy comparison. See the main text for discussions..... 113

Figure 6.1. The molecular formula of the R,R-Co(II)-salen-chxn complex, (R,R)-(-)-N, N'-Bis(3,5-di-tert-butylsalicylidene)-1,2-cyclohexanediaminocobalt(II). Here tBu indicates the tertbutyl group..... 126

Figure 6.2. The experimental UV-vis spectra (top panel) and ECD spectra (bottom panel) for both the RR- salen-chxn ligand and its metal (Co(II), Mn(III), Cu(II), and Ni(II)) complexes. The UV-vis and ECD measurements of these systems done at different concentration. The data for RR-salen-chxn ligand, Ni(II), and Cu(II) complexes were collected from Ref. 19. 132

Figure 6.3. The experimental IR spectra (top panel) and VCD spectra (bottom panel) of the salen-chxn ligand and its metal complexes, Co(II), Mn(III), Cu(II), and Ni(II) salen-chxn. The data for RR salen-chxn ligand, Ni(II), and Cu(II) complexes from Ref. 19. Please note that while the IR intensity scale used is the same for all species and the IR spectrum of each species is shifted for easy comparison. Similarly, the same VCD intensity scale is used for Mn(III), Cu(II) and Ni(II), whereas the intensity scale of Co(II) is *10 times larger* than the others. 133

Figure 6.4. Experimental IR (top panel) and VCD (bottom panel) spectra of Co(II)-salen-chxn complex in CDCl₃ solution in the range of 1400 to 3800 cm⁻¹, PEM optimized at 3000 cm⁻¹, The asterisk (*) in the spectrum is related to the strong C-D stretching band of CDCl₃ and the corresponding feature in the ΔA spectrum may be artifact. Please see the main text for additional discussion..... 134

Figure 6.5. (a) The optimized geometries of the four most stable salen-chxn ligand conformers and (b) The optimized geometries of the three most stable Co(II)-salen-chxn conformers at the B3LYP-D3BJ/6-311++G(d,p) level of theory with the PCM of CDCl₃. The relative free energies in kJ/mol at the low spin of the ligand, and low and high spin of the metal complex and the Boltzmann percentage abundances at 298 K are provided in the brackets. 138

Figure 6.6. Comparison of the experimental and simulated UV-Vis (top) and ECD (bottom) spectra of Co(II)-salen-chxn using the B3LYP-D3BJ/6-311++G(d,p)/PCM(acetonitrile) level of theory. The first 250 electronic states were included in the calculations at the level of theory indicated. For the averaged spectra, we used the same Boltzmann weights used for the IR and VCD calculations. 140

Figure 6.7. Comparison of the experimental VCD spectrum and the simulated averaged ECD spectrum of high spin Co(II)-salen-chxn in the IR region. Please note that the calculated ECD spectrum was red-shifted by 1000 cm⁻¹ for comparison with the experiment. 141

Figure 6.8. The simulated individual IR and VCD spectra of the three most stable Co(II)-salen-chxn conformers (low spin) at the B3LYP-D3BJ/6-311++G(d,p)/PCM (CHCl₃) level of theory at 298 K. 144

Figure 6.9. The simulated individual IR and VCD spectra of the three most stable Co(II)-salen-chxn conformers (high spin) at the B3LYP-D3BJ/6-311++G(d,p)/PCM (CHCl₃) level of theory at 298 K. 145

Figure 6.10. Comparison of the experimental IR and VCD spectra of Co(II)-salen-chxn with the corresponding Boltzmann averaged IR and VCD spectra at the B3LYPD3BJ/6-311++G(d,p) level with the PCM of chloroform at 298K. 147

Figure 6.11. Example normal modes to the vibrational band at 1621 cm⁻¹, and at 1610 cm⁻¹ of A and B symmetry, respectively. Atom displacements are represented by the blue arrows. 151

Figure 6.12. Comparison the Experimental VCD spectrum with the calculated VCD spectrum of the most stable conformer at high spin state for the C₂-symmetrized structure of Co (II)- salen chxn. The red arrows indicate the experimental bands which correspond to the A symmetry vibrational motions and their VCD patterns are correctly predicted. See the main text for discussion. 152

List of Figures (Appendices)

- Figure A1.** The ordered arrangement of ligands around the Cu₆ skeleton in Cu₆L₆ and Cu₆D₆, derived from the final optimization geometry. 186
- Figure A2.** Comparison of the experimental and simulated IR (top) and VCD (bottom) spectra of L/D and L in CDCl₃. The individual conformer IR and VCD spectra, as well as their Boltzmann weighted spectra at the at the B3LYP- GD3BJ/def2-TZVPD/PCM are shown. The gray spectrum represents the ligand enantiomer L. 187
- Figure A3.** Comparison of the experimental and simulated IR (top) and VCD (bottom) spectra of PD in CDCl₃. The corresponding experimental IR and VCD spectra of PL in CDCl₃ are given in grey colour. The individual conformer IR and VCD spectra, as well as their Boltzmann weighted spectra at the at the B3LYP- GD3BJ/def2-TZVPD/PCM are shown. 188
- Figure A4.** Comparison of the simulated IR and VCD spectra of Cu₆PD₆ , Cu₆D₆, Ag₆PD₆ , and Ag₆D₆ . The geometry optimizations and the IR and VCD simulations were carried out at the B3PW91-D3BJ/6-31G(d) (LanL2DZ for Cu and Ag) level. 189
- Figure A5.** Comparison of the simulated and the experimental IR and VCD spectra of Cu₆PD₆ and Cu₆D₆. The corresponding experimental IR and VCD spectra of Cu₆PL₆ and Cu₆L₆ are given in grey colour. The geometry optimizations and the IR and VCD simulations were carried out at the B3PW91-D3BJ/6-31G(d) (LanL2DZ for Cu) level. 190
- Figure A6.** The zoom-in exciton section showing the exciton coupling of the bisignate bands of the six C=N stretching modes which hare presented by the blue sticks. It is interesting to note that drastically different IR and VCD intensities of these modes. Some have greatly enhanced g factors. 191
- Figure B1.** $I_R + I_L$ (top) and $I_R - I_L$ (bottom) spectra of the racemic Eu(FOD)₃ and the chiral Ni complex solutions with a constant concentration of racemic Eu(FOD)₃ (19.1 mM) in CDCl₃ with the standard one-cell experimental setup. The concentrations of *S*- or *R*-Ni are 7.6 mM (top) and 3.8 mM (bottom). Please see the main text for discussion on the intensities of the Eu species (marked by asterisks). 192
- Figure B2.** These are the standard one-cell experimental data. Top: $I_R - I_L$ (top) spectrum of *R*-Ni (8.3 mM) in CDCl₃. Bottom: $I_R + I_L$ spectra of *R*-Ni (8.3 mM) in CDCl₃, pure CDCl₃, and

Eu(FOD)₃ (4.6 mM) in CDCl₃. From the $I_R + I_L$ spectra, one can see no visible change to the band positions of CDCl₃. 193

Figure B3. a) UV-Vis (top) and ECD (bottom) spectra of racemic Eu(FOD)₃ (0.77 mM, blue), *R*-Ni (0.31 mM, black), and a mixture (red) of Eu(FOD)₃ and *R*-Ni (0.38 mM, 0.16 mM, red) in CDCl₃. The path length used is 1 mm. The intensities for only *R*-Ni and only Eu(FOD)₃ solutions were scaled by a factor of 0.5 for easy comparison. b) The UV-Vis (blue) and ECD (black) spectra from 532 nm to 620 nm of *R*-Ni (9.2 mM) in CDCl₃, corresponding to the relevant Raman range from 0-2668 cm⁻¹ (see the Raman axis at the top). The path length used is 10 mm. 194

Figure B4. Two-cell $I_R + I_L$ (top) and $I_R - I_L$ (bottom) spectra of the achiral EuCl₃ solutions with a concentration of 7.6 mM of *S*- and *R*-Ni in CDCl₃ in Cell 1. The concentration of a chiral EuCl₃ in ethanol in Cell 2 is 38 mM. Asterisk * and ** indicates the sharp Eu band at ~1524 cm⁻¹ and the broad Eu features in the 1800-2200 cm⁻¹ region. 195

Figure C1. The C1-O1-C7-C12 dihedral angle values which correspond to the tilting of the phenyl plane are given in blue (in unit of degree) for each of the 14 most stable conformers of ph-β-glu at the B3LYP-D3BJ/def2-TZVPD level with the PCM of DMSO. 199

Figure C2. The C1-O1-C7-C12 dihedral angle values which correspond to the tilting of the phenyl plane are given in blue (in unit of degree) for each of the 19 most stable conformers of gastrodin at the B3LYP-D3BJ/def2-TZVPD level with the PCM of DMSO. 200

Figure C3. Geometries of the five less stable conformers of gastrodin with the Boltzmann population factors ≤ 0.1% at the B3LYP-D3BJ/def2-TZVPD level with the PCM of DMSO or Water. The relative free energies in kJ mol⁻¹ and the percentage Boltzmann factors at 298 K are also given for both solvents. 201

Figure C4. The simulated individual IR and VCD spectra of the 19 most stable gastrodin conformers with the Boltzmann population factors greater than 0.1% at the B3LYP-D3BJ/def2-TZVPD level with the PCM of DMSO. 202

Figure C5. The simulated individual Raman and ROA spectra of the 14 most stable ph-β-glu conformers at the B3LYP- D3BJ/def2-TZVPD level with the PCM of water. 203

Figure C6. The simulated individual Raman and ROA spectra of the 19 most stable gastrodin conformers with the Boltzmann population factors greater than 0.1% at the B3LYP-D3BJ/def2-TZVPD level with the PCM of water. 204

Figure D1. Experimental mass spectrum of (R,R)-Co(II)-salen-chxn. 206

Figure D2. The molecular formula of the R,R-Mn-Cl(III)-salen-chxn complex, (R,R)-(+)-N,N'-Bis(3,5-di-tert-butylsalicylidene)-1,2-cyclohexanediaminomanganese(III) chloride. Here tBu indicates the tertbutyl group..... 206

Figure D3. The simulated individual and Boltzmann average UV-Vis (top) and ECD (bottom) spectra of Co(II)-salen-chxn (low spin with spin multiplicity of 2) using the B3LYP-D3BJ/6-311++G(d,p)/PCM(acetonitrile) level of theory. The first 250 electronic states were included in the calculations at the level of theory indicated. For the Averaged spectra, we used the same Boltzmann weights derived from the IR and VCD calculations. 207

Figure D4. The simulated individual and Boltzmann average UV-Vis (top) and ECD (bottom) spectra of Co(II)-salen-chxn (high spin, with spin multiplicity of 4) using the B3LYP-D3BJ/6-311++G(d,p)/PCM(acetonitrile) level of theory. The first 250 electronic states were included in the calculations at the level of theory indicated. For the Averaged spectra, we used the same Boltzmann weights derived from the IR and VCD calculations. 208

List of Symbols

S_n	Improper axis of rotation
I_R	Intensity of right circularly polarized light
I_L	Intensity of left circularly polarized light
λ	Wavelength
μ_{ind}	Induced electric dipole moment
$\tilde{\alpha}_{\alpha\beta}$	Electric dipole- electric dipole polarizability tensor
E	Strength of the external electric field,
Q_K	Normal coordinates of the normal mode
\hbar	Planck's constant divided by 2π
n	Initial electronic state
m	Final electronic state
j	Excited (virtual) electronic state
ω_{jn}	Angular frequency difference between the states j and n
ω_0	Angular frequency of the scattering radiation
ω_R	Angular frequency of the incident laser radiation
$\tilde{G}_{\alpha\beta}$	Electric dipole- magnetic dipole polarizability tensor
$\tilde{A}_{\alpha\beta\gamma}$	Electric dipole- electric quadrupole polarizability tensor
Γ_j	Damping factor
$\tilde{\mu}_a$	Electric dipole moment operator
\tilde{m}_β	Magnetic dipole moment operator
$\tilde{\theta}_{\beta\gamma}$	Electric quadruple moment operator
A_L	Absorption of left circularly polarized light
A_R	Absorption of right circularly polarized light
ΔA	Differential absorption left and right circularly polarized light
R_{ge}	Rotational strength
$\cos\theta$	The angle between the electric dipole and magnetic dipole transition moment vectors
ψ_e	Wavefunction of excited state

ψ_g	Wavefunction of ground state
ε_L	Molar absorptivity coefficient for left circularly polarized light
ε_R	Molar absorptivity coefficient for right circularly polarized light
$\Delta\varepsilon$	Differential molar absorptivity coefficient
g	Anisotropy factor

List of Abbreviations

ROA	Raman optical activity
VCD	Vibrational circular dichroism
CP-Raman	Circularly polarized Raman
eCP-Raman	Electronic circular dichroism-circularly polarized Raman
ECD	Electronic circular dichroism
AC	Absolute configuration
VOA	Vibrational optical activity
CID	Circular intensity difference
IRROA	Induced resonance Raman optical activity
RROA	Resonance Raman optical activity
AIRROA	Aggregation-induced Resonance Raman optical activity
SERS	Surface-enhanced Raman scattering
SPRs	Surface plasmon resonances
CPLu	Circularly polarized luminescence
EuCl ₃	Europium (III) chloride hexahydrate
Eu(FOD) ₃	Europium (III)-tris(1,1,1,2,2,3,3-heptafluoro-7,7-dimethyl-4,6-octanedionate)
RR-Ni	RR-bis (pyrrol-2-ylmethyleneamine)-cyclohexane nickel (II)
L/D	(S)-/(R)-4-isopropylthiazolidine-2-thione
PL/PD	(S)-/(R)-4-phenylthiazolidine-2-thione
ph-β-glu	Phenyl β-D-glucopyranoside
ECM	Exciton chirality method
ETDMs	Electric dipole transition moments
LCPL	Left circularly polarized light
RCPL	Right circularly polarized light
DFT	Density functional theory
TD-DFT	Time-dependent density functional theory
PCM	Polarizable continuum model
PEM	Photoelastic modulator
SCP	Scattered circular polarization

ICP	Incident circular polarization
DCP	Dual circular polarization
CCD	Charge coupled detector
AC	Alternating current
LIA	Lock-in-amplifier
CREST	Conformer-rotamer ensemble sampling tool
xTB	A semiempirical tight-binding quantum chemistry method
RMSD	Root-mean-square deviations
D3BJ	Grimme's dispersion correction with Becke Johnson damping
B3LYP	Becke, 3-parameter, Lee–Yang–Parr, Hybrid functio

Chapter 1

Introduction

1.1 An Introduction to Molecular Chirality and Chiroptical Spectroscopy

The discovery of circularly polarized light in 1809 by É. L. Malus was a groundbreaking development in the field of optics.¹ Later, F. Arago studied the optical rotation caused by quartz crystals when exposed to polarized light.² In 1815, J. B. Biot discovered that certain natural organic compounds, such as sucrose, turpentine, camphor and tartaric acid, rotated polarized light in their liquid or solution states.³ Further research established that this phenomenon, known as optical activity or optical rotation, was related to the presence of asymmetric molecules.⁴ In 1848, L. Pasteur made the breakthrough discovery of chirality through his investigations into tartaric acid's chemical and physical properties.⁵ He observed that the two forms of tartaric acid had differing melting points and optical activities, thus paving the way for the birth of stereochemistry and the study of the three-dimensional structure of molecules.

A molecule is chiral if its mirror image cannot be superimposed onto itself,⁶ and the mirror-imaged pair are called enantiomers which have the same chemical and physical properties in an achiral environment but differ in the spatial orientations of constituent atoms, which might lead to completely different behavior in a chiral environment. In the language of molecular symmetry, a molecule is chiral if it does not have any improper axis of rotation (S_n) with any values of n .⁷ Chirality is a crucial factor in the development of stereochemical models, especially in the

pharmaceutical industry.⁸ This is because more than half of the drugs discovered and produced are chiral,^{9a} indicating a strong reliance on stereochemical principles. It is well documented that an enantiomer of a drug can be beneficial for a patient while its mirror-image could be ineffective, and even harmful. For this reason, it is essential to gain deep understanding of relationships between structural and other properties of chiral molecules to their functions. Thalidomide is one of the most notorious examples of a drug in literature. Initial studies found that the R-enantiomer was effective at alleviating the nausea experienced by pregnant women, the S-enantiomer caused serious birth defects.^{9b} Later, further studies revealed that the seemingly safe R-enantiomer could easily convert into the hazardous S-enantiomer in the human body, which can cause severe birth defects for fetuses.¹⁰

A variety of spectroscopic techniques have been developed and employed to identify and analyze the unique properties of chiral molecules. These include optical rotatory dispersion (ORD),¹¹ nuclear magnetic resonance (NMR), X-ray crystallography, electronic circular dichroism (ECD), vibrational circular dichroism (VCD),¹² and Raman optical activity (ROA) spectroscopy.¹³

NMR is a popular and powerful method for structural determination. On the other hand, to extract information about chirality, one usually needs expensive chiral shift agents which often require additional syntheses¹⁴ since NMR by itself is generally not sensitive to chirality.

X-ray crystallography has been extensively used in literature to determine 3D structures of chiral crystals with high-resolution data at the atomic level.¹⁵ One major disadvantage of this technique is that a high-quality single crystal sample is needed. In addition, researchers are increasingly aware that the conformation and even 3D chiral configuration of a chiral molecular system in the solid form may differ from that in a liquid state.¹⁶ While ORD measurements are easy to perform, the detailed interpretation is often hampered by large solvation effect.¹⁷ The ECD technique

measures the differential absorption of left- and right-circularly polarized electromagnetic radiation by a sample accompanying an electronic transition.¹⁸ It has been extensively used for analyzing absolute configurations and sometimes also conformations of chiral compounds directly in solution or in the liquid phase.¹⁹ Typically, a chiral molecule of interest needs to have one or more chromophores which are responsible for the occurrence of electronic transitions in the UV-vis region. Moreover, the very broad ECD spectral features make the accurate interpretation of these spectra, and therefore the identification of the chirality labels of stereogenic centers in the sample challenging and sometimes less reliable.^{19(a)}

In my Ph.D. research, I have primarily utilized VCD and ROA techniques, along with ECD techniques in some cases, to extract stereochemical structural information and to elucidate the mechanisms responsible for chiroptical signatures in various compounds. These compounds encompass several atomically precise silver and copper clusters, a europium complex, two highly flexible monosaccharide derivatives, which will serve as prototypes for future europium sensing studies, as well as several transition metal complexes. Additional information regarding the fundamentals of the VCD, ROA and ECD instruments will be discussed in Chapter 2.

In the following two subsections, I will provide background information related to my thesis work and explain the motivation for the projects completed in this thesis.

1.2 Chirality Transfer Mechanisms in Chiroptical Spectroscopy

Chiral transfer phenomena have generated significant interest due to its potential applications in nanotechnology, analytical chemistry, and other fields. This process involves transferring the chirality property of a chiral molecule to a nonchiral molecule, thus rendering it optically active. The most commonly encountered chirality transfer mechanism involves direct chemical or physical interactions, where a new chiral complex is formed through covalent or non-

covalent bonding between a chiral molecule and a non-chiral molecule. For example, T. Mizutani et al. recorded the induced ECD spectra of a complex formed by 2,2'-biphenol derivatives with chiral trans-1,2-cyclohexane diamine derivatives in a variety of solvents.²⁰ They indicated that the appearance of the induced ECD was caused by a combination of hydrogen bonding and Van der Waals interactions. Later on, similar phenomena were observed in VCD studies.²¹ Another interesting observation is the induced water VCD features at the water bending region where the comparison of the experimental and calculated VCD data provided insight into hydrogen bonding interactions between a chiral solute and water molecules.²² These observations provided the foundation for the clusters-in-a-liquid solvation model²³ which emphasizes the small long-lived chiral solute—water complexes and which has been utilized successfully to explain water solvent effects.²⁴

For ROA, a new chirality transfer and amplification mechanism based on long-range interactions between chiral molecules and the surface plasmons of achiral dye-tagged nanoprobe was discovered in 2015.²⁵ Pour et al. studied the chiroptical features induced in achiral benzotriazole azo dye molecules bound to silver silica nanotags when small sugar chiral molecules were added to the solution. The authors hypothesized that chirality of the sugar molecules is transferred to the achiral dye molecules through the surface plasmons generated in silver nanoparticles. In addition, very strong 'ROA' spectra were observed for carotenoid upon aggregation of the monomers, whereas the ROA spectrum of carotenoid in its monomeric form is quite weak. This significant enhancement was referred to as Aggregation-induced Resonance Raman Optical Activity (AIRROA).²⁶ Later on, it was recognized that these AIRROA observations were actually due to a new form of chiral Raman spectroscopy (*vide infra*).

Most recently, a new form of chiral Raman spectroscopy with resonant chiral molecules was uncovered.²⁷ This new form is called as eCP-Raman, which stands for a combination of electronic circular dichroism (ECD) and circularly polarized-Raman (CP-Raman). When a chiral molecule is under (near) resonance in an ROA experiment, several light-matter interaction events can occur simultaneously. Briefly, when a randomly polarized light shines on the (near) resonating chiral sample, the ECD differential absorption of the resonating chiral solute molecules generates an imbalance in the right versus left circularly polarized light. The circularly polarized light scatters off chiral solute and solvent molecules, leading to significant $I_R - I_L$ intensities of the chiral solute and (achiral) solvent molecules. Here I_R and I_L refer to the scattered intensity of the right and left circularly polarized light, respectively.

The conventional metal nanoparticles, for example the silver and gold nanoparticles, can often be excited by visible lasers commonly used in Raman and ROA experiments to generate surface plasmon resonances (SPRs). SPRs have been utilized extensively in surface-enhanced Raman spectroscopy (SERS) to detect Raman spectra of a trace amount of a sample. Nanoparticles functionalized with chiral ligands have drawn considerable interest from the scientific community due to their versatile applications. Plasmonic nanoparticles strongly affect the optically active behavior of chiral molecules adsorbed onto the nanoparticle's surface, significantly enhancing the (chir)optical response of those chiral molecules.²⁸ The direct applications of gold or silver nanoparticles in ROA have been very limited despite considerable research efforts. It is now widely known that the SPR properties of silver and gold nanoparticles are affected by the uniformity of their size and shape. The variability in size and shape among nanoparticles makes it highly challenging to obtain consistent ROA features for interpretation. On the other hand, even the most

skilled colloid chemists find it difficult to produce identical nanoparticles. These concerns have inspired chemists to work on synthesizing truly uniform nanoparticles at the atomic level.

Recent advances in synthesis have enabled chemists to produce uniform metal sub-nanoparticles at the atomic level, namely, atomically precise metal clusters. The atomically precise metal clusters consist of a few to tens of atoms of metal with well-defined chemical formula and ligand shell structures. This new category of materials has attracted extraordinary attention due to their fascinating yet well-defined structures and a wide range of unusual (optical) properties. These atomically precise metal clusters fill the gap between discrete atoms and plasmonic nanoparticles, providing unique opportunities for investigating quantum effects and precise structure-property correlations at the atomic level.²⁹ Not surprisingly, atomically precise clusters are highly prized in a nanochemist's tool box because they offer the opportunity to control the size and uniformity of metal clusters with atomic precision, facilitating fine-tuning of their targeted properties, such as spectroscopic or catalytic properties.³⁰

More specifically to vibrational optical activity research, VCD study of chiral ligands decorated on gold nanoparticles was pioneered by the research group of T. Bürgi.³¹ For example, they recorded the experimental VCD spectrum of small-sized gold nanoparticles functionalized with the chiral molecule 1,1'-binaphthyl-2,2'-dithiol (BINAS) was recorded.^{31(b)} The VCD spectrum of adsorbed BINAS is different from that of free BINAS, a consequence of chemical contact between the ligand sulfur atoms and the gold atoms. It was difficult to precisely determine the structures of functionalized AuNPs with BINAS since the exact composition and binding sites of these nanoparticles are not well defined. A simplified model was proposed by using a Au₁₀ cluster with one chiral ligand to simulate the experimental VCD spectrum where the simulated

VCD spectrum shows some agreement with the experimental VCD spectrum in the 1300 to 1600 cm^{-1} region.^{31(b)}

To the best of our knowledge, the vibrational optical activity properties of atomically precise metal clusters have rarely been explored in the literature. One recent example is the VCD study of thiolate-protected Au_{25} clusters with mixed ligands, $(\text{PET})_{18-2x}(\text{R-FBINAS})_x$.³² Here, PET = 2-phenylethylthiol and R-FBINAS = 5,5',6,6',7,7',8,8'-octafluoro-[1,1'-binaphthalene]-2,2'-dithiol. Again, a simplified model with one R-FBINAS ligand was used to explain the experimental observation. In this thesis work, we have applied VCD and ROA techniques to examine a group of atomically precise hexanuclear silver and copper clusters with separately decorated with two different ligands which were recently successfully synthesized by Han. et al. and possess ultrastability and high quantum efficiency in photoluminescence.³³ While detailed ROA measurements were hampered by overwhelming luminescence background, successful VCD studies were carried out for the ligands and the metal clusters. In particular, we focused on the gaining detailed molecular level insights into the relationships between VCD features and (structural) properties of ligands and metal cores. The experimental and theoretical results will be discussed in detail in Chapter 3.

Another area of interest in chirality transfer events in this thesis involves lanthanide complexes. These complexes have found widespread applications, such as in medicine as contrast agents for magnetic resonance imaging for cancer diagnosis and therapy.³⁴ Moreover, lanthanide complexes, exemplified by tris(dipivaloylmethanato)-europium(III) $[\text{Eu}(\text{dpm})_3]$, are frequently used in analytical chemistry and biochemistry as (chiral) shift reagents in NMR studies.³⁵ Additionally, in the realm of optical spectroscopic applications, lanthanide complexes typically exhibit intense luminescence, which is also highly sensitive to the lanthanide metal's environment,

including interactions with nearby (chiral) functional groups. The strong circularly polarized luminescence (CPLu) properties of lanthanide complexes, in particular, have attracted significant attention due to their potential applications in chiral sensing of biomolecules³⁶ and information storage in quantum computing.³⁷ While a CPLu spectrometer is typically employed to detect the luminescence and CPLu spectra of lanthanide and transition metal complexes,³⁸ it was demonstrated recently that an ROA spectrometer can also be used to detect CPLu signals.³⁹ In an ROA spectrometer, luminescence is excited via high intensity laser radiation, and circularly polarized components are detected using a highly sensitive, artifact-resistant detection scheme. This approach offers the advantages of using a laser source to detect weak CPLu signals and collecting different types of spectroscopic data, including Raman, ROA, eCP-Raman, Lu and CPLu, using one single sample solution in the same experiment.

In these ROA experiments with lanthanide complexes, multiple species commonly experience (near) resonance conditions with the excitation laser source. As mentioned earlier, the discovery processes of the new chiral Raman spectroscopy, eCP-Raman, highlight numerous potential light-matter interaction events occurring simultaneously in such chiral spectroscopic experiment. It is, therefore, essential to investigate the mechanisms behind the reported CPLu signals by an ROA instrument using an ROA instrument or, more generally, to examine the observed $I_R - I_L$ signals under (near) resonance conditions.

To achieve this goal, we designed an innovative two-cell experimental setup and utilized several sets of samples, including a racemic europium complex and an achiral europium salt, to explore all possible (chiral) light-matter events under such experimental conditions. The results will be described in Chapter 4. Additionally, to examine how a europium complex can be employed to sense the chirality of flexible biomolecules, we conducted studies on two highly flexible

monosaccharide derivatives, namely phenyl-D-glucopyranoside and 4-(hydroxymethyl)phenyl-D-glucopyranoside (commonly known as gastrodin) using both VCD and ROA spectroscopies and theoretical modelling. The results will be outlined in Chapter 5. Although not within the scope of the current thesis, future sensing studies of these compounds with a europium complex will be performed.

1.3 The Applications of Chiroptical Spectroscopy in Transition Metal Complexes

Transition metal complexes with Schiff base ligands have become increasingly popular among researchers over the last few decades due to their impressive structural topology, magnetic properties, and catalytic and biological activity.⁴⁰ The preparation and characterization of metal complexes and metal–ligand interactions has played an integral role in a range of research areas from bioinorganic chemistry to molecular framework materials to small molecule catalysis.⁴¹ In recent years, researchers have investigated chirality related properties of a range of Schiff based ligand transition metal complexes from stereochemical structural information to chirality transfer mechanisms by utilizing mainly VCD and ROA, sometimes supported with ECD spectroscopy in conjunction with theoretical modelling.⁴² For instance, Dezhahang et al. conducted an in-depth investigation of the structural characteristics, such as ligand chirality, metal helicity, and coordination geometry, of five transition metal complexes including Ni(II), Cu(II), Pd(II), Pt(II), and Zn(II) formulated with bis(pyrrol-2-ylmethyleneamine)-cyclohexane ligand in solution via a combination of ECD, VCD spectroscopy along with high-level DFT calculations.^{42(a)} These complexes were later utilized in resonance ROA studies where a new form of chiral Raman spectroscopy, i.e., eCP-Raman, was discovered.²⁷ Furthermore, the on-going development of

theoretical treatment of resonance ROA demands more reliable experimental data in this regard.⁴³ In my thesis work, I explored some related Schiff-based transition metal complexes using both VCD and ROA techniques. While the ROA experiments were unsuccessful due to the high fluorescence background, the VCD study highlights some very interesting observation associated low-lying d-d transition of the metal center. Currently, there is no proper theoretical treatment available to simulate VCD spectra of species with low-lying electronic transitions. Although we are in discussion with theorists in the field, only the experimental results and preliminary theoretical calculations will be summarized in Chapter 6 of the thesis.

1.4 Outline

The rest of my thesis is organized below. In chapter 2, I provide a comprehensive description of the fundamentals and instrumental components of ROA, VCD, and ECD spectroscopy techniques. I briefly explain the working principle and design of the major optical components of these spectroscopic techniques. Furthermore, I discuss some tips for experimental ROA and VCD measurements. In the last section, I focus on the procedures I used to search for possible conformers and to apply Density Functional Theory (DFT) simulations for Raman, ROA, IR, VCD, UV-Vis, and ECD spectra.

In Chapter 3, I applied VCD spectroscopy to investigate the stereochemical properties of atomically precise metal clusters, namely octahedral Ag_6L_6 (and Ag_6D_6), Ag_6PL_6 (and Ag_6PD_6), and Cu_6L_6 (and Cu_6PL_6) clusters, where L/D = *S*/*R*-4-isopropylthiazolidine-2-thione, and PL/PD = *S*/*R*-4-phenylthiazolidine-2-thione, as well as the associated ligands. We complemented the experimental investigations with theoretical calculations. These include systematic conformational searches for the ligands, simulations of IR and VCD spectra of the ligands and the metal clusters. One main goal is to examine the effects of different metal cores on the VCD features of chiral

ligands, which is associated with the reversed chirality transfer from the metal core to the chiral ligands. Second goal is to evaluate some simplified models which were often utilized in the previous VCD studies of chiral metal nanoparticles and atomically precise metal clusters with the outcome of full model. Finally, the exciton coupling phenomenon was discussed to elucidate the variations in the VCD signals intensity and the associated mechanisms.

Chapter 4 delves into the intricate details of chirality transfer mechanisms involving two complexes under resonance: the chiral (*R,R* and *S,S*)-bis (pyrrol-2-ylmethyleneamine)-cyclohexane nickel (II) complex, denoted as *R*-Ni and *S*-Ni, respectively, and the racemic europium (III)-tris(1,1,1,2,2,3,3-heptafluoro-7,7-dimethyl-4,6-octanedionate) complex, denoted as Eu(FOD)₃. These investigations were conducted with an ROA spectrometer with two different ROA setups, i.e., a single one-cell setup, in which all components are residing within the same cell, and a two-cell ROA setup designed to ensure that there was no chemical or physical contacts between the resonating nickel (II) complex and Eu(FOD)₃. The latter setup was employed to effectively eliminate any contributions from the chemical contact mechanism, a common one identified before.³⁹ Furthermore, we explored the detected Eu *I_R-I_L* band features and evaluate the influence of various mechanisms. Finally, the simulations based on the proposed mechanisms were compared with the experimental data to verify the mechanisms.

In Chapter 5, I used the ROA and VCD spectroscopy to investigate the conformational landscapes of two highly flexible monosaccharide derivatives, namely phenyl β-D-glucopyranoside (ph-β-glu) and 4-(hydroxymethyl)phenyl β-D-glucopyranoside. The primary objective of this study is to investigate the impact of the additional hydroxymethyl group located at the para-position of the phenyl ring of gastrodin on its chiroptical properties. Remarkably, even slight alterations in the sugar conformation can result in discernible variations in VCD and ROA

features, offering an opportunity to explore the ligand's intricate conformational landscape. Furthermore, in this project, we conducted a comparative analysis between the final experimental results and the corresponding theoretical outcomes, to validate the quality and accuracy of the created theoretical model.

In Chapter 6, I measured experimental VCD and ECD spectra of an open-shell Co(II) transition metal complex. A noticeable enhancement in the experimental VCD signals was observed and can be primarily attributed to the emergence of low-lying electronic states. By employing a range of theoretical calculations, including the exploration of different spin states and charges for the targeted complex and also symmetry consideration in vibronic coupling, I aimed to generate some agreement between the simulated and experimental spectra. Additional information about the low-lying electronic states of this open shell system was also provided by the experimental and theoretical ECD investigations.

In the last chapter of my thesis, I provide a comprehensive conclusion of my work, summarizing the key findings from each chapter. I also propose some potential future projects to further enhance our understanding of chirality transfer mechanisms in atomically precise metal clusters and in those systems containing europium salt and racemic europium complexes. Lastly, I have included several appendices at the end of my thesis which contain all the supporting information for each research chapter.

1.5 References

- [1] J. Gal, Chiral drugs from a historical point of view, WILEY-VCH, Weinheim, **2006**.
- [2] N. Berova, P. L. Polavarapu, K. Nakanishi, R. W. Woody, Comprehensive Chiroptical Spectroscopy: Instrumentation, Methodologies, and Theoretical Simulations, John Wiley & Sons, Hoboken, NJ, **2012**.
- [3] J. Gal, P. Cintas, Early History of the Recognition of Molecular Biochirality. In Biochirality: Origins, Evolution and Molecular Recognition; Cintas, P., Ed.; Springer: Berlin/Heidelberg, Germany, **2013**.
- [4] H. Morawetz, Polymers: the origins and growth of a science, Courier Corporation, **2002**.
- [5] J. Gal, *Helv. Chim. Acta*, **2013**, 96, 1617-1657.
- [6] M. Liu, L. Zhang, T. Wang, *Chem. Rev.* **2015**, 115, 7304-7397.
- [7] F. A. Cotton, Chemical Applications of Group Theory, John Wiley & Sons: New York, **1990**.
- [8] M. Abram, M. Jakubiec, K. Kamiński, *ChemMedChem*. **2019**, 14, 1744-1761.
- [9] (a) L. A. Nguyen, H. He, C. Pham-Huy, *Int. J. Biol. Sci.* **2006**, 2, 85-100; (b) T. Asatsuma-Okumura, T. Ito, H. Handa, *Pharmaceuticals* **2020**, 13, 95.
- [10] J. H. Kim, A. R. Scialli, *Toxicological Sciences* **2011**, 122, 1-6.
- [11] G. Mazzeo, E. Santoro, A. Andolfi, A. Cimmino, P. Troselj, A. G. Petrovic, S. Superchi, A. Evidente, N. Berova, *J. Nat. Prod.* **2013**, 76, 588-599.
- [12] (a) P. L. Polavarapu, *Chiroptical Spectroscopy: Fundamentals and Applications*, CRC Press, Boca Raton, FL, **2016**; (b) G. Yang, Y. Xu, *Top. Curr. Chem.* **2011**, 298, 189-236.
- [13] (a) L. A. Nafie, *Vibrational Optical Activity: Principles and Applications*, John Wiley & Sons, Ltd., UK, **2011**; (b) L. D. Barron, *Molecular light scattering and optical activity*, 2nd edn. Cambridge, **2004**.
- [14] (a) Y. Hu, K. Cheng, L. He, X. Zhang, B. Jiang, L. Jiang, C. Li, G. Wang, Y. Yang, M. Liu, *Anal. Chem.* **2021**, 93, 1866-1879; (b) M. R. Poopari, Z. Dezhahang, K. Shen, L. Wang, T. L. Lowary, Y. Xu, *J. Org. Chem.* **2015**, 80, 428-437; (c) J. M. Seco, E. Quiñoá, R. Riguera, *Chem. Rev.* **2012**, 112, 4603-4641.
- [15] (a) S. Parsons, *Tetrahedron: Asymmetry* **2017**, 28, 1304-1313; (b) Q. B. Cass, M. E. Tiritan, J. M. B. Junior, J. C. Barreiro, *Chiral Separations and Stereochemical Elucidation: Fundamentals, Methods, and Applications*, John Wiley & Sons, **2023**.

- [16] A. Pandey, S. Dalal, S. Dutta, A. Dixit, *J. Mater. Sci.-Mater. Electron.* **2021**, 32, 1341-1368.
- [17] (a) P. Lahiri, K. B. Wiberg, P. H. Vaccaro, M. Caricato, T. D. Crawford, *Angew. Chem. Int. Ed.* **2014**, 53, 1386-1389; (b) G. Yang, Y. Xu, *Phys. Chem. Chem. Phys.* **2008**, 10, 6787-6795.
- [18] G. Pescitelli, L. Di Bari, N. Berova, *Chem. Soc. Rev.* **2011**, 40, 4603-4625.
- [19] (a) G. Pescitelli, *Chirality* **2022**, 34, 333-363; (b) Z. Dezhahang, M. R. Poopari, F. E. Hernández, C. Diaz, Y. Xu, *Phys. Chem. Chem. Phys.* **2014**, 16, 12959-12967; (c) G. Yang, J. Li, Y. Liu, T. L. Lowary, Y. Xu, *Org. Biomol. Chem.* **2010**, 8, 3777-3783.
- [20] T. Mizutani, H. Takagi, O. Hara, T. Horiguchi, H. Ogoshi, *Tetrahedron Lett.* 1997, 38, 1991-1994.
- [21] T. Burgi, A. Vargas, A. Baiker, *J. Chem. Soc., Perkin Trans.* **2002**, 2, 1596-1601.
- [22] (a) G. Yang, Y. Xu, *J. Chem. Phys.* **2009**, 130, 164506; (b) M. Losada, Y. Xu, *Phys. Chem. Chem. Phys.* **2007**, 9, 3127-3135; (c) C. Merten, Y. Xu, *Angew. Chem. Int. Ed.* **2013**, 52, 2073-2076; (d) J. E. Rode, M. H. Jamróz, J. Sadlej, J. Cz. Dobrowolski, *J. Phys. Chem. A.* **2012**, 116, 7916-7926; (e) A. S. Perera, J. Cheramy, C. Merten, J. Thomas, Y. Xu, *ChemPhysChem* **2018**, 19, 2234-2242.
- [23] A. S. Perera, J. Thomas, M. R. Poopari, Y. Xu, *Front. Chem.* **2016**, 4, 1-17.
- [24] (a) Y. Yang, J. Cheramy, M. Brehm, Y. Xu, *ChemPhysChem* **2022**, 23, e202200161/1-11; (b) A. S. Perera, C. D. Carlson, J. Cheramy, Y. Xu, *Chirality* **2023**, 1-14; (c) Y. Yang, M. Alshalalfeh, Y. Xu, *Spectrochim. Acta A Mol. Biomol. Spectrosc.* **2023**, DOI: 10.1016/j.saa.2023.123634.
- [25] S. O. Pour, L. Rocks, K. Faulds, D. Graham, V. Parchaňský, P. Bouř, E. W. Blanch, *Nat. Chem.* **2015**, 7, 591-596.
- [26] G. Zajac, A. Kaczor, A. Pallares Zazo, J. Mlynarski, M. Dudek, M. Baranska, *J. Phys. Chem. B.* **2016**, 120, 4028-4033.
- [27] (a) G. Li, J. Kessler, J. Cheramy, T. Wu, M. R. Poopari, P. Bouř, Y. Xu, *Angew. Chem. Int. Ed.* **2019**, 58, 16495-16498; (b) T. Wu, G. Li, J. Kapitán, J. Kessler, Y. Xu, P. Bouř, *Angew. Chem. Int. Ed.* **2020**, 59, 21895-21898; (c) G. Li, M. Alshalalfeh, Y. Yang, J. R. Cheeseman, P. Bouř, Y. Xu, *Angew. Chem. Int. Ed.* **2021**, 60, 22004-22009; (d) E. Machalska, G. Zajac, A. J. Wierzba, J. Kapitán, T. Andruniów, M. Spiegel, D. Gryko, P. Bouř, M. Baranska, *Angew. Chem. Int. Ed.* **2021**, 60, 21205-21210.

- [28] (a) A. Nemati, S. Shadpour, L. Querciagrossa, L. Li, T. Mori, M. Gao, C. Zannoni, T. Hegmann, *Nat. Commun.* **2018**, 9, 3908; (b) T. Mori, A. Sharma, T. Hegmann, *ACS Nano*, **2016**, 10, 1552-1564; (c) S. Bettini, M. Ottolini, D. Valli, R. Pagano, C. Ingrosso, M. Roeffaers, J. Hofkens, L. Valli, G. Giancane, *Nanomaterials* **2023**, 13, 1526.
- [29] X. Kang, Y. Li, M. Zhu, R. Jin, *Chem. Soc. Rev.* **2020**, 49, 6443-6513.
- [30] M. J. Alhilaly, R.-W. Huang, R. Naphade, B. Alamer, M. N. Hedhili, A.-H. Emwas, P. Maity, J. Yin, A. Shkurenko, O. F. Mohammed, M. Eddaoudi, O. M. Bakr, *J. Am. Chem. Soc.* **2019**, 141, 9585-9592.
- [31] (a) C. Gautier, T. Bürgi, *J. Am. Chem. Soc.* **2006**, 128, 11079-11087; (b) C. Gautier, T. Bürgi, *J. Phys. Chem. C*, **2010**, 43, 15897-15902.
- [32] A. Sels, R. Azoulay, W. J. Buma, M. A. J. Koenis, V. P. Nicu, T. Bürgi, *J. Phys. Chem. C* **2019**, 123, 22586-22594.
- [33] Z. Han, X.-Y. Dong, P. Luo, S. Li, Z.-Y. Wang, S.-Q. Zang, T. C. W. Mak, *Sci. Adv.* **2020**, 6, eaay0107.
- [34] M. T. Kaczmarek, M. Zabiszak, M. Nowak, R. Jastrzab, *Coord. Chem. Rev.* **2018**, 370, 42-54.
- [35] S-H. Lam, H-Y. Hung, P-C. Kuo, D-H. Kuo, F-A. Chen, T-S. Wu, *Molecules* **2020**, 25, 5383.
- [36] S. E. Bodman, S. J. Butler, *Chem. Sci.* **2021**, 12, 2716-2734.
- [37] J. F. Sherson, H. Krauter, R. K. Olsson, B. Julsgaard, K. Hammerer, I. Cirac, E. S. Polzik, *Nature* **2006**, 443, 557-560.
- [38] O. G. Willis, F. Zinna, L. Di. Bari, *Angew. Chem. Int. Ed.* **2023**, 62, e202302358.
- [39] (a) T. Wu, *Phys. Chem. Chem. Phys.* **2022**, 24, 15672-15686; (b) T. Wu, J. Kapitán, V. Andrushchenko, P. Bouř, *Anal. Chem.* **2017**, 89, 5043-5049.
- [40] P. S. Steinlandt, L. Zhang, E. Meggers, *Chem. Rev.* **2023**, 123, 4764-4794.
- [41] S. M. Wilkinson, T. M. Sheedy, E. J. New, *J. Chem. Educ.* **2016**, 93, 351-354.
- [42] (a) G. Li, D. Li, M. Alshalalfeh, J. Cheramy, H. Zhang, Y. Xu, *Molecules* **2023**, 28, 2571; (b) Z. Dezhahang, M. R. Poopari, J. Cheramy, Y. Xu, *Inorg. Chem.* **2015**, 54, 4539-4549.
- [43] S. Lubber, *Biomed. Spectrosc. Imaging* **2015**, 4, 255-268.

Chapter 2

Experimental Chiroptical Methods and DFT Calculations

2.1 Overview

As indicated in the introduction chapter, several spectroscopic techniques have been employed in my Ph.D. research. These techniques include Raman, IR, and UV-Vis spectroscopies as well as their chiral counterparts, Raman Optical Activity (ROA), Vibrational Circular Dichroism (VCD), and Electronic Circular Dichroism (ECD) spectroscopies, respectively. Raman, IR and UV-Vis spectroscopies can provide general structural information, such as the presence of certain functional groups and some geometric and electronic properties of the systems in solution. One main drawback with these conventional techniques is that they often do not offer enough specificity to distinguish different conformers of the targeted molecular systems. For example, in recent IR and VCD spectroscopic studies of steroid hormones¹ and monosaccharides,² the predicted IR spectra are nearly the same among the different conformers and therefore could not be used to distinguish conformational species of the targeted molecules in solution. The chiroptical spectroscopic counterparts, in particular, ROA and VCD, exhibit chiroptical spectral features which are exquisitely sensitive to conformational differences, in addition to chirality, thus providing rich stereochemical including conformational information about these chiral species in solution directly.¹ I used two main instruments in my thesis research which include IR, VCD, Raman, and ROA spectroscopic techniques. Since the associated fundamental theories have been discussed in many papers and textbooks,³ the readers are referred to them for the detailed

derivations and descriptions. In this chapter, I will first briefly go over some basic terms used in these spectroscopies, their history, and some key components in these two main instruments, as well as practical tips for their operations. In addition, the information about the UV-Vis and ECD spectrometer is also included.

To interpret the experimental chiroptical spectra and to extract structural information from the experimental results, it is essential to carry out density functional theory (DFT) simulations of the corresponding IR, Raman, UV-Vis, VCD, ROA, and ECD spectra of the targeted systems and compare the simulation results with the experimental observations to extract structural and dynamical information. The simulation approach is completed using multiple steps which will be summarized in the later section, as well as the levels of theory utilized in the current thesis work.

2.2 Raman and ROA

2.2.1 Basic terms in Raman and ROA

The subsequently emitted photons may end up in different vibrational levels. This frequency shift is known as a Raman shift, and it provides information about different vibrational levels, thus information about composition and structural information of the targeted molecules. For one particular (*k*th) vibrational mode, its scattering Raman intensity is directly proportional to its square of the induced electric dipole moment (μ) as represented in equation (2.1)

$$I_{Raman} \propto \mu_{ind}^2 \quad (2.1)$$

and the induced electric dipole moment (μ) can be represented by equation (2.2).

$$\mu_{ind} = \alpha E = \left(\frac{\partial \alpha}{\partial Q_k} \right) Q_k E \quad (2.2)$$

Where (E) is the strength of the external electric field, (α) is the electric dipole- electric dipole polarizability tensor, which measures the electrons cloud distortion in the path of the incident light,

and it is closely related to the property of the molecule. The Q_k term is the normal coordinates of the k th normal mode at equilibrium positions (o). According to equation (2.2), the Raman shift is only activated when the polarizability of the molecule changes during the vibration, this can be expressed mathematically by the following equation:

$$\left(\frac{\partial\alpha}{\partial Q_k}\right)_o \neq 0 \quad (2.3)$$

In order to calculate the Raman intensity, only the electric dipole-electric dipole polarizability tensor ($\tilde{\alpha}_{\alpha\beta}$) needs to be taken into account,^{3a} which is given by.

$$\tilde{\alpha}_{\alpha\beta} = \frac{1}{\hbar} \sum_{j \neq m, n} \left[\frac{\langle m | \tilde{\mu}_\alpha | j \rangle \langle j | \tilde{\mu}_\beta | n \rangle}{\omega_{jn} - \omega_0 - i\Gamma_j} + \frac{\langle m | \tilde{\mu}_\beta | j \rangle \langle j | \tilde{\mu}_\alpha | n \rangle}{\omega_{jn} + \omega_R + i\Gamma_j} \right] \quad (2.4)$$

where \hbar is Planck's constant divided by 2π , and the summation is over all excited electronic states (virtual), j , except the initial and final states, n and m , respectively. The Greek subscripts (α, β, γ) denote vector or tensor components and can be equal to x, y or z Cartesian coordinates. The ω_{jn} , ω_0 , ω_R terms are the angular frequency difference between the states j and n , the angular frequency of the incident laser radiation, and angular frequency of the scattering radiation, respectively. The terms $i\Gamma_j$ are imaginary terms proportional to the width of the electronic state j , and hence inversely proportional to its lifetime. The first term is called resonance term, and the second term is the non-resonance term. The case of $\omega_{jn} \approx \omega_0$ results in the denominator of the first term becoming very small, causing it to become the dominant term and thus leading to a significant enhancement in the Raman intensities.

On the other hand, the chiral version of Raman spectroscopy (ROA), measures the difference in Raman scattered intensity between right and left circular polarized light when a randomly polarized light is shone on a chiral molecule. Since only a few numbers of the scattering

photons are scattered at different frequencies from the incident light frequency (Raman scattering). The main drawback of ROA spectroscopy is the weakness of the signal intensity. A typical circular intensity difference (CID) the ROA/Raman intensity ratio is $\sim 10^{-4}$. Therefore, high-concentration sample and long acquisition time under normal conditions, are often necessary for reliable ROA measurements. To improve the accuracy of the ROA intensity calculation, in addition to the electric dipole-electric dipole polarizability tensor should be considered in Raman scattering, but also two other types of polarizability tensors, magnetic dipole-electric dipole ($\tilde{G}_{\alpha\beta}$) (equation 2.5), and electric quadrupole-electric dipole ($\tilde{A}_{\alpha\beta\gamma}$) (equation 2.6) tensors should be taken in account.³

$$\tilde{G}_{\alpha\beta} = \frac{1}{\hbar} \sum_{j \neq m, n} \left[\frac{\langle m | \tilde{\mu}_a | j \rangle \langle j | \tilde{m}_\beta | n \rangle}{\omega_{jn} - \omega_0 - i\Gamma_j} + \frac{\langle m | \tilde{m}_\beta | j \rangle \langle j | \tilde{\mu}_a | n \rangle}{\omega_{jn} + \omega_R + i\Gamma_j} \right] \quad (2.5)$$

$$\tilde{A}_{\alpha\beta\gamma} = \frac{1}{\hbar} \sum_{j \neq m, n} \left[\frac{\langle m | \tilde{\mu}_a | j \rangle \langle j | \tilde{\theta}_{\beta\gamma} | n \rangle}{\omega_{jn} - \omega_0 - i\Gamma_j} + \frac{\langle m | \tilde{\theta}_{\beta\gamma} | j \rangle \langle j | \tilde{\mu}_a | n \rangle}{\omega_{jn} + \omega_R + i\Gamma_j} \right] \quad (2.6)$$

The ROA is associated with a two-photon process (one incident photon and one scattered photon). As a result, there are four configurations based on the polarization status of incident light and scattered light⁴ as shown in figure 2.1. The ICP-ROA refers to the incident circular polarization (ICP) form where circularly polarized incident laser light is used while the total scattered light intensity is monitored. The ROA form used in all commercial ROA instruments is the scattered circular polarization (SCP) form where the incident laser light is unpolarized and the scattered light is monitored as the difference in the right (I_R) and left (I_L) circularly polarized light intensity, i.e., $I_R - I_L$. In addition, the scattering form can be forward scattering (0°), right-angle scattering (90°), or backscattering (180°). In the in-phase dual circular polarization (DCP_I) and the out-of-phase dual circular polarization (DCP_{II}) forms, the incident and scattered light are both circularly

polarized. The main difference between them that in the DCP_I form the polarization statuses of incident and scattered radiation are switched synchronously, whereas in the DCP_{II} the polarization statuses of incident and scattered radiation are switched oppositely.

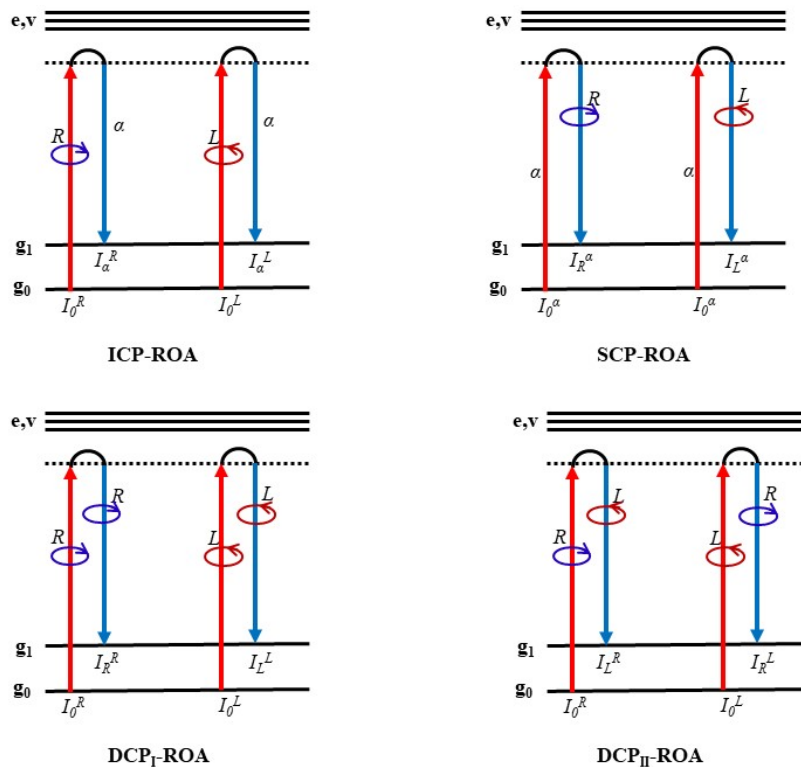


Figure 2.1. Four different forms of ROA, defined with respect to the polarization states of the incident (red) and scattered (blue) light. *R* represents right circularly polarized light, *L* represents left circularly polarized light, and α represents unpolarized light.

2.2.2 History of ROA Instrument Development

In 1969, Atkins and Barron⁵ published a paper entitled “Rayleigh scattering of polarized photons by molecules”, which provides a general theory of the polarization characteristics of Rayleigh and Raman scattered light from molecules. In 1971, Barron and Buckingham⁶ presented the first theory of the ROA, providing insight into the origins of the different scattered intensities in right and left circularly polarized light. Recording the ROA spectra at that time was hampered

by numerous artifact signal issues, leading to several entirely spurious ROA spectra being published. Much efforts had been made by Barron, Bogaard and Buckingham⁷ and subsequently in 1973 they recorded the reliable spectra of chiral α -phenylethylamine using the ICP-ROA configuration with right-angle (90°) geometry. Two years later, Hug et al.⁸ conducted further ROA measurements and reported the first complete ROA spectra of (d+)- α -phenylethylamine and (-)- α -pinene. α -pinene has since been used as a standard sample for calibrating and testing the ROA instrument.

In the past few decades, great efforts have been made to optimize and improve the performance of ROA spectrometers by modifying the instrumental configurations. These modifications have led to more reliable and accurate ROA spectra, with better signal-to-noise ratios and less artifacts in the resulting spectra. For instance, Hug and Surbeck⁹ added an analyzer to the light pathway to facilitate collections of both parallel and perpendicular scattered light, making it easier to recognize and eliminate optical artifacts. Barron et al. revolutionized the design of the ROA instrument by replacing the typical right-angle (90°) geometry with a backscattering (180°) geometry in conjunction with a cooled charge-coupled device (CCD) detector.¹⁰ This remarkable innovation renders the ROA technique much more accessible to a wide range of applications. In 1989, L. A. Nafie and his collages¹¹ introduced the dual circular polarization (DCP)-ROA configuration. They employed an analyzer in the scattered beam and needed to record only half of the ordinary Raman intensity compared to an ICP measurement under the same laser conditions.¹² Since the noise level is proportional with the square root of the ordinary Raman intensity, the DCP form improves the signal-to-noise quality of ROA spectra. In 1999, Hug and his team developed the first dual-channel design with a high-output spectrograph for their ROA instrument.¹³ Furthermore, in 2002, they introduced a novel approach of employing a half

waveplate to create *virtual* enantiomers to counteract offset and artefacts generated from optical components.¹⁴ Following that, the Bio tools company adopted Hug's breakthrough into the current commercialize SCP-ROA spectrometer.

2.2.3 The ROA Instrument Used in the Thesis Work

In this thesis, Raman and corresponding chiral Raman spectra were recorded with a commercial Chiral-Raman 2XTM spectrometer as shown in Figure (2.2). The intensity differentials of left and right circularly polarized scattered light from chiral systems were measured using the scattered circular polarization SCP-ROA configuration. This configuration uses backscattering geometry to minimize the artifacts and other optical offsets. Therefore, the charge coupled detector (CCD) is set up to be able to capture only the scattering light whose propagation direction is 180 degrees to the incident radiation. Below, I briefly describe the backscattering SCP-ROA's key optical components according to the sequence the light passes through, as outlined by Bio Tools (Figure 2.3).



Figure 2.2. A picture of Chiral Raman -2XTM spectrometer with SCP-ROA configuration.

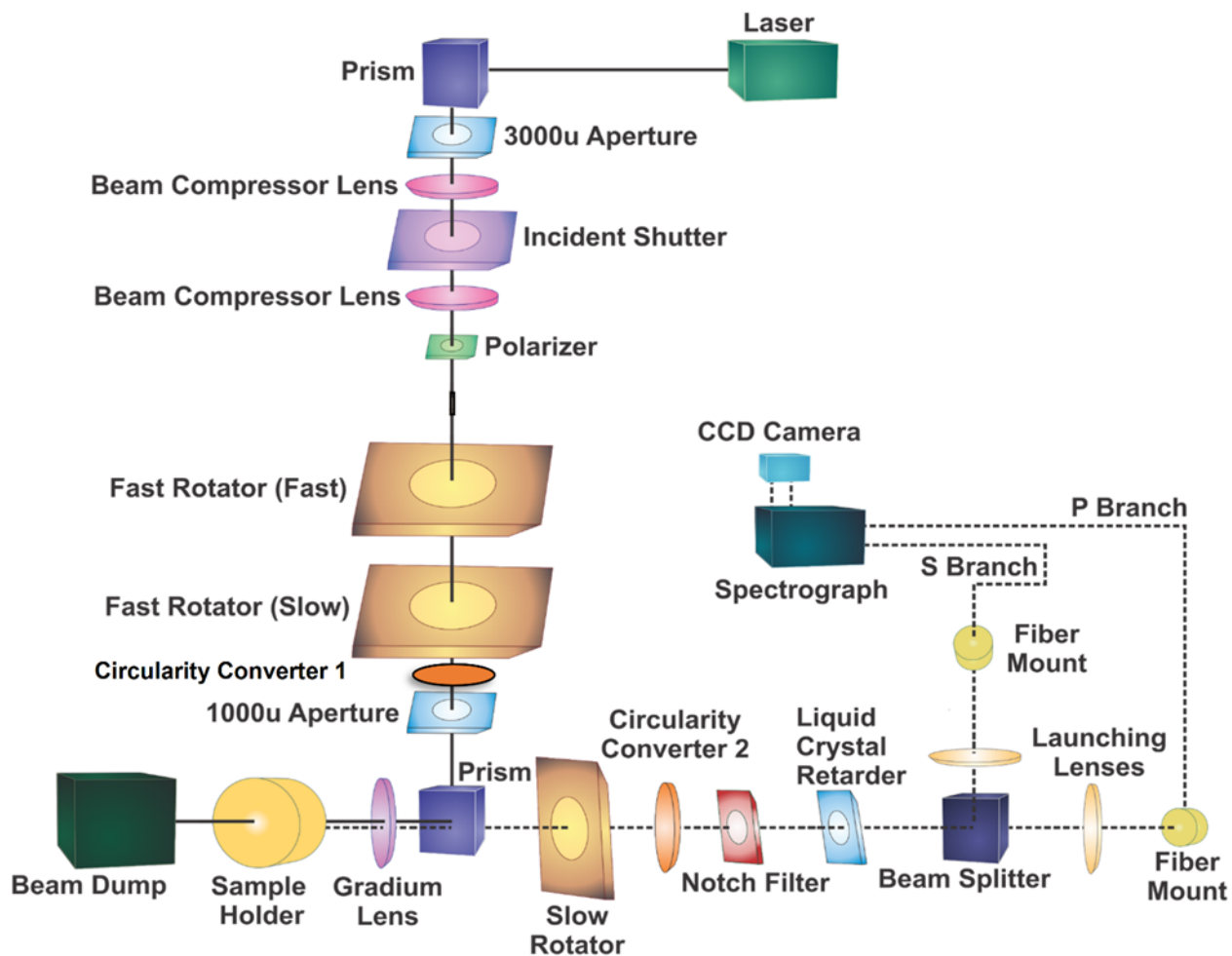


Figure 2.3. Schematic of the optical components inside the Chiral-Raman 2X™ spectrometer.¹⁵

Laser: An OPUS 532 laser can generate a continuous wave of coherent green light with a wavelength of 532nm, with adjustable power from 0W to 2W with horizontal polarization. Figure 2.4 depicts the laser control system, which uses a key and enable button to switch the laser on and off. In addition, a rotational knob can be used to adjust the laser's power.

Incident shutter: Permitting the specified amount of radiation to pass into the sample.



Figure 2.4. Laser system control module. The red “ENABLE” light indicates the laser is on.

Polarizer: Designed to allow transmission of incident beams with desired circularly polarized components, while blocking unwanted incident beams with non-desired circularly polarized components.

Fast rotators: A set of counter-rotating $\lambda/2$ waveplates that rotate in different directions, which produces linearly polarized light in all orientations and ensures that the incident beam is completely randomly polarized.

Circularity converter 1 (CC1): A half wavelength plate is used to convert *LCPL* to *RCPL* and vice versa. During measurements, the plate can be moved in and out of the beam path to adjust the unwanted circularly polarized contaminations in the incident beam pathway.

Prism: Divert the perpendicular circularly polarized incident light toward the sample cell and allow the parallel scattered light to pass through it.

Sample Holder: It can hold one or two silica cells, a parafilm block used to block the position of cell two in the event of single-cell measurements. The cell position is adjustable in X, and Y, using the screws or a rotating ring to adjust the Z direction as shown in Figure 2.5.

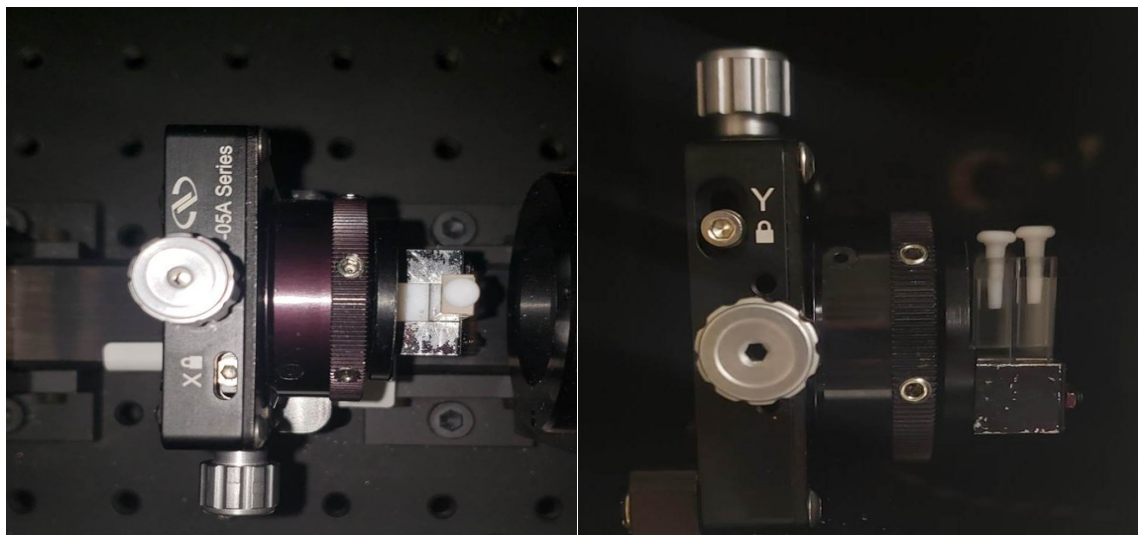


Figure 2.5. Sample cell holder left one cell setup, and the right double cell setup.

Slow rotator: A half-wave plate is utilized to rectify any linear polarization that was left behind by preceding optical components.

Circularity converter 2 (CC2): A half wavelength plate is used to create a mirrored version of the original molecule, known as the "virtual enantiomer". W. Hug is credited with originating the idea of virtual enantiomer which was further explored in Ref. 14. Since it is not possible to eliminate systematic instrumental offsets by simply extending the collection time, nor can it be identified through comparison with either reference or subsequent measurements. The CC2 was designed to counteract the instrumental offset by creating enantiomers optically, which is done by generating a circularly polarized light that is opposite to the light scattered by the sample.

Notch filter: Eliminating the strong Rayleigh scattering is crucial, as 99.9% of the scattered photons have a Rayleigh scattering and less than 0.1% of the scattered photons have a Raman effect.

Liquid crystal retarder: A quarter wavelength plate that converts the right and left circularly polarized light into either p- type or s-type linearly polarized light depending on the orientation of the fast and slow axes of the crystal.

Beam splitter: Split the p-type and s-type linearly polarized light that are generated from the liquid crystal retarder and direct each into a distinct fiber optic branch.

Fiber Optic Branches: Two fiber optic bundles are arranged to collect the light scattered at one end and disperse it in a parabolic pattern aligned with the slit of the spectrograph at the other end.

Spectrograph: Diffracting the collected scattered light onto the CCD by placing a volume-phase holographic transmission grating in the path of the beam.

CCD Camera: A back-thinned camera that is composed of a 1024x256 pixel array is split in half horizontally. The top and the bottom portions of the array capture light that is scattered from two different fiber optic branches.

2.2.4 Some Tips of Raman/ROA Measurements

The Raman and ROA measurements challenges are listed below.

- **Fluorescence effect:** It is the most common and challenging issue for Raman and ROA measurements and is often observed when a sample and sometimes even trace amount of stabilizer added by companies are in resonance with the incident radiation. To reduce the fluorescence caused by impurities, we use high laser power to burn them off. The procedure for this step requires opening the incident shutter and exposing the sample to high laser

power greater than 300mW, for 30 minutes or longer. This approach, on the other hand, may cause damage and/or fragmentation of a sample. Apply it carefully.

- Focal point: It is very challenging to achieve the optimum focal point of the incident light, especially when switching from one-cell to two-cells measurements or vice versa. We note that the cell holder can be adjusted in all directions. If the focal point of the incident light is not properly optimized (i.e., the cell position is not optimized), a strong Rayleigh scattering may be generated by the cell itself which can overpower the desired Raman signal. For this reason, it is recommended to run a (-)- α pinene standard measurement to verify the optimum cell position.
- Cell cleaning: Another challenge in the use of Raman and ROA spectroscopies for a variety of materials, such as transition metal complexes, sugars solutions, and nanomaterials, is the need for a clean cell. In order to obtain reliable results, it is essential to properly clean the cell between measurements to remove any residues from the previous material. Based on my observations, the most efficient way of cleaning a cell is to start with rinsing the cell with your solvent, followed by using a diluted acid—such as 2M HCl or 2M HNO₃ for samples containing proteins, salts, and oils. Alternatively, the cell can be rinsed with pure water more than 10 times if the sample contains alcohols, acids, and bases. Additionally, it is advisable to utilize 5M HNO₃ on fluorescence material and then rinse it with distilled water right away. Afterwards, allow the cell to dry through airflow. It is essential to delicately clean the exterior of the cell using lens cleaning paper in order to protect the cell's surface coating, as damage to the coating can cause out-of-control Rayleigh scattering. It is essential to replace the cell if its cell surface coating is compromised.

2.3 Vibrational Circular Dichroism (VCD)

2.3.1 History of VCD

The initial VCD measurements were conducted utilizing a dispersive scanning instrument, limiting the amount of data that could be collected from a single spectral region. In 1974, Holzwarth and collaborators¹⁶ were the first to document a VCD experiment, examining the C-H stretching region of enantiomers and racemic mixture of 2,2,2-trifluoro-1-phenylethanol in a neat form. A year after, Nafie and others used a VCD spectrometer with two ZnSe modulators which showed considerable performance improvement to re-examine the chiral molecule in the C-H stretching¹⁷ and O-H and N-H stretching region.¹⁸ These modifications resulted in an increased effectiveness in the mid-infrared spectral area. In 1979, the FT-VCD technique was first employed by L. A. Nafie to examine the enantiomeric forms of camphor in tetrachloromethane solvent utilizing an FT-IR spectrometer in the C-H stretching part of the spectrum. This revealed the capability of FT-IR and FT-VCD spectrometers to improve signal quality and reduce the measurement time in comparison to the standard dispersive scanning approach.¹⁹ In 1982, a landmark advancement in VCD measurements was made possible with the implementation of numerous refinements to the FT-IR and VCD instrument, including the addition of a HgCdTe cryogenically cooled detector and a CaF₂ polarizer, thereby enabling it to recognize the fingerprint range in the middle-infrared spectrum (900-1600 cm⁻¹).²⁰ In the mid-1990s, BioTools company released the first ever commercialized standalone ChiralIR FT-VCD spectrometer, opening the door for a large variety of innovative applications to be enabled by VCD spectroscopy from investigations of condensed phase peptides,²¹ to identifying exotic non-covalently bonded species in solution,²² to probing supramolecular chirality,²³ and to combining it with matrix isolation cold rare gas matrix to study unusual aggregates,²⁴ just to name a few. Nowadays, VCD accessories and

standalone spectrometers can also be purchased from different providers such as Bruker, BioTools, Jasco, and Thermo-Electron.

2.3.2 Basic Terms in VCD

The chiral version of IR spectroscopy is the VCD spectroscopy, which can measure the small difference of the left and right circularly polarized light of the chiral molecules during a vibrational transition, as it is presented in equation below.

$$\Delta A(\nu) = A_L(\nu) - A_R(\nu) \quad (2.7)$$

The intensity and sign of the VCD signals can be elucidated by the rotational strength equation provided in the equation (2.8).

$$R_{ge} = \text{Im}\{\langle \psi_g | \tilde{\mu} | \psi_e \rangle \cdot \langle \psi_e | \tilde{m} | \psi_g \rangle\} \quad (2.8)$$

Where g and e stand for the ground and the excited vibrational levels, respectively. Im stands for the imaginary part. The Im operation ensures that the rotational strength is a real quantity as required for an observable by quantum mechanics. $\tilde{\mu}$ is the electric dipole moment operator and \tilde{m} is the magnetic dipole moment operator. The rotational strength given in the equation above is a scalar product of the two different vectors, i.e., electric transition dipole moment $\langle \psi_g | \tilde{\mu} | \psi_e \rangle$ and magnetic transition dipole moment $\langle \psi_e | \tilde{m} | \psi_g \rangle$.

The rotational strength (R) of the system can also be expressed concisely using equation (2.9).

$$R = |\vec{\mu}| \cdot |\vec{m}| \cdot \cos \theta \quad (2.9)$$

where $|\vec{\mu}|$ is the magnitude of electric dipole transition moment and $|\vec{m}|$ is the magnitude of magnetic dipole transition moment. The angle θ is the angle between the electric and magnetic transition dipole moment vectors. The scalar product is positive if the angle between these two vectors is $0^\circ - (<)90^\circ$, negative if the angle is more than $(>)90^\circ - 180^\circ$, and VCD response will be

zero if the angle is 90° . One major obstacle is that VCD signals are relatively small compared to the corresponding IR signals and the anisotropy factor of intensities of VCD to the IR is typically in the range of 10^{-4} to 10^{-6} .

2.3.3 The VCD Instrument Used in the Thesis Work

In this thesis, all the IR and VCD measurements were carried out using a FTIR-VCD instrument manufactured by Bruker. The schematic diagram is shown in Figure 2.6. This module consists of two key components: a FTIR spectrometer (Vertex 70) and a VCD module (PMA 50). Below, I provide detailed explanations of the key FTIR-VCD components.

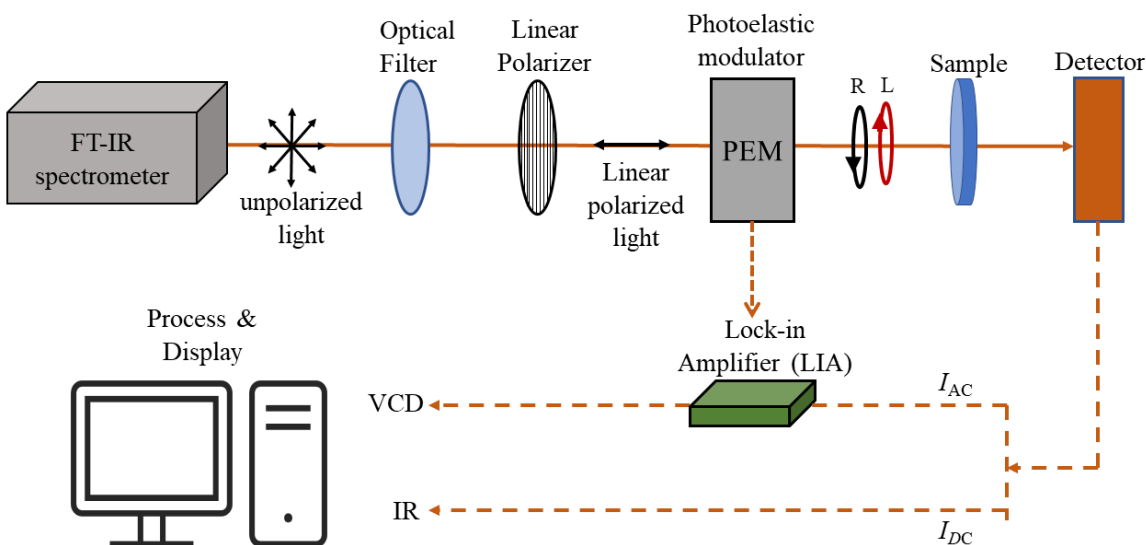


Figure 2.6. The schematic diagram of the FTIR-VCD spectrometer used in the thesis.

The unpolarized output beam generated from FT-IR spectroscopy is first filtered by passing through an optical filter component, which eliminates frequencies outside of the desired range. The unpolarized infrared light then passes through a wire-grid linear polarizer. The grid lines are oriented perpendicularly and only the horizontally polarized light to pass through, creating a

linearly polarized light before passage through a photo-elastic modulator (PEM). The PEM is made of a transparent ZnSe crystal, that is connected to a piezoelectric transducer. Here, the PEM is designed as a quarter-wave ($\lambda/4$) modulator with its optical axis aligned at 45° of the incoming horizontally polarized light. The incoming horizontally polarized light can be decomposed into two equally components, one parallel and one perpendicular to the modular axis. These two light components travel at slightly different speeds where the parallel one either leads or lags the perpendicular one by $\lambda/4$ or 90° phase difference after passing through the PEM, emerging as a circularly polarized light. The PEM is connected to a 50-kHz alternating current AC circuit to produce right and left circularly polarized light at the same modulation frequency. The left- and right-circularly polarized light passes through the chiral sample and finally reaches the liquid nitrogen cooled MCT IR detector.

The detected signals contain modulations at two different frequency regions: one between 1-2 kHz (labeled as I_{DC}) which represents the IR interferogram, and the other centered at 50 kHz (labeled as I_{AC}) representing the VCD interferogram. The IR interferogram can be directly converted into an IR spectrum through Fourier transform. Since the VCD intensity is weak compared to the corresponding IR intensity, a lock-in amplifier (LIA) is used in the experimental setup to demodulate the higher-frequency AC component while referenced to the PEM frequency. The final VCD spectrum is generated based on the ratio of the Fourier transformed spectra between the AC and DC intensity components.

2.3.4 Some Tips of VCD Measurements

- IR signal intensity: In order to achieve a good quality VCD spectrum, it is desirable to maintain the intensity of the IR bands of the chiral solute between 0.3 and 0.9 absorbances. If the absorbance is too low, it may be difficult to obtain good signal-to-noise ratio for the

VCD spectrum. Conversely, a high absorbance may lead to too few photons to the detector and also poor signal-to-noise. The appropriate IR absorbance can be achieved by adjusting the concentration of the solute and/or by selecting the correct path length spacer in accordance with the Beer-Lambert law.

- **Windows materials:** Another challenge when undertaking IR and VCD measurements is determining the most suitable window material. Our lab typically uses BaF₂, and CaF₂ for VCD experiments. KBr windows have the widest range, going as low as 250 cm⁻¹, however, they are not suitable for measuring aqueous samples due to their water solubility. On the other hand, BaF₂ and CaF₂ windows have the low cutoff values of 1100 cm⁻¹ and 850 cm⁻¹, respectively. Since our VCD instrument offer the spectra at range 800 to 1800 cm⁻¹, the BaF₂ window is the most suitable window material to achieve the most effective results for our VCD investigations.
- **Windows cell cleaning:** The current VCD instrument has used as few optical elements as possible after the sample to reduce optical artifacts. When assemble the sample cell, pay attention to reduce stress applied to the windows. Clean cell widows are important. It is best to rinse the windows thoroughly after each sets of experiments, and allow the window to dry with clean airflow. One should avoid using lens-cleaning paper to dry windows since some paper fiber may stick to the cell surface, especially if your sample is highly basic, causing artifacts. Please note that lens paper produces huge VCD intensity and is used as a standard in the VCD set-up procedure.

2.3.5 Basic Terms in ECD

The chiral counterpart to UV-Vis spectroscopy is known as ECD spectroscopy, which typically operates in the UV-Vis region. ECD spectroscopy is a sensitive technique which is often

employed to analyze the absolute configuration (AC) and conformation of chiral compounds. It measures the differential absorption of left circularly polarized light (LCPL) and right circularly polarized light (RCPL) by the chiral sample accompanying electronic transitions.

The ECD signal is often expressed in molar absorptivity, commonly referred to as "molar circular dichroism," which can be calculated using the equation provided below:

$$\Delta\varepsilon = \varepsilon_L - \varepsilon_R \quad (2.10).$$

The intensity of an electronic transition is commonly quantified by the square of its electric dipole transition moment magnitude ($\mu^{\vec{}}$), which is generated through the influence of electromagnetic radiation on an electric dipole. While the electric field causes a linear rearrangement of the electrons, the magnetic field induces a circular rearrangement of electrons. Consequently, the intensity of a CD band can be described in terms of its rotational strength (R).

$$R = |\vec{\mu}| \cdot |\vec{m}| \cdot \cos \theta \quad (2.11)$$

where \vec{m} is known as magnetic dipole transition moment. For an achiral molecule, the electron rearrangement is invariably linear ($\vec{\mu} \neq 0, \vec{m} = 0$), whereas in the case of a chiral molecule, the electron redistribution during the transition always takes on a helical pattern ($\vec{\mu} \neq 0, \vec{m} \neq 0$).²⁵

The anisotropy factor (g) defines as the ratio between the ECD and absorption intensity, typically falling within the range of 10^{-3} to 10^{-5} , and can be calculated using the equation presented below.

$$g = \frac{\Delta\varepsilon}{\varepsilon} = \frac{ECD}{Abs} \quad (2.12)$$

ECD spectroscopy has versatile applications across a wide range of fields, from protein studies in biology to materials science.

2.3.6 The ECD Instrument Used in the Thesis Work

In this thesis, we conducted all UV-Vis and ECD spectra measurements using a J-1500 CD spectrometer, depicted in Figure 2.7, which is manufactured by JASCO.



Figure 2.7. A picture of the JASCO J-1500 circular dichroism (CD) spectrometer in our laboratory.

While the intricate details of optics components are readily accessible on the JASCO website, I provide a brief summary of tips for conducting experimental measurements with this spectrometer. The J-1500, equipped with a Xenon arc lamp source and a PMT detector, allows standard spectral measurements in the range of 163 to 950 nm. To assess the performance of this spectrometer, we employed a very diluted solution of (1S)-(+)-10-camphorsulfonic acid ammonium salt as the standard, using either a quartz cell with path length of 1 mm or 10 mm. Dry nitrogen (N_2) flow must be initiated at least 5 minutes before activating the Xenon (Xe) lamp to enhanced inert UV measurements. Furthermore, the CD spectrometer is integrated with a liquid cooling system (as illustrated in Figure 2.8) for cell holders, with propylene glycol as the liquid

coolant. This state-of-the-art cooling solution introduces seven distinct temperature modes, offering a versatile range that spans from a chilly 0 °C to a comfortably warm 99 °C.



Figure 2.8. A picture of EX2-755_KOOLANCE superior liquid cooling system. F stands for the Fan mode.

2.4 Theoretical Procedures

In recent years, VCD and ROA spectroscopies have emerged as powerful spectroscopic tools for investigations non-covalent interactions directly in solution including solvent effects.²⁶ ROA and VCD often demonstrate exquisite sensitivity to solvent effects. This can be facilitated by the bulk solvent effect²⁷ (i.e., different dielectric environment) which influences conformational distributions and/or through explicit solvent-solute interactions which are commonly encountered in aqueous solutions.²⁸ Similar solvent-solute interactions were reported to be responsible for an induced ROA bands of achiral benzonitrile dissolved in several chiral alcohols.²⁹ Therefore to properly simulate ROA and VCD spectra in solution is often a challenging task and systematic approaches to account for all possible low energy conformers, new species by solute-solute interactions, and new species and/or altered conformational distributions by solvent-solute interactions, are all needed to be taken in account.

In the past, our group had utilized some molecular dynamic programs such as the AMBER 11 suite package³⁰ to search for conformers, for especially solvation sites and number of water molecules at each site.³¹ In recent years, to conduct comprehensive conformational searches, we have utilized a conformational research tool, i.e., Conformer–Rotamer Ensemble Sampling Tool (CREST), developed by Grimme and co-workers.³² The most recent edition of the CREST code is an incredibly powerful tool that can rapidly explore and identify conformations of molecules with up to one thousand atoms. Our research group has successfully utilized CREST in jet-cooled rotational spectroscopic studies of conformational landscapes of a wide range of organic molecules and their non-covalently bonded clusters³³ and used the gas phase experimental results to benchmark the performance of CREST. We note that the CREST program has two useful built-in features. The first is the ability to recognize and remove the redundant structures that may arise in a single run. More recently, CREST offers the option of using different solvents during the conformational search process to take into account the implicit solvation effect. One interesting successful example is associated with tetrahydro–2–furoic acid whose monomeric and binary conformational landscapes have been experimentally explored by rotational spectroscopy, matrix isolation-VCD and solution VCD spectroscopy³⁴ where the binary aggregates with an energy window of ~ 60 kJ mol⁻¹ were detected under different experimental conditions and properly identified in the related CREST searches. For these reasons, I have used CREST for all conformational searches needed in my thesis research.

Generally, I apply these three important steps to generate simulated spectra to compare with experimental data. These includes (1) Search for all possible conformational of the targeted chiral molecules using CREST; (2) Optimize the CREST candidates at an inexpensive DFT level; (3) Re-optimize the geometries and simulate the associated IR, VCD, Raman, ROA, UV-Vis, and ECD

spectra of all low energy candidates Step 2 at a desirable higher DFT level of theory. The purpose of step 2 is to narrow the energy window without losing any important conformers.³⁵

Below I summarize key implementation details for the above steps. While CREST does a pretty thorough job in sampling all conformational degrees of freedom, one may still miss some conformers if the related conformational interconversion barrier is too high. This may be overcome³⁶ by using not just the usual GFN2-xTB level³⁷ but also at the GFN-FF level.³⁸ This is because GFN-FF in general samples a wider conformational space since simulations at this level of theory can easily be run for a longer time. The GFN-FF candidates were also optimized at the GFN2-xTB level to generate the final set of CREST candidates.³⁹ Another practical method to ensure an exhaustive conformational search is to choose several very different starting geometries and perform CREST runs for each of them. A python script developed by our group was used to eliminate all redundant structures from the different CREST runs by computing the root-mean-square deviations (RMSD) of each structural pairs from the searches.³⁵ The pair of calculated structures are identical if the RMSD equals to zero. The larger the RMSD values, the more difference in the pair's geometries. Since a relatively large number of potential conformations remain after applying the RMSD test, a multiple strategy was developed to minimize the computational cost.³⁵ This method typically includes optimization with a relaxed convergence criteria at the revPBE-D3/def2-SVP level,⁴⁰ with the empirical D3 dispersion correction,⁴¹ and then a single-point energy evaluation at the B3LYP-D3/def2-TZVP level using Molpro program.⁴² This approach was found to generate energy rankings comparable to the higher level DFT calculations, allowing a further reduction in the number of conformer candidates for further analyses without missing any significant conformers.³⁵ The final geometry optimizations and harmonic frequency calculations were refined using the Gaussian 16 package⁴³ at a higher density

functional theory (DFT) level, including the built-in polarizable continuum model (PCM) for implicit solvation effect.

To properly simulate Raman, ROA, IR, and VCD spectra, it is important to consider the usage of hybrid functionals. Several hybrid functionals such as B3LYP, B3PW91, and ω b97xd were recommended in several previous publications,⁴⁴ and were utilized for the geometry optimizations and harmonic frequency calculations of the selected conformers. For the B3LYP, and B3PW91 functionals, the D3BJ term was also employed to account for the long – range van der Waals interactions, which combines the dispersion correction (D3)⁴⁵ and the Becke-Johnson damping (BJ)⁴⁶ factor for improved description of dispersion energy. The ω b97xd was reported to minimize the electron-electron repulsion term in the coulomb operator resulting in a more exact description of the long-range electron interactions.⁴⁷

In addition, an appropriate basis set is essential for the purpose stated above. Utilizing larger basis sets typically bolsters the agreement between the theoretical predictions and observed data. However, factors such as computational costs should also be taken into account. In this thesis, a number of basis sets, for instance, 6-311++G (2d, p), aug-cc-pVDZ, and def2-TZVPD were employed in the monosaccharides and ligands calculations. For certain atomically precise metal clusters which contain almost one hundred atoms, it was more efficient to do geometry optimizations with a small basis set, such as 6-31G(d) initially. After the preliminary calculation is completed, one can perform an additional simulation using the same basis set for the light atoms, employing the optimized structure obtained from the initial run. In calculations of atomically precise metal clusters, because the systems involving metal atoms possess many electrons, effective core potentials (ECPs) are often utilized to replace core electrons which usually require a large set of Gaussians to describe them in calculations. One prevalent ECP basis set is LanL2DZ

(Los Alamos National Laboratory 2 Double-Zeta), a widely recognized choice for transition metals, which includes relativistic effects through the use of pseudopotentials.⁴⁸

2.5 References

- [1] Y. Yang, A. Krin, X. Cai, M. R. Poopari, Y. Zhang, J. R. Cheeseman, Y. Xu, *Molecules* **2023**, 28, 771.
- [2] M. Alshalalfeh, N. Sun, A. H. Moraes, A. P. A. Utani, Y. Xu, *Molecules* **2023**, 28, 4013.
- [3] (a) L. A. Nafie, *Vibrational Optical Activity: Principles and Applications*, John Wiley & Sons, Ltd., UK, **2011**; (b) R. K. Dukor, L. A. Nafie, “Vibrational Optical activity of pharmaceuticals and biomolecules”, In *Encyclopedia of Analytical Chemistry*, John Wiley & Sons, Ltd., UK, **2000**; (c) L. A. Nafie, T. B. Freedman, R. K. Dukor, “Vibrational Circular Dichroism”, In *Handbook of Vibrational Spectroscopy*, John Wiley & Sons, Ltd., UK, **2002**; (d) G. E. Tranter, “Protein Structure Analysis by CD, FTIR, and Raman Spectroscopies”, In *Encyclopedia of Spectroscopy and Spectrometry*, Oxford: Academic Press. UK, **2017**; (e) L. D. Barron, *Molecular light scattering and optical activity*, 2nd edn. Cambridge, **2004**; (f) H. G. Kuball “Chiroptical Analysis” In *Encyclopedia of Analytical Science*, Elsevier Ltd. NL, **2005**; (g) N. Harada, N. Berova, “Separations and Analysis” In *Comprehensive Chirality*, Elsevier Ltd. NL, **2012**.
- [4] L. A. Nafie, *Annu. Rev. Phys. Chem.* **1997**, 48, 357-386.
- [5] P. W. Atkins, L. D. Barron, *Molec. Phys.* **1969**, 16, 453-466.
- [6] L. D. Barron, A. D. Buckingham, *Molec. Phys.* **1971**, 20, 1111-1119.
- [7] L. D. Barron, P. Bogaard, A. D. Buckingham, *J. Amer. Chem. Soc.* **1973**, 95, 603-605.
- [8] W. Hug, S. Kint, G. F. Bailey, J. R. Scherer, *J. Am. Chem. Soc.* **1975**, 97, 5589-5590.
- [9] W. Hug, H. Surbeck, *Chem. Phys. Lett.* **1979**, 60, 186-192.
- [10] L. D. Barron, L. Hecht, W. Hug, M. J. MacIntosh, *J. Am. Chem. Soc.* **1989**, 111, 8731-8732.
- [11] L. A. Nafie, T. B. Freedman, *Chem. Phys. Lett.* **1989**, 154, 260-266.
- [12] D. Che, L. Hecht, L. A. Nafie, *Chem. Phys. Lett.* **1991**, 180, 182-190.
- [13] W. Hug, G. Hangartner, *J. Raman Spectrosc.* **1999**, 30, 841-852.
- [14] W. Hug, *Appl. Spectrosc.* **2003**, 57, 1-13.
- [15] G. Li, *Doctoral Thesis*, **2023**.
- [16] G. Holzwarth, E. C. Hsu, H. S. Mosher, T. R. Faulkner, A. Moscovitz, *J. Am. Chem. Soc.* **1974**, 96, 251-252.
- [17] L. A. Nafie, J. C. Cheng, P. J. Stephens, *J. Am. Chem. Soc.* **1975**, 97, 3842-3843.

- [18] L. A. Nafie, T. A. Keiderling, P. J. Stephens, *J. Am. Chem. Soc.* **1976**, 98, 2715-2723.
- [19] L. A. Nafie, M. Diem, D. W. Vidrine, *J. Am. Chem. Soc.* **1979**, 101, 496-498.
- [20] E. D. Lipp, C.G. Zimba, L. A. Nafie, *Chem. Phys. Lett.* **1982**, 90, 1-5.
- [21] (a) T. A. Keiderling, *Chem. Rev.* **2020**, 120, 3381-3419; (b) C. Merten, F. Li, K. Bravo-Rodriguez, E. Sanchez-Garcia, Y. Xu, W. Sander, *Phys. Chem. Chem. Phys.* **2014**, 16, 5627-5633.
- [22] C. Merten, C. J. Berger, R. McDonald, Y. Xu, *Angew. Chem. Int. Ed.* **2014**, 53, 9940-9943.
- [23] H. Sato, *Phys. Chem. Chem. Phys.* **2020**, 22, 7671-7679.
- [24] (a) Y. Yang, J. Cheramy, Y. Xu, *ChemPhysChem* **2021**, 22, 1336-1343; (b) A. S. Perera, J. Cheramy, M. R. Poopari, Y. Xu, *Phys. Chem. Chem. Phys.* **2019**, 21, 3574-3584; (c) C. Merten, Y. Xu, *ChemPhysChem* **2013**, 14, 213-219.
- [25] M. G. Gore, *Spectrophotometry and Spectrofluorimetry: A Practical Approach*; New York, **2000**.
- [26] (a) S. Ghidinelli, S. Abbate, J. Koshoubu, Y. Araki, T. Wada, G. Longhi, *J. Phys. Chem B* **2020**, 124, 4512-4526; (b) K. Le Barbu-Debus, J. Bowles, S. Jähnigen, C. Clavaguéra, F. Calvo, R. Vuilleumier, A. Zehnacker, *Phys. Chem. Chem. Phys.* **2020**, 22, 26047-26068; (c) Y. Zhang, M. R. Poopari, X. Cai, A. Savin, Z. Dezhahang, J. Cheramy, Y. Xu, *J. Nat. Prod.* **2016**, 79, 1012-1023; (d) 97. M. R. Poopari, Z. Dezhahang, Y. Xu, *Phys. Chem. Chem. Phys.* **2013**, 15, 1655-1665.
- [27] (a) C. Merten, R. McDonald, Y. Xu, *Inorg. Chem.* **2014**, 53, 3177-3182; (b) C. Merten, Y. Xu, *Dalton Trans.* **2013**, 42, 10572-10578.
- [28] (a) M. R. Poopari, Z. Dezhahang, Y. Xu, *Spectrochim. Acta Mol. Biomol. Spectrosc.* **2013**, 136, 131-140; (b) M. R. Poopari, Z. Dezhahang, G. Yang, Y. Xu, *ChemPhysChem* 2012, 13, 2310-2321; (c) P. Zhu, G. Yang, M. R. Poopari, Z. Bie, Y. Xu, *ChemPhysChem* **2012**, 13, 1272-1281.
- [29] E. Machalska, G. Zajac, M. Baranska, D. Kaczorek, R. Kawęcki, P. F. Lipiński, J. E. Rode, J. C. Dobrowolski, *Chem. Sci.* **2021**, 12, 911-916.
- [30] D. A. Case, T. A. Darden, T. E. Cheatham III, C. L. Simmerling, J. Wang, R. E. Duke, R. Luo, R. C. Walker, W. Zhang, K. M. Merz, B. Roberts, B. Wang, S. Hayik, A. Roitberg, G. Seabra, I. Kolossváry, K. F. Wong, F. Paesani, J. Vanicek, J. Liu, X. Wu, S. R. Brozell, T. Steinbrecher, H. Gohlke, Q. Cai, X. Ye, J. Wang, M.-J. Hsieh, G. Cui, D. R. Roe, D. H. Mathews, M. G.

- Seetin, C. Sagui, V. Babin, T. Luchko, S. Gusarov, A. Kovalenko, and P. A. Kollman, AMBER 11, University of California, San Francisco, **2010**.
- [31] (a) M. R. Poopari, P. Zhu, Z. Dezhahang, Y. Xu, *J. Chem. Phys.* **2012**, 137, 194308; (b) 66. M. Losada, P. Nguyen, Y. Xu, *J. Phys. Chem. A* **2008**, 112, 5621-5627.
- [32] (a) P. Pracht, F. Bohle, S. Grimme, *Phys. Chem. Chem. Phys.* **2020**, 22, 7169-7192; (b) S. Grimme, C. Bannwarth, P. Shushkov, *J. Chem. Theory Comput.* **2017**, 13, 1989-2009.
- [33] (a) A. S. Hazrah, A. Insausti, J. Ma, M. H. Al-Jabiri, W. Jäger, Y. Xu, *Angew. Chem. Int. Ed.* **2023**, 62, e202310610; (b) F. Xie, M. Fusè, A. S. Hazrah, W. Jäger, V. Barone, Y. Xu, *Angew. Chem. Int. Ed.* **2020**, 59, 22427-22430; (c) S. Oswald, N. A. Seifert, F. Bohle, M. Gawrilow, S. Grimme, W. Jäger, Y. Xu, M. A. Suhm, *Angew. Chem. Int. Ed.* **2019**, 58, 5080-5084; (d) F. Xie, N. A. Seifert, M. Heger, J. Thomas, W. Jäger, Y. Xu, *Phys. Chem. Chem. Phys.* **2019**, 21, 15408-15416; (e) N. A. Seifert, J. Thomas, W. Jäger, Y. Xu, *Phys. Chem. Chem. Phys.* **2018**, 20, 27630-27637.
- [34] (a) F. Xie, X. Ng, N. A. Seifert, J. Thomas, W. Jäger, Y. Xu, *J. Chem. Phys.* **2018**, 149, 224306; (b) F. Xie, N. A. Seifert, W. Jäger, Y. Xu, *Angew. Chem. Int. Ed.* **2020**, 59, 15703-15710; (c) Y. Yang, J. Cheramy, Y. Xu, *ChemPhysChem* **2021**, 22, 1336-1343.
- [35] H. Wang, M. Heger, M. H. Al-Jabiri, Y. Xu, *Molecules*, **2022**, 27, 38.
- [36] A. N. Mort, F. Xie, A. S. Hazrah, Y. Xu, *Phys. Chem. Chem. Phys.* **2023**, 25, 16264-16272.
- [37] C. Bannwarth, S. Ehlert and S. Grimme, *J. Chem. Theory Comput.* **2019**, 15, 1652-1671.
- [38] S. Spicher and S. Grimme, *Angew. Chem. Int. Ed.* **2020**, 59, 15665-15673.
- [39] A. N. Mort, F. Xie, A. S. Hazrah, Y. Xu, *Phys. Chem. Chem. Phys.* **2023**, 25, 16264-16272.
- [40] F. Weigend, R. Ahlrichs, *Phys. Chem. Chem. Phys.* **2005**, 7, 3297-3305.
- [41] (a) D. G. A. Smith, L. A. Burns, K. Patkowski, C. D. Sherrill, *J. Phys. Chem. Lett.* **2016**, 7, 2197-2203; (b) S. Grimme, J. Antony, S. Ehrlich, H. Krieg, *J. Chem. Phys.* **2010**, 132, 154104.
- [42] H-J. Werner, P. J. Knowles, G. Knizia, F. R. Manby, M. Schütz, *Molpro: WIREs Comput. Mol. Sci.* **2012**, 2, 242-253.
- [43] Gaussian 16, Revision C.01, M. J. Frisch, G. W. Trucks, H. B. Schlegel, G. E. Scuseria, M. A. Robb, J. R. Cheeseman, G. Scalmani, V. Barone, G. A. Petersson, H. Nakatsuji, X. Li, M. Caricato, A. V. Marenich, J. Bloino, B. G. Janesko, R. Gomperts, B. Mennucci, H. P. Hratchian, J. V. Ortiz, A. F. Izmaylov, J. L. Sonnenberg, D. Williams-Young, F. Ding, F. Lipparini, F. Egidi, J. Goings, B. Peng, A. Petrone, T. Henderson, D. Ranasinghe, V. G. Zakrzewski, J. Gao,

N. Rega, G. Zheng, W. Liang, M. Hada, M. Ehara, K. Toyota, R. Fukuda, J. Hasegawa, M. Ishida, T. Nakajima, Y. Honda, O. Kitao, H. Nakai, T. Vreven, K. Throssell, J. A. Montgomery, Jr., J. E. Peralta, F. Ogliaro, M. J. Bearpark, J. J. Heyd, E. N. Brothers, K. N. Kudin, V. N. Staroverov, T. A. Keith, R. Kobayashi, J. Normand, K. Raghavachari, A. P. Rendell, J. C. Burant, S. S. Iyengar, J. Tomasi, M. Cossi, J. M. Millam, M. Klene, C. Adamo, R. Cammi, J. W. Ochterski, R. L. Martin, K. Morokuma, O. Farkas, J. B. Foresman, and D. J. Fox, Gaussian, Inc., Wallingford CT, **2016**.

[44] F. C. Asogwa, E.C. Agwamba, H. Louis, M.C. Muozie, I. Benjamin, T.E. Ger, G.E. Mathias, A.S. Adeyinka, A.I. Ikeuba. *Chem. Phys. Impact.* **2022**, 5, 100091.

[45] S. Grimme, S. Ehrlich, L. Goerigk, *J. Comput. Chem.* **2011**, 32, 1456-1465.

[46] A. D. Becke, E. R. Johnson, *J. Chem. Phys.* **2005**, 123, 154101.

[47] M. A. S. Yokomichi, H. R. L. Silva, L. E. V. N. Brandao, E. F. Vicente, J. M. Batista Jr, *Org. Biomol. Chem.* **2022**, 20, 1306-1314

[48] L. E. Roy, P. J. Hay, R. L. Martin, *J. Chem. Theory Comput.* **2008**, 4, 1029-1031.

Chapter 3

Chirality Transfer and Enhancement in Vibrational Circular Dichroism Spectra of Atomically-Precise Metal Clusters

3.1 Introduction

Chirality events, encompassing chirality transfer and enhancement in nanosized species, provide an opportunity to understand the origin of life and have significant applications in chiral sensing, medicine, and asymmetric catalysis^[1,2,3]. Despite their potential, a thorough understanding of these fundamental aspects remains elusive due to the inherent variability among nanoparticles: no two nanoparticles are the same^[4]. With the advance of synthesis and separation technology, atomically-precise metal clusters possess a limited number of bonded metal atoms protected by organic ligands, smaller in size than nanoparticles, have been prepared and characterized by single-crystal X-ray diffraction (SCXRD) analysis^[5,6,7]. In recent years, tens of enantiopure subnanosize chiral metal clusters have been successfully synthesized^[8,9,10,11], opening up the opportunity to gain deeper insights into chirality transfer and enhancement using spectroscopic techniques such as electronic circular dichroism (ECD), circular polarized luminescence (CPL)^[12,13,14,15] and nuclear magnetic resonance^[16]. For example, in these atomically-precise chiral metal cluster, chirality transfer events from chiral ligands to metal cores, i.e., outside-to-inside chirality transfer, were demonstrated by their experimental ECD and CPL signals in the visible region, whereas the corresponding ECD features of the peripheral chiral ligands themselves usually appear in the shorter wavelength region (≤ 400 nm).

In comparison to ECD and CPL, vibrational circular dichroism (VCD) often can provide much more detailed structural information including conformational distributions and non-covalent interactions for a wide range of chiral molecular systems including, peptides [17], asymmetric catalysts[18], exotic non-covalently formed chiral species in cold matrices[19] and chiral molecular crystals[20]. The application of VCD to atomically-precise chiral metal clusters was pioneered by Bürgi and co-workers [21,22]. For example, these authors examined VCD spectrum of nanocluster $\text{Au}_{38}(\text{2-PET})_{24}$ (2-PET= phenylethylthiolate) and used a simplified model of $\text{Au}_4(\text{2-PET})_4$ to demonstrate that a selected chiral arrangement of achiral 2-PET ligands could reproduce some prominent features in the observed VCD spectrum[21]. Overall, very few chiral metal clusters have been investigated using VCD and density functional theory (DFT) simulations. In all these studies aimed for atomic precision, simplified models with fewer metal atoms or ligands were necessary because of the drastic computational cost associated with the (relatively) large size of the metal core and the number of protective ligands involved. Furthermore, in some of these systems, the number of protective ligands may vary in different batch of experiments, introducing some additional uncertainty. These simplifications and experimental uncertainties may contribute to the result that some key VCD features observed were not theoretically reproduced.

In this paper, we focus on VCD and DFT probes of four ultra-stable small octahedral silver and copper metal clusters (< 2 nm diameter) which are capped with purposely selected short ligands, namely L_6/D_6 (= (S)/(R)-4-Isopropylthiazolidine-2-thione) and PL_6/PD_6 (= (S)-/(R)-4-Phenylthiazolidine-2-thione). The chemical formula of the two enantiomeric pairs of L/D and PL/PD ligands and the corresponding single-crystal structures of two enantiomeric pairs of octahedral metal clusters, $\text{Ag}_6\text{L}_6/\text{D}_6$ [10], and $\text{Ag}_6\text{PL}_6/\text{PD}_6$ [10] are shown in Figure 3.1, while those of $\text{Cu}_6\text{L}_6/\text{D}_6$ [11] and $\text{Cu}_6\text{PL}_6/\text{PD}_6$ [11] are in Figure A1, Appendix A. In the metal clusters, each chiral

ligand is bonded to the Ag₆ metal core through an Ag-N bond (N in the five-membered ring) and two Ag-S bonds (the thiol S), defining an associated Ag₃ triangular plane. The six C=N bonds surround the Ag₆ octahedron core, each in an approximately anti-parallel manner to the two nearest C=N bonds. It is worthy to point out that the Ag₆ core is not in a symmetric octahedral shape; instead, the tops of the upper and lower pyramids are offset in opposite directions.

On one hand, these ultrasmall chiral metal clusters are of considerable practical interest because they are promising nanoscale building blocks for super-crystals with special chiroptical properties^[10,11]. On the other hand, these clusters are themselves of significant spectroscopic interest because of the presence of strong IR and VCD functional groups such as C=N bonds which may serve as sensitive reporters of influence of the chiral metal cores on the ligand VCD signatures, that is how the asymmetric metal skeleton influences on the VCD features of chiral ligands in nanoclusters. Thanks to their relatively small sizes and ultrastability, one can systematically evaluate the simulation qualities with the complete and simplified models of metal clusters by comparing directly to the experimental data and with each other. The availability of both experimental and theoretical data of the Ag and Cu metal clusters enables one to detect and extract any subtle differences in the VCD features caused by different metal cores. In addition, such detailed modelling together with the ultrastability of the metal clusters with specific ligand composition provide an opportunity to meaningfully conformer specific examination. To the best of our knowledge, these are the first VCD studies of atomically-precise silver and copper clusters.

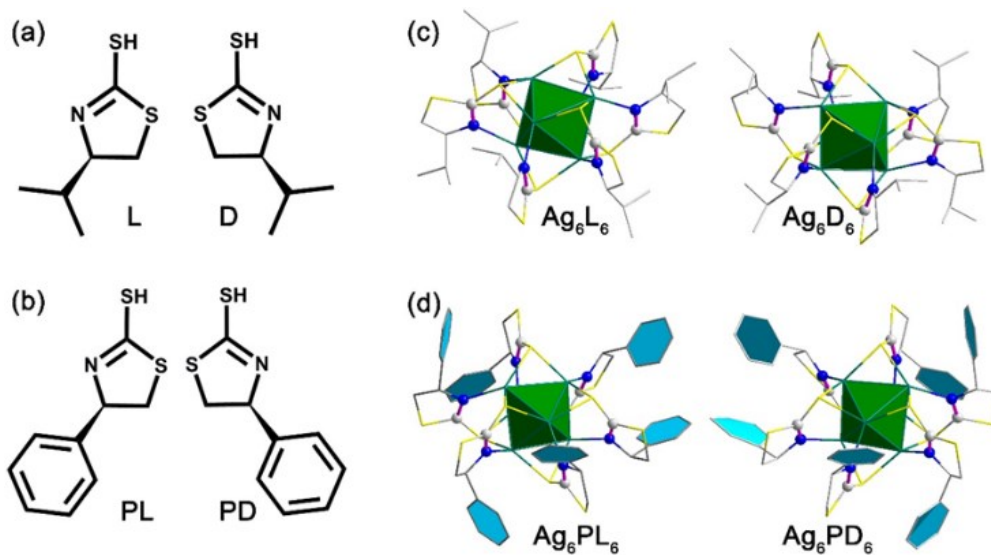


Figure 3.1. (a) and (b) are chemical formula of the L/D and PL/PD ligands, respectively. (c) and (d) show how the related ligands arrangements around the Ag₆ skeleton in the metal clusters.

3.2 Results and Discussion

Please note that the experimental and theoretical details are provided in Appendix A.

3.2.1 VCD Studies of the Ligands

In order to fully understand the VCD spectral features of the Ag and Cu metal clusters, we first explored conformational landscapes of the chiral ligands using a fast, efficient semi-empirical quantum chemistry code, called CREST (Conformer-Rotamer Ensemble Sampling Tool).^[23] This code has been successfully utilized and benchmarked in a significant number of high-resolution spectroscopic studies involving flexible molecules and non-covalently bonded clusters.^[24,25] More recently, it has also been applied together with the generalized Born based surface area (GBSA)^[26] implicit solvent model to search all possible low energy conformers in solution^[27,28]. A total of sixteen and four different CREST candidates were produced in searches of free L/D and PL/PD ligands in the GBSA of CDCl₃. CDCl₃ was chosen as a common solvent for all targeted systems

because of the reasonable solubility except that CH_2Cl_2 was used in the case of Cu_6PD_6 . Additional intermediate steps^[29] were used to allow faster identification of low energy conformers (see section 2.4). The final geometry optimizations were carried out at the B3LYP-D3BJ/def2-TZVPD and wB97XD/def2-TZVPD^[30] levels with the polarizable continuum model (PCM) of CDCl_3 . The D3 dispersion correction with the Becke–Johnson (BJ) damping function were used.^[31,32] Since L, PL and the associated metal clusters provide the same IR spectra and mirror-imaged structures and VCD spectra as those of D, PD and the related metal clusters, we used D and PD and the related metal clusters for all the discussions in the remainder of the paper for conciseness.

Six ligand D conformers were identified and are denoted as D-I to D-VI based on their relative free energy ordering, with I being the most stable one. The corresponding optimized geometries are depicted in Figure 3.2(a), along with their relative free energies and Boltzmann percentage abundances at 298 K. For the PD ligand, the phenyl functional group makes this system more rigid than ligand D. Only two low energy conformers, PD-I and PD-II, associated with the equatorial and axial positions of the phenyl group, were identified. The corresponding optimized geometries of the two stable conformers are shown in Figure 3.3(a), along with their relative free energies and Boltzmann percentage abundances at 298 K.

The individual conformer IR and VCD spectra of D-I to D-VI are depicted in Figure 3.2(b), together with the Boltzmann averaged and the experimental IR and VCD spectra of the L/D ligand in CDCl_3 solution. Since ligand L/D is the only one with acceptable solubility in CCl_4 , additional measurements for the L/D ligand were also carried out in CCl_4 for comparison (see Figure 3.2(b)). It is not surprising that the simulated IR spectra of the six conformers are nearly identical, with only minor variations in the relative intensities of some bands due to different orientations of the isopropyl functional group. One can easily correlate the experimental bands with the calculated

ones. On the other hand, the VCD features of the individual conformers vary drastically from one conformer to the next. This significant variation highlights the high sensitivity of VCD features to small conformational changes, making it an effective tool for directly extracting experimental conformational distributions in solution. Overall, the Boltzmann averaged IR and VCD spectra of the six most stable conformers agree well with the experimental spectra, although some minor differences were noted around 1500 cm^{-1} . This is perhaps because the wavenumber differences between D-I and D-II were predicted too small in comparison with the experiment and the predicted conformational weights may be slightly off. This is not surprising, considering the free energy differences are small among the six conformers.

The simulations of the IR and VCD spectra of the PD ligand followed a very similar approach. The individual IR and VCD spectra of the two stable PD ligand conformers are shown in Figure 3.3(b). Again, the IR spectra of the individual PD conformers exhibit similar features, except in the $1250\text{--}1350\text{ cm}^{-1}$ region where some minor differences are noted. Their corresponding VCD spectra, on the other hand, demonstrate considerable differences. Overall, the simulated IR and VCD spectra agree well with the experiment with the notable exception at the C=N stretching region around 1470 cm^{-1} . We hypothesized that this may be due to a similar issue as in the case of D ligand, i.e., the predicted wavenumber differences between PD-I and PD-II are too small in comparison with the experiment. If this band of PD-II were predicted a bit further to the higher wavenumber, then the experimental band at about 1500 cm^{-1} in both IR and VCD traces would be satisfactorily explained. The co-existence of PD-II was clearly verified by the experimental VCD band at 1260 cm^{-1} , since PD-I has no VCD band around this cm^{-1} .

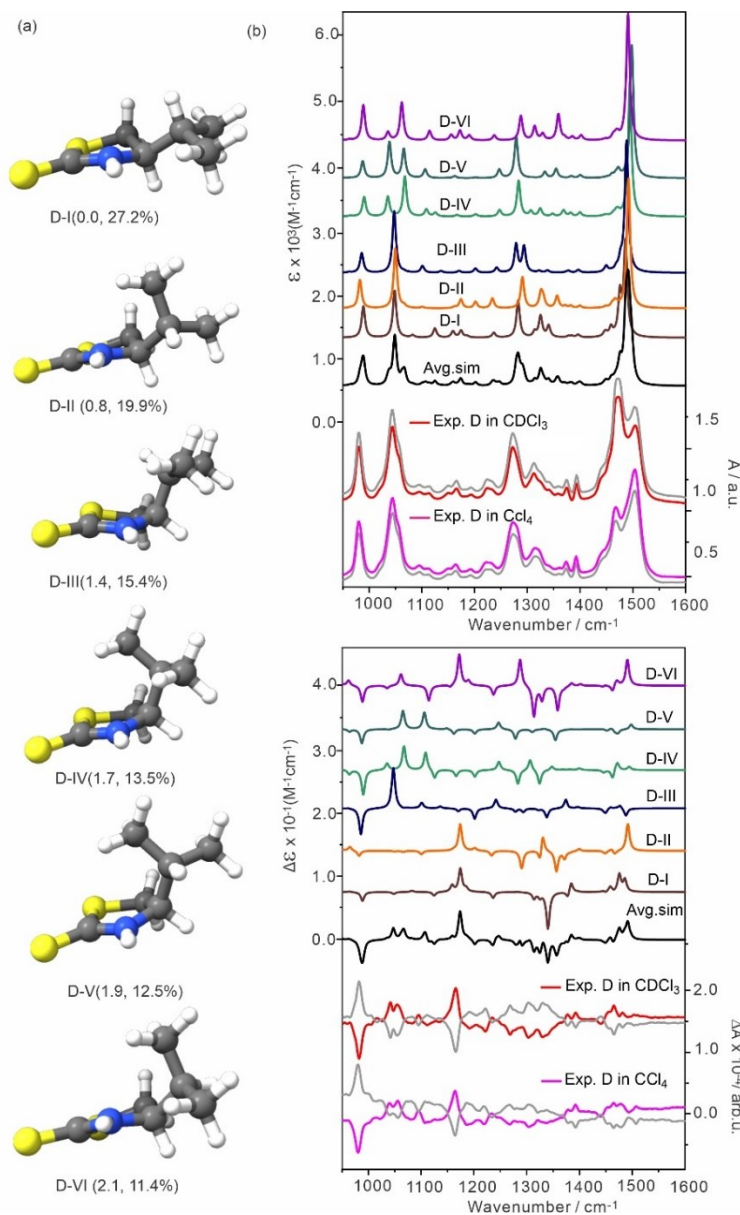


Figure 3.2. (a) The optimized geometries of the six low energy D ligand conformers. The relative free energies in kJ mol⁻¹ and the Boltzmann percentage abundances at 298 K are provided in the brackets. (b) The simulated individual IR (top) and VCD (bottom) spectra of the six most stable D ligand conformers and the related Boltzmann averaged IR and VCD spectra at the wB97XD/def2-TZVPD/PCM(CDCl₃) level of theory at 298 K. The experimental IR and VCD spectra of D ligand at two different solvents, i.e., CDCl₃ and CCl₄, are also provided. The corresponding IR and VCD spectra of the L ligand are given in grey colour.

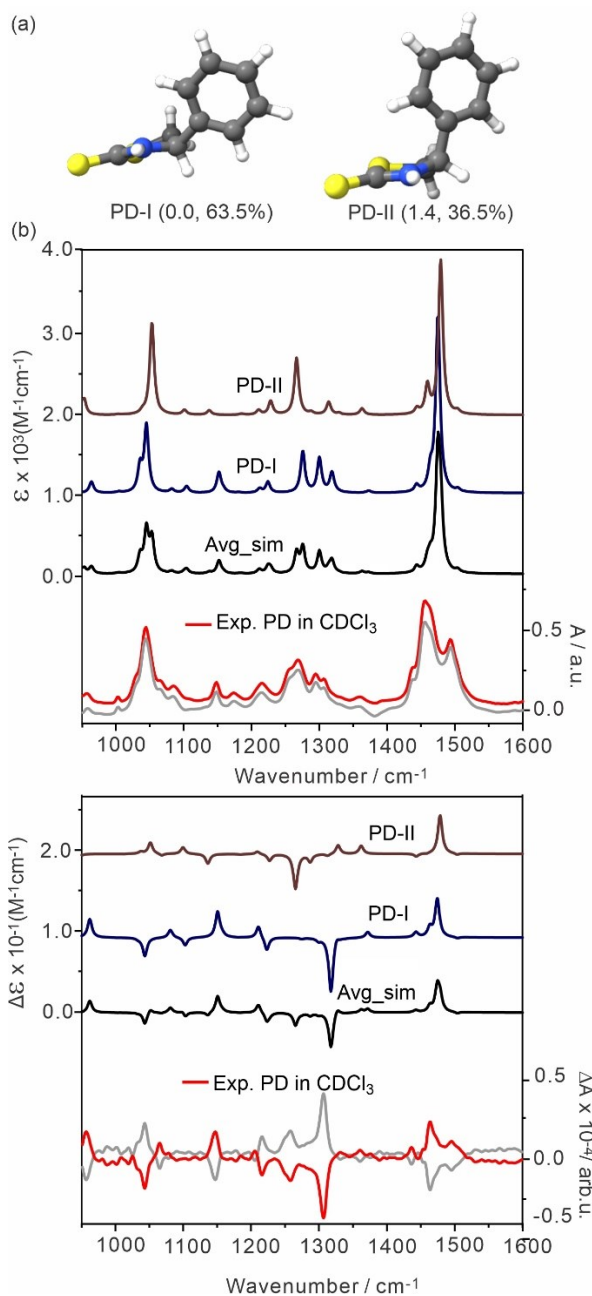


Figure 3.3. (a) The two low energy PL/PD ligand conformers identified by the CREST and optimized at a high level of DFT calculations. The relative free energies in kJ/mol and the Boltzmann percentage abundances at 298 K are provided in the brackets. (b) The simulated individual IR (top) and VCD (bottom) spectra of the two most stable/D ligand conformers and the related Boltzmann averaged IR and VCD spectra at the wB97XD/def2-TZVPD/PCM(CDCl₃)

level of theory at 298 K. The experimental IR and VCD spectra (PD red trace, and PL gray trace) in CDCl_3 are also provided.

The simulated IR and VCD spectra of D and PD conformers at the B3LYP-GD3BJ/def2-TZVPD/PCM level of theory are depicted in Figures A2 and A3, Appendix A. While the IR profiles closely resemble those obtained at the wB97XD/def2-TZVP/PCM level, some differences are present in the simulated VCD spectra. Overall, the wB97XD/def2-TZVPD/PCM simulations provide a better agreement with the experiment. Similar conclusion was reported in a recent VCD study of orbitides, bioactive head-to-tail natural cyclic peptides^[33].

3.2.2 Experimental and Simulated VCD Spectra of the Ag_6D_6 , Ag_6PD_6 , Cu_6D_6 , and Cu_6PD_6 Clusters.

For the metal clusters, we utilized the experimental crystal structures as the starting points for geometry optimizations because these are the crystals used in the VCD experiments. For both Ag_6D_6 and Cu_6D_6 , the ligand conformations are exclusively D-II in the crystals and in the final optimized geometries. In the Ag_6PD_6 crystal, there are five PD-I ligands and one distorted ligand which resembles PD-II. The optimized geometry contains five PD-I conformers and one PD-II conformer even if we purposely made all six PD-I conformers as the starting input geometry. The Cu_6PD_6 crystal consists of five PD-I and one PD-II conformers, whereas the optimized geometry is made of six PD-I conformers. The influence of conformations on the resulting VCD spectra will be discussed in the next section.

To evaluate the influence of the metal core to the ligand IR and VCD features, we first compared the experimental data of the Ag_6D_6 , Ag_6PD_6 , Cu_6D_6 , and Cu_6PD_6 with the corresponding free ligands in Figure 3.4. It is worth noting that the concentrations used for the free ligand

measurements are about 30 times higher than those used for their metal clusters (see the experimental section in Appendix A). Even taking into account that every metal cluster contains six ligand subunits, there is still a factor five difference, indicating a noticeable intensity enhancement for the VCD spectra of the metal clusters in comparison to the free ligands.

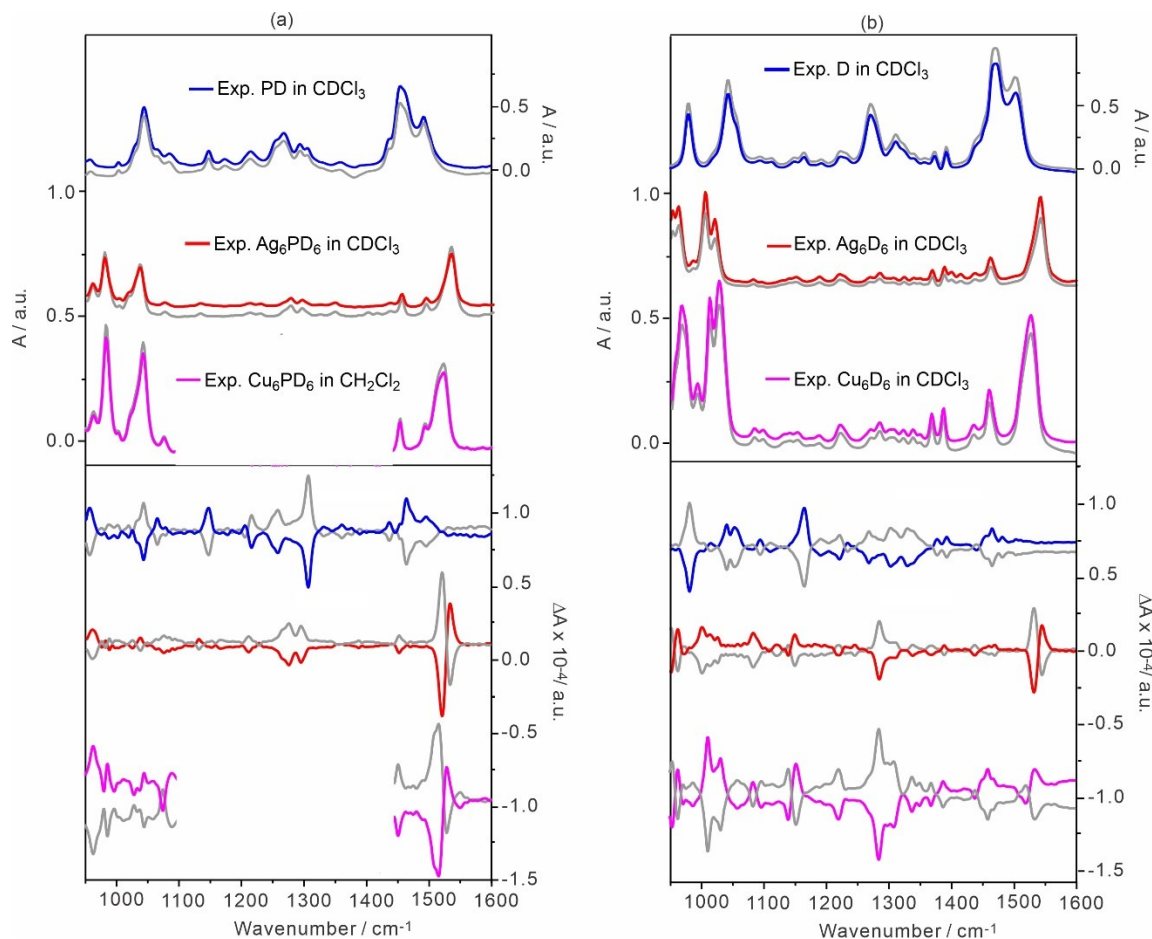


Figure 3.4. Comparison of the experimental IR and VCD spectra of (a) free ligand PD versus Ag₆PD₆ and Cu₆PD₆ and (b) free ligand D versus Ag₆D₆ and Cu₆D₆. Note that the experimental IR intensities of the metal clusters are noticeably lower and are amplified so that one can see the weak bands clearly. The corresponding IR and VCD spectra of the L and PL ligands and their metal clusters are given in grey colour. All experiments were conducted in CDCl₃ except Cu₆PD₆ whose measurements were done in CH₂Cl₂ with a much longer pathlength of 0.3 mm. Some wavenumber regions were overwhelmed by solvent bands and were removed for clarity.

Both IR and VCD band features exhibit drastic changes moving from the free ligands to their metal clusters. For discussions, it is easier to divide the IR features into three regions: lower than 1100 cm^{-1} , 1100 to 1400 cm^{-1} , and above 1400 cm^{-1} . For example, comparing PD and Ag_6PD_6 , the most prominent IR feature above 1400 cm^{-1} corresponds to the C=N stretching motion and experiences significant blue shift in the metal clusters because of the strong $\text{Ag}\cdots\text{N}$ interactions in the metal clusters. In the below 1100 cm^{-1} region, the main PD bands are related to the stretching motions of C=S and benzene C-C=C, while those are red-shifted in Ag_6PD_6 . In the middle region of 1100 to 1400 cm^{-1} , most of these modest intense bands are related to CH_2 rocking, wagging, and twisting and experience only minor changes from PD to its metal clusters. Similar observations can be made regarding ligand D and its metal clusters.

In addition, it is interesting to examine the influence of Ag versus Cu atoms on the IR and VCD features of their respective metal clusters. For example, in Ag_6D_6 and Cu_6D_6 , the IR spectra are similar because of the identical anchored positions of the six D ligands. Even though the shapes of their VCD features are similar, their VCD spectra do show noticeable relative intensity differences across the board. For example, the prominent experimental bisignate peaks of Cu_6D_6 at about 1530 cm^{-1} have weaker relative intensity compared to those of Ag_6D_6 . This observation will be further discussed with the help of theoretical simulations.

The conformational specific probes of the free chiral ligands demonstrated that there are multiple conformers of D and PD with fairly small stability differences co-exist in solution. Do all these low energy conformers play a role in the atomically-precise Ag_6 and Cu_6 clusters? Such inquiry has not been addressed fully so far. We constructed complete models with all six silver or copper metal atoms as well as six chiral ligands. Since the number of possible conformational combinations is very large for each type of metal clusters, we first utilized the available crystal

structural data of these four metal clusters as the initial input geometries for geometry optimizations, and then simulated the IR and VCD spectra in solution for comparison with the experiments. To the best of our knowledge, this is the first instance where the DFT calculations of the full atomically-precise metal cluster structures were utilized without truncation or simplification, thus allowing theoretical and experimental comparisons with atomic precision in its true sense.

The comparisons of the experimental and simulated IR and VCD spectra of the enantiomeric pairs of $\text{Ag}_6\text{L}_6/\text{D}_6$ and $\text{Ag}_6\text{PL}_6/\text{PD}_6$ are provided in Figure 3.5, together with the optimized geometries of Ag_6D_6 and Ag_6PD_6 . In general, excellent agreements were achieved between the experimental and theoretical IR and VCD spectra of the silver clusters. Nearly all visible experimental IR and VCD bands were predicted theoretically with the proper relative intensities, as well as the correct VCD signs for these two silver clusters. For example, not only the dominant, bisignate C=N stretching features around 1530 cm^{-1} were reproduced theoretically for both silver clusters, the slight blue-shift and the slightly lower intensity of Ag_6D_6 versus Ag_6PD_6 were also properly captured. Impressively, the even the more subtle, less intense VCD differences between Ag_6D_6 and Ag_6PD_6 were also reproduced quite accurately.

The simulated IR and VCD spectra of individual conformers of Cu_6D_6 and Cu_6PD_6 are provided in Figure A4, Appendix A. Similarly, the comparisons of the experimental and simulated IR and VCD spectra of the enantiomeric pairs of $\text{Cu}_6\text{L}_6/\text{D}_6$ and $\text{Cu}_6\text{PL}_6/\text{PD}_6$ are provided in Figure A5, Appendix A. Overall, good agreements between experimental and theoretical IR and VCD spectra were achieved. To highlight the influences of metal cores in these atomically-precise metal clusters, we further compared the simulated IR and VCD spectra between Ag_6D_6 and Cu_6D_6 also in Figure A5. Indeed, most VCD features of these two metal clusters were predicted to possess

matched peaks, while the bisignate VCD and the associated IR peaks of Cu_6D_6 were shown to have much lower intensities than those of Ag_6D_6 , consistent with the experimental observation. That means that the electric transition dipole moments of the C=N stretching vibrations are modulated by the inter-core metal atoms. While the ECD and CPL activities^[10,11] in these clusters demonstrated the transfer of chirality from the chiral ligands to the Ag_6 and Cu_6 metal cores, the current VCD analyses indicated that coordination with the metal atoms can affect the ligand VCD activities. Therefore, one can conclude that chirality transfer events within such metal clusters are bidirectional.

The above analyses suggest that the new VCD activities are not a local property, but a collective behaviour, that is determined by the orientation and ordered arrangement of chromophores, and the inter-core metal atoms. To further understand the origin of the significant ligand VCD enhancement, simulations of IR and VCD spectra of several model systems were carried out in the next section. In particular, we examined the roles of different ligand conformations, and their special arrangements play in the enhancement process.

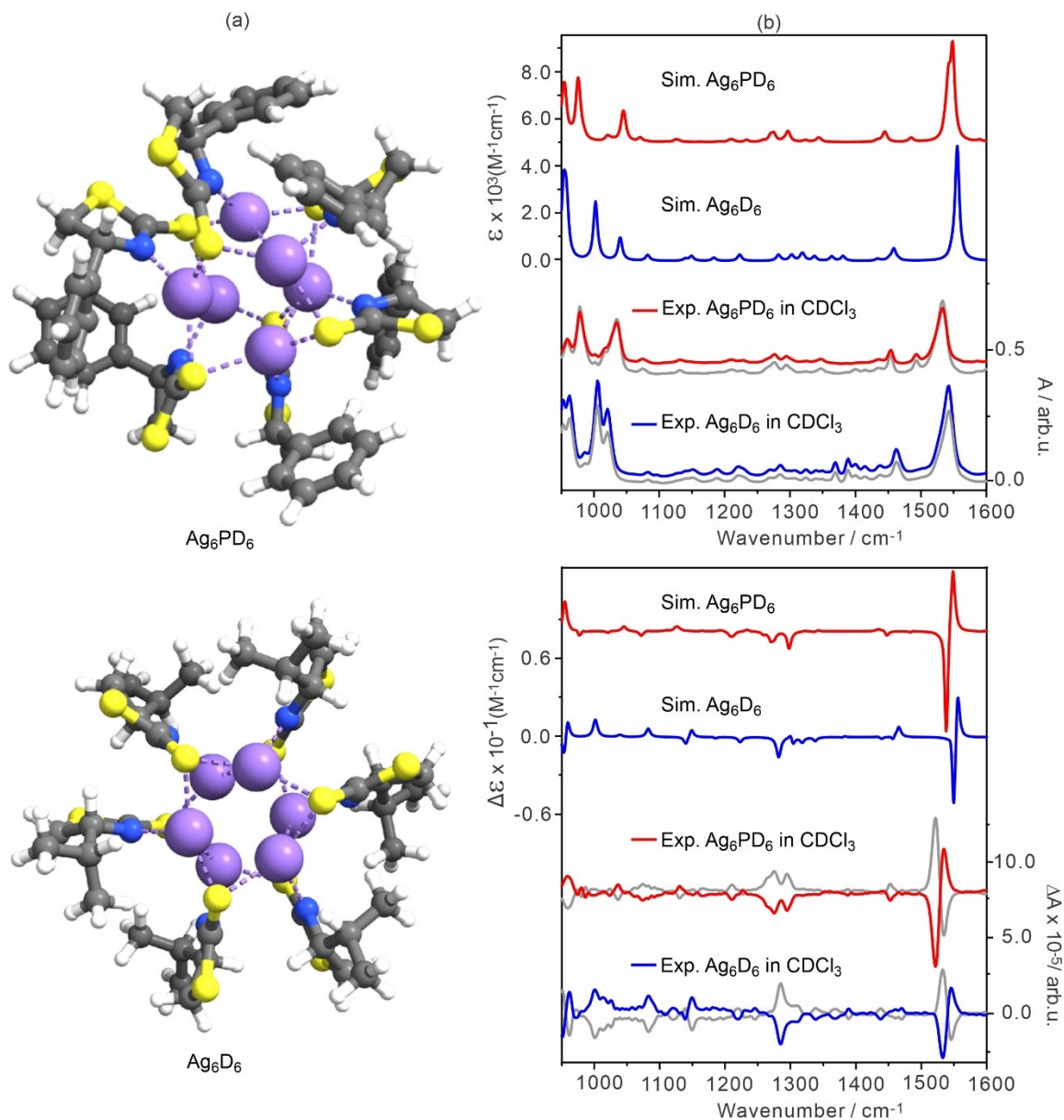


Figure 3.5. (a) The optimized geometries of Ag_6PD_6 and Ag_6D_6 ; (b) Comparison of the simulated experimental IR and VCD spectra of Ag_6PD_6 and Ag_6D_6 . The corresponding experimental IR and VCD spectra of Ag_6PL_6 and Ag_6L_6 are given in grey colour. The geometry optimizations and the IR and VCD simulations were carried out at the B3PW91-D3BJ/6-31G(d) (LanL2DZ for Ag) level.

3.2.3 Simulations of IR and VCD Spectra of Several Metal Cluster Models

In the previous VCD studies of chiral ligands decorated gold nanoparticles or atomically-precise gold clusters^[8,21,22], Bürgi and co-workers utilized simplified models to interpret the experimental VCD spectra with reasonable success. To examine in detail how VCD enhancement happens in the atomically-precise silver and copper clusters in the different wavenumber regions, we selected Ag₆PD₆ as a prototype system. One reason is that PD has only two main conformers, making it easier to take into account of possible conformational combinations.

In Figure A6, Appendix A, we plot a zoom-in picture of the IR and VCD features of the C=N stretching modes in the narrow range from 1590 to 1630 cm⁻¹ where individual IR and VCD mode intensities are indicated. Despite considerable efforts, a physical explanation of the enhancement with the entire cluster model with six ligands remains elusive^[34]. It would be helpful to utilize simplified models to consider a number of factors, such as ligand-ligand distance and ligand conformers, on the enhancement factors for a deeper understanding of the mode coupling.

Starting from the most stable free PD ligand conformer, (i) PD-I, we built a series of models. The first set includes (i) PD-I and (ii) one Ag atom with one PD-I. The next set consists of two Ag atoms with an Ag-Ag distance of ~3 Å, similar to the neighbouring Ag-Ag distance in Ag₆PD₆, with (iii) two PD-I conformers, (iv) with one PD-I and one PD-II, and (v) with two PD-II. The optimized geometries of all of them are in Figure 3.6(a) and the simulated IR and VCD spectra are depicted in Figure 3.6(b), together with those of Ag₆PD₆. Some other geometry arrangements with Ag₂ were tested although not included for conciseness.

It is interesting to note that adding just one Ag atom is enough to bring the simulated IR spectrum to be similar to that of Ag₆PD₆, although weaker because there are six PD ligands in Ag₆PD₆. The related simulated VCD spectrum differs greatly from that of Ag₆PD₆, except in the middle range

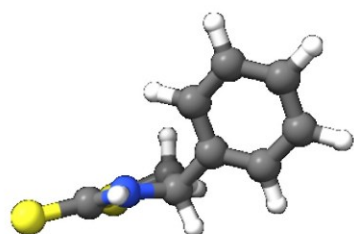
from 1050 to 1400 cm^{-1} . For example, the intense positive-negative bisignate bands at $\sim 1600 \text{ cm}^{-1}$ is totally missing in the one Ag model which predicted a small positive VCD band. This failure indicated that the intense bisignate bands are due to the exciton coupling of the C=N stretching modes, as one may anticipate.

Next, we examined the set of models consisting of Ag_2 with a similar Ag-Ag distance but different combinations of PD ligand conformers. Interestingly, the intense positive-negative bisignate bands at $\sim 1600 \text{ cm}^{-1}$ are present in all three traces, although the actual predicted intensity decreases considerably going from the model with two PD-II ligands to that with two PD-I ligands, and finally that with mixed ligands. The last observation, i.e., the bisignate bands of the Ag_2 cluster with one PD-I and one PD-II giving a noticeably weaker bisignate VCD intensity, is consistent with the anticipation that the exciton coupling strength depends on how similar the two couplers are, all else being equal.

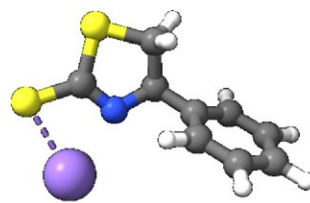
It is worthy to point out that the different conformational combinations of PD-I and PD-II have very noticeable effects on IR and especially VCD spectra in the region below 1500 cm^{-1} . The simulated VCD spectra of the models which consist of two PD-II and the mixed ligands deviate considerably from that of Ag_6PD_6 or the experimental data. This observation seems to suggest that the contribution of the PD-II conformer is not the dominant one in the metal cluster. On the other hand, it is amazing that model (iii) with two PD-I conformers captures almost all the major VCD features of Ag_6PD_6 with two exceptions. One is the positive VCD band at $\sim 1180 \text{ cm}^{-1}$ and the other is the strong positive band at $\sim 1000 \text{ cm}^{-1}$ which has a lower relative intensity in model (iii). This “hit and miss” outcome is similar to previous reports where simplified models were employed to explain the VCD spectra of gold metal clusters^[8,21,22]. The deficiency of the simplified model is also obvious when one examined the predicted C=N stretching band frequencies with the

simplified Ag or Ag₂ models. Even though in Ag₆PD₆, each N atom is only directly bonded to one Ag atom as in the Ag and Ag₂ models, the final predicted C=N band frequencies are shifted significantly to higher cm⁻¹ in the full model, Ag₆PD₆ than those predicted in the simplified models. Again, these analyses strongly indicate that the VCD activities of the metal clusters are a non-local property that is determined by the collectively ordered arrangements of chromophores and by the metal cores. All these observations indicate there is much information in the observed VCD spectra that can only be fully extracted if a complete model is used.

(a)

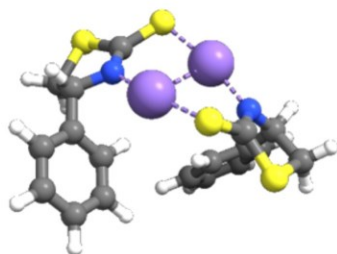


(I) PD-I

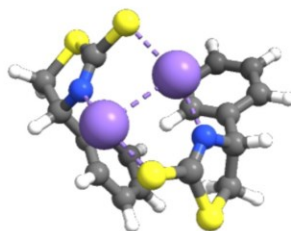


(ii) AgPD-I

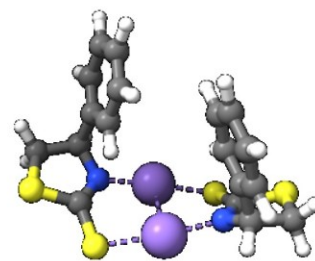
Ag₂(neighbor):



(iii) 2PD-I



(iv) 1PD-I 1PD-II



(v) 2PD-II

(b)

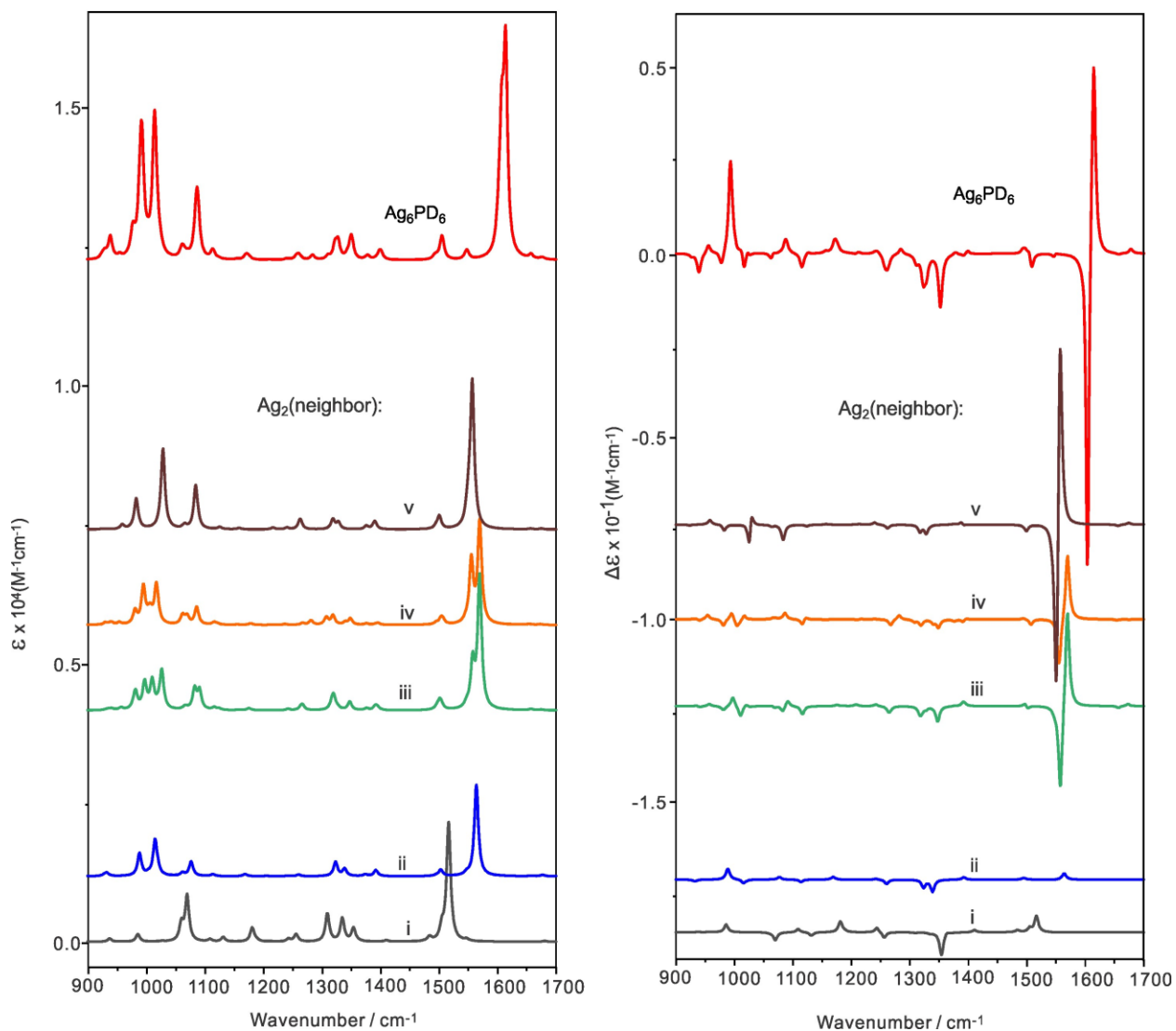


Figure 3.6. (a) The simple cluster models involve the interaction of one and/or two silver atoms with a one and/or two ligands (b) The simulated IR and VCD spectra of the simple cluster models in (a).

3.3 Conclusion

In this study, we employed VCD alongside theoretical modelling to scrutinize chirality transfer phenomena within four distinct enantiomeric pairs of atomically precise metal clusters: $\text{Ag}_6\text{L}_6/\text{D}_6$, $\text{Ag}_6\text{PL}_6/\text{PD}_6$, $\text{Cu}_6\text{L}_6/\text{D}_6$, and $\text{Cu}_6\text{PL}_6/\text{PD}_6$. These recently synthesized ultrasmall and ultrastable metal clusters showcased markedly different VCD features compared to their associated free ligands. The research outcomes revealed that the strategically arranged ligands could foster through-space coupling in the chromophores, manifesting as robust bisignate VCD signals at the C=N stretching modes. This marked a stark departure from the absence of such signals in the free ligands and simplistic Ag-PD model, whereas the simplified $\text{Ag}_2\text{-PD}_2$ models already predicted the strong exciton coupling between the C=N bonds.

The synergistic stretching modes of the six ligands were identified as instrumental in amplifying the chiroptical responses of these ultrasmall metal clusters. The VCD differences observed with the silver and copper cores reflected how the inorganic metal core influences and modulates the collective chiroptical response of the organic ligands. The current findings confirmed the bidirectional nature of chirality transfer events within the metal clusters, i.e., the well-known path from outside (chiral ligands) to inside (the metal core) that yielded induced ECD and CPL activities related to the metal cores, and the less-known pathway, from inside (the distorted chiral core) to outside (chiral ligands) that resulted in distinctly amplified VCD activities depending on the metal cores.

Detailed analyses stressed the importance of avoiding simplified models to fully extract rich information hidden in the experimental VCD features. Encouraged by these results, ongoing VCD studies of atomically-precise metal clusters aim to deepen our understanding of chiral events in

nanosized inorganic materials, particularly regarding the intricate interplay between metal cores and ligands.

3.4 References

- [1] L. A. Warning, A. R. Miandashti, L. A. McCarthy, Q. Zhang, C. F. Landes, S. Link, *ACS Nano* **2021**, 15, 15538-15566.
- [2] L. Xu, X. Wang, W. Wang, M. Sun, W. J. Choi, J.-Y. Kim, C. Hao, S. Li, A. Qu, M. Lu, X. Wu, F. M. Colombari, W. R. Gomes, A. L. Blanco, A. F. de Moura, X. Guo, H. Kuang, N. A. Kotov, C. Xu, *Nature* **2022**, 601, 366-373.
- [3] T. Yasukawa, S. Kobayashi, *Chiral Metal Nanoparticles for Asymmetric Catalysis*, In: S. Kobayashi, (eds) *Nanoparticles in Catalysis. Topics in Organometallic Chemistry*, vol 66. Springer, Cham, **2020**.
- [4] R. Jin, T. Higaki, *Commun. Chem.* **2021**, 4, 28.
- [5] Y. Jin, C. Zhang, X.-Y. Dong, S.-Q. Zang, T. C. W. Mak, *Chem. Soc. Rev.* **2021**, 50, 2297-2319.
- [6] Z. Lei, X. K. Wan, S. F. Yuan, Z. J. Guan, Q. M. Wang, *Acc. Chem. Res.* **2018**, 51, 2465-2474.
- [7] S. Takano, T. Tsukuda, *J. Am. Chem. Soc.* **2021**, 143, 1683-1698.
- [8] I. Dolamic, S. Knoppe, A. Dass, T. Bürgi, *Nat. Commun.* **2012**, 3, 798.
- [9] L.-J. Liu, F. Alkan, S. Zhuang, D. Liu, T. Nawaz, J. Guo, X. Luo, J. He, *Nat. Commun.* **2023**, 14, 2397.
- [10] Z. Han, X.-Y. Dong, P. Luo, S. Li, Z.-Y. Wang, S.-Q. Zang, T. C. W. Mak, *Sci. Adv.* **2020**, 6, eaay0107.
- [11] Z. Han, Y. Si, X.-Y. Dong, J.-H. Hu, C. Zhang, X.-H. Zhao, J.-W. Yuan, Y. Wang, S.-Q. Zang, *J. Am. Chem. Soc.* **2023**, 145, 6166-6176.
- [12] Y. Li, T. Higaki, X. Du, R. Jin, *Adv. Mater.* **2020**, 32, 1905488.
- [13] Y. Wang, B. Nieto-Ortega, T. Bürgi, *Nat. Commun.* **2020**, 11, 4562.
- [14] H. Yoshida, M. Kuzuhara, R. Tanibe, T. Kawai, T. Nakashima, *J. Phys. Chem. C* **2021**, 125, 27009-27015.
- [15] P. Luo, X. J. Zhai, S. Bai, Y. B. Si, X.-Y. Dong, Y. F. Han, S. Q. Zang, *Angew. Chem. Int. Ed.* **2023**, 62, e202219017.
- [16] L. Riccardi, F. De Biasi, M. De Vivo, T. Bürgi, F. Rastrelli, G. Salassa, *ACS Nano* **2019**, 13, 7127-7134.
- [17] T. A. Keiderling, *Chem. Rev.* **2020**, 120, 3381-3419.

- [18] C. Merten, *Eur. J. Org. Chem.* **2020**, 5892–5900.
- [19] Y. Yang, J. Cheramy, Y. Xu, *ChemPhysChem* **2021**, 22, 1336-1343.
- [20] S. Jähnigen, *Angew. Chem. Int. Ed.* **2023**, 62, e202303595.
- [21] I. Dolamic, B. Varnholt, T. Bürgi, *Nat. Commun.* **2015**, 6, 7117.
- [22] A. Sels, R. Azoulay, W. Jan Buma, M. A. J. Koenis, V. P. Nicu, T. Bürgi, *J. Phys. Chem. C* **2019**, 123, 22586-22594.
- [23] P. Pracht, F. Bohle, S. Grimme, *Phys. Chem. Chem. Phys.* **2020**, 22, 7169-7192.
- [24] F. Xie, N. A. Seifert, M. Heger, J. Thomas, W. Jäger, Y. Xu, *Phys. Chem. Chem. Phys.* **2019**, 21, 15408-15416.
- [25] F. Xie, N. A. Seifert, W. Jäger, Y. Xu, *Angew. Chem. Int. Ed.* **2020**, 59, 15703-15710.
- [26] A. W. Lange, J. M. Herbert, *J. Chem. Theory Comput.* **2012**, 8, 1999-2011.
- [27] Y. Yang, J. Cheramy, M. Brehm, Y. Xu, *ChemPhysChem.* **2022**, 23, e202200161.
- [28] Y. Yang, M. Alshalalfeh, Y. Xu, *Spectrochim. Acta A Mol. Biomol. Spectrosc.* **2023**, 307, 123634.
- [29] H. Wang, M. Heger, M. H. Al-Jabiri, Y. Xu, *Molecules*, **2022**, 27, 38/1-19.
- [30] F. Weigend, R. Ahlrichs, *Phys. Chem. Chem. Phys.* **2005**, 7, 3297-3305.
- [31] S. Grimme, J. Antony, S. Ehrlich, H. Krieg, *J. Chem. Phys.* **2010**, 132, 154104.
- [32] A. D. Becke, E. R. Johnson, *J. Chem. Phys.* **2005**, 123, 154101.
- [33] M. A. S. Yokomichi, H. R. L. Silva, L. E. V. N. Brandao, E. F. Vicente, J. M. Batista Jr. *Org. Biomol. Chem.* **2022**, 20, 1306-1314.
- [34] J. R. Cheeseman, private communication.

Chapter 4

Mechanisms of Chiral Signals of a Racemic Eu Complex and an Achiral Eu Salt Revealed by Two-Cell Experiments

This chapter is directly copied and adapted the new format from the following submitted paper:

Mutasem Alshalalfeh, Guojie Li, Yanqing Yang, Josef Kapitán, Petr Bouř, and Yunjie Xu

4.1 Introduction

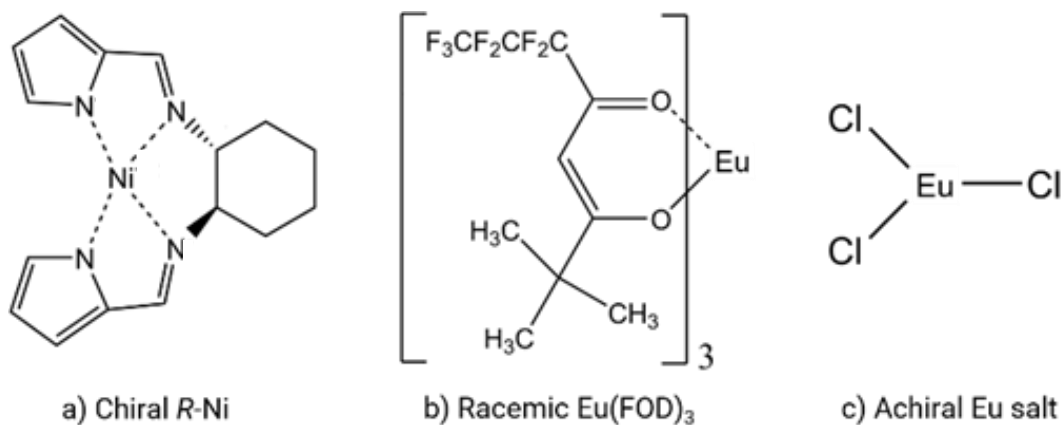
While Raman spectroscopy serves as an effective tool for structural information, Raman optical activity (ROA), which measures the small intensity difference of the right versus left-circularly polarized light¹ in a Raman scattering event, contains sensitive information about absolute configurations and conformational distributions of chiral (bio)molecules.^{2,3} In recent years, ROA applications have expanded to a wide range of chiral systems. Examples include lanthanide complexes,⁴ amyloid fibrils,⁵ retinal chromophore in sensory rhodopsin II,⁶ helicenes,⁷ and engineered nanostructures.⁸ One family of compounds of special recent interest is lanthanide complexes. In particular, the strong circularly polarized luminescence (CPLu) of lanthanide complexes has attracted significant attention, owing to its potential applications in chiral sensing of biomolecules,⁹ in authenticating products and documents as security inks,¹⁰ and in information storage in quantum computing.¹¹ Generally, the CPLu capability is imprinted into lanthanide luminophores through incorporation of a chiral ligand, inducing a chiral response in the lanthanide cores via ligand-to-metal charge transfer.^{12,13} In addition, more complex CPLu systems that do not rely on enantiomerically pure molecules have also been reported. For instance, in an asymmetric photolysis experiment, an increase in enantiomeric excess (ee) was detected because the enantiomer with a higher extinction coefficient was preferentially photo-decomposed in a chiral environment.^[14] Similar systems were recently reviewed,¹⁵ which include supramolecular luminophores composed of solely of achiral organic molecules,¹⁶ achiral or racemic luminophores under external magnetic field,^{17,18} and so-called cryptochiral CPLu systems that are CD-silent but can emit CPLu in the photoexcited state.¹⁹ While CPLu signals in these experiments are typically monitored using a CPLu spectrometer,^{20,21} Wu and co-workers and others^{22,23} showed the applicability of a backscattering ROA spectrometer as well. The usage of a laser excitation source

facilitates CPLu measurements of weaker signals, and enables the acquisition of different types of data Raman/ROA and Lu/CPLu from a single sample solution in the same experiment.

Very recently, a novel form of chiral Raman spectroscopy, known as electronic circular dichroism (ECD)-circularly polarized Raman (CP-Raman), abbreviated as eCP-Raman, was discovered.²⁴⁻²⁸ For example, the strong $I_R - I_L$ signals observed in a resonating Ni complex (*R*-Ni, depicted in Scheme 4.1) using an ROA spectrometer were found to be primarily attributed to eCP-Raman, rather than the previously thought resonance ROA. eCP-Raman spectroscopy provides a deeper insight into multiple concurrent light-matter interaction events. To detect the $I_R + I_L$ luminescence features of Eu species, one pre-requisite is that the system must absorb photons, i.e., to be under (near) resonance conditions. Given these recently discovered processes, important questions may arise regarding the mechanism behind previously reported signals obtained on an ROA instrument under (near) resonance conditions.

One question of interest is whether the reported signals contain significant contributions from mechanisms beyond CPLu. Additionally, if multiple resonating species coexist in a solution, will they significantly influence each other's $I_R - I_L$ signals? Given that ROA experiments of Eu sensing of biomolecular systems generally contain species under (near) resonance conditions, it becomes crucial to meticulously and systematically address contributions, such as eCP-Raman or ECD, to the obtained experimental $I_R - I_L$ data. Motivated by these questions, we designed a series of experiments to examine the resulting $I_R - I_L$ signals, using mixtures of chiral *R*-Ni complex with the racemic deuterated Eu^{III} -tris(1,1,1,2,2,3,3-heptafluoro-7,7-dimethyl-4,6-octanedionate- d_{27}) complex, abbreviated as $\text{Eu}(\text{FOD})_3$, and an achiral EuCl_3 salt (refer to Scheme 4.1) using an ROA spectrometer. Employing a specially designed two-cell experimental setup, we aimed to answer not only the questions posed above, but also whether the chiral signals detected at the Eu CPLu

bands are caused by chemical interactions between the Eu with the chiral *R*-Ni species or by other mechanisms, such as the generation of ee through the excited electronic state mechanism reported previously for some racemic Eu compounds.^{29,30}



Scheme 4.1. Three (near) resonance molecular systems investigated in the current study: a) enantiomeric pure *R*-Ni; b) racemic Eu(FOD)₃ complex; and c) an achiral Eu salt.

4.2 Results and Discussion

4.2.1 One-cell Experiments

Based on previous reports,^{39,24} it is established that both Ni and Eu(FOD)₃ are under (near) resonance condition with the 532 nm excitation laser used in the ROA spectrometer. The ${}^7F_0 \rightarrow {}^5D_0$ electronic transition of Eu³⁺ aligns is under (near) resonance with the 532 nm green laser of the ROA instrument. While Ni is (nearly) enantiomeric pure, the Eu(FOD)₃ complex exists as a racemic mixture with a dynamic equilibrium between the Δ and Λ axial chiral forms. We deliberately chose the racemic Eu complex so that we could detect subtle changes in the Eu $I_R - I_L$ spectra, potentially arising from factors other than inherent chirality. Two different sets of experiments were carried out: one with constant Ni concentration and varying Eu(FOD)₃ concentrations and the other with constant Eu(FOD)₃ concentration and varying Ni concentrations.

Additionally, experiments with pure Ni and $\text{Eu}(\text{FOD})_3$ solutions were also performed. The $I_R + I_L$ and $I_R - I_L$ spectra with a constant Ni and $\text{Eu}(\text{FOD})_3$ concentrations are presented in Figures 4.1 and B1, in the Appendix B, respectively. Spectra of solutions with only Ni and $\text{Eu}(\text{FOD})_3$ in CDCl_3 , and of pure CDCl_3 are shown in Figure B2(Appendix B).

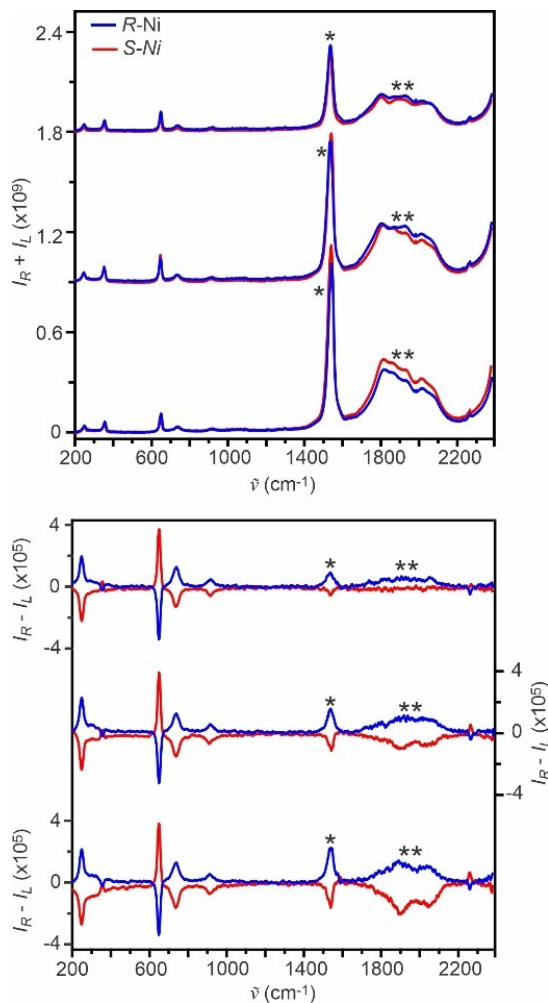


Figure 4.1. $I_R + I_L$ (top) and $I_R - I_L$ (bottom) spectra of the racemic $\text{Eu}(\text{FOD})_3$ solutions with a constant concentration of S - and R -Ni (7.6 mM) in CDCl_3 with the standard one-cell experimental setup. The concentrations of $\text{Eu}(\text{FOD})_3$ 4.9 mM (top), 9.5 mM (middle), and 19.1 mM (bottom). Asterisk * and ** indicates the sharp Eu band at $\sim 1532 \text{ cm}^{-1}$ and the broad Eu features in the 1800-2200 cm^{-1} region.

In all the $I_R + I_L$ spectra, the main solvent CDCl_3 bands remain consistent at 242, 356, 648, 732, 905 and 2255 cm^{-1} , showing no noticeable frequency shift or relative intensity alternation in the presence of Ni, $\text{Eu}(\text{FOD})_3$, or their mixtures. This observation suggests the absence of strong chemical or intermolecular interaction between the CDCl_3 and the solutes. Upon the addition of $\text{Eu}(\text{FOD})_3$, the strongest $I_R + I_L$ bands appear in the $1400\text{-}2200\text{ cm}^{-1}$ region, featuring a distinct band at 1532 cm^{-1} and a broad feature spanning from $1630\text{ to }2200\text{ cm}^{-1}$. These features, labelled with “*” and “***” in Figure 4.1, are not Raman bands of $\text{Eu}(\text{FOD})_3$; instead, they are luminescence bands associated with the electronic transitions of the Eu ion core, particularly the ${}^7\text{F}_0 \rightarrow {}^7\text{F}_4$ and ${}^7\text{F}_0 \rightarrow {}^7\text{F}_3$ transitions.^{31,32} Similar luminescence signals were reported for mixed solutions of an europium complex (deuterated Eu^{III} -tris(1,1,1,2,2,3,3-heptafluoro-7,7-dimethyl-4,6-octanedionate- d_{27} , or $\text{Eu}([\text{D}_9]\text{FOD})_3$) with small chiral molecules, such as *R*-1-phenylethanol, *R*-2,2,2-trifluoro-1-phenylethanol, and *R*-carvone.³¹ While these Eu bands were initially referred to as the induced resonance Raman bands, this mis-assignment was corrected in a later report.^{33,34} Note that the strongest Raman bands of Ni at $\sim 1582\text{ cm}^{-1}$ is nearly invisible in all the $I_R + I_L$ spectra reported in Figures 4.1 and Appendix B.

Correspondingly, strong $I_R - I_L$ features were observed at the Raman bands of CDCl_3 in all solutions with chiral Ni. These unusually large induced solvent chiral signals can be satisfactorily explained by the eCP-Raman mechanism.²⁸ Briefly, with the chiral Ni complex being under (near) resonance condition, the right circularly polarized light (*CPL*) and left *CPL* components of the incoming randomly polarized light are absorbed differently, due to ECD of the chiral Ni solute solution, leading to an imbalance in right *CPL* versus left *CPL* as the light passes through the cell. The partially *CPL* scatters on all molecules in its path, whether they are chiral or achiral, generating CP-Raman $I_R - I_L$ features at the related Raman band position. Furthermore, the outcoming

scattered light passes through the same chiral Ni solution and is again absorbed differently due to ECD of Ni, producing the final eCP-Raman signals.^{24b-d} Thus eCP-Raman bands of the chiral Ni are also present although their intensity are generally weak, only visible if one amplifies the $I_R - I_L$ features (vide infra). The simulations of eCP-Raman features will be further discussed in the **Simulations of $I_R - I_L$ spectra** section.

The prominent $I_R - I_L$ features at the luminescence bands of $\text{Eu}(\text{FOD})_3$ are somewhat surprising because a racemic sample was used. In the previous Eu experiments, very strong $I_R - I_L$ Eu signals were also reported when $\text{Eu}(\text{FOD})_3$ was mixed with small chiral molecules, such as *R*-1-phenylethanol, *R*-2,2,2-trifluoro-1-phenylethanol, and *R*-carvone, or when achiral EuCl_3 was mixed with chiral polymeric glutamic acid and fibril.³³ In those cases, strong coordination and/or covalent bindings between the Eu and chiral species were proposed by the previous authors as the mechanism for chirality transfer from the chiral species to the Eu probes. Similarly, non-covalent intermolecular interactions, such as hydrogen bonding interactions between a chiral solute and achiral molecules, had been reported to be responsible for induced vibrational circular dichroism (VCD) signals of the achiral molecules in solution^{35,36} and in cold rare gas matrices.³⁷ The induced chiral signal tends to be of similar intensity as regular VCD bands.

The presence of two (near) resonance species (Eu and Ni) in solution gives rise to interesting variations in the observed spectra. The impact of (near) resonance absorption is especially prominent in the experiments with different [Ni] (see Figure B1). For example, the observed $I_R + I_L$ band intensities of Eu and solvent bands are markedly higher at lower Ni concentrations, even though the experimental $[\text{CDCl}_3]$ and $[\text{Eu}(\text{FOD})_3]$ remain essentially constant. Conversely, the corresponding $I_R - I_L$ band intensities remain nearly the same with [Ni] values of 7.6 mM and 3.8 mM. Moreover, in the one-cell experiments with a fixed chiral [Ni] and

varying $[\text{Eu}(\text{FOD})_3]$, the $\text{Eu}(\text{FOD})_3$ band intensities do not exhibit a proportional relationship to its concentration. While these observations were confusing initially, they were explained by considering the absorption by Ni and Eu. Higher $[\text{Ni}]$ results in weaker overall scattered light intensity, leading to weaker Eu and solvent bands, even though their concentrations remain the same in all experiments. Similar effects were observed with varying $[\text{Eu}]$, though to a lesser extent. The dependence of the $I_R - I_L$ intensities on $[\text{Ni}]$ will be further explored below.

The normalized circular intensity difference (CID) values, calculated as $(I_R - I_L)/(I_R + I_L)$, are presented in Table B1, Appendix B. The CID values of the solvent bands remain very similar at a constant $[\text{Ni}]$ of 7.6 mM with different $\text{Eu}(\text{FOD})_3$ concentrations including $[\text{Eu}(\text{FOD})_3] = 0$ mM, i.e., the Ni only solution. This suggests that the addition of $\text{Eu}(\text{FOD})_3$ has a negligible effect on the CID values of the induced solvent chiral features. In the mixture solutions, the strongest Ni band at 1582 cm^{-1} significantly overlaps with the very strong Eu band centred at 1531 cm^{-1} , making it difficult to extract the CID values of Ni for comparison. Overall, $\text{Eu}(\text{FOD})_3$ appears to have minimal effects, indicating no additional enhancement on the chiral features of the solvent and Ni bands where the main chiral mechanism is eCP-Raman.^{24,28} It also appeared that the CID values of the induced solvent CDCl_3 features roughly scaled with $[\text{Ni}]$, as evidenced by the CID values listed at two different Ni concentrations. This aligns with the eCP-Raman formula (1). In our experiments, the CID is controlled by the main ECD agent, Ni, which explains why concentrations of the other Raman scattering species have a minor effect. Indeed, the CID values of the Eu bands seem to scale with $[\text{Ni}]$ in a similar fashion to CDCl_3 . The mechanism behind the chiral Eu bands will be discussed further in the following sections.

To investigate whether the $I_R - I_L$ signals of Eu may also stem from a direct chemical/physical contact with a chiral species (Ni), we conducted UV-Vis and ECD

measurements of Ni in CDCl_3 and Ni+Eu(FOD) $_3$ in CDCl_3 . The resulting spectra are compared in Figure B3, Appendix B. The Ni vs Ni+Eu(FOD) $_3$ ECD spectra exhibit little difference, indicating the absence of strong chemical/physical interactions. While minor effects, undetectable by our spectrometer, cannot be entirely ruled out, the ECD of Ni remains as the main likely mechanism for the observed Eu chiral features. To substantiate this hypothesis, we devised a two-cell set up, as described in the next section, where direct chemical/physical contact can be avoided.

4.2.2 Two-cell Experiments

Schematic diagrams illustrating the setups for the two-cell and one-cell experiments are depicted in Figure 4.2. CDCl_3 served as the solvent in the one-cell experiments. In the two-cell experiments, we chose CDCl_3 as the solvent for the chiral Ni complex in Cell 1, while ethanol was used as a solvent for both Eu(FOD) $_3$ and EuCl $_3$ in Cell 2. One reason to use ethanol is the low solubility of EuCl $_3$ in CDCl_3 . Also, it is beneficial to use two different solvents so that one can separately monitor the (chiral) responses of solvent bands in Cell1 and Cell2.

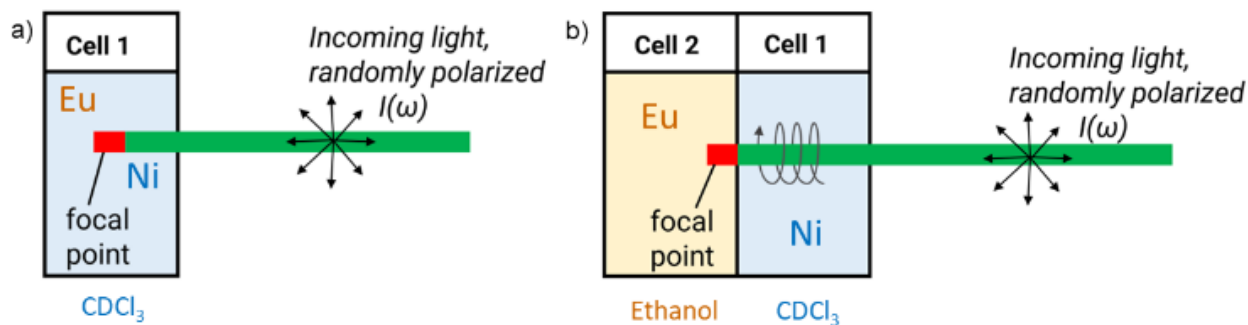


Figure 4.2. Schematic diagrams of a) one-cell and b) two-cell experimental setup using an ROA instrument. In the one-cell set up, both Eu and Ni complexes are dissolved in CDCl_3 and the excitation laser focal point is placed at the center of the cell. In the two-cell setup, only the Ni complex in CDCl_3 is placed in Cell 1, while Eu(FOD) $_3$ in ethanol or EuCl $_3$ in ethanol are placed in Cell 2. The laser focal point is placed very close to the front side of Cell 2 as shown in the figure.

Considerable efforts were made to keep the experimental conditions stable, including the position of the focusing points. The two-cell results with three different $\text{Eu}(\text{FOD})_3$ concentrations of 4.9, 9.5, and 19.1 mM at a constant $[\text{Ni}]$ of 7.6 mM are provided in Figure 4.3, and they can be directly compared with the one-cell results in Figure 4.1. CID values of the visible vibrational bands of $R\text{-Ni}$ and CDCl_3 in Cell 1 and of $\text{Eu}(\text{FOD})_3$ and ethanol in Cell 2 are summarized in Table B2, Appendix B.

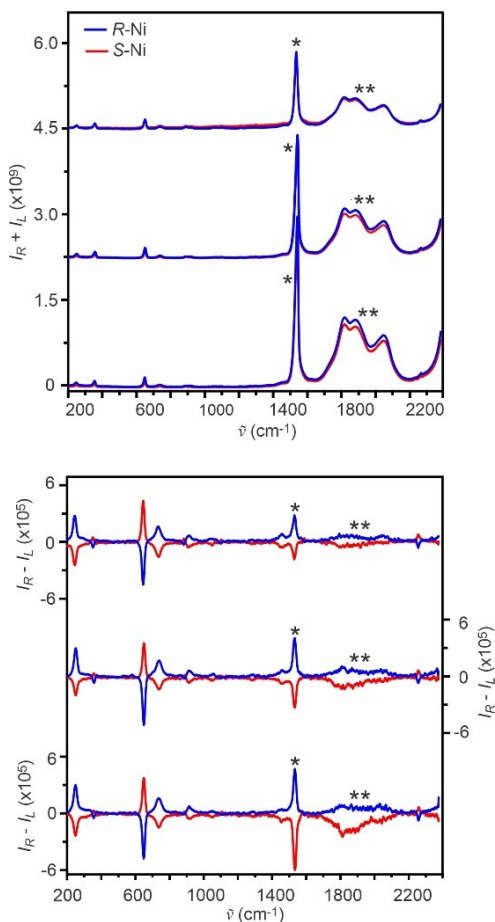


Figure 4.3. The two-cell $I_R + I_L$ (top) and $I_R - I_L$ (bottom) spectra of the racemic $\text{Eu}(\text{FOD})_3$ solutions with a constant concentration of 7.6 mM of S - and R -Ni in CDCl_3 in Cell 1. The concentrations of $\text{Eu}(\text{FOD})_3$ in ethanol in Cell 2 are 4.9 mM (top), 9.5 mM (middle), and 19.1 mM (bottom). Asterisk * and ** indicates the sharp Eu band at $\sim 1532 \text{ cm}^{-1}$ and the broad Eu features in the 1800-2200 cm^{-1} region.

As shown in Figure 4.3, the $I_R - I_L$ signals of the luminescence bands of the racemic $\text{Eu}(\text{FOD})_3$ complexes remain conspicuous in the spectra, showcasing similar features to those observed in the corresponding one-cell spectra. This recurrence strongly suggests that direct physical contact is not the primary cause for the observed chiral features. Given that the used $\text{Eu}(\text{FOD})_3$ is racemic and lacks visible Raman bands in this wavenumber range, we can exclude its CPLu and eCP-Raman as the main mechanisms, respectively. Drawing on the analysis on potential light-matter interaction events in this type of experiments,^{24,28} we proposed that the most likely mechanism stemmed from the differential absorption of Eu luminescence bands by the chiral Ni solution or ECD of Ni. We will discuss this topic in detail when we present the simulations based on this mechanism and describe other experimental evidences.

Since ECD of chiral Ni generates a small amount of CPL, which interacts with the racemic $\text{Eu}(\text{FOD})_3$ complex, a second mechanism was also proposed. Based on the previous literature on lanthanide compounds, when a racemic sample is irradiated by CPL, an ee may be generated in the excited state.^{29,38} For example, in one report, the $I_R - I_L$ features of racemic $\text{Eu}(\text{DPA})_3$ (DPA = dipicolinate), at an excitation wavelength of 526.3 nm, in H_2O and D_2O solutions, were reported with a g factor of 8.5×10^{-2} for the band at 615.7 nm and -1.9×10^{-2} for the band at 594.7 nm.²⁹ To verify whether this mechanism is also relevant, we carried out similar two-cell experiments by replacing racemic $\text{Eu}(\text{FOD})_3$ with achiral EuCl_3 . The $I_R + I_L$ and $I_R - I_L$ experimental spectra obtained with EuCl_3 are summarized in Figure B4 (Appendix B). The $I_R + I_L$ spectra are dominated by the sharp Eu band at $\sim 1524 \text{ cm}^{-1}$ and the broad Eu features in the $1600\text{-}2200 \text{ cm}^{-1}$ region, which can be assigned to ${}^5\text{D}_0 \rightarrow {}^7\text{F}_0$ and mainly ${}^5\text{D}_1 \rightarrow {}^7\text{F}_3$ and ${}^5\text{D}_0 \rightarrow {}^7\text{F}_1$, respectively.³⁹ Since EuCl_3 is achiral, the excited state ee mechanism is not expected to play a role. The associated CID values of the visible vibrational bands of *R*-Ni and CDCl_3 in Cell 1 and of EuCl_3 and ethanol in Cell 2 are

also provided in Table B2 (Appendix B). Overall, both the sharp (*) and broad (**) Eu features are also present in the $I_R + I_L$ and $I_R - I_L$ spectra, exhibiting similar CID magnitudes as in the case of $\text{Eu}(\text{FOD})_3$. This suggests that neither physical contact nor the excited state ee mechanism plays a dominant role in the observed $I_R - I_L$ features of EuCl_3 .

In the experiments presented above, however, the light produced by ECD of Ni is only polarized partially. We therefore also explored the excited state ee mechanism by using 100% CPL to excite the racemic $\text{Eu}(\text{FOD})_3$ complex in CDCl_3 and ethanol. Comparison experiments were carried out with achiral EuCl_3 in ethanol, pure CDCl_3 , and pure ethanol. The $I_R + I_L$ and $I_R - I_L$ spectra obtained are summarized in Figure 4.4. Comparing the experimental traces of $I_R + I_L$ features of $\text{Eu}(\text{FOD})_3$ with those in the corresponding pure solvents, it is evident that the dominant features in the $1400\text{-}2200\text{ cm}^{-1}$ region are luminescence bands of Eu. These include the sharp band (*) at 1532 cm^{-1} and the very broad band (**) in the $1800\text{-}2200\text{ cm}^{-1}$ region, which closely resemble the features obtained in the one-cell experiments.

It is of no surprise that the dominant $I_R - I_L$ features are associated with the solvent CP-Raman bands^[40,41] which can be easily identified by comparing to the pure solvent $I_R - I_L$ traces. We note that, at the typical scale used for CP-Raman signals, no $I_R - I_L$ features are visible in the $1400\text{-}2200\text{ cm}^{-1}$ region for both $\text{Eu}(\text{FOD})_3$ and EuCl_3 . This observation is interesting. In the $I_R + I_L$ spectra, the Eu luminescence bands are obviously much stronger than the Eu Raman bands (if any) in the same region. On the other hand, if there were Eu Raman bands of similar intensity to those of solvents, one would expect to observe Eu $I_R - I_L$ CP-Raman bands since the interference by the Eu luminescence is removed. Only when magnified 50 times (see the inserts in Figure 4.4), some weak $I_R - I_L$ features become visible. In CDCl_3 solution, while most of these weaker features belong to the CP-Raman bands of CDCl_3 , it is interesting to observe a positive band at the Eu band

at 1532 cm^{-1} with a g factor of 1.4×10^{-3} , and a slightly positive and broad feature in the $1800\text{--}2200\text{ cm}^{-1}$ region. Notably, the latter is present only in the racemic $\text{Eu}(\text{FOD})_3$ solution, not in the pure solvent. We therefore tentatively assigned these positive Eu features to the excited state ee mechanism.

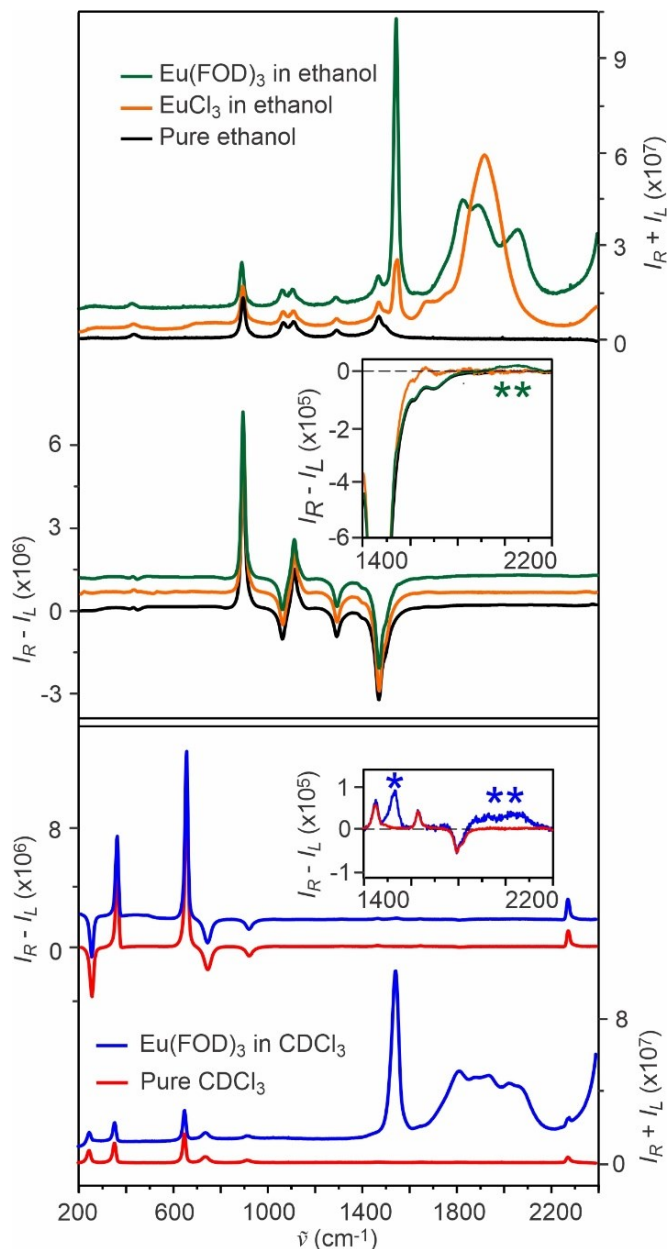


Figure 4.4. Top: Experimental $I_R + I_L$ and $I_R - I_L$ spectra of ethanol solutions of racemic $\text{Eu}(\text{FOD})_3$ (9.5 mM), achiral EuCl_3 (19.1 mM) and pure ethanol. Bottom: Experimental $I_R + I_L$ and $I_R - I_L$

spectra of CDCl_3 solutions of racemic $\text{Eu}(\text{FOD})_3$ (4.8 mM) and pure CDCl_3 . These experiments were performed by using 100% left *CPL* at 532 nm as the excitation source. Please note that the spectra traces are shifted vertically so that they do not overlap on top of each other and the experimental of $I_R + I_L$ and $I_R - I_L$ intensities were scaled by the same factor for easy comparison among the different ethanol or CDCl_3 solutions. Please see the main text for the discussion about luminescence baseline. The inserts show the zoom-in $I_R - I_L$ features in the 1400-2200 cm^{-1} region. Here asterisk * and ** indicate the sharp $I_R - I_L$ Eu band at $\sim 1532 \text{ cm}^{-1}$ and the broad Eu features in the 1800-2200 cm^{-1} region, respectively.

In ethanol solutions of $\text{Eu}(\text{FOD})_3$ and EuCl_3 , extracting conclusive information about the sharp $I_R - I_L$ band of either Eu species is challenging due to severe interference from the nearby strong CP-Raman ethanol band. On the other hand, the broad band of $\text{Eu}(\text{FOD})_3$ (green trace) shows a broad, positive $I_R - I_L$ feature centered about 2000 cm^{-1} , whereas the corresponding feature of EuCl_3 (orange trace) is virtually zero. This contrast observation further supports the assignment that the $I_R - I_L$ features racemic $\text{Eu}(\text{FOD})_3$ are caused by the excited state ee mechanism, similar to what was reported for racemic $\text{Eu}(\text{DPA})_3$ and other Eu species.^{29,38} Since EuCl_3 is achiral, we do not expect the excited state ee mechanism here, which is consistent with our experimental observation.

Overall, the two-cell experiments reveal that direct physical contact is not necessary for the $I_R - I_L$ features observed in racemic $\text{Eu}(\text{FOD})_3$ and achiral EuCl_3 . Additionally, in the case of racemic $\text{Eu}(\text{FOD})_3$, the excited state ee mechanism may also be involved. In the next section, we directly simulated the experimental $I_R - I_L$ features based on the proposed mechanisms to quantitatively interpret experimental chiral spectroscopic features.

4.2.3 Simulations of $I_R - I_L$ Spectra

Here, we simulated the observed $I_R - I_L$ features obtained in the two-cell experiments. In our ROA experiments, randomly polarized light passes through Cell 1 containing R -Ni, resulting in an imbalance between right and left CPL due to ECD of R -Ni. In the case of R -Ni, there is a positive differential absorption (defined as $\Delta\varepsilon = \varepsilon_L - \varepsilon_R$) at 532 nm (i.e., $\varepsilon_L > \varepsilon_R$). This leads to reduced absorption of $RCPL$, leading to more right than left CPL shining on $\text{Eu}(\text{FOD})_3$, EuCl_3 , and their solvents in Cell 2. We can extend the previous derivation of the CID equation of a solvent to include all species, such as racemic $\text{Eu}(\text{FOD})_3$ and achiral EuCl_3 species in Cell 2:

$$CID = \frac{I_R - I_L}{I_R + I_L} = \frac{\ln 10}{4} cL \Delta\varepsilon \left(\frac{\Delta\varepsilon'}{\Delta\varepsilon} + DOC \right) \quad (4.1)$$

where $\Delta\varepsilon$ and $\Delta\varepsilon'$ are ECD intensities of R -Ni for the excitation and scattered light, respectively. DOC is the degree of circularity of either the solute or solvent Raman vibration, and c is the concentration of (near resonance) R -Ni. L is the optical path length of R -Ni. For the CID calculations of species in Cell 1, L was assumed to be ~ 2.5 mm, with the focus at the center of Cell 1. For species in Cell 2, L is ~ 5 mm because the light passes through the whole Cell 1 before interacting with species in Cell 2. While it is possible to calculate the DOC values, e.g. by DFT, this would be currently not accurate enough. For example, in the ethanol solutions, ethanol monomers, dimers and larger aggregates are all present, making it challenging to simulate the final CP-Raman of ethanol. Rather, we extracted the DOC curves of all species in Cell 1 and Cell 2 directly, using the experimental results summarized in Figure 4.4. Please note that $(I_R - I_L) / (I_R + I_L)$ ratios associated with the luminescent bands of Eu species were also included.

Important points related to the simulations include: 1) The DOC values were obtained by dividing the experimental $(I_R - I_L)$ and $(I_R + I_L)$ spectra presented in Figure 4.4, after removing

fluorescence baselines. 2) Because these experiments were performed with 100% left *CPL*, whereas *R*-Ni generates an excess of right *CPL*, a factor of (-1) was used to apply to the DOC used in the final simulations. 3) The CID values for the species in Cell 1 (i.e., *R*-Ni and CDCl₃) and Cell 2 (i.e., Eu(FOD)₃ or EuCl₃ and ethanol) are expected to differ by a factor of ~1/2 based on the estimated path lengths. 4) To correct for the absorption, minor adjustment was applied to the intensity of Cell 1 versus Cell 2. 5) The CID values for the species in the same cell were calculated without any scaling factors. 6) The final $I_R - I_L$ simulations were generated by multiplying the obtained CID values based on equation (4.1) and the obtained two-cell $I_R + I_L$ spectra after minor baseline correction.

The final simulations are showcased in Figure 4.5 and compared with the two-cell $I_R - I_L$ spectra obtained with *R*-Ni in CDCl₃ in Cell 1 and EuCl₃ in ethanol in Cell 2 (top) and *R*-Ni in CDCl₃ in Cell 1 and Eu(FOD)₃ in ethanol in Cell 2 (bottom). It is gratifying to note that the relative intensity of all visible $I_R - I_L$ bands are well reproduced quantitatively. The simulated CID values for all these bands are compared with the experimental ones in Table B3 (Appendix B) demonstrating an excellent agreement between experimental and simulated values.

It is interesting to point out that despite the observation of very tiny positive $I_R - I_L$ features for Eu(FOD)₃ with 100% left *CPL* (Figure 4.4 inserts), the intensities are so low in comparison to the strong CP-Raman solvent bands that they make no discernible contribution to the final simulated features based on equation (4.1). This was confirmed by the DOC curve obtained from the experimental data of Eu(FOD)₃ in ethanol, which quantitatively matched the pattern derived from pure ethanol data (Figure 4.4). Evidently, the $I_R - I_L$ spectral features of Eu(FOD)₃ are *not* generated by direct chemical/physical contact or the excited state ee mechanism. Rather, both the $I_R - I_L$ spectral features of Eu(FOD)₃ and EuCl₃ are produced when the Eu luminescent light

generated in Cell 2 passes through Cell 1, undergoes preferential absorption of left versus right *CPL* by ECD of chiral *R*-Ni, and finally reaches the detector. Overall, the excellent quantitative agreement between the simulated and experimental $I_R - I_L$ spectra strongly supports the conclusion that the ECD Ni absorption of the Eu luminescence bands is the primary mechanism for the observed $I_R - I_L$ bands of $\text{Eu}(\text{FOD})_3$ and EuCl_3 .

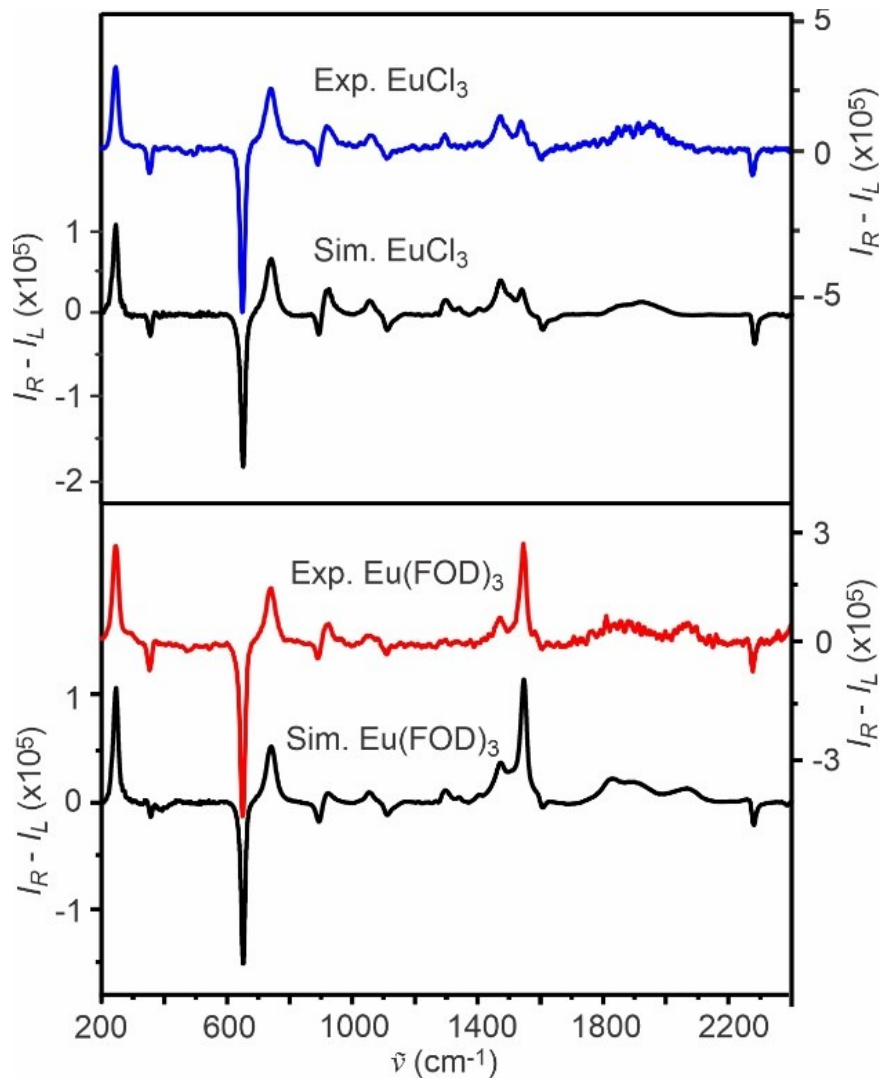


Figure 4.5. Comparison of the simulated and experimental $I_R - I_L$ spectra of (top) *R*-Ni (7.6 mM) in CDCl_3 in Cell 1 with EuCl_3 (38.0 mM) in ethanol in Cell 2 and (bottom) *R*-Ni (7.6 mM) in CDCl_3 in Cell 1 with $\text{Eu}(\text{FOD})_3$ (19.1mM) in ethanol in Cell 2. Please see the main text for simulation details and discussions.

The experimental one-cell $I_R - I_L$ and $I_R + I_L$ spectra of $\text{Eu}(\text{FOD})_3$ in CDCl_3 exhibit very similar Eu features to those observed in the two-cell experiments, with only minor deviations noted. Similarly, very slight differences were observed for the ECD spectra between pure $R\text{-Ni}$ and the mixture of $\text{Eu}(\text{FOD})_3$ and $R\text{-Ni}$ (see Figure B3, Appendix B). It was reported previously that mixtures of small Eu^{3+} ions (i.e., EuCl_3) and chiral polymeric glutamic acid, fibril, and some monosaccharides exhibit strongly induced ECD and $I_R - I_L$ features at the Eu positions due to the formation of new chiral Eu species through chemical (coordination) interactions between the Eu^{3+} ions and the chiral species.³³ One may hypothesize that a very small amount of $\text{Eu}(\text{FOD})_3$ species may interact chemically with $R\text{-Ni}$, generating subtle changes between the observed one-cell and two-cell $I_R - I_L$ and $I_R + I_L$ spectra discussed above.

Overall, the present experiments conclusively prove that the $I_R - I_L$ features of the Eu species are predominantly generated by chiral light-matter events, rather than direct chemical/physical interactions of the Eu species with the chiral species, or more specifically, the ECD of $R\text{-Ni}$. This conclusion can likely be extended to other chiral species under (near) resonance condition, for example, chiral Eu complexes studied in many previous reports. The same approach can also be employed to disentangle different contributions to chiral signals detected in more complex systems.

4.3 Conclusions

Eu related ROA experiments are conducted under (near) resonance conditions, where multiple light-matter interaction events can contribute to the observed $I_R - I_L$ features. These contributions extend beyond direct chemical interactions, such as the formation of new chiral Eu complexes. To assess the relative contributions of each of these mechanisms to the observed $I_R - I_L$ features of the Eu and other species, we designed both one-cell and two-cell experimental setups

using various sample sets. The subtle distinctions observed between the one-cell and two-cell $I_R - I_L$ features of the Eu and Ni mixtures suggest that direct chemical or physical interactions play only a minor role. The complementary CP-Raman experiments involving racemic Eu(FOD)₃ and achiral EuCl₃ showed that the excited state ee mechanism also had a limited impact on the final $I_R - I_L$ features of the Eu species. Our investigation reveals that the primary mechanism responsible for the observed $I_R - I_L$ features of Eu species involves a two-step process: i) Absorption of the 532 nm laser light leads to luminescence ($I_R + I_L$) of Eu(FOD)₃ and EuCl₃; ii) Preferential absorption of the luminescence because of ECD of *R*-(or *S*-)Ni gives the final $I_R - I_L$ imbalance for the Eu species. The simulated $I_R - I_L$ spectra for all species, including Eu(FOD)₃, EuCl₃, CDCl₃, ethanol and *R*-Ni, based on this proposed mechanism, accurately reproduce the experimental ones. The current study underscores the challenges in interpreting chiral responses in Eu ROA experiments. It provides a foundation for evaluating chiral responses in all situations where chiral Eu complexes themselves or other more complex systems are under (near) resonance conditions.

4.4 Experimental Section

The enantiomeric pure *R*- and *S*-Ni complexes were synthesized and purified following to the reported synthetic procedures.^[42,43] The racemic Eu(FOD)₃ (99%) and achiral EuCl₃ (99.99%) were purchased from Sigma-Aldrich and used without further purification. Sample solutions of *R*-Ni and *S*-Ni in CDCl₃ and in ethanol were prepared by dissolving 12.5 mg the respective compounds in 1 ml of the respective solvents for a concentration 38.0 mM, while solutions of Eu(FOD)₃ in both solvents were prepared by dissolving 39.6 mg of racemic Eu(FOD)₃ in 1.0 ml of the respective solvents for a concentration of 38.2 mM. Finally, 9.8 mg of achiral EuCl₃ was dissolved in 1ml of ethanol to achieve a concentration of 38.0 mM. A dilution factor was applied

to obtain the desired concentrations for the specific samples used in the one- and two-cell measurements.

A scattered circular polarized (SCP), backscattering Chiral Raman-2xTM spectrometer (BioTools) which operates with a 532 nm laser excitation source, was used for all experimental measurements in the 200 to 2400 cm^{-1} region. Note that in SCP, a randomly polarized laser light is used as the excitation source. The laser power was set at 12 mW at the source, and an accumulation time of 2 hours, i.e., 7008 scans, was used for each experiment. For the one-cell experiments, the focal point was approximately at the centre of Cell 1 for a path length of ~ 2.5 mm. For the two-cell experiments, the focal point was approximately at the front face of Cell 2 for a path length of ~ 5 mm.

The UV-Vis and ECD spectra in the 250-700 nm of racemic $\text{Eu}(\text{FOD})_3$ (0.77 mM), *R*-Ni (0.31 mM), and a mixture of *R*-Ni (0.16 mM) and $\text{Eu}(\text{FOD})_3$ (0.38 mM) in CDCl_3 were measured using a JASCO-810 ECD spectrometer with a path length of 1.0 mm. In addition, we also carried out measurements of UV-Vis and ECD spectra of *R*-Ni in CDCl_3 in the 532 nm to 620 nm region, corresponding to 0 to 2668 cm^{-1} shifted Raman wavenumber scale. Since the UV-Vis and ECD spectra in this region are relatively weak, the measurements were done with a concentration of 9.2 mM and a path length of 10 mm to ensure good signal-to-noise ratios that are essential for proper spectral simulations. Furthermore, a python script was used to interpolate the obtained ECD and Raman spectra with a step size 0.25 cm^{-1} for simulations.

4.5 References

- [1] L. A. Nafie, *Vibrational optical activity: Principles and applications*, Wiley, Chichester, **2011**.
- [2] T. Keiderling, *Chem. Rev.* **2020**, 120, 3381-3419.
- [3] J. Bogaerts, F. Desmet, R. Aerts, P. Bultinck, W. Herrebout, C. Johannessen, *Phys. Chem. Chem. Phys.* **2020**, 22, 18014-18024.
- [4] T. Wu, R. Pelc, P. Bouř, *Chem. Plus. Chem.* **2023**, 88, e202300385.
- [5] A. Kolodziejczyk, L. A. Nafie, A. Wajda, A. Kaczor, *Chem. Commun.* **2023**, 59, 10793-10796.
- [6] K. Nishikawa, R. Kuroiwa, J. Tamogami, M. Unno, T. Fujisawa, *J. Phys. Chem. B* **2023**, 127, 7244-7250.
- [7] C. Shen, M. Srebro-Hooper, T. Weymuth, F. Krausbeck, J. T. L. Navarrete, F. J. Ramírez, B. Nieto-Ortega, J. Casado, M. Reiher, J. Autschbach, J. Crassous, *Chem. Eur. J.* **2018**, 24, 15067-15079.
- [8] J. Kwon, K. H. Park, W. J. Choi, N. A. Kotov, J. Yeom, *Acc. Chem. Res.* **2023**, 56, 1359-1372.
- [9] S. E. Bodman, S. J. Butler, *Chem. Sci.* **2021**, 12, 2716-2734.
- [10] L. E. MacKenzie, R. Pal, *Nature Rev. Chem.* **2021**, 5, 109-124.
- [11] J. F. Sherson, H. Krauter, R. K. Olsson, B. Julsgaard, K. Hammerer, I. Cirac, E. S. Polzik, *Nature* **2006**, 443, 557-560.
- [12] F. Zinna, C. Resta, S. Abbate, E. Castiglioni, G. Longhi, P. Mineoe, L. Di Bari, *Chem. Commun.* **2015**, 51, 11903-11906.
- [13] B. Zercher, T. A. Hopkins, *Inorg. Chem.* **2016**, 55, 10899-10906.
- [14] C. Meinert, S. V. Hoffmann, P. Cassam-Chena, A. C. Evans, C. Giri, L. Nahon, U. J. Meierhenrich, *Angew. Chem. Int. Ed.* **2014**, 53, 210-214; *Angew. Chem.* **2014**, 126, 214-218.
- [15] Y. Imai, *Symmetry* **2020**, 12, 1786.
- [16] Q. Jin, S. Chen, Y. Sang, H. Guo, S. Dong, J. Han, W. Chen, X. Yang, F. Li, P. Duan, *Chem. Commun.* **2019**, 55, 6583-6586.
- [17] F. Richardson, H.G. Brittain, *J. Am. Chem. Soc.* **1981**, 103, 18-24.
- [18] H. Okada, N. Hara, D. Kaji, M. Shizuma, M. Fujiuki, Y. Imai, *Phys. Chem. Chem. Phys.* **2020**, 22, 13862-13866.
- [19] T. Amako, K. Nakabayashi, N. Suzuki, S. Guo, N.A.A. Rahim, T. Harada, M. Fujiki, Y. Imai, *Chem. Commun.* **2015**, 51, 8237-8240.

- [20] G. Longhi, E. Castiglioni, J. Koshoubu, G. Mazzeo, S. Abbate, *Chirality*, **2016**, 28, 696-707.
- [21] G. Mazzeo, M. Fusè, A. Evidente, S. Abbate, G. Longhi, *Phys. Chem. Chem. Phys.* **2023**, 25, 22700-22710.
- [22] T. Wu, *Phys. Chem. Chem. Phys.* **2022**, 24, 15672-15686.
- [23] L. Palomo, L. Favereau, K. Senthilkumar, M. Stepień, J. Casado, F. J. Ramírez, *Angew. Chem. Int. Ed.* **2022**, 61, e202206976; *Angew. Chem.* **2022**, 134, e202206976.
- [24] G. Li, J. Kessler, J. Cheramy, T. Wu, M. R. Poopari, P. Bouř, Y. Xu, *Angew. Chem. Int. Ed.* **2019**, 58, 16495-16498; *Angew. Chem.* **2019**, 131, 16647-16650.
- [25] T. Wu, G. Li, J. Kapitán, J. Kessler, Y. Xu, P. Bouř, *Angew. Chem. Int. Ed.* **2020**, 59, 21895-21898; *Angew. Chem.* **2020**, 132, 22079-22082.
- [26] G. Li, M. Alshalalfeh, Y. Yang, J. R. Cheeseman, P. Bouř, Y. Xu, *Angew. Chem. Int. Ed.* **2021**, 60, 22004-22009; *Angew. Chem.* **2021**, 133, 22175-22180.
- [27] E. Machalska, G. Zajac, A. J. Wierzba, J. Kapitán, T. Andruniów, M. Spiegel, D. Gryko, P. Bouř, M. Baranska, *Angew. Chem. Int. Ed.* **2021**, 60, 21205-21210; *Angew. Chem.* **2021**, 133, 21375-21380.
- [28] G. Li, M. Alshalalfeh, J. Kapitán, P. Bouř, Y. Xu, *Chem. Eur. J.* **2022**, e202104302 (1-12).
- [29] G. Hilmes, J. P. Riehl, *Inorg. Chem.* **1986**, 25, 2617-2622.
- [30] J. P. Riehl, G. Muller, in *Comprehensive Chiroptical Spectroscopy, Volume 1: Instrumentation, Methodologies, and Theoretical Simulations, First Edition*. Edited by N. Berova, P. L. Polavarapu, K. Nakanishi, R. W. Woody. **2012** John Wiley & Sons, Inc.
- [31] S. Yamamoto, P. Bouř, *Angew. Chem. Int. Ed.* **2012**, 51, 11058-11061; *Angew. Chem.* **2015**, 124, 11220-11223.
- [32] J. A. Koningstein, *J. Chem. Phys.* **1967**, 46, 2811-2816.
- [33] T. Wu, J. J. Kapitán, V. Mašek, P. Bouř, *Angew. Chem. Int. Ed.* **2015**, 54, 14933-14936; *Angew. Chem.* **2015**, 127, 15146-15149.
- [34] T. Wu, P. Bouř, V. Andrushchenko, *Sci. Rep.* **2019**, 9, 1-5.
- [35] M. Losada, H. Tran, Y. Xu, *J. Chem. Phys.* **2008**, 128, 014508; b) G. Yang, Y. Xu, *J. Chem. Phys.* **2009**, 130, 164506.
- [36] A. S. Perera, J. Cheramy, C. Merten, J. Thomas, Y. Xu, *Chem.Phys.Chem.* **2018**, 19, 2234-2242.

- [37] C. Merten, Y. Xu, *Angew. Chem. Int. Ed.* **2013**, 52, 2073-2076; *Angew. Chem.* **2013**, 125, 2127-2130.
- [38] P. Gawryszewska, G. Oczko, J. Riehl, V. Tsaryuk, J. Legendziewicz, *J. Alloys Compd.* **2004**, 380, 352-356.
- [39] T. Wu, P. Bouř, *Chem. Commun.* **2018**, 54, 1790-1792.
- [40] L. D. Barron, *Molecular Light Scattering and Optical Activity*, Cambridge University Press, Cambridge, UK, **2004**.
- [41] R. Clark, S. R. Jeyes, A. J. McCaffery, R. A. Shatwell, *J. Am. Chem. Soc.* **1974**, 96, 5586-5588.
- [42] Z. Dezhahang, M. R. Poopari, J. Cheramy, Y. Xu. *Inorg. Chem.* **2015**, 54, 4539-4549.
- [43] X. F. Shan, D. H. Wang, C. H. Tung, L. Z. Wu. *Tetrahedron* **2008**, 64, 5577-5582.

Chapter 5

Conformational Distributions of Phenyl β -D Glucopyranoside and Gastrodin in Solution by Vibrational Optical Activity and Theoretical Calculations

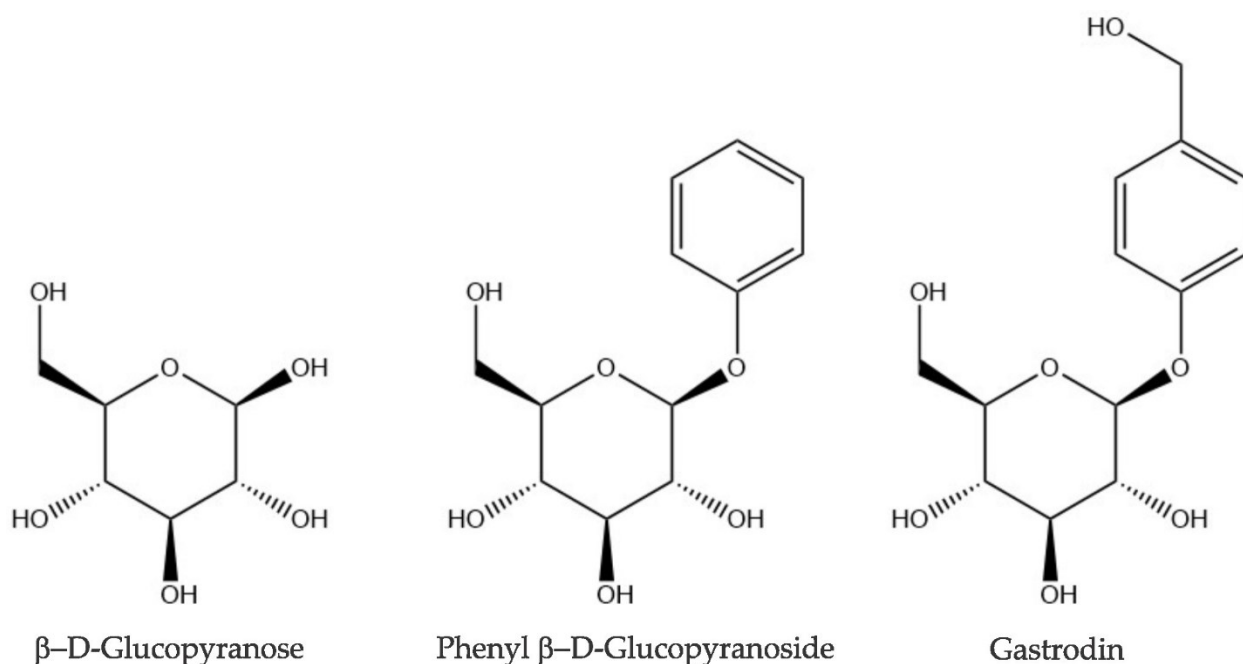
This chapter is directly copied and adapted the new format from the following publications:

M. Alshalalfeh, N. Sun, A. H. Moraes, A. P. A. Utani, Y. Xu, *Molecules* 2023, 28, 4013.

5.1 Introduction

Monosaccharides are the basic building units for all carbohydrates and have been shown to provide vital biological functions, from delivering energy for cells to treating a number of genetic disorders^{1,2}. Generally, there is a strong connection between the stereochemical properties, including absolute configuration and conformations of a chiral drug molecule and its drug activity. As a result, there has been a great deal of research interest in unravelling the associated chirality and conformational distributions of monosaccharides in solution^{3,4}.

The two monosaccharide derivatives of interest in this work are shown in Scheme 5.1, namely phenyl β -D-glucopyranoside (ph- β -glu) and 4-(hydroxymethyl)phenyl β -D-glucopyranoside, which is commonly known as gastrodin. Ph- β -glu is a phenolic compound that can be extracted from some medicinally used plants⁵. It has been shown to exhibit anti-inflammatory and anti-cancer activity and has protective effects on the liver when it is exposed to toxic substances⁶. Gastrodin is one main ingredient of *Gastrodia elata* tuber, a traditional Chinese medicine which is used for treating vascular and neurological diseases^{7,8}. Although the detailed mechanisms of these bioactivities have not been well understood, some research work in this direction was recently reported. For example, the binding activity of gastrodin to several targets was investigated⁹ and the immunomodulatory effects of gastrodin¹⁰ were monitored with a range of tools including near infrared (IR) spectroscopy. These two molecules share the same β -D-glucopyranoside subunit, which is also depicted in Scheme 5.1. While ph- β -glu has a benzene substituent at the anomeric position, gastrodin has a phenyl-para-methanol substituent at the anomeric position.



Scheme 5.1. Structures of β -D-glucopyranoside, phenyl β -D-glucopyranoside (ph- β -glu), and gastrodin.

The possible conformations of ph- β -glu in the gas phase were first investigated by Talbot and Simons¹¹ by using mass-selected resonant two-photon ionization and IR ion dip spectroscopy where the authors identified three low-energy conformers of the β -anomer which all show the exocyclic hydroxyl group in the equatorial position. Later, Simons and co-workers reported that the addition of just one water molecule was enough to drastically change the conformational landscape of ph- β -glu and discussed the implications of this for measurements done in solution¹². In searching for vibrational circular dichroism (VCD) markers for differentiation of the α - and β -anomeric configuration in solution, Monde and co-workers¹³ surveyed the experimental IR and VCD spectra of several naturally occurring monosaccharides, including ph- β -glu and ph- α -glu in deuterated-dimethyl sulfoxide (DMSO) solution. They identified an intense, sharp, and negative VCD signature at about 1145 cm^{-1} as a marker for the α -D-anomers, whereas no such strong

feature was observed for the β -D-anomers. For gastrudin, no similar conformational or chiroptical spectroscopic investigations have been reported in the gas phase or in solution so far.

The vibrational optical activity (VOA) spectroscopies have emerged in the last ten years as powerful spectroscopic tools for determining absolute configuration and dominating conformations of a wide range of chiral molecules directly in solution, such as amino acids^{14,15}, peptides¹⁶, proteins¹⁷, and carbohydrates^{18,19}. These methods include VCD²⁰, Raman optical activity (ROA)²¹, and a recently discovered new form of chiral Raman spectroscopy^{22,23}, which has already been utilized in several studies of chiral molecules under (near) resonance²⁴. To extract stereochemical properties, including chirality and conformational distributions from the VOA spectroscopic data, it is essential to utilize an efficient strategy to identify all possible low-energy conformers of the molecular targets. The recently developed conformer-rotamer ensemble sampling tool (CREST) by Grimme and co-workers²⁵ has emerged as an effective and efficient conformational search tool. CREST has been successfully utilized and at the same time benchmarked in rotational spectroscopic studies of flexible molecules²⁶ and non-covalently bonded clusters^{27,28} where rotational spectra of individual conformers can be identified separately, in contrast to most condensed phase studies. So far, the only documented failure of CREST in producing a conformational candidate is the case of the heterochiral trimer of propylene oxide²⁹ whose geometry was established experimentally by rotational spectroscopic data of different isotopologues. More recently, CREST has been utilized in several VOA studies, for example, the recent report of conformations of steroid hormones by VCD³⁰ and the development of a computational protocol for VCD spectra of cyclic oligopeptides³¹.

Since no conformational distribution investigations have been reported for ph- β -glu and gastrudin in solution directly, we applied a combined experimental and theoretical approach by using both

VCD and ROA spectroscopies to extract conformational distributions of these two chiral molecular targets in DMSO and in water. First, we aimed to systematically identify all possible low-energy conformers of ph- β -glu and gastrodin by applying CREST²⁴. The subsequent DFT calculations were carried out to facilitate theoretical IR, VCD, Raman, and ROA simulations and comparisons with the experimental data. Second, the influence of conformations on the resulting VCD and ROA spectral features was discussed in detail, since these VOA features are much more sensitive to small structural changes than their parent spectroscopies. Finally, the conformational distributions of ph- β -glu and gastrodin in DMSO and in water were obtained and compared and were also compared to those obtained in the gas phase whenever available to appreciate the effects of solvents on conformational preferences.

5.2 Results and Discussion

In the following, we first describe the general conformational searches and DFT geometry optimizations performed for ph- β -glu and gastrodin and summarize all the low-energy minima identified in DMSO and in water in Section 5.2.1. Next, comparisons of the simulated and experimental IR and VCD spectra of ph- β -glu and of gastrodin in DMSO are discussed in Section 5.2.2. In Section 5.2.3, the experimental and theoretical Raman and ROA spectra of ph- β -glu and of gastrodin in water are explained. Overall, the good agreements between experiment and theory allow one to conclusively identify the main conformers of ph- β -glu and gastrodin in these two solvents. Finally, we examined how the conformational preferences alter from the gas phase to DMSO and to water and compared their conformational distributions in Section 5.2.4.

5.2.1 Low-Energy Conformers of Phenyl β -D-Glucopyranoside and Gastrodin

As can be seen in Scheme 5.1, β -D-glucose, ph- β -glu, and gastrodin share the same pyranose ring. To facilitate the discussion of the conformational geometries, we first introduced the naming scheme, similar to those used in the rotational spectroscopic investigation of β -D-glucose³² and in the previous literature¹². Briefly, the letter β was used to describe the anomer type where the exocyclic O group at the anomeric carbon (C1) and the hydroxymethyl group are on the same face of the ring. Since one does not expect a conversion between the β and the α anomers for the substituted glucoses such as ph- β -glu and gastrodin, we do not include this part in the conformational naming for conciseness. For ph- β -glu, the naming starts with the conformation of the pyranose ring hydroxymethyl group which is labelled with G+, G-, or T for the torsion angle O6–C6–C5–O5 of about 60°, –60°, or 180°, respectively, and g+, g-, or t for the torsion angle H6–O6–C6–C5 in the same way (See Figure 5.1). Next, the ring hydroxyl groups in the lower-energy conformers typically form a counter-clockwise (cc) or clockwise (c) chain of (weak) cooperative network of intramolecular hydrogen bonding type contacts, as reported in the previous studies^{12,31}. Furthermore, the phenyl group attached to O1 may rotate about the C1–O1 bond to generate several torsional conformations. Again, we label them as G+, G-, or T where the torsion angle C2–C1–O1–C7 is about 60°, –60°, or 180°, respectively. Finally, the phenyl plane may tilt differently by rotating about the O1–C7 bond. The systematic names are given in Figure 5.2 to identify the specific conformers of ph- β -glu. For example, the global minimum in DMSO (vide infra) is G-g+/cc/T where the ring hydroxymethyl group, G-g+, is listed first, followed by a slash and the symbol for the OH \cdots O contact directions of the ring hydroxyl groups, i.e., cc, and finally after a second slash, the phenyl torsional conformation T. Regarding the tilting of the phenyl plane, the corresponding C1–O1–C7–C12 dihedral angle varies from about 13° to 16° for conformers with

the T phenyl torsional conformation, and from -51° to -52° for the G- phenyl torsional conformation, respectively (See Figure C1, Appendix C for the detailed dihedral angle values). For conciseness, we decided not to further label the conformation associated with the tilting of the phenyl plane because it has a one-to-one relationship with the phenyl torsional conformation.

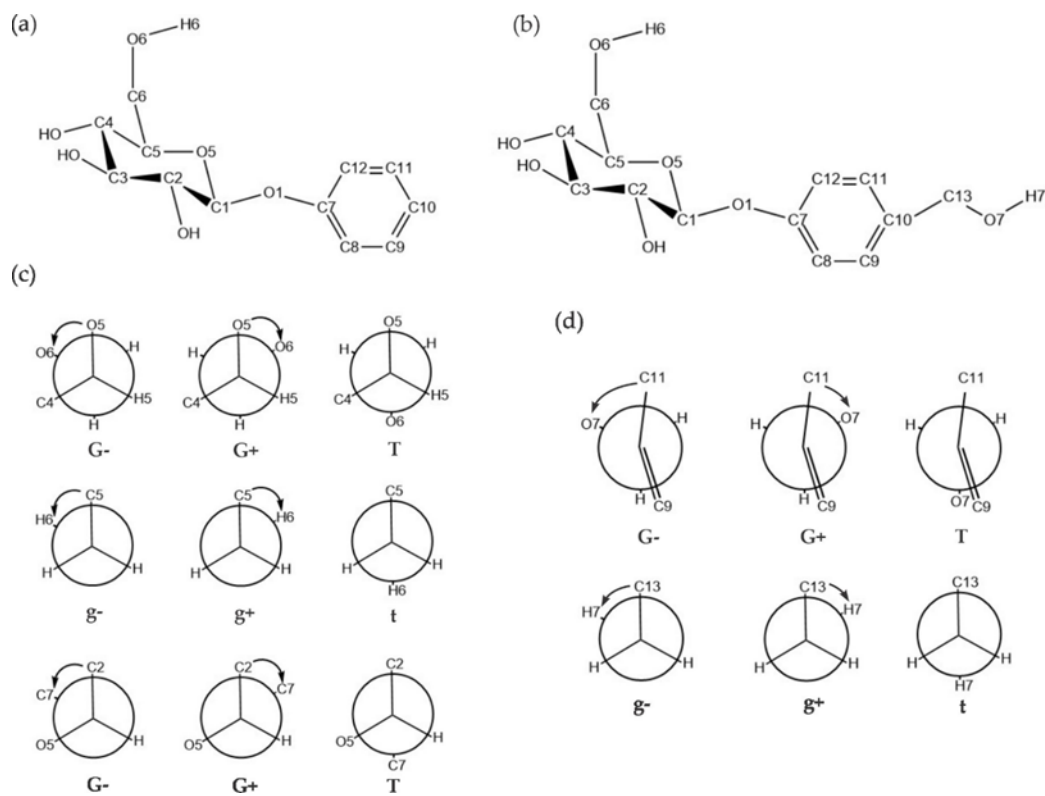


Figure 5.1. The structural formula of (a) ph-β-glu and (b) gastrodin where both molecules are shown in the 4C1 chair conformations. (c) Newman projections of the plausible conformations of the hydroxymethyl group of the pyranose ring around the C5–C6 and C6–O6 bonds and the plausible conformations of the phenyl group around the C1–O1 bond. (d) Newman projections of the plausible conformations of the hydroxymethyl group of the phenyl ring around the C10–C13 and C13–O7 bonds.

For gastrodin, an additional label is needed for the hydroxymethyl group attached in the para position to the phenyl group is needed. Here, we use G⁺, G⁻, or T when the torsion angle C11–C10–C13–O7 is about 60°, –60°, or 180°, respectively, and g⁺, g⁻, or t are similarly defined for the torsion angle C10–C13–O7–H7 for the phenyl hydroxymethyl group. For example, the global minimum of gastrodin in DMSO (*vide infra*) is G-g⁺/cc/T/G+g⁻ where the first three units describe the conformation of the ph-β-glu part. As described above, a further slash followed by G+g⁻ describes the conformation of the hydroxymethyl group at the phenyl ring (see Figure 5.1d). These systematic names are used in Figure 5.2 and Figure 5.3 to identify the specific conformers of ph-β-glu and gastrodin. The C1–O1–C7–C12 dihedral angle values which correspond to the tilting degrees of the phenyl plane are given in Figure C2, Appendix C.

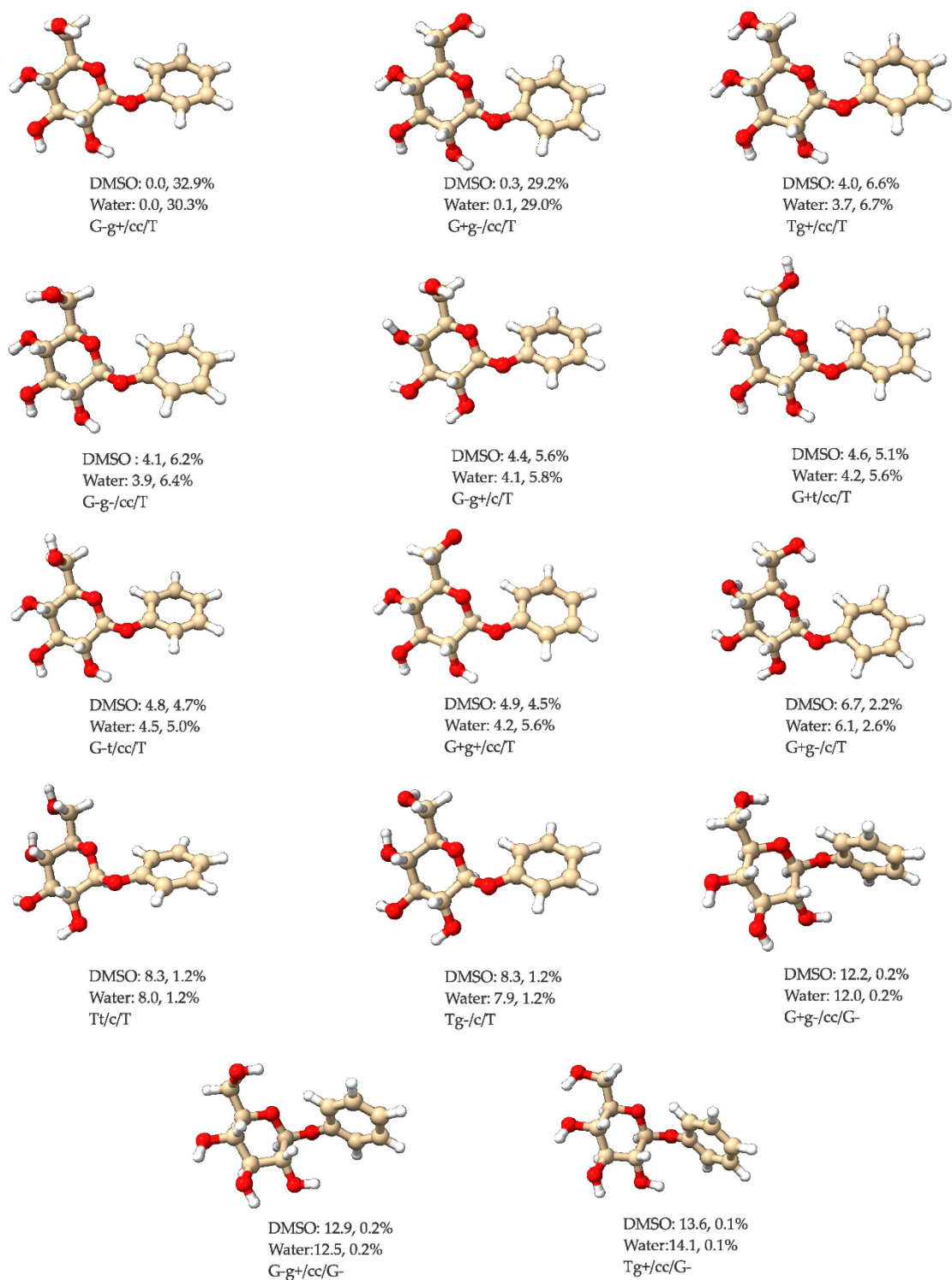


Figure 5.2. Geometries of the 14 most stable conformers of ph- β -glu at the B3LYP-D3BJ/def2-TZVPD level with the PCM of DMSO and water. The relative free energies in kJ mol⁻¹ and the percentage Boltzmann factors at 298 K are also given.

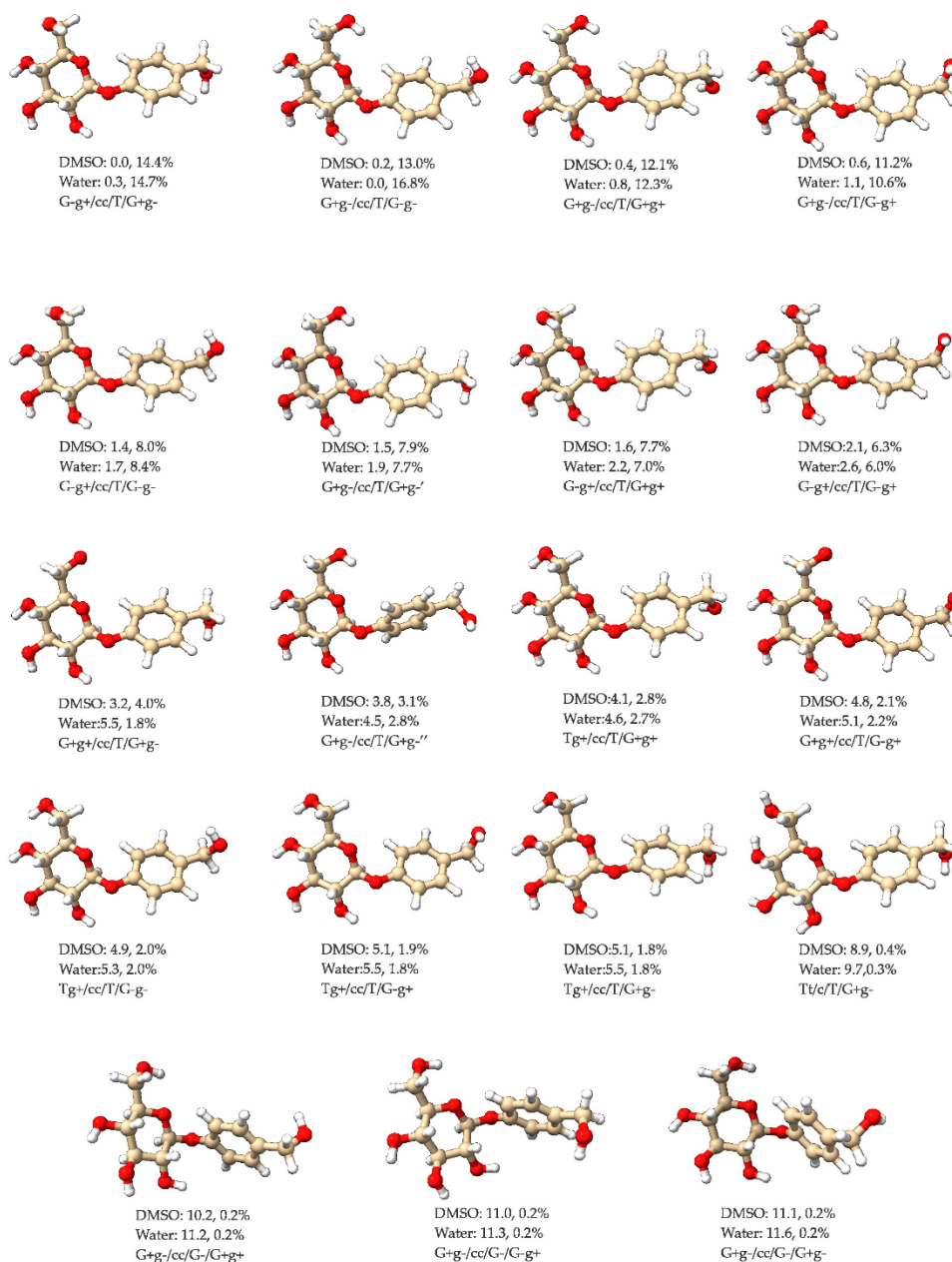


Figure 5.3. Geometries of the 19 most stable conformers (i.e., conformers with Boltzmann population $> 0.1\%$) of gastrodin at the B3LYP-D3BJ/def2-TZVPD level with the PCM of DMSO and Water. The relative free energies in kJ mol^{-1} and the percentage Boltzmann factors at 298 K are also listed. Note that conformer No. 6 and 10 have the same name based on the current scheme but have different phenyl group titling positions and are differentiated by adding ‘and’ at the end.

We applied CREST for systematic conformational searches of ph- β -glu and gastrodin with the GFN2-xTB GBSA³³ implicit solvation model, where GBSA stands for the generalized Born (GB) model with surface area (SA) contributions³⁴. An energy cut-off window of 60 kJ mol⁻¹ was applied for the CREST searches, leading to several hundred structural candidates for ph- β -glu and gastrodin in DMSO and water. We further utilized a previously developed multitier approach³⁵ to potentially capture all low-energy conformers within an energy window of 15 kJ mol⁻¹ before the final DFT geometry optimizations and spectral simulations at the B3LYP^{36,37}-D3BJ/def2-TZVPD³⁸ level. Here, the D3 dispersion correction^{39,40} with the Becke–Johnson (BJ) damping function⁴¹ was utilized. The details of the CREST and the DFT calculations are described in Section 5.3. Materials and Methods.

Initially, we applied the CREST searches in the gas phase and then carried out the final geometry optimizations in the respective solvents, i.e., DMSO and H₂O. This approach caused some issues in the DFT geometry optimization step because some CREST geometries were too far from the final optimized geometries and extra time was needed to reach convergence. We therefore redid the CREST searches in the respective solvents directly. The above procedures resulted in fourteen low-energy conformers of ph- β -glu. For gastrodin, which has an additional -CH₂OH substitution, twenty-four low-energy conformers were identified. Overall, similar sets of conformers of ph- β -glu were identified in DMSO and in water, although their relative energy ordering was altered in some cases. A similar conclusion can be drawn for the conformers of gastrodin in DMSO and in water. The resulting geometries, relative free energies, and percentage Boltzmann factors at room temperature of the ph- β -glu conformers are summarized in Figure 5.2. The corresponding results of the 19 gastrodin conformers with a percentage Boltzmann factor > 0.1% are given in Figure 5.3,

while the five less stable gastrodin conformers whose Boltzmann factors are $\leq 0.1\%$ are depicted in Figure C3, Appendix C).

Some general observations can be made about these low-energy structures of both molecules in DMSO and in water. First, all their pyranose rings take on the 4C_1 chair configuration. This is expected since the boat configuration tends to be in the order of 40 kJ mol^{-1} less stable than the chair global minimum¹². Second, the three equatorial hydroxyl groups at C2, C3, and C4 of the glucose ring form a chain of weak intramolecular attractive $\text{OH}\cdots\text{O}$ contacts, linking each hydroxyl group to its neighbor with a typical $\text{OH}\cdots\text{O}$ distance of about 2.5 \AA (see Table 5.1 and Table 5.2). In all the conformers present in Figure 5.2 and Figure 5.3, these contact networks either take on the cc or c arrangements. Furthermore, in the most preferred conformations of both ph- β -glu and gastrodin, the ring hydroxyl groups take on the cc network, whereas those with the c hydrogen contact networks appear in the (much) less preferred conformations.

Table 5.1. The parameters of four main conformers of ph β -glu at the B3LYP-D3BJ/def2-TZVPD level in DMSO.

Structural parameters	G-g+/cc/T	G+g-/cc/T	Tg+/cc/T	G-g-/cc/T
$r(\text{H}_2\text{-O}_1)/\text{\AA}$	2.583	2.590	2.583	2.582
$r(\text{H}_3\text{-O}_2)/\text{\AA}$	2.528	2.540	2.551	2.542
$r(\text{H}_4\text{-O}_3)/\text{\AA}$	2.426	2.420	2.471	2.419
$r(\text{H}_6\text{-O}_4/\text{O}_5)/\text{\AA}$	2.423	2.407	1.994	3.060
$\theta(\text{C}_2\text{-C}_1\text{-O}_1\text{-C}_7)/^\circ$	160.1	161.2	160.0	160.1
$\theta(\text{C}_3\text{-C}_2\text{-O}_2\text{-H}_2)/^\circ$	-172.4	-172.3	-172.2	-172.5
$\theta(\text{C}_4\text{-C}_3\text{-O}_3\text{-H}_3)/^\circ$	176.8	175.8	176.3	176.6
$\theta(\text{C}_5\text{-C}_4\text{-O}_4\text{-H}_4)/^\circ$	173.3	171.9	179.3	172.5
$\theta(\text{O}_5\text{-C}_5\text{-C}_6\text{-O}_6)/^\circ$	-60.2	61.6	169.7	-66.5
$\theta(\text{C}_5\text{-C}_6\text{-O}_6\text{-H}_6)/^\circ$	57.2	-56.6	48.2	-82.1
$\theta(\text{C}_1\text{-O}_1\text{-C}_7\text{-C}_{12})/^\circ$	14.8	12.6	14.8	14.4

Table 5.2. The parameters of four main conformers of gastrodin at the B3LYP-D3BJ/def2-TZVPD level in DMSO.

Structural parameters	G-g+/cc/T/G+g-	G+g-/cc/T/G-g-	G+g-/cc/T/G+g+	G+g-/cc/T/G-g+
r(H ₂ -O ₁)/Å	2.596	2.595	2.596	2.593
r(H ₃ -O ₂) /Å	2.531	2.529	2.532	2.531
r(H ₄ -O ₃) /Å	2.409	2.412	2.409	2.411
r(H ₆ -O ₅) /Å	2.405	2.400	2.403	2.401
r(H ₁₂ -O ₅) /Å	2.553	2.558	2.556	2.550
θ(C ₂ -C ₁ -O ₁ -C ₇)/°	161.6	161.5	161.6	161.1
θ(C ₃ -C ₂ -O ₂ -H ₂) /°	-171.6	-171.6	-171.6	-171.7
θ(C ₄ -C ₃ -O ₃ -H ₃) /°	176.2	176.4	176.2	176.2
θ(C ₅ -C ₄ -O ₄ -H ₄) /°	171.2	171.4	171.2	171.4
θ(O ₅ -C ₅ -C ₆ -O ₆) /°	-60.2	61.4	61.4	61.4
θ(C ₅ -C ₆ -O ₆ -H ₆) /°	57.4	-57.1	-57.3	-57.2
θ(C ₁ -O ₁ -C ₇ -C ₁₂) /°	12.5	12.7	12.5	13.3
θ(C ₉ -C ₁₀ -C ₁₃ -O ₇) /°	101.2	-73.4	74.6	-100.9
θ(C ₁₀ -C ₁₃ -O ₇ -H ₇) /°	-56.4	-56.4	56.4	56.7

For the ph-β-glu conformers in DMSO, one can roughly classify them into four groups based on their relative energies. (i) This group includes the global minimum (G-g+/cc/T) and the next nearly iso-energy (i.e., ΔG = 0.3 kJ mol⁻¹) conformer (G+g-/cc/T); (ii) The second group is about 4~5 kJ mol⁻¹ less stable and mainly includes a set of cc conformers, Tg+/cc/T, G-g-/cc/T, G+t/cc/T, G-t/cc/T, and G+g+/cc/T, as well as one c conformer G-g+/c/T; (iii) The next group is about 7~8 kJ mol⁻¹ higher in energy than those in (i) and consists of only c-conformers, G+g-/c/T, Tt/c/T, and Tg-/c/T; and (iv) The final groups were about 12~14 kJ mol⁻¹ with G+g-/cc/G-, G-g+/cc/G-, and Tg+/cc/G-. A similar classification can be made for the ph-β-glu conformers in water, even though the relative energy ordering of the ph-β-glu conformers in water within a group are often altered somewhat from those in DMSO. Some important structural parameters of the four most stable ph-β-glu conformers in DMSO are summarized in Table 5.1, while the corresponding ones in water

are listed in Table C1, Appendix C. The structural values in DMSO and in water are very similar where the largest change in bond lengths is ~ 0.007 Å and the largest change in angles is 0.3° .

In comparison to ph- β -glu, the additional -CH₂OH substituent in the para position of the phenyl group in gastrodin increases the number of low-energy conformers significantly and blurs the energy separations for the four ph- β -glu groups discussed above. For example, while the most stable gastrodin conformers still adopt the G-g+/cc/T or G+g-/cc/T ph- β -glu cores, their free energy difference can be as large as 3.6 kJ mol⁻¹ between G+g-/cc/T/G-g- and G+g-/cc/T/G+g-', highlighting the importance of the phenyl hydroxymethyl conformation on the overall stability. Some important structural parameters of the four most stable gastrodin conformers in DMSO are listed in Table 5.2 to facilitate the differentiation of these conformers, while the corresponding values in water are given in Table C2, Appendix C. The structural values of gastrodin in DMSO and in water exhibit more noticeable differences than ph- β -glu. For example, the largest change in bond lengths is ~ 0.02 Å and in angles it is 2.0° for G-g+/cc/T/G+g-.

5.2.2 Experimental and Simulated IR and VCD Spectra of ph- β -Glu and Gastrodin

The individual IR and VCD spectra of the most stable ph- β -glu conformers shown in Figure 5.4 were simulated at the B3LYP-D3BJ/def2-TZVPD level. The simulated IR and VCD spectra of the conformers are essentially identical, indicating that the addition of the extra dispersion function provided little difference. We therefore present only the results obtained at the B3LYP-D3BJ/def2-TZVPD level. The individual conformer IR and VCD spectra of ph- β -glu are depicted in Figure 5.4. It is interesting to note that while the simulated IR spectra of the individual conformers appear similar, their VCD features differ greatly. For example, the VCD features in the vicinity of 1200 cm⁻¹, which mainly correspond to the wagging motions of the CH and OH groups of the pyranose ring, vary drastically from one conformer to the next. This significant variation highlights the high

sensitivity of VCD features to small conformational changes, providing an effective tool to extract experimental conformational distributions in solution directly.

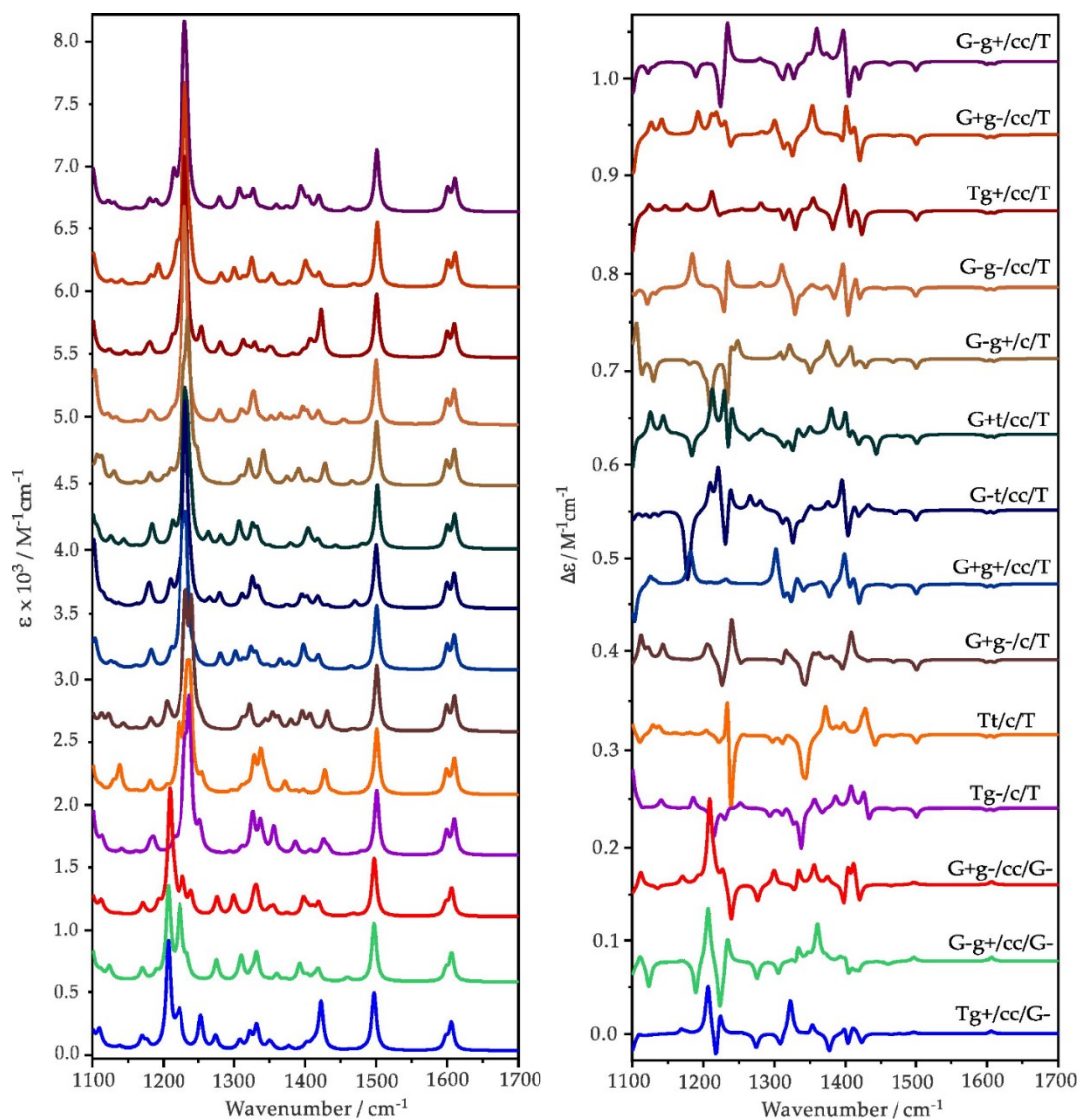


Figure 5.4. The simulated individual IR and VCD spectra of the ph- β -glu conformers at the B3LYP D3BJ/def2-TZVPD level with the PCM of DMSO. The conformers are shown based on their theoretical stability, with the most stable one at the top to the least stable one at the bottom.

To analyze the experimental spectra, we first compared the Boltzmann averaged IR and VCD spectra of the 14 most stable conformers with the experimental spectra in Figure 5.5, using the Boltzmann population factors provided in Figure 5.2. In general, the Boltzmann average IR

and VCD spectra exhibit an acceptable agreement with the experimental data. On the other hand, the main experimental features in the 1200–1300 cm^{-1} region are not as well captured, especially the bisignate VCD, which was centered at about 1229 cm^{-1} . It is well accepted in the IR and VCD community that the vibrational spectral features predicted are generally quite robust, whereas the relative free energy values are more difficult to reliably predict. A close examination of the individual conformer spectra and the experimental ones in Figure 5.3 indicates that the global minimum, G-g+/cc/T, exhibits the VCD pattern closely resembling the experimental one, whereas the simulated VCD pattern of the second main conformer, G+g-/cc/T, deviates greatly from the experimental one in the 1200–1300 cm^{-1} region. Taking into account both the IR and VCD comparison and the general stability trend predicted, we arrived at the empirical weights of 60% for G-g+/cc/T, 10% for G+g-/cc/T, Tg+/cc/T, and G-g-/cc/T, and 2.5% for the next four most stable conformers: G-g+/c/T, G+t/cc/T, G-t/cc/T, and G+g+/cc/T. The resulting re-weighted IR and VCD based on the empirical weights obtained above are also presented in Figure 5.5.

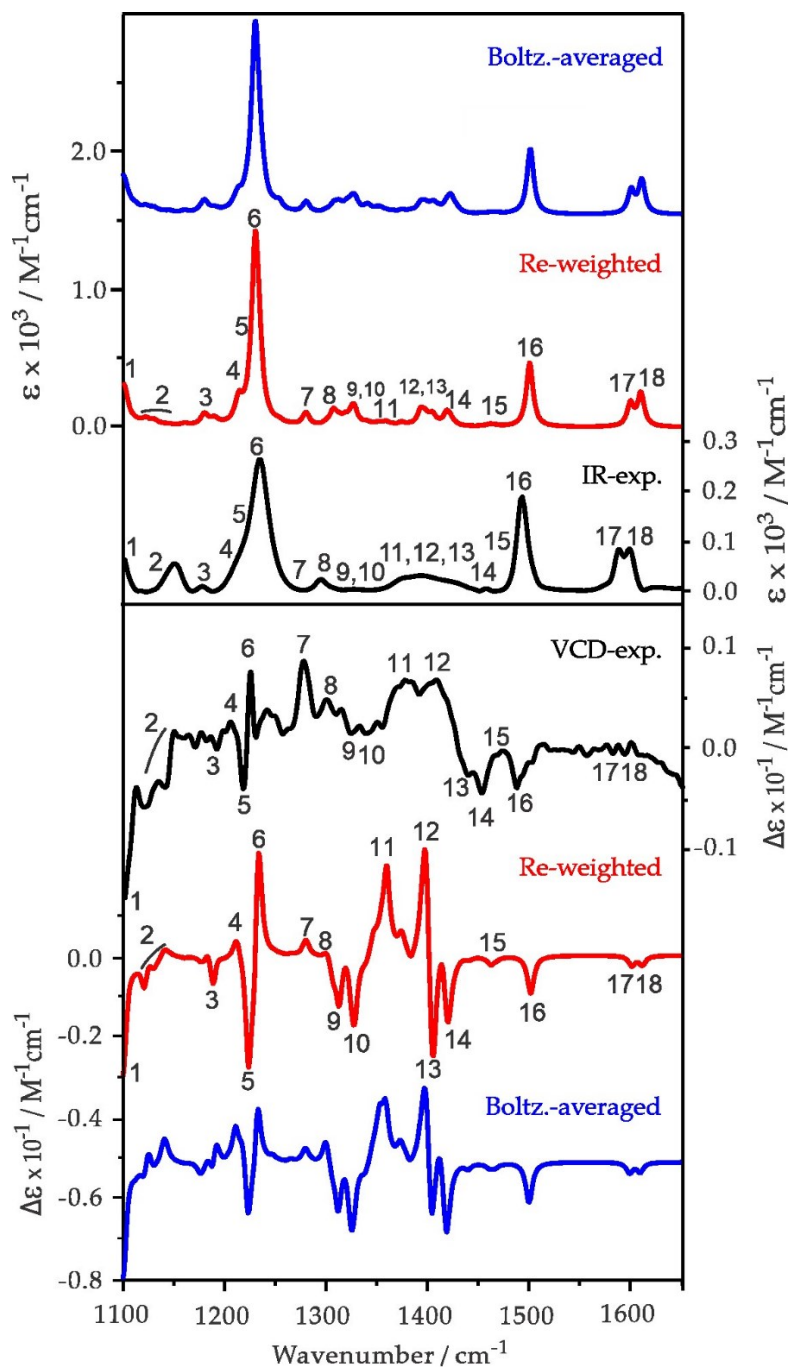


Figure 5.5. Comparison of the experimental IR and VCD spectra of ph- β -glu in DMSO with the corresponding Boltzmann averaged and re-weighted IR and VCD spectra, simulated at the B3LYP-D3BJ/def2-TZVPD level with the PCM(DMSO). The predicted Boltzmann percentage factors are listed in Figure 5.2 and the adjusted Boltzmann factors are described in the main text. The main IR and VCD features are numbered to facilitate easy comparison.

The re-weighted IR and VCD spectra show a very good agreement with the experimental data. Below, we discuss some specific features in more detail. By increasing the Boltzmann percentage factor of the global minimum, G-g+/cc/T, and reducing that of the second conformer, G+g-/cc/T, the experimental negative/positive bisignate features, labelled as 5 and 6, are now much better captured. In fact, the VCD features below 1300 cm^{-1} are better reproduced overall by the re-weighted spectrum. For example, VCD band 7 is now more intense than VCD band 8, consistent with the experimental observation. It is interesting to note that the third most stable conformer, Tg+/cc/T, contributes noticeably to this feature 7, and its weight was raised in the re-weighting scheme.

For the analysis of the IR and VCD spectra of gastrodin in DMSO, we applied a very similar approach to that described above. The individual IR and VCD spectra of the 19 most stable gastrodin conformers are shown in Figure C4, Appendix C, while those of the five least stable conformers with percentage abundances $\leq 0.1\%$ are not shown. The IR spectra of individual gastrodin conformers are generally quite similar, whereas the corresponding VCD spectra differ greatly, offering an opportunity to extract the conformational distribution of gastrodin in solution. To analyze the experimental spectra, we first compared the Boltzmann averaged IR and VCD spectra of the nineteen most stable conformers with the experimental spectra in Figure 5.6.

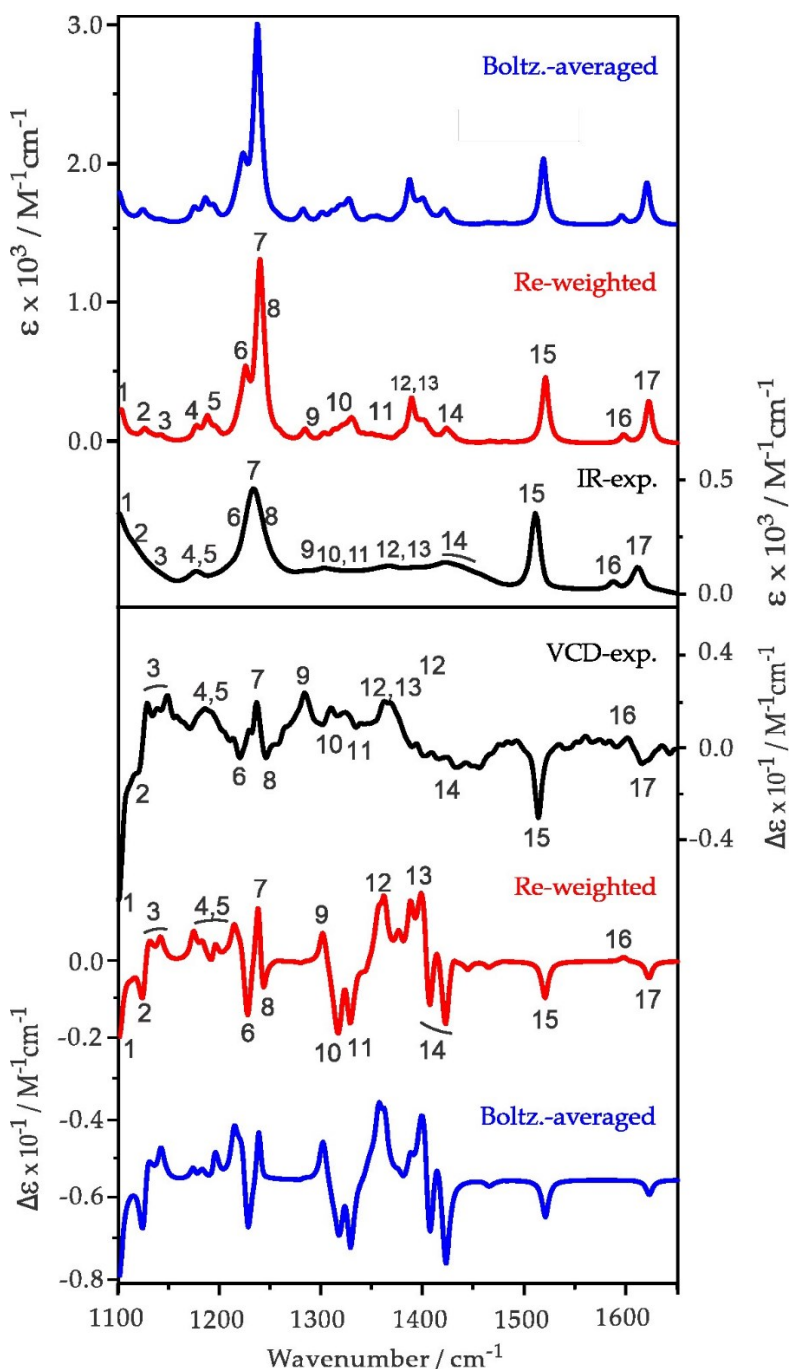


Figure 5.6. Comparison of the experimental IR and VCD spectra of gastrodin with the corresponding Boltzmann averaged IR and VCD spectra at the B3LYP-D3BJ/def2-TZVPD level with the PCM of DMSO theory at 298 K, and the re-weighted IR and VCD spectra. The percentage Boltzmann factors are given in Figure 5.3, while the empirical ones are provided in the main text. The main IR and VCD features are numbered to facilitate easy comparison.

In general, the Boltzmann average IR and VCD spectra exhibit an acceptable agreement with the experimental data of gastrodin. When one examines the individual VCD spectra of the gastrodin conformers, the VCD spectral features of Tt/c/T/G+g- seem to largely resemble the observed VCD features in the 1200–1300 cm^{-1} region. We therefore re-adjusted the percentage abundances to reflect the contribution of Tt/c/T/G+g-. Since there are a large number of possible conformers, we simplified the process by using the same percentages for those with similar stabilities and left out those with percentages less than 0.5%. Taking into account the IR, VCD comparison, and the general conformational stability trend, we arrived at the empirical weights of 14% for G-g+/cc/T/G+g- and 6% for the next three conformers: G+g-/cc/T/G-g-, G+g-/cc/T/G+g+, and G+g-/cc/T/G-g+, 8% for the next six conformers: G-g+/cc/T/G-g-, G+g-/cc/T/G+g-', G-g+/cc/T/G+g+, G-g+/cc/T/G-g+, G+g+/cc/T/G+g-, and G+g-/cc/T/G+g-', 2% for the next five conformers: Tg+/cc/T/G+g+, G+g+/cc/T/G-g+, Tg+/cc/T/G-g-, Tg+/cc/T/G-g+, and Tg+/cc/T/G+g-, and finally 15% Tt/c/T/G+g-. The resulting re-weighted IR and VCD are also presented in Figure 5.6. The main observed VCD features and the corresponding simulated ones were numbered to facilitate easier comparison. As one can see, the re-weighted VCD spectrum improves the agreement with the experiment in the 1200–1300 cm^{-1} noticeably, while the agreements in other regions remain of similar quality to the Boltzmann weighted one.

Since ph- β -glu and gastrodin differ only in the extra hydroxymethyl group at the para position at the phenyl ring for the latter, one may expect some similarity and/or relationships of their IR and VCD bands. How well are these systematic changes captured by the current theoretical modelling? In Figure 5.7, we provide a comparison of the experimental and theoretical IR and VCD of these two compounds. Three regions are highlighted in the figure, which are centered at about 1220, 1500, and 1600 cm^{-1} . The IR and VCD pattern changes from ph- β -glu to gastrodin in the 1600

cm⁻¹ region, corresponding to the C=C stretching modes of the phenyl ring, are well reproduced theoretically. Similar statements can be made for the other two shaded regions, supporting the interpretation of the experimental results.

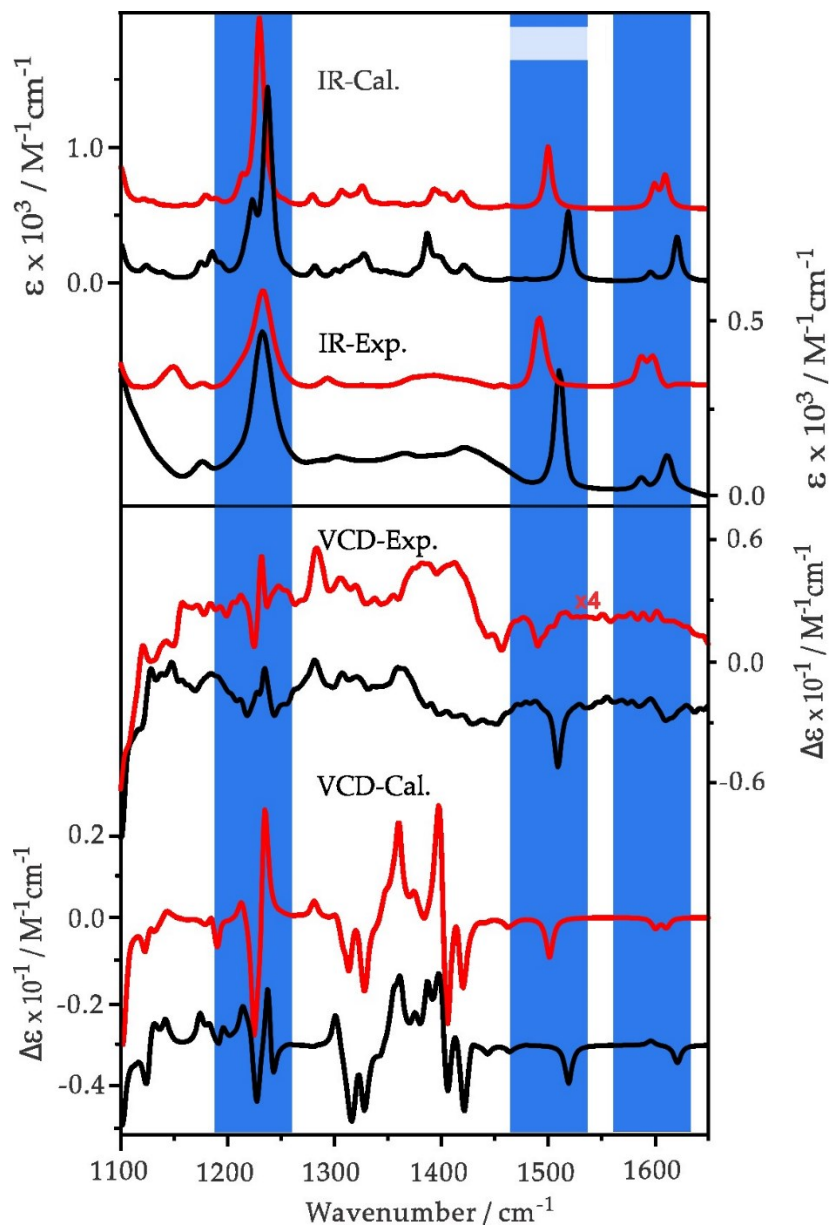


Figure 5.7. Comparison of the experimental IR and VCD spectra of ph- β -glu and gastrodin with the corresponding re-weighted simulated IR and VCD spectra at the B3LYP-D3BJ/def2-TZVPD level with the PCM of DMSO. Several regions are shaded to draw attention to the changes in the IR and VCD features in the experiments and how well they were reproduced by the modelling.

5.2.3 Experimental and Simulated Raman and ROA Spectra of ph- β -Glu and Gastrodin in Water

The individual conformer Raman and ROA spectra of the 14 most stable ph- β -glu conformers at the B3LYP-D3BJ/def2-TZVPD/PCM (water) level of theory are depicted in Figure C5, Appendix C. Both Raman and ROA spectra exhibit some variations from one conformer to the next, although the changes are not as severe as what were observed in the case of VCD features of ph- β -glu discussed in the previous section. In Figure 5.8, the Boltzmann weighted Raman and ROA spectra are given, with the Boltzmann percentage factors of all the individual conformers in water listed in Figure 5.3. Compared to the conformational distribution of ph- β -glu in DMSO, its distribution in water is more spread out with many more conformers which were predicted to contribute nearly equally, making detailed band assignment more challenging.

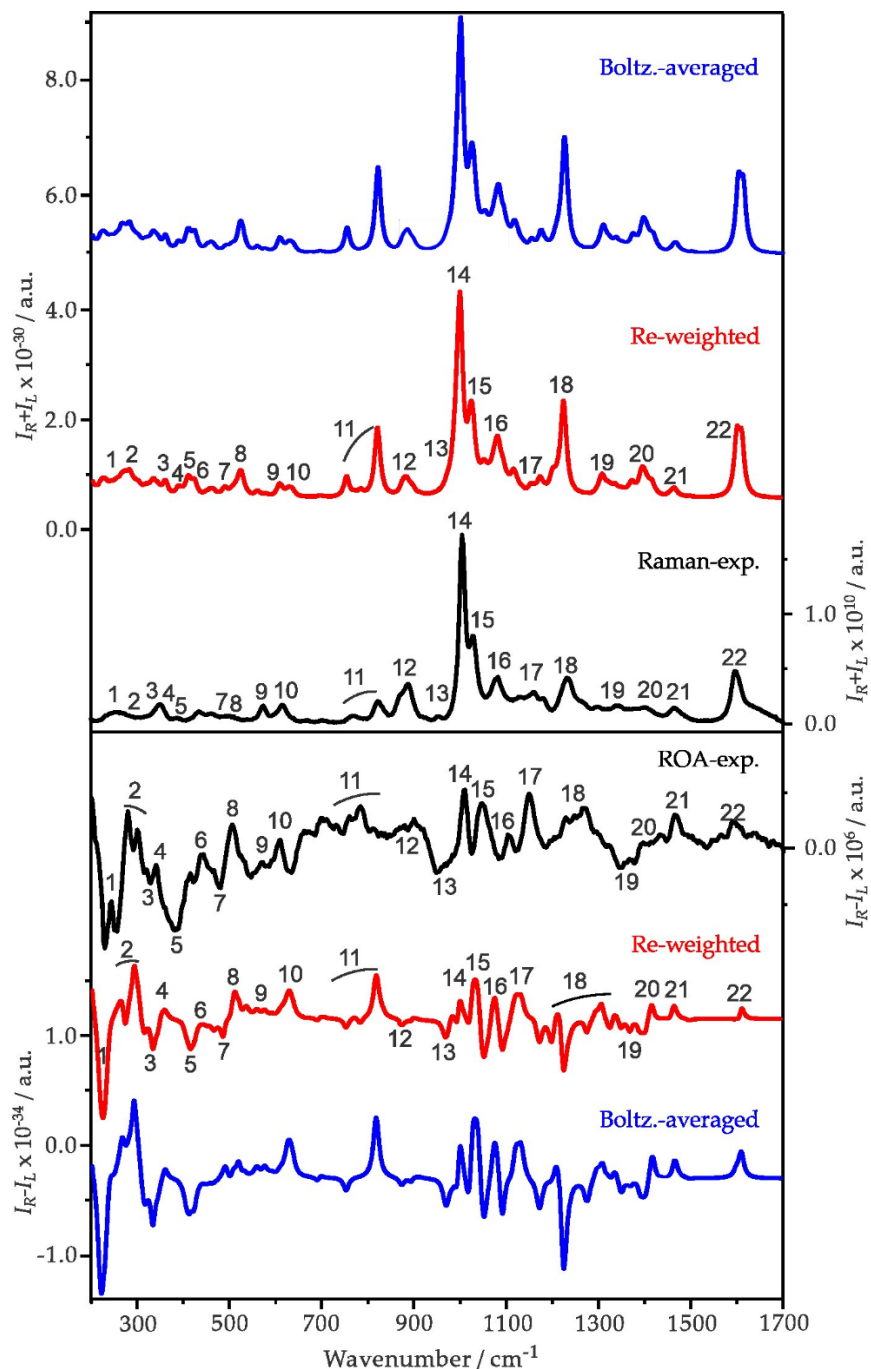


Figure 5.8. Comparison of the experimental Raman and ROA spectra of ph- β -glu in water with the corresponding Boltzmann averaged and re-weighted Raman and ROA spectra, simulated at the B3LYP-D3BJ/def2-TZVPD level with the PCM (water). The predicted Boltzmann percentage factors are listed in Figure 5.2 and the adjusted Boltzmann factors are described in the main text. The main Raman and ROA features are numbered to facilitate easy comparison.

In general, the Boltzmann averaged and the experimental Raman spectra of ph- β -glu in water exhibit good agreement. While the experimental and simulated ROA spectra agree overall, a closer examination of the individual ROA spectra suggests that some improvement can be made by emphasizing the contribution of several conformers than what were indicated by their theoretical Boltzmann factors. The empirical weighting factors were chosen based on the same general principle discussed in the previous section and their values are as follows: 20% for G-g+/cc/T, 30% for G+g-/cc/T, 5% for Tg+/cc/T, 10% for G-g-/cc/T, 5% for the next four most stable conformers: G-g+/c/T, G+t/cc/T, G-t/cc/T, and G+g+/cc/T, 3% for G+g-/c/T, 1% for Tt/c/T and Tg-/c/T, and finally 10% for G+g-/cc/G-. Generally, these percentage values in water differ somewhat from those in DMSO, a point which we will further address in Section 5.2.4. The percentage changes are relatively small compared to the calculated Boltzmann percentages, except that the weight of G+g-/cc/G- was increased noticeably because it reproduced the ROA feature around 500 cm^{-1} better than others. The resulting re-weighted Raman and ROA spectra are also presented in Figure 5.8. While the Boltzmann versus re-weighted Raman spectra appear essentially unaltered, the re-weighted ROA spectrum exhibits some noticeable improvements in the whole frequency range, highlighting the specific conformational sensitivity of ROA. For example, the ROA pattern in the lower wavenumber region for the bands 1 to 10 is much better reproduced, as is the relative intensity of most bands in the whole frequency region.

For gastrodin, the individual conformer Raman and ROA spectra of the 19 most stable conformers at the B3LYP-D3BJ/def2-TZVPD/PCM (water) level of theory are presented in Figure C6, Appendix C. The Boltzmann averaged Raman and ROA spectra of gastrodin, using the Boltzmann percentage factors listed in Figure 5.3, are presented in Figure 5.9, as well as the re-weighted Raman and ROA spectra. Since gastrodin has a large number of low-energy conformers, small

adjustments were made to the percentage abundances of a number of the lowest energy conformers, whereas the rest of the conformers were held at the predicted values. The changes made are: 10% for G-g+/cc/T/G+g-, 10% for G+g-/cc/T/G-g-, 8% for G+g-/cc/T/G+g+, 10% G+g-/cc/T/G-g+, 12% for G-g+/cc/T/G-g-, 4% for G+g-/cc/T/G+g-, 12% for G-g+/cc/T/G+g+, 10% for G-g+/cc/T/G-g+, and 7% for G+g+/cc/T/G+g-.

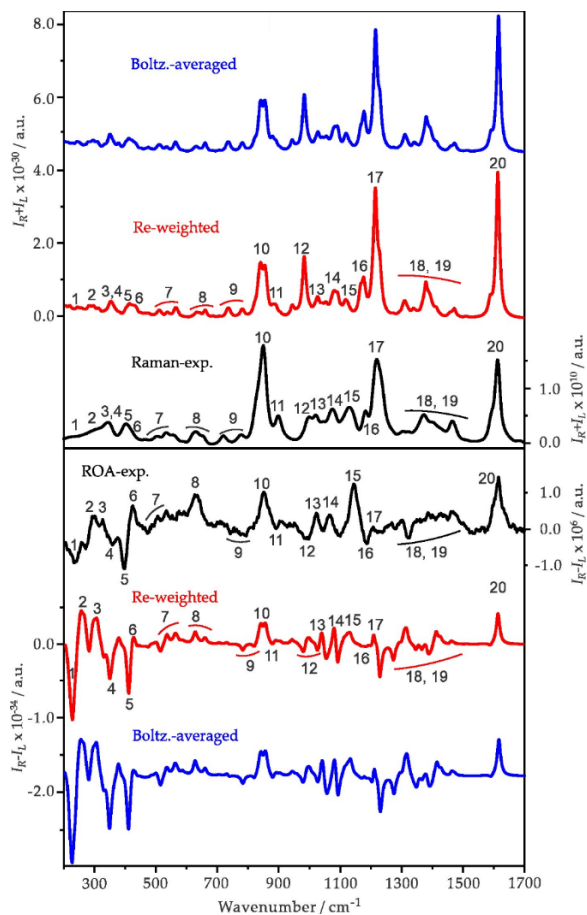


Figure 5.9. Comparison of the experimental Raman and ROA spectra of gastrodin in water with the corresponding Boltzmann averaged and re-weighted Raman and ROA spectra, simulated at the B3LYP-D3BJ/def2-TZVPD level with the PCM (water). The predicted Boltzmann percentage factors are listed in Figure 5.3 and the adjusted Boltzmann factors are described in the main text. The main ROA and the corresponding Raman features are numbered for easy comparison. See the main text for discussions.

To facilitate the detailed comparison, the main ROA and the corresponding Raman features of gastrodin in water were numbered from 1 to 20. Because of the overlapping bands, a Raman band peak does not necessarily correspond to a ROA band peak, making it occasionally difficult to correlate the experimental Raman and ROA bands. For the simulated ROA and Raman bands, on the other hand, it is easy to line up the corresponding ROA and Raman features. We utilized this corresponding relationship extensively in assigning the experimental ROA and the related Raman bands.

Overall, the simulated and experimental Raman and ROA spectra agree well with each other, while the re-weighted spectra offer somewhat better agreement with the experiment. For example, the relative intensities of the ROA bands labelled as four to six were better captured in the re-weighted spectra. For the Raman spectra, the simulated partially resolved double bands labelled as “10” may be used to explain the appearance of lower band intensity compared to the corresponding experimental intensity. Based on the good agreement achieved for both Raman and ROA, we can conclude that the important gastrodin conformers in water with percentage abundances over 6% are: G-g+/cc/T/G+g-, G+g-/cc/T/G-g-, G+g-/cc/T/G+g+, G+g-/cc/T/G-g+, G-g+/cc/T/G-g-, G-g+/cc/T/G+g+, G-g+/cc/T/G-g+, and G+g+/cc/T/G+g-, strongly favoring the gauche conformations of the hydroxymethyl group at the pyranose ring.

5.2.4 Some General Comments about the Conformational Distribution of ph-β-Glu and Gastrodin in DMSO and in Water

Anomeric effects associated with carbohydrate chemistry are of continuous research interest and have recently been reviewed^{42,43}. When α or β-D-glucopyranosides are dissolved in water, an equilibrium is established with about 36% α and 64% β-D-glucopyranosides at room temperature, and this conformational equilibrium can be further influenced by the solvent(s)

used^{42,44}. In the two β -anomers studied here, their glycosides have “protected” anomeric centers due to the substitution at the O1 position and they do not undergo mutarotation in DMSO or in water. This is why we do not need to be concerned about such an equilibrium in the current study. We would expect to observe the equilibrium between the β - and α -anomers of these two compounds if, for example, an acidic condition was provided⁴⁵.

With the combined experimental and theoretical results obtained for these two carbohydrates in DMSO and in water, we can now compare the conformational distributions obtained in these two different solvents and in the gas phase when available. For ph- β -glu in DMSO, G-g+/cc/T (60%) is by far the most important conformer, followed by G+g-/cc/T, Tg+/cc/T, and G-g-/cc/T (about 10% each). In the previous IR-UV hole-burning spectroscopic study of ph- β -glu, only three conformers were observed experimentally, namely G+g-/cc/T, G-g+/cc/T, and Tg+/cc/T, with 68%, 25%, and 7% abundances, respectively¹¹. No other less-stable conformers were detected experimentally in the gas phase. Although the same three conformers are also among the most abundant conformers of ph- β -glu identified in DMSO and in the gas phase, the most abundant conformer in DMSO is G-g+/cc/T (60%) in contrast to G+g-/cc/T (68%) identified in the gas phase. This observation highlights the noticeable solvent influence on the relative stability of the ph- β -glu conformers. If one groups the abundances based on the hydroxymethyl (at the pyranose ring) conformations G+:G-:T, the values in DMSO are 15%:75%:10%, respectively, emphasizing the presence of T conformation, as was the case in the previous gas phase study¹¹.

For ph- β -glu in water, the four main conformers identified in DMSO are still important, but the conformational distribution becomes more widely spread with many more conformers contribute above 5%. The four most abundant ones are G-g+/cc/T (20%), G+g-/cc/T (30%), G-g-/cc/T (10%),

and G+g-/cc/G- (10%). In the current experiments, we have the percentage abundances of the hydroxymethyl conformations G+:G-:T in water to be 53%:40%:7%, which is very different from the distribution in DMSO.

For gastrodin, there have been no detailed conformational studies reported in the gas phase or in solution. We therefore focus on the comparison of its conformational distribution in DMSO and in water, as well as the comparison to ph- β -glu. The main gastrodin conformers in water and in DMSO are in general similar, with some modest variation in their individual abundances. If we group together the gastrodin conformers based on whether their ph- β -glu part takes on the G+g-/cc/T, G-g+/cc/T, G+g+/cc/T, Tg+/cc/T, or Tt/cc/T conformations, the corresponding abundances are 47%, 22%, 9%, 8%, or 14% in DMSO, respectively, versus 61%, 21%, 9%, 8%, and 0% (~0.3%) in water. These numbers can be further grouped into the abundances based on the hydroxymethyl (at the pyranose ring) conformations G+:G-:T, which are 56%, 22%, and 22% for gastrodin in DMSO and 70%, 21%, and 8% for gastrodin in water. Again, the preference for the T conformation of the hydroxymethyl group at the pyranose ring was enhanced in DMSO compared to in water, while a similar trend was also observed with ph- β -glu in the discussion above.

The re-weighted percentage abundances to better reproduce the experimental IR, VCD, Raman, and ROA spectra differ somewhat from the theoretical Boltzmann factors while generally following the predicted stability trend. Such deviation is likely caused by some explicit solvent effects which have not been taken into account in the current modeling. However, in a recent IR and VCD study of methyl- β -D-glucose in water by some of the authors⁴⁶, we attempted solvation with multiple water molecules with the help of the newly developed Quantum Cluster Growth (QCG) program⁴⁷. The choice to stay with the implicit solvation model was made because of the complexity of the two molecular targets and the challenge to sample all important solvation

positions of solvent molecules like water. Recently, ab initio molecular dynamics (AIMD) simulations have become possible for VCD^{48,49} and ROA^{50,51}, although their applications are still limited because of the high computing cost. Nevertheless, the AIMD VCD and ROA simulations of lactic acid and N-acetyl-L-cysteine, both of which are flexible chiral molecules in water, were recently reported^{48,50}. Future work by using AIMD for VCD and ROA of ph- β -glu and gastrodin would be of significant interest for further exploration of the solvation effects.

5.3 Materials and Methods

5.3.1 Experimental

The gastrodin and ph- β -glu (both purity $\geq 98.0\%$) were purchased from Sigma-Aldrich and used without further purification. Deuterated dimethyl sulfoxide and methanol were also purchased from Sigma Aldrich, St. Louis, MO, USA, and used as they were. All IR and VCD spectra were collected using a FTIR spectrometer (Bruker Vertex 70, Billerica, MA, USA) coupled to a VCD model (PMA 50). The photoelastic modulator (PEM) was set at 1400 cm^{-1} for all measurements. The liquid nitrogen cooled mercury cadmium telluride (MCT) detector was used, and the resolution was set at 4 cm^{-1} . The DMSO solutions of the gastrodin and ph- β -glu were prepared with a concentration of 0.35 M and 0.80 M, respectively. A demountable BaF₂ cell with a 0.05 mm Teflon space was used for all measurements, and the collection time was two hours for each. The final IR and VCD spectra were baseline corrected by the subtraction of the solvent spectrum measured under the same conditions.

The aqueous solutions of gastrodin and ph- β -glu were prepared with a concentration of 0.70 M. The Raman and ROA spectra of gastrodin and ph- β -glu in water were measured using a ChiralRaman-2XTM spectrometer (BioTools, Jupiter, FL, USA). The spectra were collected in the

200~2000 cm^{-1} region using a 532 nm laser excitation source and the sample was irradiated using a laser power of 200 mW (at the source) for about 48 h.

5.3.2 Theoretical

To systematically explore the conformational landscapes of ph- β -glu and gastrodin, we utilized the CREST code²⁴ by Grimme and co-workers with the inclusion of the generalized Born (GB)-based GBSA implicit solvation model^{32,33}, using DMSO and water as the solvents. Built upon the previous semiempirical tight-binding (TB) quantum chemistry method, called GFN-xTB⁵², the new CREST code is capable of the fast and reliable exploration and screening of the conformational space of mid- to large-sized molecules with up to about a thousand atoms. To reduce computational costs, we followed the multitiered approach developed before³⁴: (i) searched for all the CREST candidates; (ii) performed a relaxed geometry optimization at the revPBE-D3/def2-SVP level⁵³, with the empirical D3 dispersion correction for the CREST candidates, followed by a single-point energy evaluation at the B3LYP-D3/def2-TZVP level of the optimized structures. This step was done using Molpro⁵⁴, and the purpose was to narrow the energy window to 15 kJ mol^{-1} without losing any important conformers. The relative conformational energies obtained at this step were shown to correlate well with the results obtained with the final DFT calculations at a higher level of theory³⁴; (iii) carried out the final geometry optimization and harmonic frequency calculations using the Gaussian 16 package⁵⁵. In the current study, the simulations of IR, VCD, Raman, and ROA spectra were done at the B3LYP-D3BJ/def2-TZVP and def2-TZVPD levels, although minimal differences were observed between them. All results presented are at the latter level. The implicit solvent was included using the integral equation formalism (IEF) version of the PCM⁵⁶ to account for the bulk DMSO and water solvent environment.

A Lorentzian band shape with a half-width at half-height (HWHH) of 4 cm^{-1} was applied to the simulations of IR, VCD, Raman, and ROA spectra. We also applied a linear correlation method proposed in Ref.⁵⁷ to scale the simulated frequencies in the current study. This procedure was applied recently in a study of transition metal complexes⁵⁸ and was shown to facilitate better comparison with the experimental IR and VCD spectra.

5.4 Conclusions

The conformational distributions of ph- β -glu and gastrodin in DMSO and in water were investigated using a combined experimental and theoretical approach with IR, VCD, Raman, and ROA spectroscopies. A large number of conformational candidates were generated with the systematic CREST searches, which ensured a proper exploration of the complicated conformational landscapes of these two carbohydrates. In general, good agreements between the experimental and simulation IR, VCD, Raman, and ROA spectra at the B3LYP-D3BJ/def2-TZVPD level were achieved. It is noted that the VCD and ROA spectral features vary greatly among different conformers, whereas the parent IR and Raman features exhibit much less variation. Consequently, the dominant conformations of ph- β -glu and gastrodin in DMSO and in water were extracted experimentally based mainly on the comparison of the simulated and experimental VCD and ROA spectra, with the guidance of theoretical conformational stability trends. Since ph- β -glu and gastrodin share the same core ph- β -glu part, it is interesting to compare the changes induced by the extra substitution of the hydroxymethyl group at the para-position of the phenyl ring. It is particularly gratifying to note that the experimental variation observed in the IR and VCD spectra of these two compounds are very well reproduced theoretically, confirming the good quality of the current theoretical modelling. Furthermore, the current study shows that the conformational abundances based on the hydroxymethyl (at the pyranose ring) conformations,

i.e., G⁺:G⁻:T, are 15%:75%:10% in DMSO, in contrast to 68%:25%:7% in the gas phase¹¹ and 53%:40%:7% in water, respectively, emphasizing the importance of the solvent effects. For gastrodin, the aforementioned percentage abundances are 56%, 22%, and 22% in DMSO and 70%, 21%, and 8% in water. The abundance the T conformation was shown to be enhanced in DMSO compared to in water, similar to the situation with ph- β -glu. The current work showcases the power of using multiple chiroptical tools, i.e., VCD and ROA, aided by theoretical calculations, in exploring conformational distributions of carbohydrate derivatives directly in solution.

5.5 References

- [1] P. Sosicka, B.G. Ng, H. H. Freeze, *Biochem.* **2020**, 59, 3064-3077.
- [2] J. Wang, Y. Zhang, Q. Lu, D. Xing, R. Zhang, *Front Pharmacol.* **2021**, 12, 756724.
- [3] H. B. Mayes, L. J. Broadbelt, G. T. Beckham, *J. Am. Chem. Soc.* **2014**, 136, 1008-1022.
- [4] J. N. Chythra, S. S. Mallajosyula, *J. Chem. Inf. Model.* **2023**, 63, 208-223.
- [5] J. B. Johnson, J. S. Mani, D. Broszczak, S. S. Prasad, C. P. Ekanayake, P. Strappe, P. Valeris, M. Naiker, *Phytother. Res.* **2021**, 35, 3484-3508.
- [6] S. J. Hwang, H. J. Lee, *Inflammation* **2015**, 38, 1071-1079.
- [7] M. Hu, H. Yan, Y. Fu, Y. Jiang, W. Yao, S. Yu, L. Zhang, Q. Wu, A. Ding, M. Shan, *Molecules* **2019**, 24, 547.
- [8] F. Yang, G. Li, B. Lin, K. Zhang, *J. Integr. Neurosci.* **2022**, 21, 72.
- [9] Z. Song, G. Luo, C. Han, G. Jia, B. Zhang, *Evid. Based Complement. Altern. Med.* **2022**, 2022, 3607053.
- [10] L. Li, Q. Li, L. Gui, Y. Deng, L. Wang, J. Jiao, Y. Hu, X. Lan, J. Hou, Y. Li, D. Lu, *Bioact. Mater.* **2023**, 19, 24-37.
- [11] F. O. Talbot, J. P. Simons, *Phys. Chem. Chem. Phys.* **2002**, 4, 3562-3565.
- [12] J. P. Simons, B. G. Davis, E. J. Cocinero, D. P. Gamblin, E. C. Stanca-Kaposta, *Tetrahedron: Asymmetry* **2009**, 20, 718-722.
- [13] K. Monde, T. Taniguchi, N. Miura, S.-I. Nishimura, *J. Am. Chem. Soc.* **2004**, 126, 9496-9497.
- [14] P. Zhu, G. Yang, M. R. Poopari, Z. Bie, Y. Xu, *ChemPhysChem* **2012**, 13, 1272-1281.
- [15] J. Cz. Dobrowolski, P. F. J. Lipiński, J. E. Rode, J. Sadlej, *α -Amino Acids in Water: A Review of VCD and ROA Spectra. In Optical Spectroscopy and Computational Methods in Biology and Medicine: Challenges and Advances in Computational Chemistry and Physics; Baranska, M., Ed.; Springer: Dordrecht, The Netherlands, 2014.*
- [16] C. Merten, F. Li, K. Bravo-Rodriguez, E. Sanchez-Garcia, Y. Xu, W. Sander, *Phys. Chem. Chem. Phys.* **2014**, 16, 5627-5633.
- [17] J. Kessler, V. Andrushchenko, J. Kapitán, P. Bouř, *Phys. Chem. Chem. Phys.* **2018**, 20, 4926-4997.
- [18] J. R. Cheeseman, M. S. Shaik, P. L. A. Popelier, E. W. Blanch, *J. Am. Chem. Soc.* **2011**, 133, 4991-4997.

- [19] V. Palivec, V. Kopecký, P. Jungwirth, P. Bouř, J. Kaminský, H. Martinez-Seara, *Phys. Chem. Chem. Phys.* **2020**, 22, 1983-1993.
- [20] L. A. Nafie, *Vibrational Optical Activity: Principles and Applications*; John Wiley & Sons, Ltd.: Chichester, UK, **2011**.
- [21] L. D. Barron, *Molecular Light Scattering and Optical Activity*, 2nd ed.; Cambridge University Press: Cambridge, UK, **2009**.
- [22] G. Li, M. Alshalalfeh, J. Kapitán, P. Bouř, Y. Xu, *Chem. Eur. J.* **2022**, 28, e202104302.
- [23] T. Wu, G. Li, J. Kapitán, J. Kessler, Y. Xu, P. Bouř, *Angew. Chem., Int. Ed.* **2020**, 59, 21895-21898.
- [24] E. Machalska, G. Zajac, J. E. Rode, *Acta A Mol. Biomol.* **2022**, 281, 121604.
- [25] P. Pracht, F. Bohle, S. Grimme, *Phys. Chem. Chem. Phys.* **2020**, 22, 7169-7192.
- [26] F. Xie, N. A. Seifert, M. Heger, J. Thomas, W. Jäger, Y. Xu, *Phys. Chem. Chem. Phys.* **2019**, 21, 15408-15416.
- [27] N. A. Seifert, J. Thomas, W. Jäger, Y. Xu, *Phys. Chem. Chem. Phys.* **2018**, 20, 27630-27637.
- [28] S. Oswald, N. A. Seifert, F. Bohle, M. Gawrilow, S. Grimme, W. Jäger, Y. Xu, M. A. Suhm, *Angew. Chem. Int. Ed.* **2019**, 58, 5080-5084.
- [29] F. Xie, M. Fusè, S. Hazrah, A. W. Jaeger, V. Barone, Y. Xu, *Angew. Chem., Int. Ed.* **2020**, 59, 22427-22430.
- [30] Y. Yang, A. Krin, X. Cai, M. R. Poopari, Y. Zhang, J. R. Cheeseman, Y. Xu, *Molecules* **2023**, 28, 771.
- [31] K. D. R. Eikås, M. T. P. Beerepoot, K. Ruud, *J. Phys. Chem. A* **2022**, 126, 5458-5471.
- [32] J. L. Alonso, M. A. Lozoya, I. Peña, J. C. López, C. Cabezas, S. Mata, S. Blanco, *Chem. Sci.* **2014**, 5, 515-522.
- [33] C. Bannwarth, E. Caldeweyher, S. Ehlert, A. Hansen, P. Pracht, J. Seibert, S. Spicher, S. Grimme, *WIREs Comput. Mol. Sci.* **2021**, 11, e1493.
- [34] A. V. Onufriev, D. A. Case, *Annu. Rev. Biophys.* **2019**, 48, 275-296.
- [35] H. Wang, M. Heger, M. H. Al-Jabiri, Y. Xu, *Molecules* **2022**, 27, 38.
- [36] A. D. Becke, *Phys. Rev. A* **1988**, 38, 3098-3100.
- [37] C. Lee, W. Yang, R. Parr, *Phys. Rev. B* **1988**, 37, 785-789.
- [38] D. Rappoport, F. Furche, *J. Chem. Phys.* **2010**, 133, 134105.
- [39] S. Grimme, J. Antony, S. Ehrlich, H. Krieg, *J. Chem. Phys.* **2010**, 132, 154104.

- [40] D. G. A. Smith, L. A. Burns, K. Patkowski, C. D. Sherrill, *J. Phys. Chem. Lett.* **2016**, *7*, 2197-2203.
- [41] A. D. Becke, A. D. Johnson, *J. Chem. Phys.* **2005**, *123*, 154101.
- [42] B. Xu, L.Unione, J. Sardinha, S. Wu, M. Ethve-Quellejeu, A. P. Rauter, Y. Blriot, Y. Zhang, S. Martín-Santamaría, D. Díaz, J. Jimnez-Barbero, M. Sollogoub, *Angew. Chem. Int. Ed.* **2014**, *53*, 9597-9602.
- [43] I. V. Alabugin, L. Kuhn, N. V. Krivoschchapov, P. Mehaffy, M. G. Medvedev, *Chem. Soc. Rev.* **2021**, *50*, 10212-10252.
- [44] R. U. Lemieux, A. A. Pavia, J. C. Martin, K. A. Watanabe, *Can. J. Chem.* **1969**, *47*, 4427-4439.
- [45] K. B. Wiberg, M. Marquez, *J. Am. Chem. Soc.* **1994**, *116*, 2197-2198.
- [46] A. S. Perera, C. D. Carlson, J. Cheramy, Y. Xu, *Chirality* **2023**, *35*, 718-731.
- [47] S. Spicher, C. Plett, P. Pracht, A. Hansen, S. Grimme, *J. Chem. Theory Comput.* **2022**, *18*, 3174-3189.
- [48] M. Thomas, B. Kirchner, *J. Phys. Chem. Lett.* **2016**, *7*, 509-513.
- [49] S. Jähnigen, D. Sebastiani, R. Vuilleumier, *Phys. Chem. Chem. Phys.* **2021**, *23*, 17232-17241.
- [50] M. Brehm, M. Thomas, *J. Phys. Chem. Lett.* **2017**, *8*, 3409-3414.
- [51] Y. Yang, J. Cheramy, M. Brehm, Y. Xu, *ChemPhysChem* **2022**, *23*, e202200161.
- [52] S. Grimme, C. Bannwarth, P. Shushkov, *J. Chem. Theory Comput.* **2017**, *13*, 1989.
- [53] F. Weigend, R. Ahlrichs, *Phys. Chem. Chem. Phys.* **2005**, *7*, 3297-3305.
- [54] H.-J. Werner, P. J. Knowles, G. Knizia, F. R. Manby, M. Schütz, *Wires Comput. Mol. Sci.* **2012**, *2*, 242-253.
- [55] M. J. Frisch, G. W. Trucks, H. B. Schlegel, G. E. Scuseria, M. A. Robb, J. R. Cheeseman, G. Scalmani, V. Barone, G. A. Petersson, H. Nakatsuji, et al. *Gaussian 16; Revision C.03*; Gaussian, Inc.: Wallingford, CT, USA, **2019**.
- [56] B. Mennucci, J. Tomasi, R. Cammi, J. R. Cheeseman, M. J. Frisch, F. J. Devlin, S. Gabriel, P. J. Stephens, *J. Phys. Chem. A* **2002**, *106*, 6102-6113.
- [57] M. Katari, E. Nicol, V. Steinmetz, G. van der Rest, D. Carmichael, G. Frison, *Chem. Eur. J.* **2017**, *23*, 8414-8423.
- [58] G. Li, D. Li, M. Alshalalfeh, J. Cheramy, H. Zhang, Y. Xu, *Molecules* **2023**, *28*, 2571.

Chapter 6

Chiroptical Spectroscopic and DFT Study of a Chiral Transition Metal Complex with Low-Lying Electronic States

6.1 Introduction

Schiff bases ligands belong to a category of organic compounds distinguished by the presence an imine ($-C=N-$) functional group, resulting from the reaction between the amine amino group and the aldehyde or ketone carbonyl group¹. These ligands have gained significant attention due to their unique coordination chemistry properties. This special class of ligands are known as “privileged ligands” since they can form coordination complexes with a variety of metal ions and lanthanides that exist in various oxidation states and geometries². The unique properties of Schiff-bases and their complex transition metal derivatives, mainly attributed to the imine functionality and its chelating character, have sparked the interest of researchers to explore their potential in a wide range of fields, such as catalysis³, sensing⁴, food industry⁵, and biochemistry⁶. Detailed stereochemical properties of Schiff base metal complexes including conformational distribution, ligand chirality, and induced chiral configuration of the metal centers, can provide new insights into structural-functional relationships of this fascinating class of chiral molecular systems in solution. Electronic circular dichroism (ECD), vibrational circular dichroism (VCD), and Raman optical activity (ROA), especially a combination of these chiroptical tools in conjunction with density functional theory (DFT) calculations, have been effectively utilized to extract chirality related information of these transition metal complexes and their ligands directly in solution⁷⁻¹⁰.

Typically, VCD (or ROA) band intensity is on the order of 10^{-6} to 10^{-4} (10^{-5} to 10^{-3}) relative to the parent IR (Raman) bands, thus requiring a long acquisition time as well as a high sample concentration for reliable VCD (ROA) measurements. Therefore, much research efforts have been devoted to VCD and ROA intensity enhancement. Chiral transition metal complexes have attracted significant interest in this regard because they often exhibit certain fascinating chirality transfer and enhancement phenomena. For example, strongly induced solvent chiral Raman signals in solutions with a chiral Ni(II) transition metal complex were also reported, leading to the very recent discovery of a new type of chiral Raman spectroscopy named ECD-CP-Raman, or abbreviated as eCP-Raman^{11,12}. By using a metal ion bound to a ligand, one can greatly enhance the typically weaker ligand VCD intensity, as reported in several Co(II)^{7,8}, Ni(II)^{13,14} and Cu(II)¹⁴ complexes. Domingos et al. showed that one can drastically amplify VCD signals associated with the local chiral environment in biomolecules by adding a Cobalt salt¹⁵. More recently, Bürgi and co-workers reported a significant amplification of VCD signals of a thiolate-protected gold cluster Au₂₅(Capt)₁₈ (Capt = captopril) in aqueous solution by simply adding a cobalt salt to the aqueous solution¹⁶. One common property associated with these systems is the presence of unpaired d electrons and consequently the low-lying electronic states (LLESs). While the LLESs theory by Nafie¹⁷ in 2004 provides a foundation for the current understanding of the VCD enhancement, no current theoretical model can actually reproduce the experimental observation of enhancement.

In this Chapter, we applied ECD, VCD and ROA chiroptical spectroscopic techniques to investigate a synthesized chiral transition metal complex with unpaired d-electrons, namely Co(II)-salen-chxn, as shown in Figure 6.1. While the experimental VCD spectra of the Co(II) complex was reported previously¹⁸, this chapter includes additionally extensive theoretical calculations were carried out to search for possible conformers of the complex with Co at different oxidation

states and spin multiplicities. The corresponding simulated UV-Vis, ECD, IR and VCD spectra are compared with the experimental ones to extract stereochemical information. Furthermore, some unusual experimental VCD observed are highlighted and the causes for the poor agreement between the experimental and simulated VCD spectra are discussed in detail. We note that although several attempts were made to obtain experimental Raman and ROA spectra of the Co complex, the measurements were not successfully because of severe fluorescence interference and are therefore not included in the current chapter.

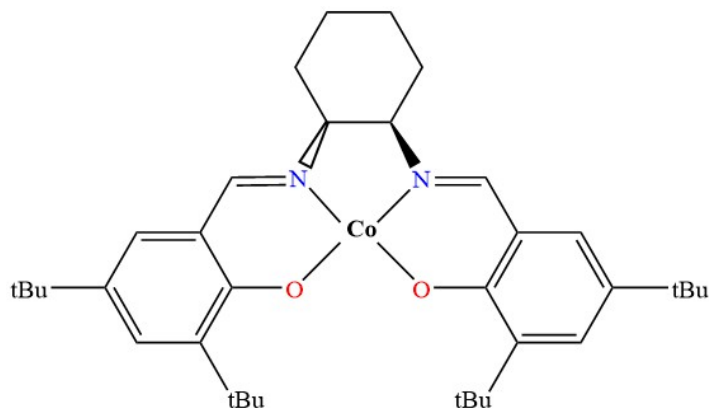


Figure 6.1. The molecular formula of the R,R-Co(II)-salen-chxn complex, (R,R)-(-)-N, N'-Bis(3,5-di-tert-butylsalicylidene)-1,2-cyclohexanediaminocobalt(II). Here tBu indicates the tertbutyl group.

6.2 Experimental and Theoretical Details

6.2.1 Experimental Details

The (R, R) and (S, S) salen-chxn ligands (98%) were purchased from Sigma-Aldrich and used without further purification. The chiral transition metal complex Co(II)-salen-chxn was synthesized using the same procedure for Ni(II) and Cu(II)-salen-chxn complexes¹⁹. Briefly, the salen-chxn ligand was dissolved in anhydrous ethanol, and then the solution was heated to reflux until boiling. Cobalt (II) perchlorate hexahydrate in absolute ethanol was then added to the solution and refluxed for 3 hours. Next, the solution mixture was concentrated using a rotavapor, and the residue was further dissolved in dichloromethane and ethyl acetate. The resulting solution was then filtered under suction, and the solvent in the filtrate was removed using a rotavapor to collect the remaining solid powder, which was further recrystallized using a mixture of dichloromethane and ethanol. The mass spectrum of the synthetic sample revealed only one major peak at 603.3354 (Figure D1, Appendix D), consistent with the mass expected based on the formula given in Figure 1, assuming a charge of +1. The same procedure was applied for the preparation of Mn(III)-salen-chxn (structural formula shown in Figure D2, Appendix D), and manganese(II) acetate was used as the metal source.

The experimental IR and VCD spectra of the Co(II)-salen-chxn complex were collected using a FTIR spectrometer (Bruker Vertex 70, Milton, Canada) coupled to a VCD model (PMA 50). The deuterated chloroform was used as a solvent to prepare a solution with a concentration of 60mg/1ml. A demountable BaF₂ window cell was used for all measurements with a 50 μm spacer. The PEM (photoelastic modulator) was set at 1400 cm^{-1} for the VCD spectra in the range 950 - 1700 cm^{-1} , and it was set at 3000 cm^{-1} for VCD spectra in the range 1700 - 3800 cm^{-1} . The

collection time is 2 hours. The same procedure was used for the measurements of Mn(III)-salen-chxn.

The UV-Vis and ECD spectra of the ligand salen-chxn and the Co(II) transition metal complex in acetonitrile were measured using a Jasco-1700 spectrometer with a with variant concentration of 0.2 mM and a path length of 1 cm.

6.2.2 Theoretical Details

The single mass spectrum peak at ~ 603.3 represents the cobalt complex (as shown in Figure D1) with a +1 charge, i.e., Co(III)-salen-chxn. Since the mass spectrum cannot tell us whether the species in solution is Co(II) and lost one electron in the electrospray ionization process or the original species is already Co(III) in solution, we decided to conduct DFT IR and VCD simulations for both oxidation states. Interestingly, upon scrutinizing the simulated IR spectra, we observed a notable disagreement between the Co(III) spectra of all conformers and the experimental IR spectrum, whereas the simulated IR spectra of Co(II) aligned well with the experimental one. For conciseness, we described only the results associated with Co(II) in the rest of the chapter.

To systematically explore the possible conformers of the Co(II)-salen-chxn complex in CDCl₃, we utilized the CREST²⁰ code by Grimme and co-workers with the inclusion of the generalized Born (GB) model augmented with solvent accessible surface area (SA), i.e., the GBSA implicit solvation model²¹. Built upon the previous semiempirical tight-binding (TB) quantum chemistry method, called GFN-xTB²², the latest CREST code provides an efficient and accurate exploration and screening of the conformational space for molecules consisting of up to a thousand atoms in size. To reduce computational costs, we implemented a multitiered approach^{23,24}: (i) searched for all the CREST candidates; (ii) performed a relaxed geometry optimization at the revPBE-D3/def2-SVP level²⁵, with the empirical D3 dispersion correction for the CREST

candidates, followed by a single-point energy evaluation at the B3LYP-D3/def2-TZVP level of the optimized structures. In the final step, Gaussian 16 package²⁶ was used to perform the final geometry optimization and harmonic frequency calculations of all possible conformers. In the current study, the conformational search of the Co(II)-salen-chxn complex was carried out at different oxidation states and different spins. The B3LYP-D3BJ /6-311++G(d,p) level of theory was used for the final geometry optimization and IR/VCD calculations. The implicit solvent was included using the integral equation formalism (IEF) version of the PCM²⁷ to account for the bulk solvent environment.

The time-dependent DFT (TDDFT) calculations were employed to calculate the excited state energies and oscillator strengths. In general, it is challenging to accurately capture excited state properties, especially for open-shell systems, and the performance of different combination of DFT functionals and basis sets can vary considerably. Based on the previous ECD simulations of Co(II) transition metal complexes^{7,28} and of other related Ni(II) and Cu(II) complexes¹⁹, we chose the combination of B3LYP-D3BJ/6-311++G (d,p) level of theory with the PCM of acetonitrile. The first 250 electronic states were taken into account for the Co(II)-salen-chxn complex in simulating its UV-Vis and ECD spectra. A Gaussian line shape with a half-width at half-height (HWHH) of 0.15 eV was used for the simulations of the UV-Vis and ECD spectra.

6.3 Results and Discussion

6.3.1 Comparison of the Experimental UV-Vis, ECD, IR and VCD Spectra of the Co(II)-salen-chxn Complex with those of its Ligand and other Related Complexes.

The experimental UV-Vis and ECD spectra of the ligand salen-chxn and its metal complexes (Co(II), Mn(III), Cu(II), and Ni(II)) are presented in Figure 6.2. The UV-Vis spectrum of the ligand salen-chxn exhibits three main, broad bands at 225 nm, 260 nm, and 325 nm,

corresponding to the $\pi-\pi^*$ transitions of the ligand's aromatic chromophores.²⁸ The UV-Vis spectra of for the metal complexes, the band features extend to longer wavelength and some new bands appear which can be attributed to new electronic transitions resulting from the metal interactions with the O and N atoms of the ligand. Similarly, the ECD spectrum of the salen-chxn ligand exhibits some notable differences compared to the ECD spectra of its metal counterparts. For example, in the longer wavelength region of 350 nm to 500 nm, there is no visible ECD features of the ligand, whereas each metal complex has its own distinctive ECD bands.

Figure 6.3 illustrates the experimental IR and VCD spectra of the ligand salen-chxn and the metal-salen-chxn complex family. Broadly speaking, the IR spectrum of the pure ligand bears resemblance to the IR spectra of the metal ligands where a marginal shift is discerned in most IR bands of the metal complexes relative to those of the pure ligand. This suggests that the observed vibrational bands predominantly originate from the ligands. We note that some small, new bands emerge in the 1250 to 1550 cm^{-1} range. Overall, different metal species, whether they are closed-shell such as the Ni(II) complex, or the open-shell complexes such as Cu(II), Co(II), and Mn(III), the observed IR band features remain similar. It appears that the presence of various metals does not cause substantial changes in the IR spectra.

On the contrary, the VCD spectra of the metal-salen-chxn complexes undergo significant changes when compared to the pure ligand and to each other, as illustrated in the lower panel of Figure 6.3. It is noteworthy that the VCD spectra of the Cu, Ni, and Mn-salen-chxn complexes display both positive and negative bands, while the VCD spectrum of Co-salen-chxn in this range consists of nearly all monosignate bands with drastically enhanced g factors. For instance, the band at approximately 1599 cm^{-1} , corresponding to the C=N symmetric stretch, exhibits g-values of 2.3×10^{-3} , 5.7×10^{-5} , 8.9×10^{-5} , and 6.8×10^{-5} for the Co(II), Mn(III), Cu(II), and Ni(II) complexes,

respectively. Similarly, the aromatic ring C=C stretches at around 1526 cm^{-1} display g-values of 2.9×10^{-3} , 3.9×10^{-5} , 3.8×10^{-5} , and 4.3×10^{-5} for Co(II), Mn(III), Cu(II), and Ni(II) complexes, respectively. The enhancement observed in the VCD bands of the Co-salen-chxn is attributed to the phenomenon of vibronic coupling¹⁷. This phenomenon arises from the vibronic coupling between ground-state vibrational transitions and magnetic-dipole allowed low-lying electronic excited states (LLESs)¹⁷.

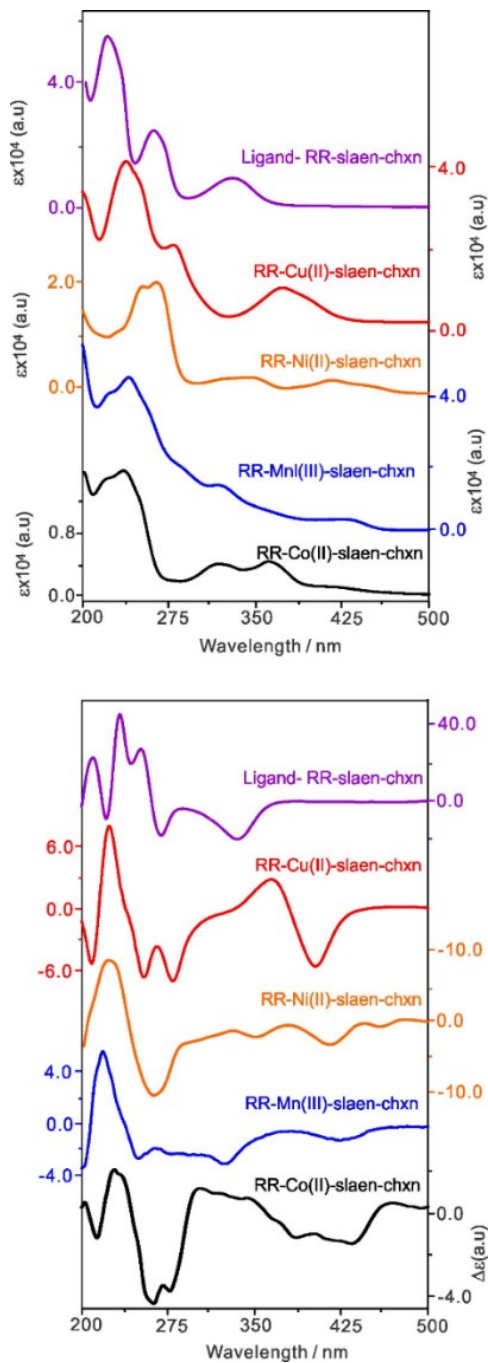


Figure 6.2. The experimental UV-vis spectra (top panel) and ECD spectra (bottom panel) for both the RR- salen-chxn ligand and its metal (Co(II), Mn(III), Cu(II), and Ni(II)) complexes. The UV-vis and ECD measurements of these systems done at different concentration. The data for RR-salen-chxn ligand, Ni(II), and Cu(II) complexes were collected from Ref. 19.

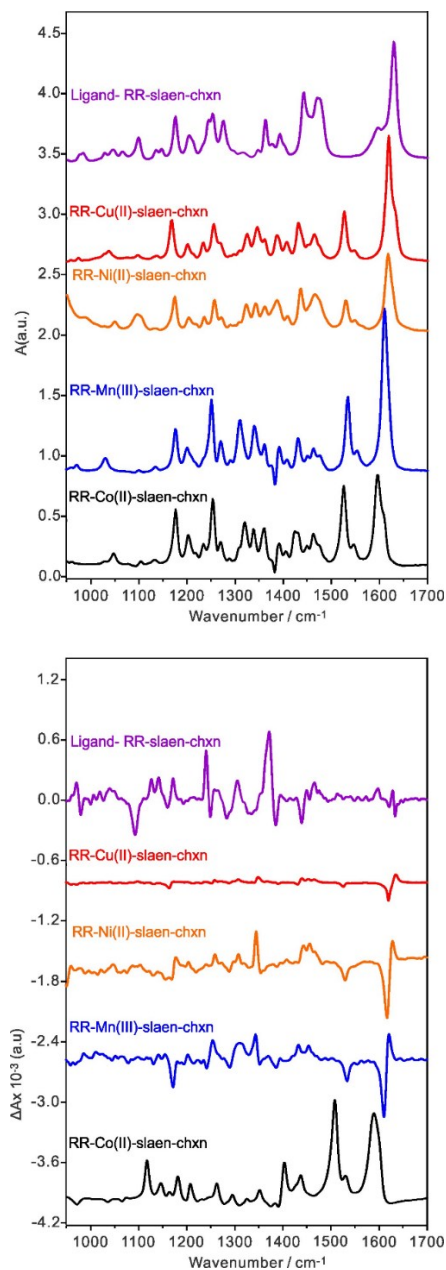


Figure 6.3. The experimental IR spectra (top panel) and VCD spectra (bottom panel) of the salen-chxn ligand and its metal complexes, Co(II), Mn(III), Cu(II), and Ni(II) salen-chxn. The data for RR salen-chxn ligand, Ni(II), and Cu(II) complexes from Ref. 19. Please note that while the IR intensity scale used is the same for all species and the IR spectrum of each species is shifted for easy comparison. Similarly, the same VCD intensity scale is used for Mn(III), Cu(II) and Ni(II), whereas the intensity scale of Co(II) is *10 times larger* than the others.

To confirm the monosignate phenomenon for the Co-salen-chxn complex, the experimental IR and VCD spectra in the range 1400 to 3800 cm^{-1} for a pair of enantiomers of Co-salen-chxn were also measured. These are summarized in Figure 6.4. The IR spectra of the enantiomeric pair show

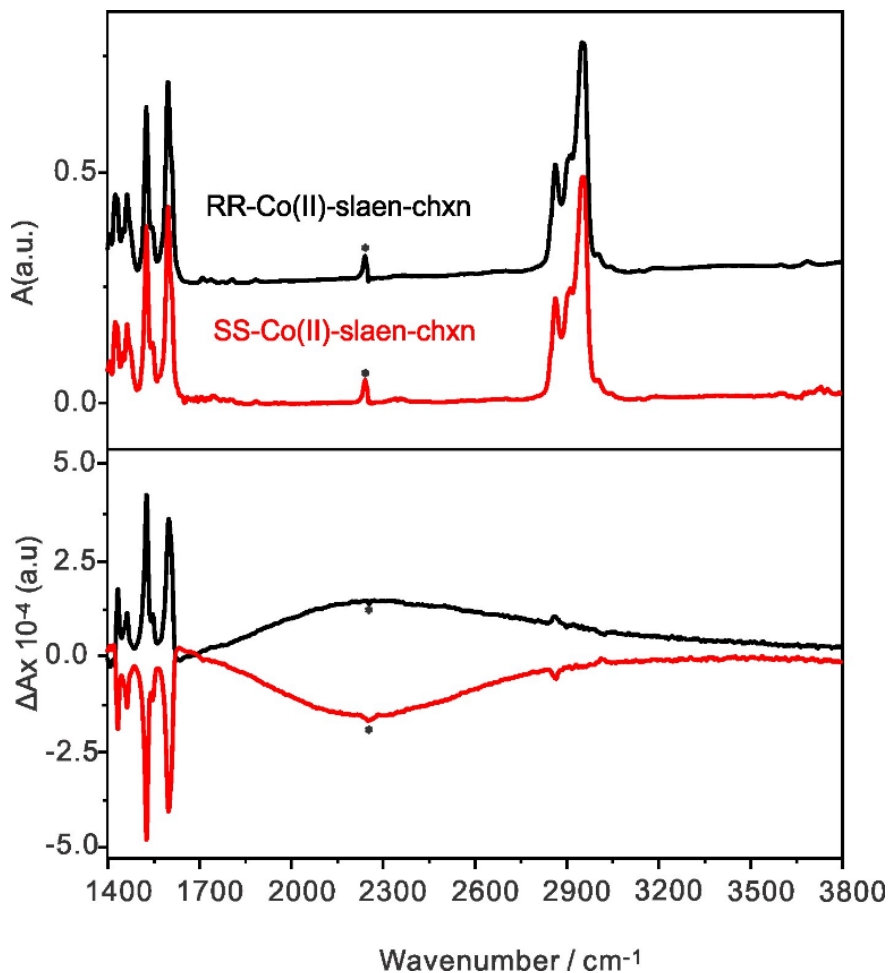


Figure 6.4. Experimental IR (top panel) and VCD (bottom panel) spectra of Co(II)-salen-chxn complex in CDCl_3 solution in the range of 1400 to 3800 cm^{-1} , PEM optimized at 3000 cm^{-1} . The asterisk (*) in the spectrum is related to the strong C-D stretching band of CDCl_3 and the corresponding feature in the ΔA spectrum may be artifact. Please see the main text for additional discussion.

essentially the same features, while the VCD spectra of the enantiomers exhibit good mirror image quality. Interestingly, the VCD features contain a monosignate, broad feature spanning from 1700-3800 cm^{-1} . This unusual broad feature actually corresponds to an ECD band, centered around 2300 cm^{-1} . This ECD band originates from some low-lying electronic transitions within the Co(II)-salen-chxn complex. Our assignment is based on similar features reported in the literature for several Schiff base Co(II) complexes, for example an ECD band centered around 2700 cm^{-1} was observed for the Co(II)-(-)-sparteine complex¹⁸, around 2100 cm^{-1} for Co(II)-Saldiphenyl complex²⁹, and around 3900 cm^{-1} for an achiral Co(II) complex³⁰. This assignment is also based on the current TDDFT calculation results which are described in Section 6.3.3. In addition, there are some weaker, and sharp bands in the ΔA spectrum in the 2800-3100 cm^{-1} region. These features exhibit good mirror imaged quality for the pair of Co(II) enantiomers and correspond to the C-H stretching vibrational bands of the complex. Because of the interference of the ECD of the LLESs, it is difficult to extract the g values of these VCD bands. The tiny band marked with * in the ΔA traces in Figure 6.4, on the other hand, does not show good mirror imaged quality. This is likely due to minor measurement artifact.

In light of the notable enhancements detected in the VCD spectrum of Co(II)-salen-chxn, this chapter will exclusively focus on this complex. In the following sections, detailed theoretical exploration and symmetry consideration in the vibronic coupling will be presented to understand the observed enhancement phenomenon.

6.3.2 The most stable conformers of the Co(II)-salen-chxn complex

To understand the observed chiroptical spectra, simulations of the UV-Vis, ECD, IR and VCD spectra of the Co(II) complex were carried out. This started with the search of possible

conformers of the Co(II) complex. The conformational landscape of the salen-chxn ligand was thoroughly investigated in a previous study¹⁹. A large number of CREST geometry candidates of the ligand were generated. These are associated with the cyclohexane ring conformations, the axial and equatorial positions of the two large substituents on the cyclohexane ring, the rotatable motions about the N-C_{cyclohexane} bonds, the orientation of the OH group, and the staggered and eclipsed conformations of the two tBu groups in each substituent. Four stable ligand conformers were identified at the B3LYP-D3BJ/6-311++G(d,p) within an energy window of 15 kJ mol⁻¹ which are reproduced in Figure 6.5 to facilitate easy comparison with the Co(II) complex.

The correspond cobalt complex is considerably more rigid than the ligand thanks to the coordination bonds. As mentioned in the experimental session, there is an ambiguity if Co can take on both Co(III) and Co(II) oxidation states. Therefore CREST searches were carried out for both oxidation states. Twelve CREST candidates were identified for each oxidation state. The geometry optimization of all possible candidates at the B3LYP-D3BJ/6-311++G(d,p) level of theory revealed only three stable conformers of the complex. These conformers are associated with different tBu orientations. It is interesting to note that the same conformers were detected for the Co(II)-salen-chxn complex at different oxidation states and spin states after the final DFT geometry optimization. This indicates that using different charges in the CREST searches does not affect the generation of potential conformers. On the other hand, the charges and the spin drastically change the simulated IR and VCD spectral features, as we will describe in the next section. The optimized geometries of the three conformers for the natural Co(II)-salen-chxn complex at the high and low spin, are summarized in Figure 6.5, together with their free energies and Boltzmann factors at 298 K.

Another crucial aspect of consideration pertains to the absolute configuration of the chiral metal center, i.e., the helicity at the metal center. Given the nearly square geometries displayed by all these metal complexes, it is conceivable that both Λ and Δ helicity are achievable, as a slight alteration in the dihedral angle of O-Metal-N in the opposite direction would suffice for a helicity switch. With R chirality ligands, a distinct inclination toward Λ metal chirality over Δ was observed, in several previously reported Cu(R or S-N-(Ar)ethyl-2-oxo-1-naphthaldiminato- κ^2 N,O)³¹ and Co(bis[(R/S)-N-(1-(Ar)ethyl)salicylaldiminato]) complex.⁸ In our earlier investigation into the chirality of Ni(II) and Cu(II) no Δ helicity geometry candidates were identified. Intriguingly, all initially constructed Δ helicity geometries transferred to Λ helicity during DFT geometry optimizations¹⁹.

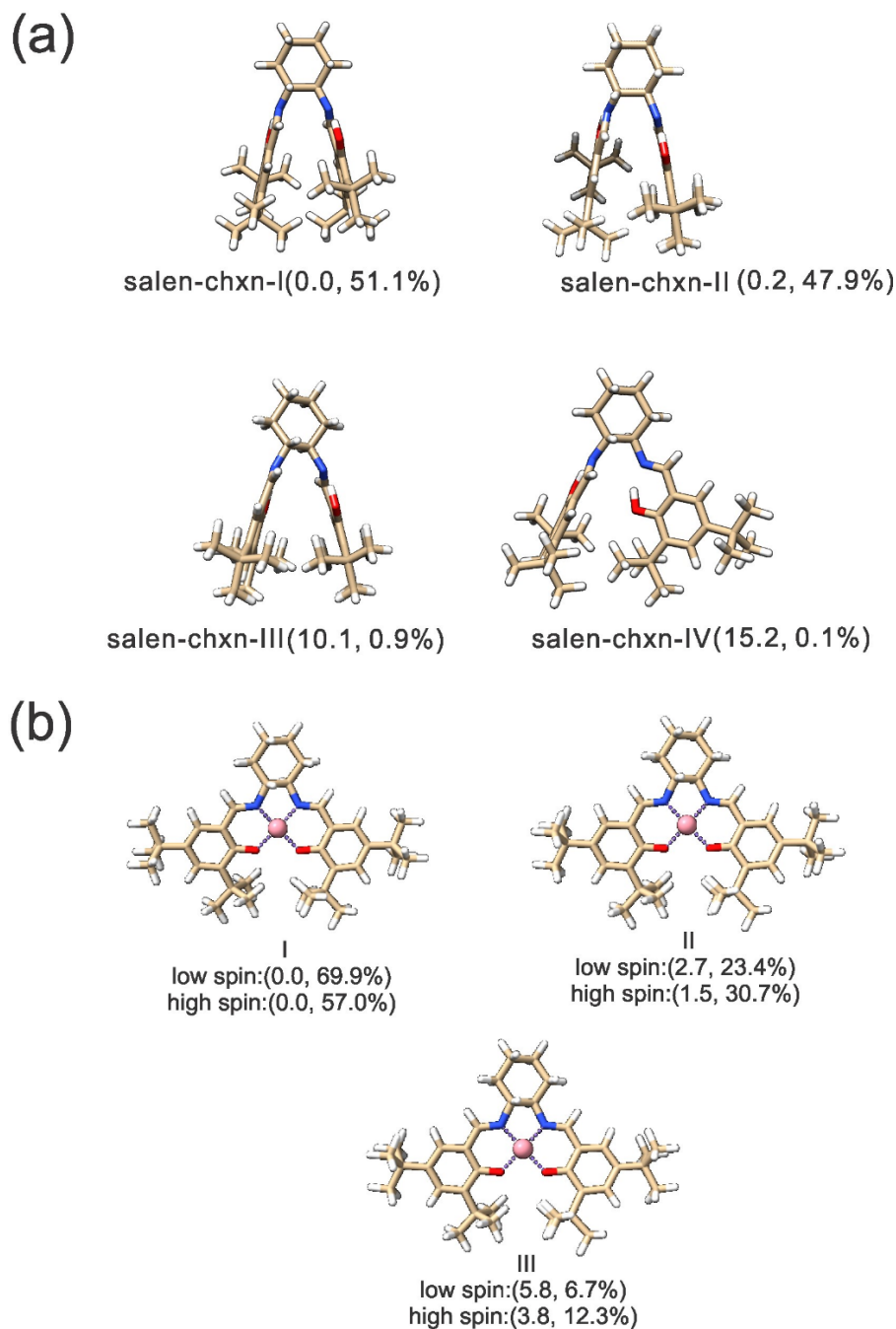


Figure 6.5. (a) The optimized geometries of the four most stable salen-chxn ligand conformers¹⁹ and (b) The optimized geometries of the three most stable Co(II)-salen-chxn conformers at the B3LYP-D3BJ/6-311++G(d,p) level of theory with the PCM of CDCl₃. The relative free energies in kJ/mol at the low spin of the ligand, and low and high spin of the metal complex and the Boltzmann percentage abundances at 298 K are provided in the brackets.

6.3.3 Simulated UV-Vis and ECD Spectra and the Experimental Results

Based on the simple crystal field theory, square planar complexes are usually low spin because of the high crystal field splitting energy. On the other hand, high spin Co(II) ions in square planar coordination arrangements were also reported.³² It would be interesting to see if high versus low spin configurations generate any detectable difference in UV-Vis and ECD spectra. Therefore, the individual UV-Vis and ECD spectra of the three predominant conformers of the Co(II)-salen-chxn complex at both low and high spin states in acetonitrile were calculated and are illustrated in Figure D3, and D4, respectively (Appendix D). The UV-Vis and ECD spectra of Co(II)-salen-chxn conformers I, II, and III at low spin display a remarkable degree of similarity. This similarity arises from the UV-Vis and ECD features being less sensitive to subtle tBu conformations. The same conclusion holds true for the high spin state. Moreover, the Boltzmann averaged UV-Vis spectra for both high and low spin states appear similar with only minor differences in the 200-700 nm. The Boltzmann-averaged ECD spectra of high and low spin states, on the other hand, do exhibit notable differences in the same range (see Figures D3 and D4, Appendix D). In Figure 6.6, we compared the simulated averaged UV-Vis and ECD spectra (for both low and high spin states) with the experimental spectra. Although the broad nature of the spectral features in the UV-Vis region made it difficult to achieve a conclusive assignment, the simulated high spin ECD spectrum appears to agree better with the experimental result than the low spin one, successfully reproducing most significant features observed in the experimental spectra. Overall, good agreements between experimental and simulated UV-Vis and ECD spectra of high spin were achieved.

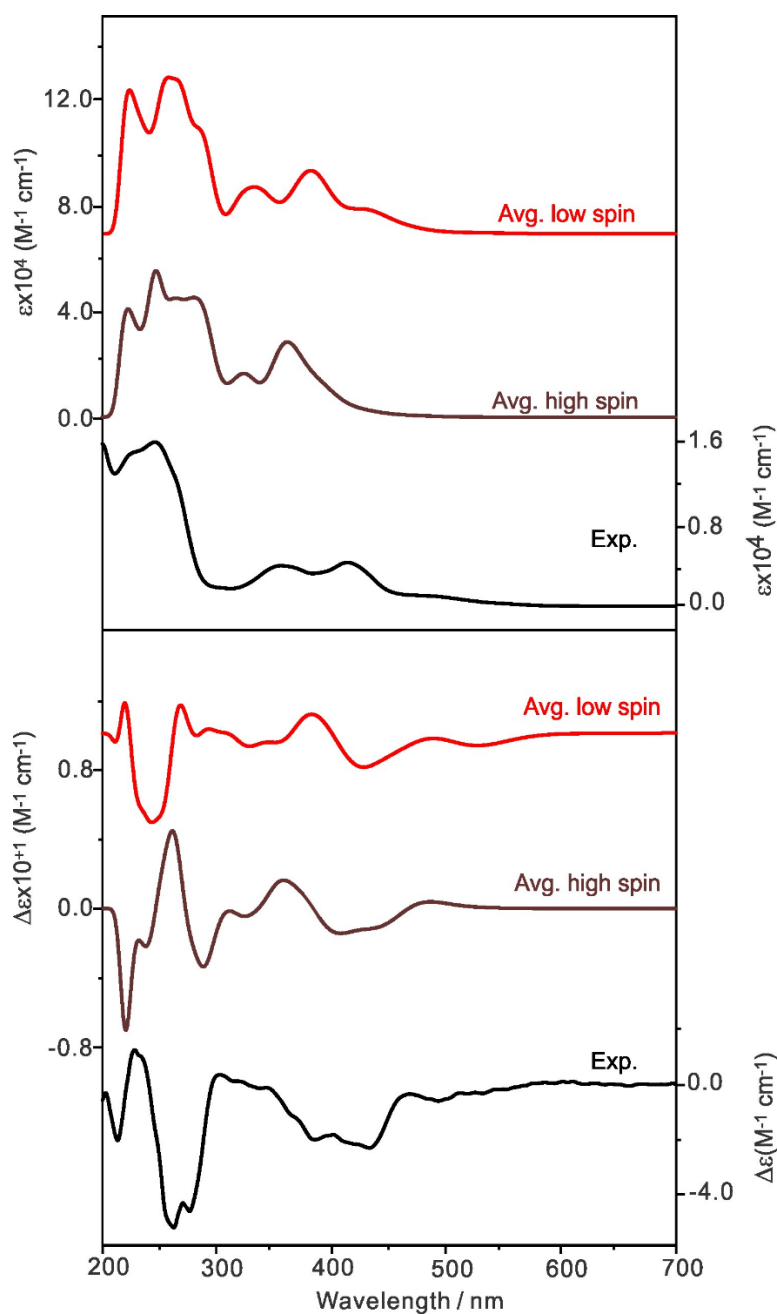


Figure 6.6. Comparison of the experimental and simulated UV-Vis (top) and ECD (bottom) spectra of Co(II)-salen-chxn using the B3LYP-D3BJ/6-311++G(d,p)/PCM(acetonitrile) level of theory. The first 250 electronic states were included in the calculations at the level of theory indicated. For the averaged spectra, we used the same Boltzmann weights used for the IR and VCD calculations.

Another goal of the current study is to validate the observed d-d low-lying electronic transition for Co(II)-salen-chxn, as evidenced in the experimental VCD spectrum in the 1700-3800 cm^{-1} region with a broad, positive ECD intensity for the (R,R) enantiomer and a negative intensity for the (S,S) enantiomer (as shown in Figure 6.4). The ECD spectrum of the high spin state, subjected to Boltzmann statistics averaging in the infrared (IR) region, was converted from nanometers to wavenumbers (cm^{-1}). It was then red-shifted to lower wavenumbers by 1000 cm^{-1} to better align with the broad ECD experimental peak in this region. Similar peak position uncertainties in the order of 1000 cm^{-1} were previously reported for TDDFT calculations or even those with more sophisticated approaches, such as adiabatic Hessian calculations.³³ This converted spectrum was then compared with the experimental VCD spectrum (see Figure 6.7). Notably, the broad ECD feature arising from the d-d low-lying electronic transitions observed in the experimental VCD spectrum was effectively reproduced in the simulated ECD spectrum.

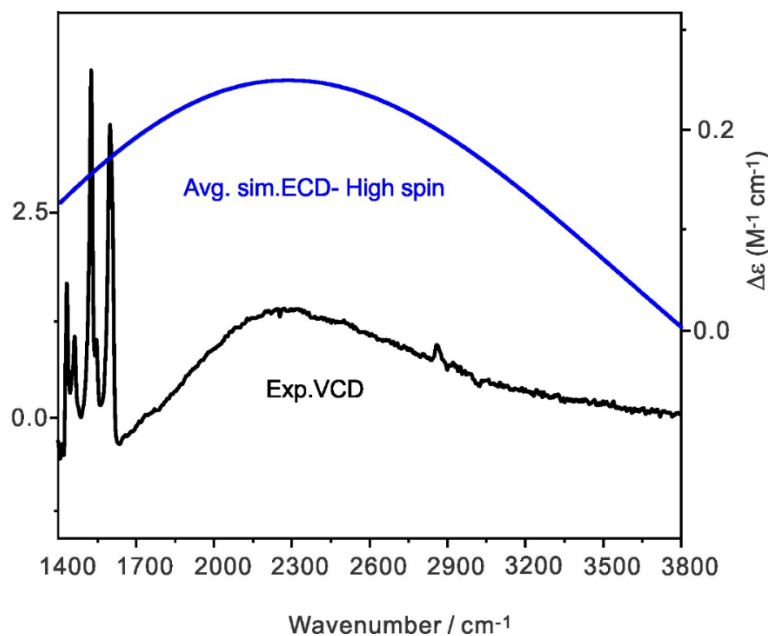


Figure 6.7. Comparison of the experimental VCD spectrum and the simulated averaged ECD spectrum of high spin Co(II)-salen-chxn in the IR region. Please note that the calculated ECD spectrum was red-shifted by 1000 cm^{-1} for comparison with the experiment.

6.3.4 Comparison of the Experimental and Simulated IR and VCD Spectra

As mentioned before, it is of considerable interest to probe if the low and high spin states of Co(II) would give rise to any noticeable differences in their IR and especially VCD features. The individual conformer IR and VCD spectra of the three most stable low spin (multiplicity is doublet) Co(II)-salen-chxn conformers are depicted in Figure 6.8. These were simulated at the B3LYP-D3BJ/6-311++G(d,p) level of theory with the PCM of chloroform. The simulated IR and VCD spectra of the individual conformers are almost the same, except in the regions of 1440-1470 cm^{-1} and 1150-1225 cm^{-1} (highlighted) where some minor differences are observed in the simulated VCD spectra. For example, the bi-signate band at the region 1440-1470 cm^{-1} , which mainly correspond to the bending motions of the C-H of the tBu groups, vary drastically from one conformer to the next. Conformer I display a negative-positive pattern in that region, while conformers II and III show opposite signs of those bands (positive-negative). Moreover, the band at 1150-1225 cm^{-1} region, which is assigned to the C-H wagging motion from the tBu groups, the VCD spectra of the conformers II and III show a negative band, it is noteworthy that this particular band is absent in the conformer I spectrum.

Similarly, the IR and VCD spectra of the high spin (multiplicity is quartets) Co(II)-salen-chxn conformers were simulated at the same level as stated above. The individual conformer IR and VCD spectra of the three most stable Co(II)-salen-chxn complex conformers at high spin are provided in Figure 6.9. The IR spectra of individual Co(II)-salen-chxn complex conformers at high spin look almost identical, whereas the corresponding VCD spectra exhibit minor differences in the highlighted regions among different conformers. For example, conformer I has a negative VCD band at 1347 cm^{-1} , which is associated with the C-H cyclohexane wagging motion; conversely, conformers II and III display a very small positive band at the same position. A strong negative

band attributed to the C=C stretching from the benzene ring was observed in the VCD spectra of conformer III at 1335 cm^{-1} . In contrast, no such band is observed in the VCD spectra of conformers I and II. Additionally, for the conformer III, the C-H twisting motions of the cyclohexane and benzene ring in the region 1143 cm^{-1} exhibits a much different pattern in terms of sign and relative intensity when compared to those of conformer I and II.

Overall, the VCD variation highlights the higher sensitivity of VCD features to small conformational changes than those of IR, making it a more effective tool to extract experimental conformational distributions in solution directly.

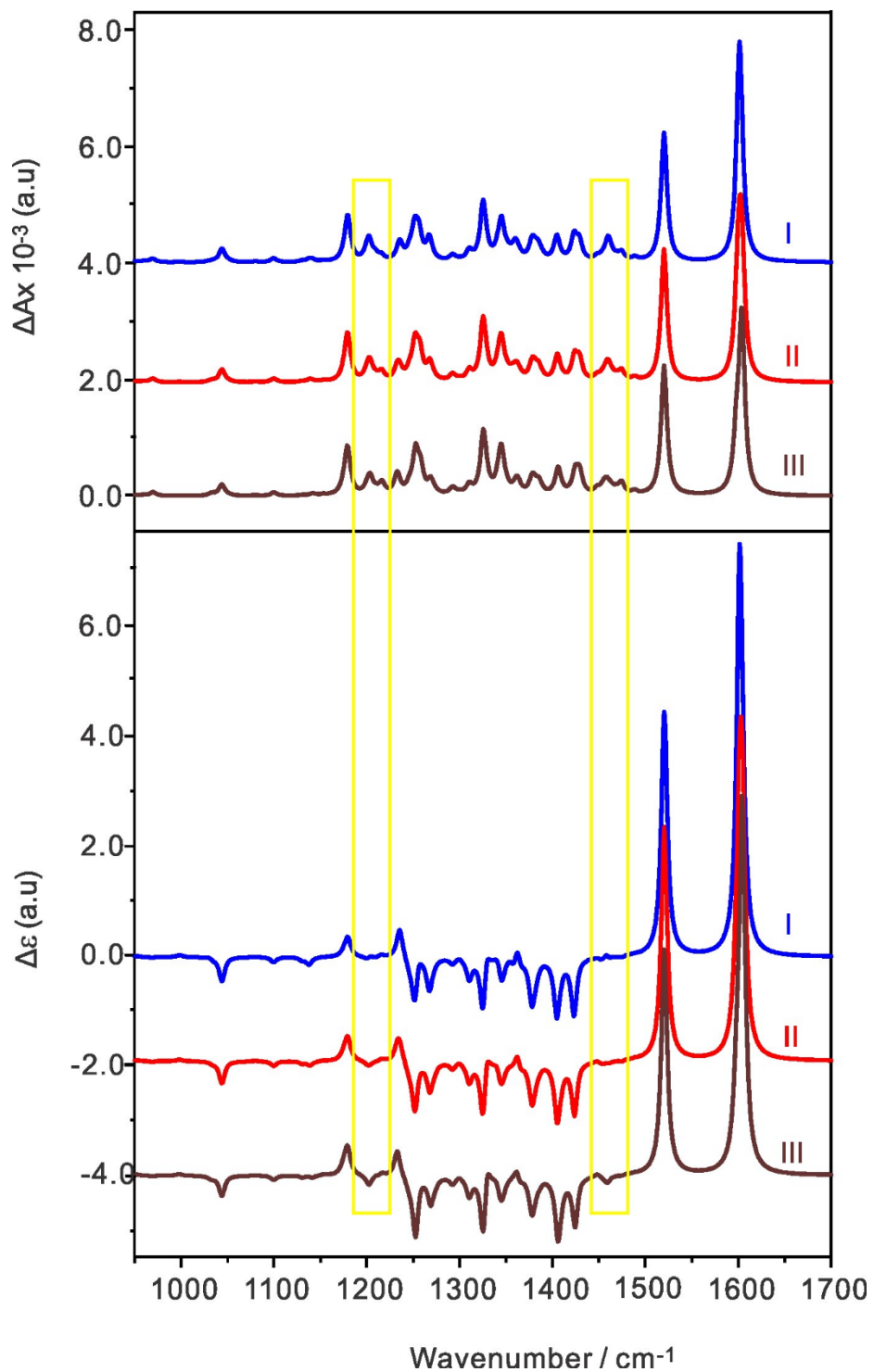


Figure 6.8. The simulated individual IR and VCD spectra of the three most stable Co(II)-salen-chxn conformers (low spin) at the B3LYP-D3BJ/6-311++G(d,p)/PCM (CHCl₃) level of theory at 298 K.

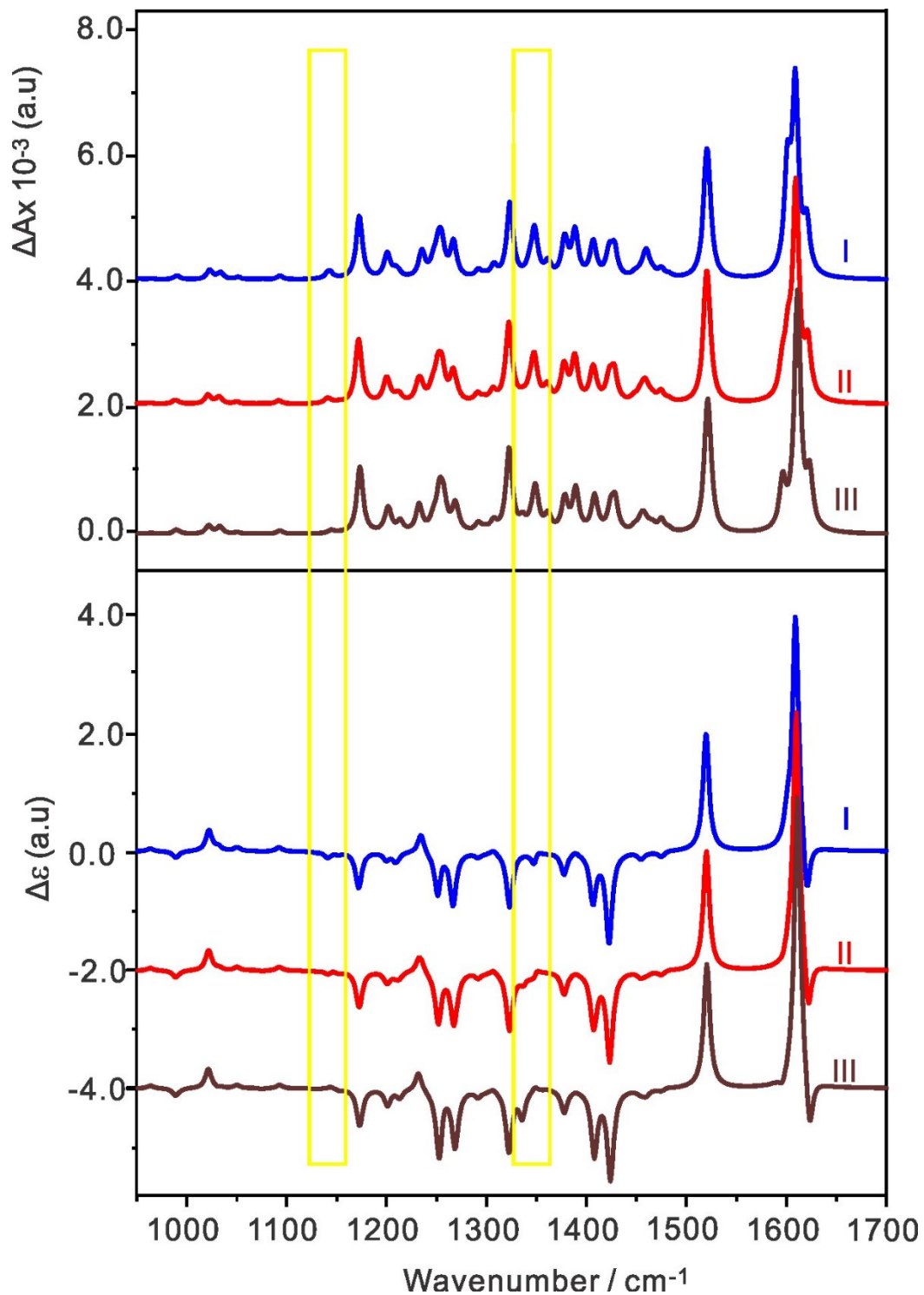


Figure 6.9. The simulated individual IR and VCD spectra of the three most stable Co(II)-salen-chxn conformers (high spin) at the B3LYP-D3BJ/6-311++G(d,p)/PCM (CHCl₃) level of theory at 298 K.

Last, we compared the Boltzmann averaged IR spectra of the low and high spin Co(II)-salen-chxn complex in the top panel of Figure 6.10 with the experimental IR spectrum. No significant changes to the relative intensities or features of the spectrum are noted in the IR spectra. However, upon closer inspection of the IR spectra, some minor differences in the relative intensities and the patterns of some bands could be detected in the high versus low spin spectra, particularly at lower wavelengths. The slight changes observed in the features of the IR spectra between the two spin states are likely to be a result of variations in the metal-ligand binding energy caused by alterations in the lengths of the metal-ligand bonds³⁴. Overall, the computed Boltzmann averaged IR spectra of both high and low spin Co(II) complexes show good agreement with the experimental one.

On the other hand, the Boltzmann averaged VCD spectra of the two spin states exhibit noticeable differences in the bottom panel of Figure 6.10. For instance, the calculated VCD spectra of the low and high spin states exhibit opposite VCD signs for the region below 1200 cm^{-1} . Moreover, the simulated VCD spectrum of the high spin state has a characteristic negative band at $\sim 1625 \text{ cm}^{-1}$, which is completely absent in the simulated VCD spectrum of the low spin state. Furthermore, the relative intensity bands in the low-spin VCD spectra are higher than those in the high-spin VCD spectra, particularly at wavenumbers greater than 1500 cm^{-1} while their corresponding IR bands are of similar intensity.

The simulated VCD of the two spin state spectra show drastic deviation from the experimental VCD spectrum (see the bottom panel of Figure 6.10). This suggests that the current theoretical VCD methodology which was developed for far-off resonance situations, fails to capture the experimental VCD spectrum of Co(II), a system which exhibits strong vibronic coupling between the vibrational levels and LLEs.

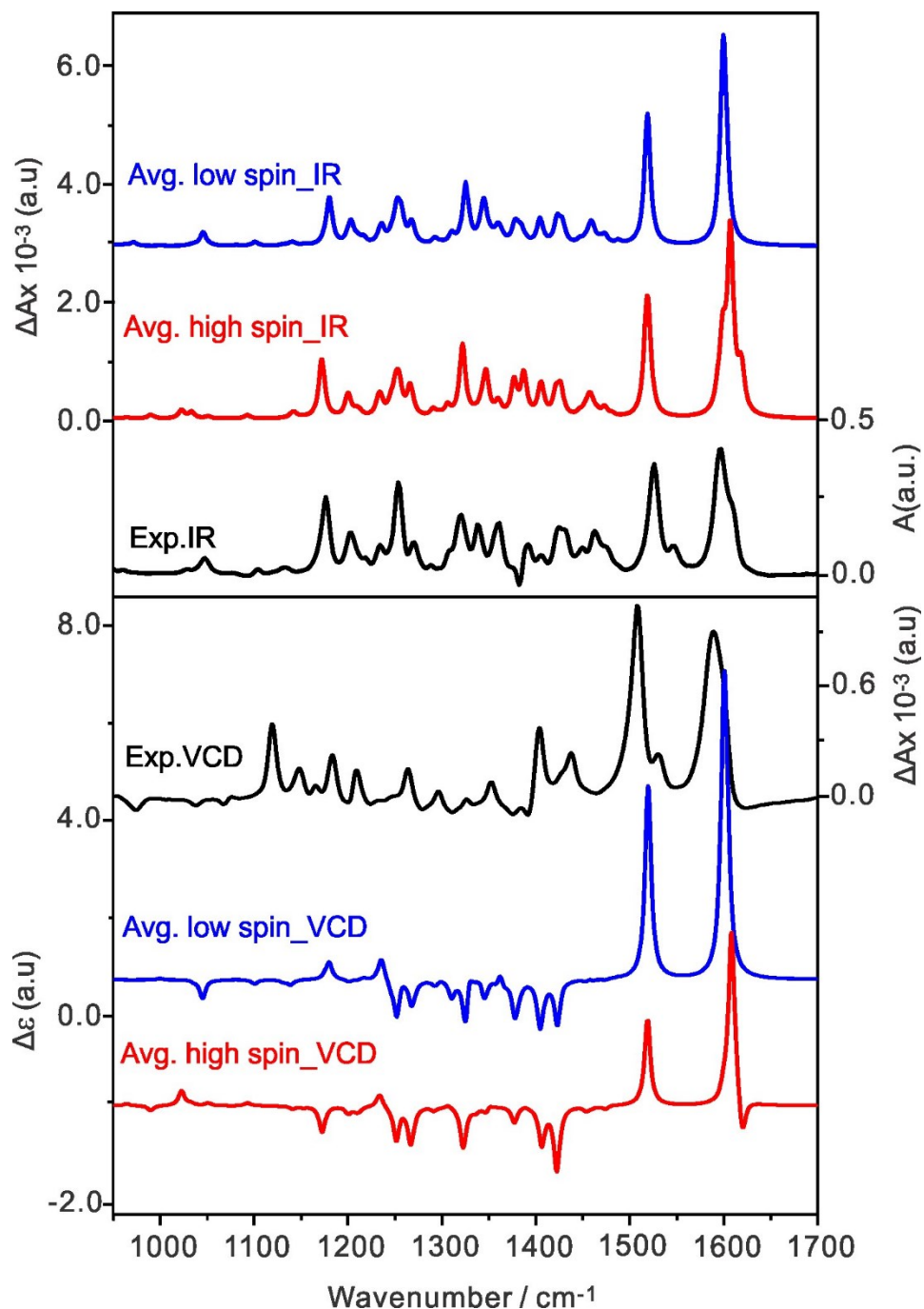


Figure 6.10. Comparison of the experimental IR and VCD spectra of Co(II)-salen-chxn with the corresponding Boltzmann averaged IR and VCD spectra at the B3LYPD3BJ/6-311++G(d,p) level with the PCM of chloroform at 298K.

While VCD simulations generally show commendable agreement with the experimental observations for closed shell transition metal complexes, such as the Ni(II)-salen-chxn complex¹⁹, navigating the simulations of open-shell transition metal complexes proves to be a more intricate and unpredictable endeavor. We note that for the Cu(II)-salen-chxn complex, an open shell complex, the simulated VCD spectrum agrees well with the experimental one.¹⁹ In addition, the Cu(II)-salen-chxn complex demonstrates no VCD intensity enhancement. In fact, its VCD intensity appears to be noticeably weaker than those of the other salen-chxn metal complexes and even the ligand itself shown in Figure 6.3. Furthermore, unlike the current Co(II) case whose VCD is monosignate, the Cu(II)-salen-chxn has both positive and negative VCD bands in the region (see Figure 6.3). All these characters indicate that the VCD property of Cu(II) behaves similarly to other closed shell systems even though its electronic configuration is $3d^9$ and has an unpaired electron.

The lack agreement between the experimental and simulated VCD spectra of open shell chiral transition metal complexes have been documented in the literature^{7,8,13}. The first observation of enhanced VCD intensity due to the low-lying d-d transition was reported by T. B. Freedman et al. for the chiral sparteine Ni(II) and Co(II) open shell complexes.¹³ As pointed out by Nafie and colleagues, the low-lying d-d transitions inherent to such systems can facilitate strong vibronic couplings between the vibration levels in the ground electronic state with the LLESs of the electronic states.¹² These LLESs arise from the splitting of degenerate energy levels in the core metal when coordinated with ligands.^{13(b),14} Through the vibronic couplings, the VCD intensity can be significantly enhanced where the vibrational transitions can borrow of the LLES magnetic-dipole terms.¹³ The theoretical model, currently implemented in G16 or other electronic structural calculation packages, does not take into account the vibronic coupling between ligand vibrations

in the ground electronic state and the metal-centered LLESs. This is the main reason for the significant discrepancy between theoretical and experimental results.

Very recently, P. Bouř and his co-worker introduced a new perturbation theory approach, referred to as beyond the Born-Oppenheimer (BBO) approach, to address this challenge³⁵. Within this perturbation approach, the coupling between the electronic and vibrational state is estimated using the harmonic approximation and simplified wave functions extracted from DFT calculations. The authors applied the BBO approach to calculate the VCD intensities of several open-shell chiral transition metal complexes, such as sparteine–Co (II)¹³ and salicyl–Co(II) complexes⁸ by coupling their electronic and vibrational states wave functions. The BBO approach generated provided significant enhancement of VCD bands, thus bring the predicted VCD intensities to the same range as the experimental ones for these two open shell complexes. While the experimental VCD spectrum of sparteine–Co (II) was reasonably reproduced, the monosignate nature of salicyl–Co(II) was not captured. Based on the previous simulated BBO result on salicyl–Co(II), we may anticipate that the current monosignate VCD spectrum of Co(II)-salen-chxn would be difficult to reproduce even with the most advanced BBO treatment.

Despite the overall challenge in accurately capturing the LLES induced VCD enhancement and peculiar monosignate sign, a recent study shows that one may be able to carry out some degree of analysis on the experimental monosignate VCD features by considering symmetry of the vibrational normal modes and those of the LLESs. These discussions are described in the next section.

6.3.5 Discussion on Symmetry-Dependent VCD Enhancement

As discussed in the previous section, it is not feasible to extract structural information by following the usual route of comparing the experimental and simulated VCD spectra for Co(II)-salen-chxn complex because the severe vibronic coupling between the ground electronic state normal mode vibrations and LLEs is not captured in the current DFT calculations. That being said, we did notice that the signs and intensities of some VCD features of Co(II)-salen-chxn, especially those in the 1580-1700 cm^{-1} region were largely correctly predicted in the current DFT calculations. In the first instance, one does not know if this is just a coincident or meaningful. In a recent paper, Pescitelli et al. uncovered an interesting aspect of vibronic coupling, i.e., VCD enhancement and sign reversal selectively affect the normal modes of B-symmetry in salicyl-Co(II), a pseudo-tetrahedral species belonging to the C_2 -symmetry group. This encouraged us to carry out similar symmetry analysis to gain further understanding of the VCD enhancement and possibly extract some structural information from the experiment versus theory comparison.

Since the VCD features of the three Co(II) conformers are very much the same, we focused on the most stable one for conciseness. This nearly planar conformer is of C_2 -symmetry with A and B symmetry species. In Figure 6.11, two example vibrational normal modes with A and B symmetries are presented. In Figure 6.12, we labelled the most prominent VCD bands with A and B symmetries. Some of them have both labels because there are multiple vibrational modes under one visible band. It is interesting to note that the simulated VCD bands with A symmetry appear to be in agreement with the corresponding experimental VCD features in terms of signs and relative intensities, while those labelled with B are in general disagreement with the experimental data. This is because in the aforementioned vibronic coupling scheme, only those vibrational modes with the same symmetry species as that of the LLEs can actually borrow magnetic dipole

moment from LLES. As analyzed before, the LLES of a C_2 symmetry species has B symmetry label.⁸ Therefore, the normal vibrational modes with A symmetry labels do not couple with the LLESs and their corresponding VCD intensity pattern can be properly modelled with the current DFT calculations.

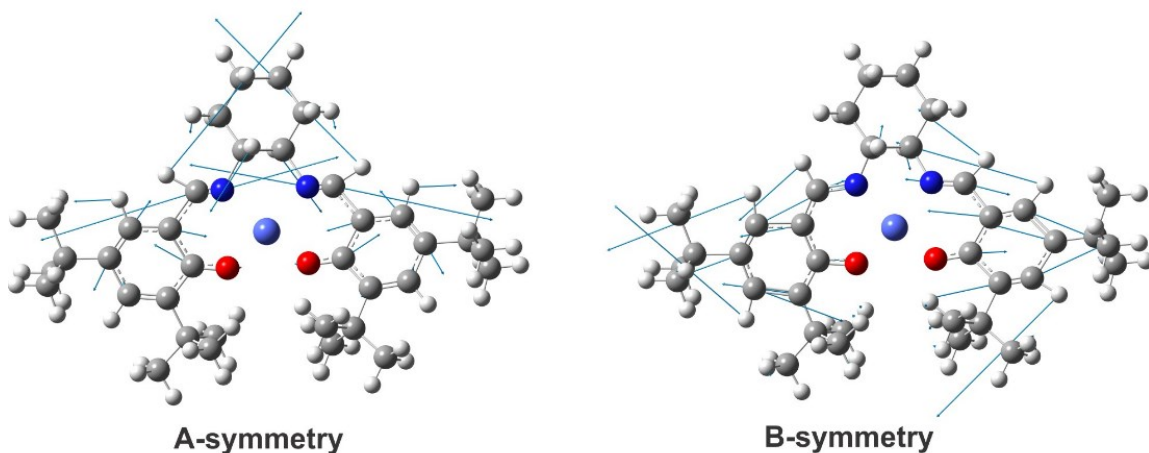


Figure 6.11. Example normal modes to the vibrational band at 1621 cm^{-1} , and at 1610 cm^{-1} of A and B symmetry, respectively. Atom displacements are represented by the blue arrows.

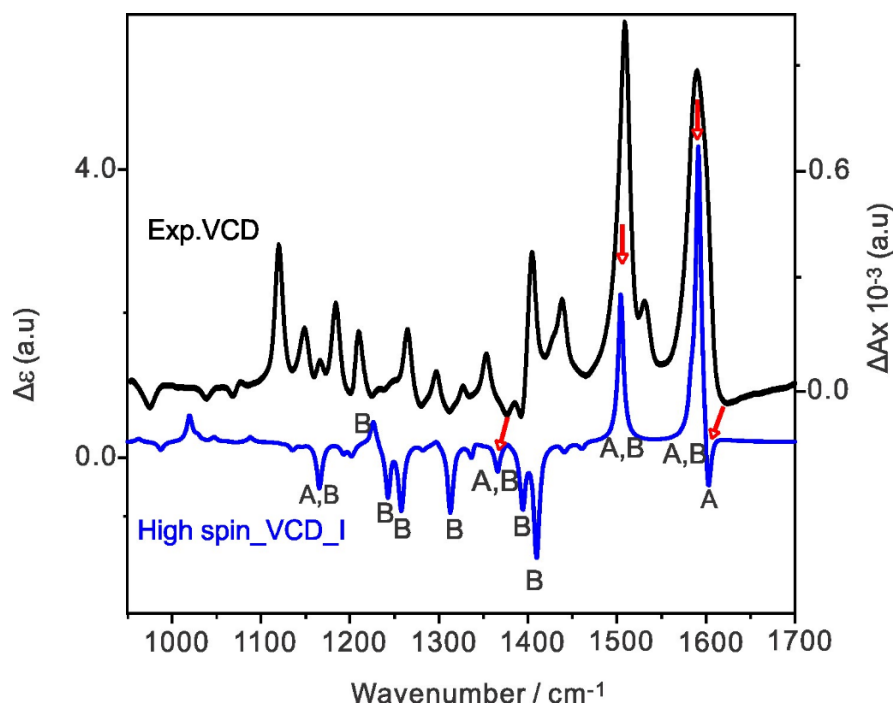


Figure 6.12. Comparison the Experimental VCD spectrum with the calculated VCD spectrum of the most stable conformer at high spin state for the C_2 -symmetrized structure of Co (II)- salen chxn. The red arrows indicate the experimental bands which correspond to the A symmetry vibrational motions and their VCD patterns are correctly predicted. See the main text for discussion.

In the previous report¹⁸ of the Co(II)-salen-chn complex, the author assumed that the complex is low spin based on an EPR study of some related Co(II) complexes.³⁰ We note that high spin, Schiff base-Co(II) complexes with distorted square planar geometries, similar to that of the Co(II)-salen-chn complex, have been reported.³⁶ For example, it was reported recently that an investigated Schiff base-Co(II) complex at high spin state with square planar geometry is more stable than low spin state.⁸ It is worth noting that the current calculations showed that the high spin complex is roughly 15 kJ mol^{-1} less stable than the low spin.

If one can trust the VCD prediction for the A-symmetry species, it is particularly interesting to look at the band at 1621 cm^{-1} . While the Boltzmann-averaged VCD spectrum with the high spin Co(II) exhibits a subtle negative band at approximately 1621 cm^{-1} , a similar feature is noticeably absent in the Boltzmann-averaged VCD spectrum with the low spin Co(II). Our preliminary VCD analysis indicates that the Co(II)-salen-chxn complex predominantly assumes a high spin state in solution.

6.4 Conclusion

The stereochemistry properties of the transition metal complex Co(II)-salen-chxn with LLESs were investigated using the UV-Vis and ECD, IR and VCD chiroptical tools. A systematic conformational search was done for the complex, resulting in a few CREST conformational candidates and subsequent DFT geometry optimizations led to three conformers. The three low-energy conformers of Co(II)-salen-chxn are associated with the different tBu arrangements. The UV-Vis, ECD, IR and VCD spectra of these three conformers with two different spin states were calculated at the B3LYP-D3BJ/6-311++G(d,p)/PCM (CHCl₃) level of theory. While reasonable agreements were achieved in the UV-Vis range and for IR spectra, no agreement was observed between the simulated and experimental VCD data. This disagreement is due to the low-lying electronic d-d transitions which produce strong vibronic coupling with some ground-state vibrations. By using the recently discovered symmetry selective vibronic coupling, we were able to analyze some VCD bands associated with the A-symmetry and therefore provide stereochemical information about the Co(II) system. We hope that the current work will generate interest in future theoretical development in treating LLES effect in VCD.

6.5 References

- [1] A. Soroceanu, A. Bargan, *Crystals* **2022**, 12, 1436.
- [2] P. Ghosh, S. K. Dey, M. H. Ara, K. Karim, A. B. M. N. Islam, *Egypt. J. Chem.* **2019**, 62, 523-547.
- [3] X. Liu, C. Manzur, N. Novoa, S. Celedón, D. Carrillo, J. R. Hamon, *Coord. Chem. Rev.* **2018**, 357, 144-172.
- [4] M. K. Goshisht, N. Tripathi, *J. Mater. Chem. C* **2021**, 9, 9820-9850.
- [5] F. Faridbod, M. R. Ganjali, R. Dinarvand, P. Norouzi, *Comb. Chem. High. Throughput Screen.* **2007**, 10, 527-546.
- [6] E. Akila, M. Usharani, S. Vimala, R. Rajavel, *Chem. Sci. Rev. Lett.* **2012**, 1, 181-194.
- [7] M. Górecki, M. Enamullah, M. A. Islam, M. K. Islam, S.-P. Höfert, D. Woschko, C. Janiak, G. Pescitelli, *Inorg. Chem.* **2021**, 60, 14116-14131.
- [8] G. Pescitelli, S. Lüdeke, M. Górecki, L. D. Bari, *J. Phys. Chem. Lett.* **2019**, 10, 650-654.
- [9] Z. Dezhahang, M. R. Poopari, Y. Xu, *Chem. Asian J.* **2013**, 8, 1205-1212.
- [10] Z. Dezhahang, C. Merten, M. R. Poopari, Y. Xu, *Dalton Trans.* **2012**, 41, 10817-10824.
- [11] G. Li, M. Alshalalfeh, J. Kapitán, P. Bouř, Y. Xu, *Eur. J. Chem.* **2022**, 28, e202104302.
- [12] T. Wu, G. Li, J. Kapitán, J. Kessler, Y. Xu, P. Bouř, *Angew. Chem. Int. Ed.* **2020**, 59, 21895-21898.
- [13] Y. He, X. Cao, L. A. Nafie, T. B. Freedman, *J. Am. Chem. Soc.* **2001**, 123, 11320-11321.
- [14] C. Merten, K. Hiller, Y. Xu, *Phys. Chem. Chem. Phys.* **2012**, 14, 12884-12891.
- [15] S. R. Domingos, F. Hartl, W. J. Brma, S. Woutersen, *ChemPhysChem.* **2015**, 16, 3363-3373.
- [16] S. R. Bhattacharya, T. Bürgi, *Nanoscale*, **2019**, 11, 23226-23233.
- [17] L. A. Nafie, *J. Phys. Chem. A* **2004**, 108, 7222-7231.
- [18] Y. He, *Doctoral Thesis*, **2005**.
- [19] G. Li, D. Li, M. Alshalalfeh, J. Cheramy, H. Zhang, Y. Xu, *Molecules* **2023**, 28, 2571.
- [20] P. Pracht, F. Bohle, S. Grimme, *Phys. Chem. Chem. Phys.* **2020**, 22, 7169-7192.
- [21] J. L. Alonso, M. Lozoya, I. Peña, J. C. López, C. Cabezas, S. Mata, S. Blanco, *Chem. Sci.* **2014**, 5, 515-522.
- [22] S. Grimme, C. Bannwarth, P. Shushkov, *J. Chem. Theory Comput.* **2017**, 13, 1989-2009.

- [23] A. S. Hazrah, A. Insausti, J. Ma, M. H. Al-Jabiri, W. Jäger, Y. Xu, *Angew. Chem. Int. Ed.* **2023**, 62, e202310610; *Angew. Chem.* **2023**, 135, e202310610.
- [24] C. D. Carlson, A. S. Hazrah, D. Mason, Q. Yang, N. A. Seifert, Y. Xu, *J. Phys. Chem. A* **2022**, 126, 7250-7260.
- [25] F. Weigend, R. Ahlrichs, *Phys. Chem. Chem. Phys.* **2005**, 7, 3297-3305.
- [26] M. J. Frisch, et al., *Gaussian 16; Revision C.03; Gaussian, Inc.: Wallingford, CT, USA*, **2019**.
- [27] B. Mennucci, J. Tomasi, R. Cammi, J. R. Cheeserman, M. J. Frischet, F. J. Devlin, S. Gabriel, P. J. Stephens, *J. Phys. Chem. A* **2002**, 106, 6102-6113.
- [28] G. Pescitelli, S. Lüdeke, A.-C. Chamayou, M. Marolt, V. Justus, M. Górecki, L. Arrico, L. Di Bari, M. A. Islam, I. Gruber, *Inorg. Chem.* **2018**, 57, 13397-13408.
- [29] P. R. Lassen, *Doctoral Thesis*. **2006**.
- [30] M. A. Hitchman, *Inorg. Chem.* **1977**, 16, 1985-1993.
- [31] M. Enamullah, A. R. Uddin, G. Pescitelli, R. Berardozzi, G. Makhloufi, V. Vasylyeva, A.-C. Chamayou and C. Janiak, *Dalton Trans.* **2014**, 43, 3313-3329.
- [32] C. F. Smura, D. R. Parker, M. Zbiri, M. R. Johnson, Z. A. Ga'1 and S. J. Clarke, *J. Am. Chem. Soc.* **2011**, 133, 2691-2705.
- [33] S. Izadnia, A. C. LaForge, F. Stienkemeier, J. R. Cheeseman, J. Bloino, J. Cheramy, W. Jäger, Y. Xu, *Phys. Chem. Chem. Phys.* **2021**, 23, 13862-13872.
- [34] (a) L. Kabalan, S. F. Matar, M. Zakhour, J. F. Letard, *Z. Naturforsch. B*, **2008**, 63, 154-160; (b) S. Kaviani, M. Izadyar, M. R. Housaindokht, *Polyhedron* **2016**, 117, 623-627; (c) A. Ould-Hamouda, B. Viquerat, J. Degert, S.F. Matar, J.-F. Létard, F. Guillaume, E. Freysz, *Eur. J. Inorg. Chem.* **2018**, 2018, 385-393.
- [35] J. Tomeček, P. Bouř, *J. Chem. Theory Comput.* **2020**, 16, 2627-2634.
- [36] B. Kaya, D. Akyüz, T. Karakurt, O. Şahin, A. Koca, B. Ülküseven, *Appl. Organomet. Chem.* **2020**, 34, e5930.

Chapter 7

Conclusions and Future Work

7.1 Conclusions

During my PhD research, I have primarily concentrated on understanding the mechanisms that underlie the observed chiroptical spectral features of various families of transition metal clusters and flexible molecular systems. I have delved into the chiroptical properties of atomically precise metal clusters, racemate lanthanide complexes, metal complexes with Schiff base ligands, and highly flexible monosaccharide derivatives. My exploration has involved the utilization of several advanced chiroptical spectroscopic techniques, including Raman optical activity (ROA), vibrational circular dichroism (VCD), and electronic circular dichroism (ECD). These experimental investigations have been closely complemented by density functional theory (DFT) calculations. This integration aimed to comprehensively understand the chiroptical behavior of the studied systems, including the relationships between the observed spectral features and structural properties, such as conformational distributions.

The key findings of my PhD research are summarized in the four result chapters, presenting diverse directions within the overarching theme of chirality transfer and amplification. First, I explored VCD features of atomically precise metal clusters protected by monolayer organic ligands and their respective ligands. A novel concept, 'bidirectional chirality transfer', was introduced to elucidate the intriguing phenomenon where noticeable chirality transfer effects were observed from the chiral ligands to the metal core and vice versa. To understand these effects comprehensively, extensive theoretical modelling was carried out, uncovering the mechanisms responsible for the substantial enhancement of the chiral ligand signals. Next, I designed an

innovative two-cell experimental setup, pairing it specially selected (chiral) molecular targets which include a racemic europium complex, an achiral europium salt and a (near) resonance Ni complex. The aim was to unravel the mechanisms responsible for the intensive chiral (I_R-I_L) signals detected from the racemic europium complex using an ROA spectrometer. I then probed the conformational distributions of two highly flexible monosaccharide derivatives using VCD and ROA and theoretical calculations. This study provides a solid foundation for utilizing the aforementioned europium complex and salt as enhancement sensors to detect chiroptical (ROA) responses of these monosaccharide derivatives. The final result chapter centres on the drastic VCD enhancements associated with the chiral transition metal complexes with low-lying electronic states molecules. Below, I summarize the main research results from each of these four chapters.

The detailed mechanisms of chirality transfer and enhancement at the nanoscale are especially intriguing and important because they are closely related to nanotechnology and various biological processes, yet a deeper understanding remains largely elusive because of imprecisions of chiral nanoparticles. While the inherent imprecision of nanoparticles hinders a thorough comprehension of chirality transfer and enhancement events at the nanoscale, recent synthetic developments in ultrastable, chiral metal clusters offer a unique opportunity to tackle this issue with atomic precision. In Chapter 3, I investigated four atomically-precise metal clusters with octahedral metal cores protected by monolayer organic ligands, namely $\text{Ag}_6\text{L}_6/\text{D}_6$, $\text{Ag}_6\text{PL}_6/\text{PD}_6$, $\text{Cu}_6\text{L}_6/\text{D}_6$, $\text{Cu}_6\text{PL}_6/\text{PD}_6$ and $\text{Cu}_6\text{PL}_6/\text{PD}_6$, ($\text{L}_6/\text{D}_6 = (\text{S})/(\text{R})$ -4-Isopropylthiazolidine-2-thione; $\text{PL}_6/\text{PD}_6 = (\text{S})/(\text{R})$ -4-Phenylthiazolidine-2-thione), as well as their corresponding chiral ligands, using VCD in conjunction with theoretical modelling. Drastically different VCD patterns were observed for the free ligands and their Ag_6 and Cu_6 clusters where the ligand C=N stretching modes exhibit exceptional VCD intensity enhancement, especially in Ag_6PD_6 . The IR and VCD

simulations, using the complete models for these four metal clusters, demonstrated excellent agreements with the experimental observations, while simplified models with fewer metal atoms and ligands exhibited various deficiencies. Additionally, the observed differences in VCD features between the Ag₆ and Cu₆ clusters underscore the influence of inner core metal atoms on the outer shell ligands. This study highlights the crucial importance of a complete model for extracting rich information hidden in the experimental VCD features, including bidirectional chirality transfer between ligands and metal cores, as well as the VCD enhancement mechanism. These investigations are expected to generate substantial interest in silver clusters and other metal clusters with monolayer ligand protection, particularly in the context of future applications in optical functionality, energy conversion and biomedical fields. Furthermore, these atomically precise metal clusters can serve as fundamental building blocks for Metal-Organic Frameworks (MOFs). MOFs, in turn, prove highly effective for tasks such as gas storage and transportation, gas separation, water absorption, catalysis, adsorption cooling, and drug delivery.

In recent years, Raman optical activity (ROA) applications have significantly expanded, encompassing diverse systems such as transition metal clusters, bio-supramolecular architectures, and novel nanostructures. Deciphering the complex contributions to the observed chiral signals remains a formidable yet pressing challenge, especially in experiments conducted under (near) resonance conditions. One illustrative example involves monitoring circularly polarized luminescence responses of lanthanide series of metal complexes using a ROA spectrometer, offering spontaneous measurement of multiple types of chiroptical spectra from a single sample solution in a single experiment. In Chapter 4, we designed a series of experiments employing both one-cell and two-cell experimental setups to evaluate the contributions of various light-matter interaction events. The innovative two-cell design offers the possibility of avoiding chemical or

physical interactions between species of interest, thereby separating contributions caused by direct contact from other mechanisms. Leveraging a racemic europium complex (Europium (III)-tris(1,1,1,2,2,3,3-heptafluoro-7,7-dimethyl-4,6-octanedionate) complex (Eu(FOD)₃), an achiral europium salt (EuCl₃), and a (near) resonant chiral Ni transition metal complex (*RR/SS*-bis (pyrrol-2-ylmethyleneamine)-cyclohexane nickel (II) complex), we evaluated the factors which influenced the observed $I_R - I_L$ features of the Eu and other species. Our investigation revealed that the primary mechanism responsible for the observed $I_R - I_L$ features of Eu species involves a two-step process: i) Absorption of the 532 nm laser light leads to luminescence ($I_R + I_L$) signals of Eu(FOD)₃ and EuCl₃; ii) Preferential absorption of the luminescence light due to the ECD of *R/S*-Ni gives the final $I_R - I_L$ imbalance for the Eu species. The simulated chiral responses based on the proposed mechanisms are in excellent agreement with the experimental data, providing a comprehensive understanding of the intricate chiroptical phenomena observed. The deeper understanding gained of the chiral Eu features using an ROA instrument will contribute to the technology advancement of chiral luminescent devices and nanodevices, and also to their applications in biological fields and DNA engineering.

In Chapter 5, the conformational landscapes of two highly flexible monosaccharide derivatives, namely phenyl β-D-glucopyranoside (ph-β-glu) and 4-(hydroxymethyl)phenyl β-D-glucopyranoside, also commonly known as gastrodin, were explored using a combined experimental and theoretical approach. For the infrared, Raman, and the associated vibrational optical activity (VOA), i.e., vibrational circular dichroism and Raman optical activity, experiments of these two compounds in DMSO and in water were carried out. Extensive and systematic conformational searches were performed using a recently developed conformational searching tool called CREST (conformer-rotamer ensemble sampling tool) in the two solvents. Fourteen and

twenty-four low-energy conformers were identified at the DFT level for ph- β -glu and gastrodin, respectively. The spectral simulations of individual conformers were done at the B3LYP-D3BJ/def2-TZVPD level with the polarizable continuum model of the solvents. The VOA spectral features exhibit much higher specificity to conformational differences than their parent infrared and Raman. The excellent agreements achieved between the experimental and simulated VOA spectra allow for the extraction of experimental conformational distributions of these two carbohydrates in solution directly. The experimental percentage abundances based on the hydroxymethyl (at the pyranose ring) conformations G⁺, G⁻, and T for ph- β -glu were obtained to be 15%, 75%, and 10% in DMSO and 53%, 40%, and 7% in water, respectively, in comparison to the previously reported gas phase values of 68%, 25%, and 7%, highlighting the important role of solvents in conformational preferences. The corresponding experimental distributions for gastrodin are 56%, 22%, and 22% in DMSO and 70%, 21%, and 9% in water.

In Chapter 6, I examined the stereochemical properties of the open shell Schiff-based transition metal complex with low-lying electronic states, namely, (R,R)-(-)-N,N'-Bis(3,5-di-tert-butylsalicylidene)-1,2-cyclohexanediaminocobalt(II) (Co(II)-salen-chxn). Multiple spectroscopic tools, including IR, VCD, UV-Vis and ECD were employed to explore the related chiroptical properties. The experimental results of several other transition metal complexes which are either closed-shell or open-shell but without low-lying electronic states were systematically compared to those of Co(II)-salen-chxn. The VCD spectrum of Co-salen-chxn exhibits predominantly monosignate bands with drastically enhanced asymmetric g factors. In addition, extensive theoretical calculations were carried out for the Co(II) complex with different charges and spin multiplicities. The corresponding simulated UV-Vis, ECD, IR and VCD spectra at the B3LYP-D3BJ/6-311++G(d,p)/PCM level of theory were compared with the experimental ones to extract

stereochemical information. While reasonable agreements were achieved for the UV-Vis and ECD spectra, as well as the IR spectrum, no agreement could be achieved between the simulated and experimental VCD data. This absence of agreement is because the current theoretical model does not consider the vibronic coupling between the ground-state vibrational transitions and the magnetic-dipole allowed low-lying electronic excited states. By applying the symmetry-selective vibronic coupling method to Co(II)-salen-chxn, belonging to the C_2 symmetry group, I separated the vibrational bands with A and B symmetries. Since the low-lying electronic states can only mix with vibrational bands of B-symmetry and therefore have no impact on A-symmetry bands, I was able to identify VCD bands with A-symmetry and use the theoretical simulation to extract the high-spin nature of the Co(II) complex.

7.2 Future Work

Throughout this thesis, chiral optical spectroscopic techniques have been extensively utilized to investigate multiple systems. These techniques possess a remarkable sensitivity to molecular conformations, thereby enabling not only the determination of absolute stereochemistry but also facilitating conformational analysis in solution. Additionally, these techniques have been pivotal in determining the absolute configuration of the studied systems. Consequently, further investigations into various aspects of the research conducted within this thesis could prove highly advantageous and fruitful.

In Chapter 3, we introduced the bidirectional chiral transfer mechanism for atomically precise metal clusters. Since this study is the first of its kind, to advance our understanding of the bidirectional chiral transfer mechanism, it is highly recommended to investigate the chirality of various metal clusters by employing different metal cores¹ and chiral ligands^{2,3} in future studies. This extension of research would enable a more holistic comprehension of the underlying

mechanisms driving this intriguing phenomenon. In addition, it would be highly beneficial to investigate the chirality transfer mechanism using larger metal cluster modules for theoretical measurements. This would allow us to validate the accuracy of our theoretical models and ensure that they align well with experimental results under diverse conditions. Another possible future direction is to investigate VCD of crystal samples of these atomically precise chiral metal clusters directly. It was reported very recently, these clusters may be crystalized under different conditions, for example using different solvents, to produce chiral superstructures⁴. So far, no such VCD studies have ever been reported.

In Chapter 4, our research revealed the mechanisms for the intense chiral features at the europium luminance band positions using a near resonant chiral Ni⁺² complex and both one-cell and double-cell ROA setups. The outcome of our investigation indicated that the presence of the chemical contact mechanism is not necessary for such observation. On the other hand, these Eu complexes and salt can be used as an enhancer for the otherwise weak ROA signals of some chiral functional groups through direct chemical contacts for example in chirality transfer from monosaccharide molecules to racemic lanthanide complexes⁵. While in Chapter 5, our focus was mainly on analyzing the conformational landscapes of phenyl β -D-glucopyranoside and gastrodin monosaccharide, adding the Eu complex or even achiral Eu salt, may change the chiral signal detected. It is worth noting that lanthanide complexes in general exhibit robust luminescence signals arising from $^5D_1 \rightarrow ^7F_2$, $^5D_0 \rightarrow ^7F_0$, and $^5D_0 \rightarrow ^7F_1$ transitions,⁶ which can be effectively detected through ROA spectroscopy. Furthermore, sugar-based compounds offer multiple metal binding groups, such as the hydroxyl (OH) group. One may expect to observe strong chiral responses at luminescent bands of the lanthanide complexes, which reflect the chirality of the sugar-based compounds. The two-cell approach described in Chapter 4 will allow us to dissect the

contributions to the chiral signatures detected in those cases in considerable detail. This effort can be used on the sugar derivatives reported in Chapter 5.

While Chapter 6, along with other previously reported VCD studies^{7,8,9} on the open shell complexes with low-lying electronic states, has showcased strongly enhanced VCD signatures, a comprehensive theoretical framework to fully explain this enhancement has not yet been developed. It is worth noting that some promising results have been reported with recently developed methods which employed the beyond the Born-Oppenheimer (BBO) approach.¹⁰ In these approaches the coupling between low-lying electronic states and vibrational states in the ground electronic state is incorporated by utilizing the harmonic approximation and simplified wave functions obtained from DFT computations. Our experimental VCD spectra of the Co(II) complex display distinctive monosignate features, a rarity among similar open-shell systems with low-lying electronic states. Furthermore, applying symmetry consideration, we were able to explain some of the observed spectral features, providing further insight into this complex problem. Our future plans involve conducting further studies on related complexes and collaborate with theorists in this area to advance our understanding of this enhancement behavior.

7.3 References

- [1] Z. Han, X. L. Zhao, P. Peng, S. Li, C. Zhang, M. Cao, K. Li, Z. Y. Wang, S. Q. Zang, *Nano Res.* 2020, 13, 3248-3252.
- [2] Y.-J. Kong, J.-H. Hu, X.-Y. Dong, Y. Si, Z.-Y. Wang, X.-M. Luo, H.-R. Li, Z. Chen, S.-Q. Zang, T. C. W. Mak, *J. Am. Chem. Soc.* 2022, 144, 19739-19747.
- [3] M. M. Zhang, X. Y. Dong, Z. Y. Wang, X. M. Luo, J. H. Huang, S. Q. Zang, T. C. W. Mak, *J. Am. Chem. Soc.* 2021, 143, 6048-6053.
- [4] Z. Han, Y. Si, X. Y. Dong, J. H. Hu, C. Zhang, X. H. Zhao, J. W. Yuan, Y. Wang, S. O. Zang, *J. Am. Chem. Soc.* 2023, 145, 6166- 6176.
- [5] T. Wu, P. Bouř, *Chem. Commun.* 2018, 54, 1790-1792.
- [6] T. Wu, J. Kapitan, V. Masek, P. Bour, *Angew. Chem., Int. Ed.* 2015, 54, 14933-14936.
- [7] G. Pescitelli, S. Lüdeke, A.-C. Chamayou, M. Marolt, V. Justus, M. Górecki, L. Arrico, L. Di Bari, M. A. Islam, I. Gruber, *Inorg. Chem.* 2018, 57, 13397-13408.
- [8] M. Górecki, M. Enamullah, M. A. Islam, M. K. Islam, S.-P. Höfert, D. Woschko, C. Janiak, G. Pescitelli, *Inorg. Chem.* 2021, 60, 14116-14131.
- [9] G. Pescitelli, S. Lüdeke, M. Górecki, L. D. Bari, *J. Phys. Chem. Lett.* 2019, 10, 650-654.
- [10] J. Tomeček, P. Bouř, *J. Chem. Theory Comput.* 2020, 16, 2627-2634.

Bibliography

- [1] J. Gal, Chiral drugs from a historical point of view, WILEY-VCH, Weinheim, **2006**.
- [2] N. Berova, P. L. Polavarapu, K. Nakanishi, R. W. Woody, Comprehensive Chiroptical Spectroscopy: Instrumentation, Methodologies, and Theoretical Simulations, John Wiley & Sons, Hoboken, NJ, **2012**.
- [3] J. Gal, P. Cintas, Early History of the Recognition of Molecular Biochirality. In Biochirality: Origins, Evolution and Molecular Recognition; Cintas, P., Ed.; Springer: Berlin/Heidelberg, Germany, **2013**.
- [4] H. Morawetz, Polymers: the origins and growth of a science, Courier Corporation, **2002**.
- [5] J. Gal, *Helv. Chim. Acta*, **2013**, 96, 1617-1657.
- [6] M. Liu, L. Zhang, T. Wang, *Chem. Rev.* **2015**, 115, 7304-7397.
- [7] F. A. Cotton, Chemical Applications of Group Theory, John Wiley & Sons: New York, **1990**.
- [8] M. Abram, M. Jakubiec, K. Kamiński, *ChemMedChem*. **2019**, 14, 1744-1761.
- [9] L. A. Nguyen, H. He, C. Pham-Huy, *Int. J. Biol. Sci.* **2006**, 2, 85-100.
- [10] T. Asatsuma-Okumura, T. Ito, H. Handa, *Pharmaceuticals* **2020**, 13, 95.
- [11] J. H. Kim, A. R. Scialli, *Toxicological Sciences* **2011**, 122, 1-6.
- [12] G. Mazzeo, E. Santoro, A. Andolfi, A. Cimmino, P. Troselj, A. G. Petrovic, S. Superchi, A. Evidente, N. Berova, *J. Nat. Prod.* **2013**, 76, 588-599.
- [13] P. L. Polavarapu, Chiroptical Spectroscopy: Fundamentals and Applications, CRC Press, Boca Raton, FL, **2016**.
- [14] G. Yang, Y. Xu, *Top. Curr. Chem.* **2011**, 298, 189-236.

- [15] L. A. Nafie, *Vibrational Optical Activity: Principles and Applications*, John Wiley & Sons, Ltd., UK, **2011**.
- [16] L. D. Barron, *Molecular light scattering and optical activity*, 2nd edn. Cambridge, **2004**.
- [17] Y. Hu, K. Cheng, L. He, X. Zhang, B. Jiang, L. Jiang, C. Li, G. Wang, Y. Yang, M. Liu, *Anal. Chem.* **2021**, 93, 1866-1879.
- [18] M. R. Poopari, Z. Dezhahang, K. Shen, L. Wang, T. L. Lowary, Y. Xu, *J. Org. Chem.* **2015**, 80, 428-437.
- [19] J. M. Seco, E. Quiñoá, R. Riguera, *Chem. Rev.* **2012**, 112, 4603-4641.
- [20] S. Parsons, *Tetrahedron: Asymmetry* **2017**, 28, 1304-1313.
- [21] Q. B. Cass, M. E. Tiritan, J. M. B. Junior, J. C. Barreiro, *Chiral Separations and Stereochemical Elucidation: Fundamentals, Methods, and Applications*, John Wiley & Sons, **2023**.
- [22] A. Pandey, S. Dalal, S. Dutta, A. Dixit, *J. Mater. Sci.-Mater. Electron.* **2021**, 32, 1341-1368.
- [23] P. Lahiri, K. B. Wiberg, P. H. Vaccaro, M. Caricato, T. D. Crawford, *Angew. Chem. Int. Ed.* **2014**, 53, 1386-1389.
- [24] G. Yang, Y. Xu, *Phys. Chem. Chem. Phys.* **2008**, 10, 6787-6795.
- [25] G. Pescitelli, L. Di Bari, N. Berova, *Chem. Soc. Rev.* **2011**, 40, 4603-4625.
- [26] G. Pescitelli, *Chirality* **2022**, 34, 333-363.
- [27] Z. Dezhahang, M. R. Poopari, F. E. Hernández, C. Diaz, Y. Xu, *Phys. Chem. Chem. Phys.* **2014**, 16, 12959-12967.
- [28] G. Yang, J. Li, Y. Liu, T. L. Lowary, Y. Xu, *Org. Biomol. Chem.* **2010**, 8, 3777-3783.
- [29] T. Mizutani, H. Takagi, O. Hara, T. Horiguchi, H. Ogoshi, *Tetrahedron Lett.* **1997**, 38, 1991-1994.

- [30] T. Burgi, A. Vargas, A. Baiker, *J. Chem. Soc., Perkin Trans.* **2002**, 2, 1596-1601.
- [31] E. Machalska, G. Zajac, M. Baranska, D. Kaczorek, R. Kawęcki, P. F. Lipiński, J. E. Rode, J. C. Dobrowolski, *Chem. Sci.* **2021**, 12, 911-916.
- [32] G. Yang, Y. Xu, *J. Chem. Phys.* **2009**, 130, 164506.
- [33] M. Losada, Y. Xu, *Phys. Chem. Chem. Phys.* **2007**, 9, 3127-3135.
- [34] C. Merten, Y. Xu, *Angew. Chem. Int. Ed.* **2013**, 52, 2073-2076.
- [35] J. E. Rode, M. H. Jamróz, J. Sadlej, J. Cz. Dobrowolski, *J. Phys. Chem. A.* **2012**, 116, 7916-7926.
- [36] A. S. Perera, J. Cheramy, C. Merten, J. Thomas, Y. Xu, *ChemPhysChem* **2018**, 19, 2234-2242.
- [37] A. S. Perera, J. Thomas, M. R. Poopari, Y. Xu, *Front. Chem.* **2016**, 4, 1-17.
- [38] Y. Yang, J. Cheramy, M. Brehm, Y. Xu, *ChemPhysChem.* **2022**, 23, e202200161/1-11.
- [39] A. S. Perera, C. D. Carlson, J. Cheramy, Y. Xu, *Chirality* **2023**, 35, 718-731.
- [40] Y. Yang, M. Alshalalfeh, Y. Xu, *Spectrochim. Acta A Mol. Biomol. Spectrosc.* **2023**, DOI: 10.1016/j.saa.2023.123634.
- [41] S. O. Pour, L. Rocks, K. Faulds, D. Graham, V. Parchaňský, P. Bouř, E. W. Blanch, *Nat. Chem.* **2015**, 7, 591-596.
- [42] G. Zajac, A. Kaczor, A. Pallares Zazo, J. Mlynarski, M. Dudek, M. Baranska, *J. Phys. Chem. B.* **2016**, 120, 4028-4033.
- [43] G. Li, J. Kessler, J. Cheramy, T. Wu, M. R. Poopari, P. Bouř, Y. Xu, *Angew. Chem. Int. Ed.* **2019**, 58, 16495-16498; *Angew. Chem.* **2019**, 131, 16647-16650.
- [44] T. Wu, G. Li, J. Kapitán, J. Kessler, Y. Xu, P. Bouř, *Angew. Chem. Int. Ed.* **2020**, 59, 21895-21898.

- [45] G. Li, M. Alshalalfeh, Y. Yang, J. R. Cheeseman, P. Bouř, Y. Xu, *Angew. Chem. Int. Ed.* **2021**, 60, 22004-22009.
- [46] E. Machalska, G. Zajac, A. J. Wierzba, J. Kapitán, T. Andruniów, M. Spiegel, D. Gryko, P. Bouř, M. Baranska, *Angew. Chem. Int. Ed.* **2021**, 60, 21205-21210.
- [47] A. Nemati, S. Shadpour, L. Querciagrossa, L. Li, T. Mori, M. Gao, C. Zannoni, T. Hegmann, *Nat. Commun.* **2018**, 9, 3908.
- [48] T. Mori, A. Sharma, T. Hegmann, *ACS Nano.* **2016**, 10, 1552-1564.
- [49] S. Bettini, M. Ottolini, D. Valli, R. Pagano, C. Ingrosso, M. Roeffaers, J. Hofkens, L. Valli, G. Giancane, *Nanomaterials* **2023**, 13, 1526.
- [50] X. Kang, Y. Li, M. Zhu, R. Jin, *Chem. Soc. Rev.* **2020**, 49, 6443-6513.
- [51] M. J. Alhilaly, R.-W. Huang, R. Naphade, B. Alamer, M. N. Hedhili, A.-H. Emwas, P. Maity, J. Yin, A. Shkurenko, O. F. Mohammed, M. Eddaoudi, O. M. Bakr, *J. Am. Chem. Soc.* **2019**, 141, 9585-9592.
- [52] C. Gautier, T. Bürgi, *J. Am. Chem. Soc.* **2006**, 128, 11079-11087.
- [53] C. Gautier, T. Bürgi, *J. Phys. Chem. C.* **2010**, 43, 15897-15902.
- [54] A. Sels, R. Azoulay, W. J. Buma, M. A. J. Koenis, V. P. Nicu, T. Bürgi, *J. Phys. Chem. C* **2019**, 123, 22586-22594.
- [55] Z. Han, X.-Y. Dong, P. Luo, S. Li, Z.-Y. Wang, S.-Q. Zang, T. C. W. Mak, *Sci. Adv.* **2020**, 6, eaay0107.
- [56] M. T. Kaczmarek, M. Zabiszak, M. Nowak, R. Jastrzab, *Coord. Chem. Rev.* **2018**, 370, 42-54.
- [57] S-H. Lam, H-Y. Hung, P-C. Kuo, D-H. Kuo, F-A. Chen, T-S. Wu, *Molecules* **2020**, 25, 5383.
- [58] S. E. Bodman, S. J. Butler, *Chem. Sci.* **2021**, 12, 2716-2734.

- [59] J. F. Sherson, H. Krauter, R. K. Olsson, B. Julsgaard, K. Hammerer, I. Cirac, E. S. Polzik, *Nature* **2006**, 443, 557-560.
- [60] O. G. Willis, F. Zinna, L. Di. Bari, *Angew. Chem. Int. Ed.* **2023**, 62, e202302358.
- [61] T. Wu, *Phys. Chem. Chem. Phys.* **2022**, 24, 15672-15686.
- [62] T. Wu, J. Kapitán, V. Andrushchenko, P. Bouř, *Anal. Chem.* **2017**, 89, 5043-5049.
- [63] P. S. Steinlandt, L. Zhang, E. Meggers, *Chem. Rev.* **2023**, 123, 4764-4794.
- [64] S. M. Wilkinson, T. M. Sheedy, E. J. New, *J. Chem. Educ.* **2016**, 93, 351-354.
- [65] G. Li, D. Li, M. Alshalalfeh, J. Cheramy, H. Zhang, Y. Xu, *Molecules* **2023**, 28, 2571.
- [66] Z. Dezhahang, M. R. Poopari, J. Cheramy, Y. Xu, *Inorg. Chem.* **2015**, 54, 4539-4549.
- [67] S. Luber, *Biomed. Spectrosc. Imaging* **2015**, 4, 255-268.
- [68] Y. Yang, A. Krin, X. Cai, M. R. Poopari, Y. Zhang, J. R. Cheeseman, Y. Xu, *Molecules* **2023**, 28, 771.
- [69] M. Alshalalfeh, N. Sun, A. H. Moraes, A. P. A. Utani, Y. Xu, *Molecules* **2023**, 28, 4013.
- [70] L. A. Nafie, *Vibrational Optical Activity: Principles and Applications*, John Wiley & Sons, Ltd., UK, **2011**.
- [71] R. K. Dukor, L. A. Nafie, "Vibrational Optical activity of pharmaceuticals and biomolecules", In *Encyclopedia of Analytical Chemistry*, John Wiley & Sons, Ltd., UK, **2000**.
- [72] L. A. Nafie, T. B. Freedman, R. K. Dukor, "Vibrational Circular Dichroism", In *Handbook of Vibrational Spectroscopy*, John Wiley & Sons, Ltd., UK, **2002**.
- [73] G. E. Tranter, "Protein Structure Analysis by CD, FTIR, and Raman Spectroscopies", In *Encyclopedia of Spectroscopy and Spectrometry*, Oxford: Academic Press. UK, **2017**.
- [74] L. D. Barron, *Molecular light scattering and optical activity*, 2nd edn. Cambridge, **2004**.

- [75] H. G. Kuball “Chiroptical Analysis” In Encyclopedia of Analytical Science, Elsevier Ltd. NL, **2005**.
- [76] N. Harada, N. Berova, “Separations and Analysis” In Comprehensive Chirality, Elsevier Ltd. NL, **2012**.
- [77] L. A. Nafie, Annu. Rev. Phys. Chem. **1997**, 48, 357-386.
- [78] P. W. Atkins, L. D. Barron, Molec. Phys. **1969**, 16, 453-466.
- [79] L. D. Barron, A. D. Buckingham, Molec. Phys. **1971**, 20, 1111-1119.
- [80] L. D. Barron, P. Bogaard, A. D. Buckingham, J. Amer. Chem. Soc. **1973**, 95, 603-605.
- [81] W. Hug, S. Kint, G. F. Bailey, J. R. Scherer, J. Am. Chem. Soc. **1975**, 97, 5589-5590.
- [82] W. Hug, H. Surbeck, Chem. Phys. Lett. **1979**, 60, 186-192.
- [83] L. D. Barron, L. Hecht, W. Hug, M. J. MacIntosh, J. Am. Chem. Soc. **1989**, 111, 8731-8732.
- [84] L. A. Nafie, T. B. Freedman, Chem. Phys. Lett. **1989**, 154, 260-266.
- [85] D. Che, L. Hecht, L. A. Nafie, Chem. Phys. Lett. **1991**, 180, 182-190.
- [86] W. Hug, G. Hangartner, J. Raman Spectrosc. **1999**, 30, 841-852.
- [87] W. Hug, Appl. Spectrosc. **2003**, 57, 1-13.
- [88] G. Li, Doctoral Thesis, **2023**.
- [89] G. Holzwarth, E. C. Hsu, H. S. Mosher, T. R. Faulkner, A. Moscowitz, J. Am. Chem. Soc. **1974**, 96, 251-252.
- [90] L. A. Nafie, J. C. Cheng, P. J. Stephens, J. Am. Chem. Soc. **1975**, 97, 3842-3843.
- [91] L. A. Nafie, T. A. Keiderling, P. J. Stephens, J. Am. Chem. Soc. **1976**, 98, 2715-2723.
- [92] L. A. Nafie, M. Diem, D. W. Vidrine, J. Am. Chem. Soc. **1979**, 101, 496-498.
- [93] E. D. Lipp, C.G. Zimba, L. A. Nafie, Chem. Phys. Lett. **1982**, 90, 1-5.
- [94] T. A. Keiderling, Chem. Rev. **2020**, 120, 3381-3419.

- [95] C. Merten, F. Li, K. Bravo-Rodriguez, E. Sanchez-Garcia, Y. Xu, W. Sander, *Phys. Chem. Chem. Phys.* **2014**, 16, 5627-5633.
- [96] C. Merten, C. J. Berger, R. McDonald, Y. Xu, *Angew. Chem. Int. Ed.* **2014**, 53, 9940-9943.
- [97] H. Sato, *Phys. Chem. Chem. Phys.* **2020**, 22, 7671-7679.
- [98] Y. Yang, J. Cheramy, Y. Xu, *ChemPhysChem* **2021**, 22, 1336-1343.
- [99] A. S. Perera, J. Cheramy, M. R. Poopari, Y. Xu, *Phys. Chem. Chem. Phys.* **2019**, 21, 3574-3584.
- [100] C. Merten, Y. Xu, *ChemPhysChem* **2013**, 14, 213-219.
- [101] M. G. Gore, *Spectrophotometry and Spectrofluorimetry: A Practical Approach*; New York, **2000**.
- [102] S. Ghidinelli, S. Abbate, J. Koshoubu, Y. Araki, T. Wada, G. Longhi, *J. Phys. Chem B* **2020**, 124, 4512-4526.
- [103] K. Le Barbu-Debus, J. Bowles, S. Jähnigen, C. Clavaguéra, F. Calvo, R. Vuilleumier, A. Zehnacker, *Phys. Chem. Chem. Phys.* **2020**, 22, 26047-26068.
- [104] Y. Zhang, M. R. Poopari, X. Cai, A. Savin, Z. Dezhahang, J. Cheramy, Y. Xu, *J. Nat. Prod.* **2016**, 79, 1012-1023.
- [105] M. R. Poopari, Z. Dezhahang, Y. Xu, *Phys. Chem. Chem. Phys.* **2013**, 15, 1655-1665.
- [106] C. Merten, R. McDonald, Y. Xu, *Inorg. Chem.* **2014**, 53, 3177-3182.
- [107] C. Merten, Y. Xu, *Dalton Trans.* **2013**, 42, 10572-10578.
- [108] M. R. Poopari, Z. Dezhahang, Y. Xu, *Spectrochim. Acta Mol. Biomol. Spectrosc.* **2013**, 136, 131-140.
- [109] M. R. Poopari, Z. Dezhahang, G. Yang, Y. Xu, *ChemPhysChem* **2012**, 13, 2310-2321.
- [110] P. Zhu, G. Yang, M. R. Poopari, Z. Bie, Y. Xu, *ChemPhysChem* **2012**, 13, 1272-1281.

- [111] E. Machalska, G. Zajac, M. Baranska, D. Kaczorek, R. Kawęcki, P. F. Lipiński, J. E. Rode, J. C. Dobrowolski, *Chem. Sci.* **2021**, 12, 911-916.
- [112] D. A. Case, T. A. Darden, T. E. Cheatham III, C. L. Simmerling, J. Wang, R. E. Duke, R. Luo, R. C. Walker, W. Zhang, K. M. Merz, B. Roberts, B. Wang, S. Hayik, A. Roitberg, G. Seabra, I. Kolossváry, K. F. Wong, F. Paesani, J. Vanicek, J. Liu, X. Wu, S. R. Brozell, T. Steinbrecher, H. Gohlke, Q. Cai, X. Ye, J. Wang, M.-J. Hsieh, G. Cui, D. R. Roe, D. H. Mathews, M. G. Seetin, C. Sagui, V. Babin, T. Luchko, S. Gusarov, A. Kovalenko, P. A. Kollman, AMBER 11, University of California, San Francisco, **2010**.
- [113] M. R. Poopari, P. Zhu, Z. Dezhahang, Y. Xu, *J. Chem. Phys.* **2012**, 137, 194308.
- [114] M. Losada, P. Nguyen, Y. Xu, *J. Phys. Chem. A* **2008**, 112, 5621-5627.
- [115] P. Pracht, F. Bohle, S. Grimme, *Phys. Chem. Chem. Phys.* **2020**, 22, 7169-7192.
- [116] S. Grimme, C. Bannwarth, P. Shushkov, *J. Chem. Theory Comput.* **2017**, 13, 1989-2009.
- [117] A. S. Hazrah, A. Insausti, J. Ma, M. H. Al-Jabiri, W. Jäger, Y. Xu, *Angew. Chem. Int. Ed.* **2023**, 62, e202310610.
- [118] F. Xie, M. Fusè, A. S. Hazrah, W. Jäger, V. Barone, Y. Xu, *Angew. Chem. Int. Ed.* **2020**, 59, 22427-22430.
- [119] S. Oswald, N. A. Seifert, F. Bohle, M. Gawrilow, S. Grimme, W. Jäger, Y. Xu, M. A. Suhm, *Angew. Chem. Int. Ed.* **2019**, 58, 5080-5084.
- [120] F. Xie, N. A. Seifert, M. Heger, J. Thomas, W. Jäger, Y. Xu, *Phys. Chem. Chem. Phys.* **2019**, 21, 15408-15416.
- [121] N. A. Seifert, J. Thomas, W. Jäger, Y. Xu, *Phys. Chem. Chem. Phys.* **2018**, 20, 27630-27637.
- [122] F. Xie, X. Ng, N. A. Seifert, J. Thomas, W. Jäger, Y. Xu, *J. Chem. Phys.* **2018**, 149, 224306.
- [123] F. Xie, N. A. Seifert, W. Jäger, Y. Xu, *Angew. Chem. Int. Ed.* **2020**, 59, 15703-15710.

- [124] T. Wu, J. Kapitan, V. Masek, P. Bour, *Angew. Chem., Int. Ed.* **2015**, 54, 14933-14936.
- [125] H. Wang, M. Heger, M. H. Al-Jabiri, Y. Xu, *Molecules*, **2022**, 27, 38.
- [126] A. N. Mort, F. Xie, A. S. Hazrah, Y. Xu, *Phys. Chem. Chem. Phys.* **2023**, 25, 16264-16272.
- [127] C. Bannwarth, S. Ehlert, S. Grimme, *J. Chem. Theory Comput.* **2019**, 15, 1652-1671.
- [128] S. Spicher, S. Grimme, *Angew. Chem., Int. Ed.* **2020**, 59, 15665-15673
- [129] F. Weigend, R. Ahlrichs, *Phys. Chem. Chem. Phys.* **2005**, 7, 3297-3305.
- [130] D. G. A. Smith, L. A. Burns, K. Patkowski, C. D. Sherrill, *J. Phys. Chem. Lett.* **2016**, 7, 2197-2203.
- [131] S. Grimme, J. Antony, S. Ehrlich, H. Krieg, *J. Chem. Phys.* **2010**, 132, 154104.
- [132] H-J. Werner, P. J. Knowles, G. Knizia, F. R. Manby, M. Schütz, *Molpro: WIREs Comput. Mol. Sci.* **2012**, 2, 242-253.
- [133] Gaussian 16, Revision C.01, M. J. Frisch, G. W. Trucks, H. B. Schlegel, G. E. Scuseria, M. A. Robb, J. R. Cheeseman, G. Scalmani, V. Barone, G. A. Petersson, H. Nakatsuji, X. Li, M. Caricato, A. V. Marenich, J. Bloino, B. G. Janesko, R. Gomperts, B. Mennucci, H. P. Hratchian, J. V. Ortiz, A. F. Izmaylov, J. L. Sonnenberg, D. Williams-Young, F. Ding, F. Lipparini, F. Egidi, J. Goings, B. Peng, A. Petrone, T. Henderson, D. Ranasinghe, V. G. Zakrzewski, J. Gao, N. Rega, G. Zheng, W. Liang, M. Hada, M. Ehara, K. Toyota, R. Fukuda, J. Hasegawa, M. Ishida, T. Nakajima, Y. Honda, O. Kitao, H. Nakai, T. Vreven, K. Throssell, J. A. Montgomery, Jr., J. E. Peralta, F. Ogliaro, M. J. Bearpark, J. J. Heyd, E. N. Brothers, K. N. Kudin, V. N. Staroverov, T. A. Keith, R. Kobayashi, J. Normand, K. Raghavachari, A. P. Rendell, J. C. Burant, S. S. Iyengar, J. Tomasi, M. Cossi, J. M. Millam, M. Klene, C. Adamo, R. Cammi, J. W. Ochterski, R. L. Martin, K. Morokuma, O. Farkas, J. B. Foresman, D. J. Fox, *Gaussian, Inc., Wallingford CT*, **2016**.

- [134] F.C. Asogwa, E.C. Agwamba, H. Louis, M.C. Muozie, I. Benjamin, T.E. Ger, G.E. Mathias, A.S. Adeyinka, A.I. Ikeuba. *Chem. Phys. Impact.* **2022**, 5, 100091.
- [135] S. Grimme, S. Ehrlich, L. Goerigk, *J. Comput. Chem.* **2011**, 32, 1456-1465.
- [136] A. D. Becke, E. R. Johnson, *J. Chem. Phys.* **2005**, 123, 154101.
- [137] M. A. S. Yokomichi, H. R. L. Silva, L. E. V. N. Brandao, E. F. Vicente, J. M. Batista Jr, *Org. Biomol. Chem.* **2022**, 20, 1306-1314
- [138] L. A. Warning, A. R. Miandashti, L. A. McCarthy, Q. Zhang, C. F. Landes, S. Link, *ACS Nano* **2021**, 15, 15538-15566.
- [139] L. Xu, X. Wang, W. Wang, M. Sun, W. J. Choi, J.-Y. Kim, C. Hao, S. Li, A. Qu, M. Lu, X. Wu, F. M. Colombari, W. R. Gomes, A. L. Blanco, A. F. de Moura, X. Guo, H. Kuang, N. A. Kotov, C. Xu, *Nature* **2022**, 601, 366-373.
- [140] T. Yasukawa, S. Kobayashi, *Chiral Metal Nanoparticles for Asymmetric Catalysis*. *Chiral Metal Nanoparticles for Asymmetric Catalysis BT - Nanoparticles in Catalysis*; Kobayashi, S., Ed.; Springer International Publishing: Cham, **2020**.
- [141] R. Jin, T. Higaki, *Commun. Chem.* 2021, 4, 28.
- [142] Y. Jin, C. Zhang, X.-Y. Dong, S.-Q. Zang, T. C. W. Mak, *Chem. Soc. Rev.* **2021**, 50, 2297-2319.
- [143] Z. Lei, X. K. Wan, S. F. Yuan, Z. J. Guan, Q. M. Wang, *Acc. Chem. Res.* **2018**, 51, 2465-2474.
- [144] S. Takano, T. Tsukuda, *J. Am. Chem. Soc.* **2021**, 143, 1683-1698.
- [145] I. Dolamic, S. Knoppe, A. Dass, T. Bürgi, *Nat. Commun.* **2012**, 3, 798.
- [146] L. -J. Liu, F. Alkan, S. Zhuang, D. Liu, T. Nawaz, J. Guo, X. Luo, J. He, *Nat. Commun.* **2023**, 14, 2397.

- [147] Z. Han, Y. Si, X.-Y. Dong, J.-H. Hu, C. Zhang, X.-H. Zhao, J.-W. Yuan, Y. Wang, S.-Q. Zang, *J. Am. Chem. Soc.* **2023**, 145, 6166-6176.
- [148] Y. Li, T. Higaki, X. Du, R. Jin, *Adv. Mater.* **2020**, 32, 1905488.
- [149] Y. Wang, B. Nieto-Ortega, T. Bürgi, *Nat. Commun.* **2020**, 11, 4562.
- [150] H. Yoshida, M. Kuzuhara, R. Tanibe, T. Kawai, T. Nakashima, *J. Phys. Chem. C* **2021**, 125, 27009-27015.
- [151] P. Luo, X. J. Zhai, S. Bai, Y. B. Si, X.-Y. Dong, Y. F. Han, S. Q. Zang, *Angew. Chem. Int. Ed.* **2023**, 62, e202219017.
- [152] L. Riccardi, F. De Biasi, M. De Vivo, T. Bürgi, F. Rastrelli, G. Salassa, *ACS Nano* **2019**, 13, 7127-7134.
- [153] T. A. Keiderling, *Chem. Rev.* **2020**, 120, 3381-3419.
- [154] S. Jähnigen, *Angew. Chem. Int. Ed.* **2023**, 62, e202303595.
- [155] I. Dolamic, B. Varnholt, T. Bürgi, *Nat. Commun.* **2015**, 6, 7117.
- [156] A. Sels, R. Azoulay, W. Jan Buma, M. A. J. Koenis, V. P. Nicu, T. Bürgi, *J. Phys. Chem. C* **2019**, 123, 22586-22594.
- [157] F. Xie, N. A. Seifert, M. Heger, J. Thomas, W. Jäger, Y. Xu, *Phys. Chem. Chem. Phys.* **2019**, 21, 15408-15416.
- [158] Y. Yang, M. Alshalalfeh, Y. Xu, *Spectrochim. Acta A Mol. Biomol. Spectrosc.* **2023**, 307, 12363.
- [159] H. Wang, M. Heger, M. H. Al-Jabiri, Y. Xu, *Molecules*, **2022**, 27, 38.
- [160] C. Gautier, T. Burgi, *J. Am. Chem. Soc.* **2006**, 128, 11079-11087.
- [161] C. Gautier, T. Burgi, *J. Phys. Chem. C* **2010**, 114, 15897-15902.

- [162] L. Riccardi, F. De Biasi, M. De Vivo, T. Bürgi, F. Rastrelli, G. Salassa, *ACS Nano*. **2019**, 13, 7127-7134.
- [163] C. Gautier, T. Burgi, *Chem. Commun.* **2005**, 21, 5393-5395.
- [164] L. A. Nafie, *Vibrational optical activity: Principles and applications*, Wiley, Chichester, **2011**.
- [165] T. Keiderling, *Chem. Rev.* **2020**, 120, 3381-3419.
- [166] J. Bogaerts, F. Desmet, R. Aerts, P. Bultinck, W. Herrebout, C. Johannessen, *Phys. Chem. Chem. Chem. Phys.* **2020**, 22, 18014-18024.
- [167] T. Wu, R. Pelc, P. Bouř, *Chem. Plus. Chem.* **2023**, 88, e202300385.
- [168] A. Kolodziejczyk, L. A. Nafie, A. Wajda, A. Kaczor, *Chem. Commun.* **2023**, 59, 10793-10796.
- [169] K. Nishikawa, R. Kuroiwa, J. Tamogami, M. Unno, T. Fujisawa, *J. Phys. Chem. B* **2023**, 127, 7244-7250.
- [170] C. Shen, M. Srebro-Hooper, T. Weymuth, F. Krausbeck, J. T. L. Navarrete, F. J. Ramírez, B. Nieto-Ortega, J. Casado, M. Reiher, J. Autschbach, J. Crassous, *Chem. Eur. J.* **2018**, 24, 15067-15079.
- [171] J. Kwon, K. H. Park, W. J. Choi, N. A. Kotov, J. Yeom, *Acc. Chem. Res.* **2023**, 56, 1359-1372.
- [172] L. E. MacKenzie, R. Pal, *Nature Rev. Chem.* **2021**, 5, 109-124.
- [173] F. Zinna, C. Resta, S. Abbate, E. Castiglioni, G. Longhi, P. Mineoe, L. Di Bari, *Chem. Commun.* **2015**, 51, 11903-11906.
- [174] B. Zercher, T. A. Hopkins, *Inorg. Chem.* **2016**, 55, 10899-10906.
- [175] C. Meinert, S. V. Hoffmann, P. Cassam-Chena, A. C. Evans, C. Giri, L. Nahon, U. J. Meierhenrich. *Angew. Chem. Int. Ed.* **2014**, 53, 210-214; *Angew. Chem.* **2014**, 126, 214-218.

- [176] Y. Imai, *Symmetry* **2020**, 12, 1786.
- [177] Q. Jin, S. Chen, Y. Sang, H. Guo, S. Dong, J. Han, W. Chen, X. Yang, F. Li, P. Duan, *Chem. Commun.* **2019**, 55, 6583-6586.
- [178] F. Richardson, H.G. Brittain, *J. Am. Chem. Soc.* **1981**, 103, 18-24
- [179] H. Okada, N. Hara, D. Kaji, M. Shizuma, M. Fujiiki, Y. Imai, *Phys. Chem. Chem. Phys.* **2020**, 22, 13862-13866.
- [180] T. Amako, K. Nakabayashi, N. Suzuki, S. Guo, N.A.A. Rahim, T. Harada, M. Fujiki, Y. Imai, *Chem. Commun.* **2015**, 51, 8237-8240.
- [181] G. Longhi, E. Castiglioni, J. Koshoubu, G. Mazzeo, S. Abbate, *Chirality*, **2016**, 28, 696-707.
- [182] G. Mazzeo, M. Fusè, A. Evidente, S. Abbate, G. Longhi, *Phys. Chem. Chem. Phys.* **2023**, 25, 22700-22710.
- [183] L. Palomo, L. Favereau, K. Senthilkumar, M. Stępień, J. Casado, F. J. Ramírez, *Angew. Chem. Int. Ed.* **2022**, 61, e202206976.
- [184] G. Li, M. Alshalalfeh, J. Kapitán, P. Bouř, Y. Xu, *Chem. Eur. J.* **2022**, e202104302 (1-12).
- [185] G. Hilmes, J. P. Riehl, *Inorg. Chem.* **1986**, 25, 2617-2622.
- [186] J. P. Riehl, G. Muller, in *Comprehensive Chiroptical Spectroscopy, Volume 1: Instrumentation, Methodologies, and Theoretical Simulations, First Edition*. Edited by N. Berova, P. L. Polavarapu, K. Nakanishi, R. W. Woody. **2012** John Wiley & Sons, Inc.
- [187] S. Yamamoto, P. Bouř, *Angew. Chem. Int. Ed.* **2012**, 51, 11058-11061; *Angew. Chem.* **2012**, 124, 11220-11223.
- [188] J. A. Koningstein, *J. Chem. Phys.* **1967**, 46, 2811-2816.
- [189] T. Wu, J. J. Kapitán, V. Mašek, P. Bouř, *Angew. Chem. Int. Ed.* **2015**, 54, 14933-14936; *Angew. Chem.* **2015**, 127, 15146-15149.

- [190] T. Wu, P. Bouř, V. Andrushchenko, *Sci. Rep.* **2019**, 9, 1-5.
- [191] M. Losada, H. Tran, Y. Xu, *J. Chem. Phys.* **2008**, 128, 014508.
- [192] A. S. Perera, J. Cheramy, C. Merten, J. Thomas, Y. Xu, *Chem.Phys.Chem.* **2018**, 19, 2234-2242.
- [193] P. Gawryszewska, G. Oczko, J. Riehl, V. Tsaryuk, J. Legendziewicz, *J. Alloys Compd.* **2004**, 380, 352-356.
- [194] T. Wu, P. Bouř, *Chem. Commun.* **2018**, 54, 1790-1792.
- [195] L.D. Barron, *Molecular Light Scattering and Optical Activity*, Cambridge University Press, Cambridge, UK, **2004**.
- [196] R. Clark, S. R. Jeyes, A. J. McCaffery, R. A. Shatwell, *J. Am. Chem. Soc.* **1974**, 96, 5586-5588.
- [197] X. F. Shan, D. H. Wang, C. H. Tung, L. Z. Wu, *Tetrahedron* **2008**, 64, 5577-5582.
- [198] P. Sosicka, B.G. Ng, H. H. Freeze, *Biochem.* **2020**, 59, 3064-3077.
- [199] J. Wang, Y. Zhang, Q. Lu, D. Xing, R. Zhang, *Front Pharmacol.* **2021**, 12, 756724.
- [200] H. B. Mayes, L. J. Broadbelt, G. T. Beckham, *J. Am. Chem. Soc.* **2014**, 136, 1008-1022.
- [201] J. N. Chythra, S. S. Mallajosyula, *J. Chem. Inf. Model.* **2023**, 63, 208-223.
- [202] J. B. Johnson, J. S. Mani, D. Broszczak, S. S. Prasad, C. P. Ekanayake, P. Strappe, P. Valeris, M. Naiker, *Phytother. Res.* **2021**, 35, 3484-3508.
- [203] S. J. Hwang, H. J. Lee, *Inflammation* **2015**, 38, 1071-1079.
- [204] M. Hu, H. Yan, Y. Fu, Y. Jiang, W. Yao, S. Yu, L. Zhang, Q. Wu, A. Ding, M. Shan, *Molecules* **2019**, 24, 547.
- [205] F. Yang, G. Li, B. Lin, K. Zhang, *J. Integr. Neurosci.* **2022**, 21, 72.

- [206] Z. Song, G. Luo, C. Han, G. Jia, B. Zhang, *Evid. Based Complement. Altern. Med.* **2022**, 2022, 3607053.
- [207] L. Li, Q. Li, L. Gui, Y. Deng, L. Wang, J. Jiao, Y. Hu, X. Lan, J. Hou, Y. Li, D. Lu, *Bioact. Mater.* **2023**, 19, 24-37.
- [208] F.O. Talbot, J. P. Simons, *Phys. Chem. Chem. Phys.* **2002**, 4, 3562-3565.
- [209] J. P. Simons, B. G. Davis, E. J. Cocinero, D. P. Gamblin, E. C. Stanca-Kaposta, *Tetrahedron: Asymmetry* **2009**, 20, 718-722.
- [210] K. Monde, T. Taniguchi, N. Miura, S.-I. Nishimura, *J. Am. Chem. Soc.* **2004**, 126, 9496-9497.
- [211] J. Cz. Dobrowolski, P. F. J. Lipiński, J. E. Rode, J. Sadlej, α -Amino Acids in Water: A Review of VCD and ROA Spectra. In *Optical Spectroscopy and Computational Methods in Biology and Medicine: Challenges and Advances in Computational Chemistry and Physics*; Baranska, M., Ed. Springer: Dordrecht, The Netherlands, **2014**.
- [212] C. Merten, F. Li, K. Bravo-Rodriguez, E. Sanchez-Garcia, Y. Xu, W. Sander, *Phys. Chem. Chem. Phys.* **2014**, 16, 5627-5633.
- [213] J. Kessler, V. Andrushchenko, J. Kapitán, P. Bouř, *Phys. Chem. Chem. Phys.* **2018**, 20, 4926-4997.
- [214] J. R. Cheeseman, M. S. Shaik, P. L. A. Popelier, E. W. Blanch, *J. Am. Chem. Soc.* **2011**, 133, 4991-4997.
- [215] E. Machalska, G. Zajac, J. E. Rode, *Acta A Mol. Biomol.* **2022**, 281, 121604.
- [216] F. Xie, M. Fusè, S. Hazrah, A. W. Jaeger, V. Barone, Y. Xu, *Angew. Chem., Int. Ed.* **2020**, 59, 22427-22430.
- [217] K. D. R. Eikås, M. T. P. Beerepoot, K. Ruud, *J. Phys. Chem. A* **2022**, 126, 5458-5471.

- [218] J. L. Alonso, M. A. Lozoya, I. Peña, J. C. López, C. Cabezas, S. Mata, S. Blanco, *Chem. Sci.* **2014**, 5, 515-522.
- [219] C. Bannwarth, E. Caldeweyher, S. Ehlert, A. Hansen, P. Pracht, J. Seibert, S. Spicher, S. Grimme, *WIREs Comput. Mol. Sci.* **2021**, 11, e1493.
- [220] A. V. Onufriev, D. A. Case, *Annu. Rev. Biophys.* **2019**, 48, 275-296.
- [221] A. D. Becke, *Phys. Rev. A* **1988**, 38, 3098-3100.
- [222] C. Lee, W. Yang, R. Parr, *Phys. Rev. B* **1988**, 37, 785-789.
- [223] D. Rappoport, F. Furche, *J. Chem. Phys.* **2010**, 133, 134105.
- [224] A. D. Becke, A. D. Johnson, *J. Chem. Phys.* **2005**, 123, 154101.
- [225] B. Xu, L. Unione, J. Sardinha, S. Wu, M. Ethve-Quellejeu, A. P. Rauter, Y. Blriot, Y. Zhang, S. Martín-Santamaría, D. Díaz, J. Jimnez-Barbero, M. Sollogoub, *Angew. Chem. Int. Ed.* **2014**, 53, 9597-9602.
- [226] I. V. Alabugin, L. Kuhn, N. V. Krivoshchapov, P. Mehaffy, M. G. Medvedev, *Chem. Soc. Rev.* **2021**, 50, 10212-10252.
- [227] R. U. Lemieux, A. A. Pavia, J. C. Martin, K. A. Watanabe, *Can. J. Chem.* **1969**, 47, 4427-4439.
- [228] K. B. Wiberg, M. Marquez, *J. Am. Chem. Soc.* **1994**, 116, 2197-2198.
- [229] S. Spicher, C. Plett, P. Pracht, A. Hansen, S. Grimme, *J. Chem. Theory Comput.* **2022**, 18, 3174-3189.
- [230] M. Thomas, B. Kirchner, *J. Phys. Chem. Lett.* **2016**, 7, 509-513.
- [231] S. Jähnigen, D. Sebastiani, R. Vuilleumier, *Phys. Chem. Chem. Phys.* **2021**, 23, 17232-17241.
- [232] M. Brehm, M. Thomas, *J. Phys. Chem. Lett.* **2017**, 8, 3409-3414.

- [233] F. Weigend, R. Ahlrichs, *Phys. Chem. Chem. Phys.* **2005**, 7, 3297-3305.
- [234] H.-J. Werner, P. J. Knowles, G. Knizia, F. R. Manby, M. Schütz, *Wires Comput. Mol. Sci.* **2012**, 2, 242-253.
- [235] B. Mennucci, J. Tomasi, R. Cammi, J. R. Cheeseman, M. J. Frisch, F. J. Devlin, S. Gabriel, P. J. Stephens, *J. Phys. Chem. A* **2002**, 106, 6102-6113.
- [236] M. Katari, E. Nicol, V. Steinmetz, G. van der Rest, D. Carmichael, G. Frison, *Chem. Eur. J.* **2017**, 23, 8414-8423.
- [237] A. Soroceanu, A. Bargan, *Crystals* **2022**, 12, 1436.
- [238] P. Ghosh, S. K. Dey, M. H. Ara, K. Karim, A. B. M. N. Islam, *Egypt. J. Chem.* **2019**, 62, 523-547.
- [239] X. Liu, C. Manzur, N. Novoa, S. Celedón, D. Carrillo, J. R. Hamon, *Coord. Chem. Rev.* **2018**, 357, 144-172.
- [240] M. K. Goshisht, N. Tripathi, *J. Mater. Chem. C* **2021**, 9, 9820-9850.
- [241] F. Faridbod, M. R. Ganjali, R. Dinarvand, P. Norouzi, *Comb. Chem. High. Throughput Screen.* **2007**, 10, 527-546.
- [242] E. Akila, M. Usharani, S. Vimala, R. Rajavel, *Chem. Sci. Rev. Lett.* **2012**, 1, 181-194.
- [243] M. Górecki, M. Enamullah, M. A. Islam, M. K. Islam, S.-P. Höfert, D. Woschko, C. Janiak, G. Pescitelli, *Inorg. Chem.* **2021**, 60, 14116-14131.
- [244] G. Pescitelli, S. Lüdeke, M. Górecki, L. D. Bari, *J. Phys. Chem. Lett.* **2019**, 10, 650-654.
- [245] Z. Dezhahang, M. R. Poopari, Y. Xu, *Chem. Asian J.* **2013**, 8, 1205-1212.
- [246] Z. Dezhahang, C. Merten, M. R. Poopari, Y. Xu, *Dalton Trans.* **2012**, 41, 10817-10824.
- [247] Y. He, X. Cao, L. A. Nafie, T. B. Freedman, *J. Am. Chem. Soc.* **2001**, 123, 11320-11321.
- [248] C. Merten, K. Hiller, Y. Xu, *Phys. Chem. Chem. Phys.* **2012**, 14, 12884-12891.

- [249] S. R. Domingos, F. Hartl, W. J. Brma, S. Woutersen, *ChemPhysChem*. **2015**, 16, 3363-3373.
- [250] S. R. Bhattacharya, T. Bürgi, *Nanoscale*, **2019**, 11, 23226-23233.
- [251] L. A. Nafie, *J. Phys. Chem. A* **2004**, 108, 7222-7231.
- [252] Y. He, Doctoral Thesis, **2005**.
- [253] J. L. Alonso, M. Lozoya, I. Peña, J. C. López, C. Cabezas, S. Mata, S. Blanco, *Chem. Sci.* **2014**, 5, 515-522.
- [254] C. D. Carlson, A. S. Hazrah, D. Mason, Q. Yang, N. A. Seifert, Y. Xu, *J. Phys. Chem. A* **2022**, 126, 7250-7260.
- [255] M. J. Frisch, et al., *Gaussian 16; Revision C.03; Gaussian, Inc.: Wallingford, CT, USA*, **2019**.
- [256] G. Pescitelli, S. Lüdeke, A.-C. Chamayou, M. Marolt, V. Justus, M. Górecki, L. Arrico, L. Di Bari, M. A. Islam, I. Gruber, *Inorg. Chem.* **2018**, 57, 13397-13408.
- [257] P. R. Lassen, Doctoral Thesis. **2006**.
- [258] M. A. Hitchman, *Inorg. Chem.* **1977**, 16, 1985-1993.
- [259] M. Enamullah, A. R. Uddin, G. Pescitelli, R. Berardozzi, G. Makhloufi, V. Vasylyeva, A.-C. Chamayou and C. Janiak, *Dalton Trans.* **2014**, 43, 3313-3329.
- [260] C. F. Smura, D. R. Parker, M. Zbiri, M. R. Johnson, Z. A. Ga'l, S. J. Clarke, *J. Am. Chem. Soc.* **2011**, 133, 2691-2705.
- [261] S. Izadnia, A. C. LaForge, F. Stienkemeier, J. R. Cheeseman, J. Bloino, J. Cheramy, W. Jäger, Y. Xu, *Phys. Chem. Chem. Phys.* **2021**, 23, 13862-13872.
- [262] L. Kabalan, S. F. Matar, M. Zakhour, J. F. Letard, *Z. Naturforsch. B*, **2008**, 63, 154-160.
- [263] S. Kaviani, M. Izadyar, M. R. Housaindokht, *Polyhedron* **2016**, 117, 623-627.
- [264] A. Ould-Hamouda, B. Viquerat, J. Degert, S.F. Matar, J.-F. Létard, F. Guillaume, E. Freysz, *Eur. J. Inorg. Chem.* **2018**, 2018, 385-393.

- [265] J. Tomeček, P. Bouř, *J. Chem. Theory Comput.* **2020**, 16, 2627-2634.
- [266] B. Kaya, D. Akyüz, T. Karakurt, O. Şahin, A. Koca, B. Ülküseven, *Appl. Organomet. Chem.* **2020**, 34, e5930.
- [267] Z. Han, X. L. Zhao, P. Peng, S. Li, C. Zhang, M. Cao, K. Li, Z. Y. Wang, S. Q. Zang, *Nano Res.* **2020**, 13, 3248-3252.
- [268] Y.-J. Kong, J.-H. Hu, X.-Y. Dong, Y. Si, Z.-Y. Wang, X.-M. Luo, H.-R. Li, Z. Chen, S.-Q. Zang, T. C. W. Mak, *J. Am. Chem. Soc.* **2022**, 144, 19739-19747.
- [269] M. M. Zhang, X. Y. Dong, Z. Y. Wang, X. M. Luo, J. H. Huang, S. Q. Zang, T. C. W. Mak, *J. Am. Chem. Soc.* **2021**, 143, 6048-6053.
- [270] Z. Han, Y. Si, X. Y. Dong, J. H. Hu, C. Zhang, X. H. Zhao, J. W. Yuan, Y. Wang, S. O. Zang, *J. Am. Chem. Soc.* **2023**, 145, 6166- 6176.

Appendix A: Supporting Information for Chapter 3

Experimental Procedures

Ligands and Clusters Synthesis

The chiral ligands (L/D, and PL/PD), the silver clusters $\text{Ag}_6\text{L}_6/\text{D}_6$ and $\text{Ag}_6\text{PL}_6/\text{PD}_6$, and the copper clusters $\text{Ag}_6\text{L}_6/\text{D}_6$ and $\text{Ag}_6\text{PL}_6/\text{PD}_6$ were synthesized as described in collected from Prof. Zang's research group. The ligands and clusters were synthesized according to the literature (Ref. 55). First, the (S/R)-2-amino- 3-methyl-1-butanol was used to prepare the L/D ligand, and (S/R)-2-phenylglycinol was used to prepare the second chiral ligand (PL/PD). The two pairs of the silver clusters enantiomers $\text{Ag}_6\text{L}_6/\text{D}_6$ and $\text{Ag}_6\text{PL}_6/\text{PD}_6$ were prepared by the simple reactions of ligands with the silver nitrate (AgNO_3) as a precursor in the mixture of solvents dimethylacetamide/acetonitrile (DMAc/ CH_3CN).

IR and VCD spectroscopy

The IR and vibrational circular dichroism (VCD) spectra were recorded using a Fourier transform (FT) IR spectrometer Vertex 70 (Bruker) equipped with a VCD module PMA 50 (Bruker). A linear polarizer and a 50 kHz ZnSe photoelastic modulator (PEM) were used. A low pass filter with a cutting wavenumber $<1800\text{ cm}^{-1}$ put in the front of the PEM to enhance the signal /noise ratio. The absorption signals were detected using a liquid nitrogen-cooled MCT infrared detector with a BaF_2 window.

All IR and VCD spectra of the Ligands and clusters were collected in the CDCl_3 solvent since it is the only common solvent for all samples. We employed a ligand concentration of 0.4M and a cluster concentration of 0.01M, with an accumulation time 2 hours, and path length of 50 μm , except the cluster $\text{Ag}_6\text{PL}_6/\text{PD}_6$ was 100 μm , to generate an IR absorption band greater than 0.3. For Cu_6PD_6 , the measurements were done in CH_2Cl_2 with a much longer pathlength of 0.3 mm.

Background correction by subtracting solvent spectra has been carried out for the IR spectra while the VCD spectra are shown as obtained.

Methods

The conformer–rotamer ensemble sampling tool (CREST) is a quantum chemistry code developed specifically for conformational searches of flexible organic molecules. We applied CREST for comprehensive conformers research of the chiral ligands (L/D, and PL/PD), and to ensure that all conformers were generated, multiple runs with different initial geometry were used.

The CREST structural candidates of the chiral ligands were then re-optimized employing the Gaussian16 program. The DFT level of theory wb97xd/def2-TZVPD/PCM in chloroform solvent was carried out for all geometry optimizations and VCD frequency calculations of the chiral ligands. In addition, for the silver atoms an effective core potential (ECP) was used, the geometry optimization and harmonic frequency calculations of the silver clusters were performed using the hybrid functional b3pw91 combined with Grimme's dispersion correction (GD3), Becke–Johnson damping (BJ) and LANL2DZ basis set for the Ag and 6-31G(d) for all other atoms, with PCM in chloroform solvent.

The reported IR and VCD harmonic frequencies were uniformly scaled with a scaling factor of 0.975 for comparison with the experimental result. The IR and VCD spectra were created from the Gauss view program using the half-width at half-maximum (HWHM) of 4 cm^{-1} .

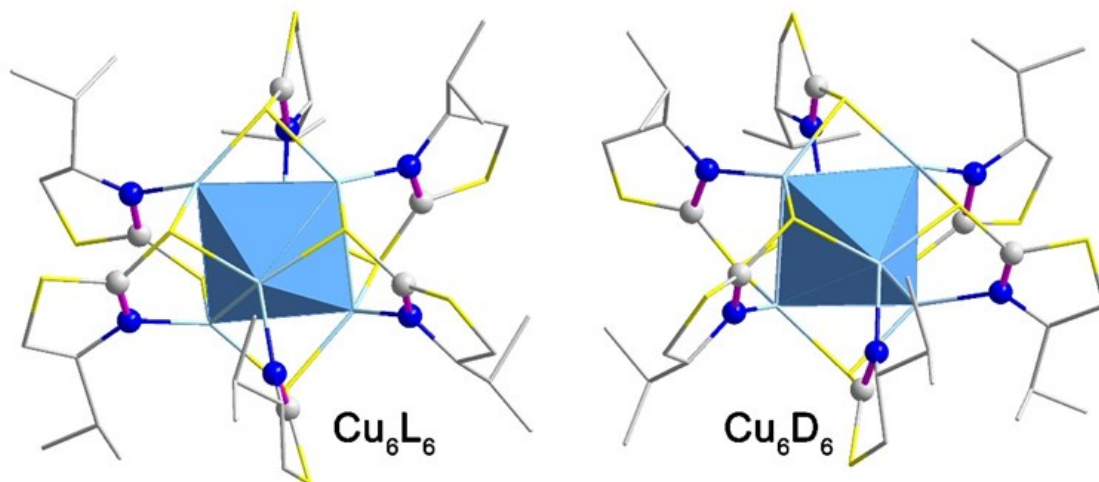


Figure A1. The ordered arrangement of ligands around the Cu_6 skeleton in Cu_6L_6 and Cu_6D_6 , derived from the final optimization geometry.

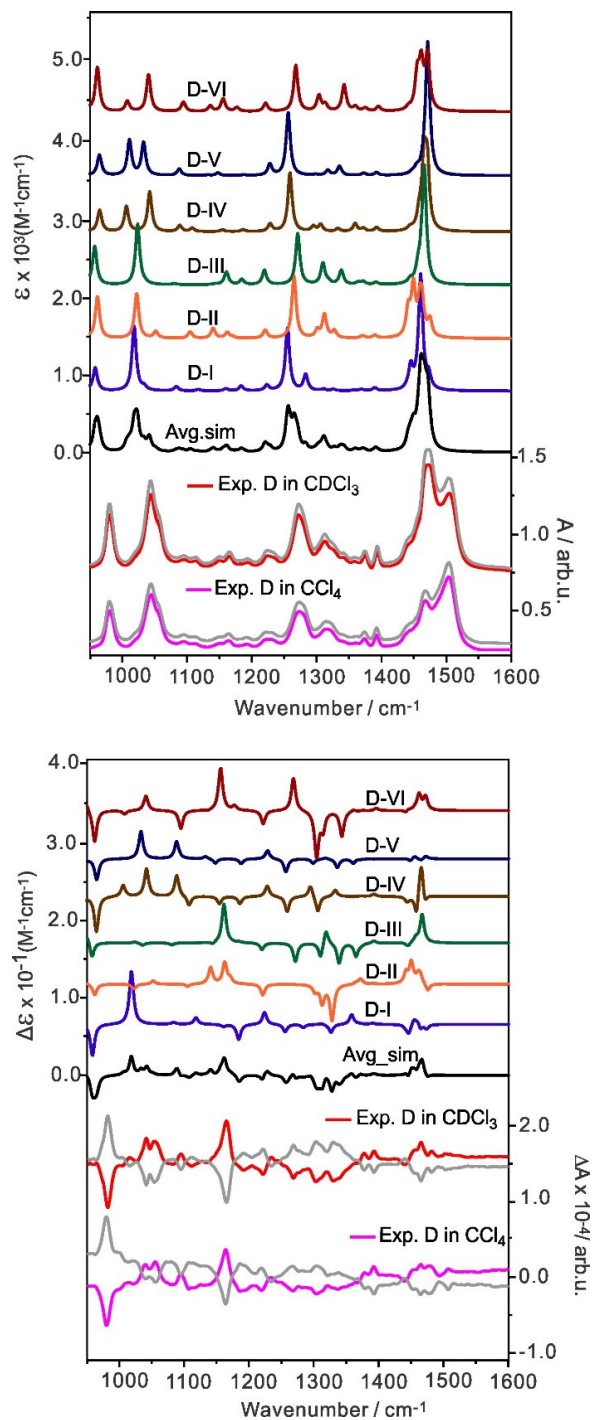


Figure A2. Comparison of the experimental and simulated IR (top) and VCD (bottom) spectra of L/D and L in CDCl_3 . The individual conformer IR and VCD spectra, as well as their Boltzmann weighted spectra at the B3LYP- GD3BJ/def2-TZVPD/PCM are shown. The gray spectrum represents the ligand enantiomer L.

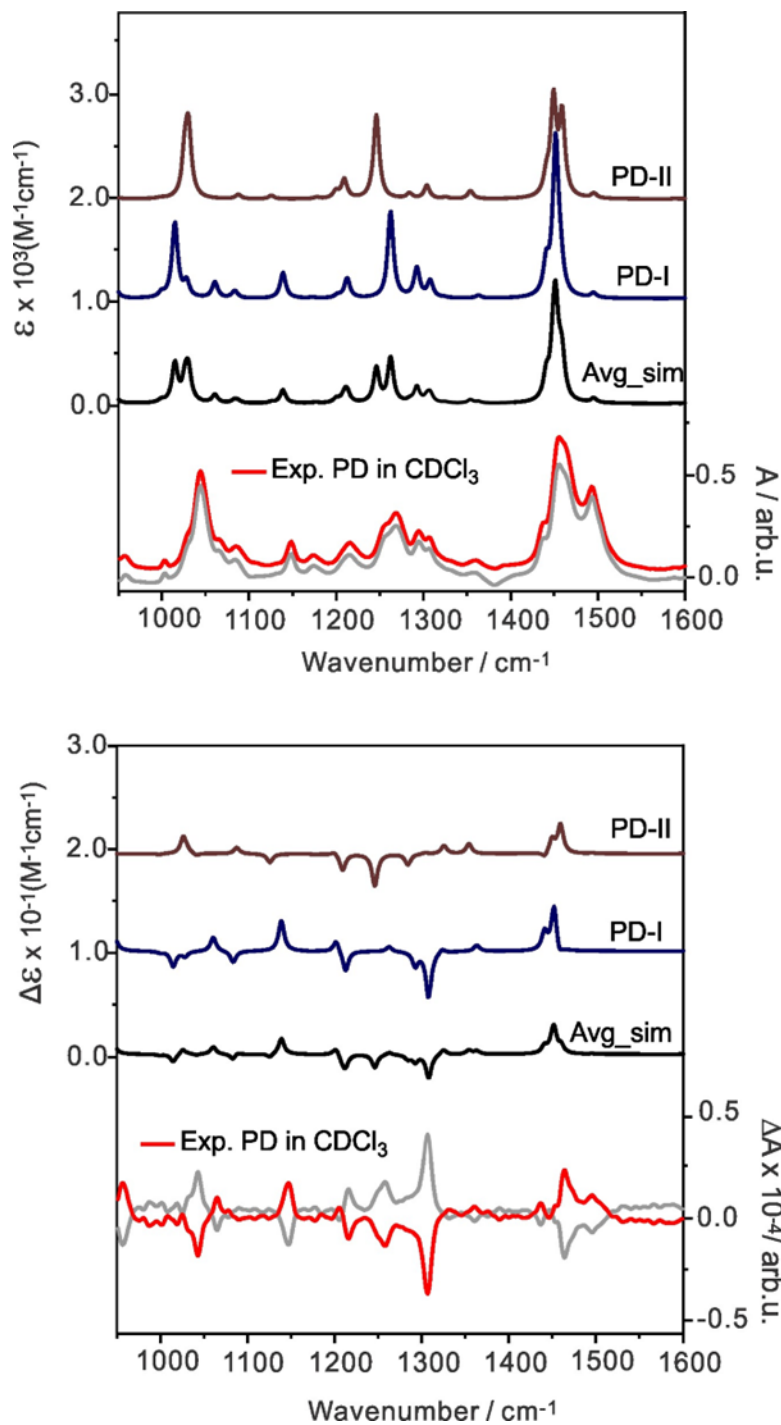


Figure A3. Comparison of the experimental and simulated IR (top) and VCD (bottom) spectra of PD in CDCl_3 . The corresponding experimental IR and VCD spectra of PL in CDCl_3 are given in grey colour. The individual conformer IR and VCD spectra, as well as their Boltzmann weighted spectra at the at the B3LYP- GD3BJ/def2-TZVPD/PCM are shown.

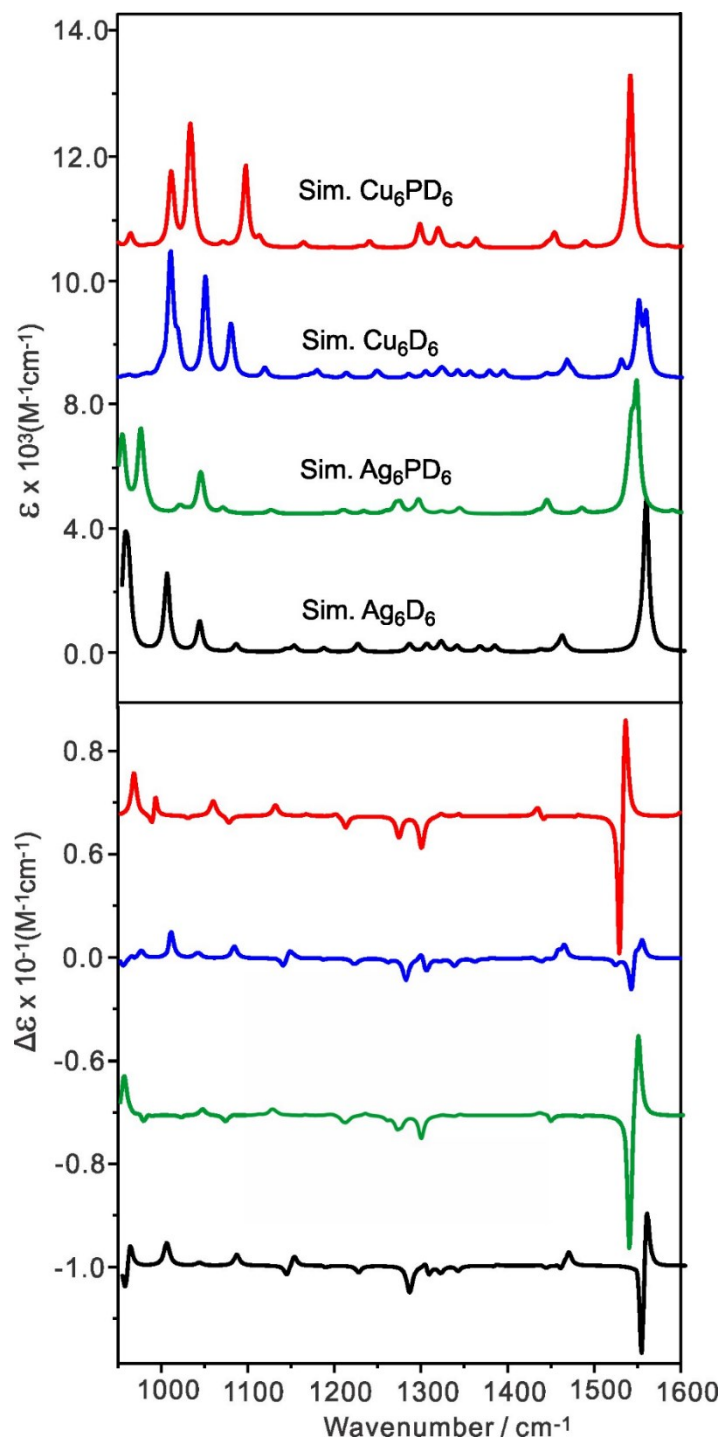


Figure A4. Comparison of the simulated IR and VCD spectra of Cu₆PD₆, Cu₆D₆, Ag₆PD₆, and Ag₆D₆. The geometry optimizations and the IR and VCD simulations were carried out at the B3PW91-D3BJ/6-31G(d) (LanL2DZ for Cu and Ag) level.

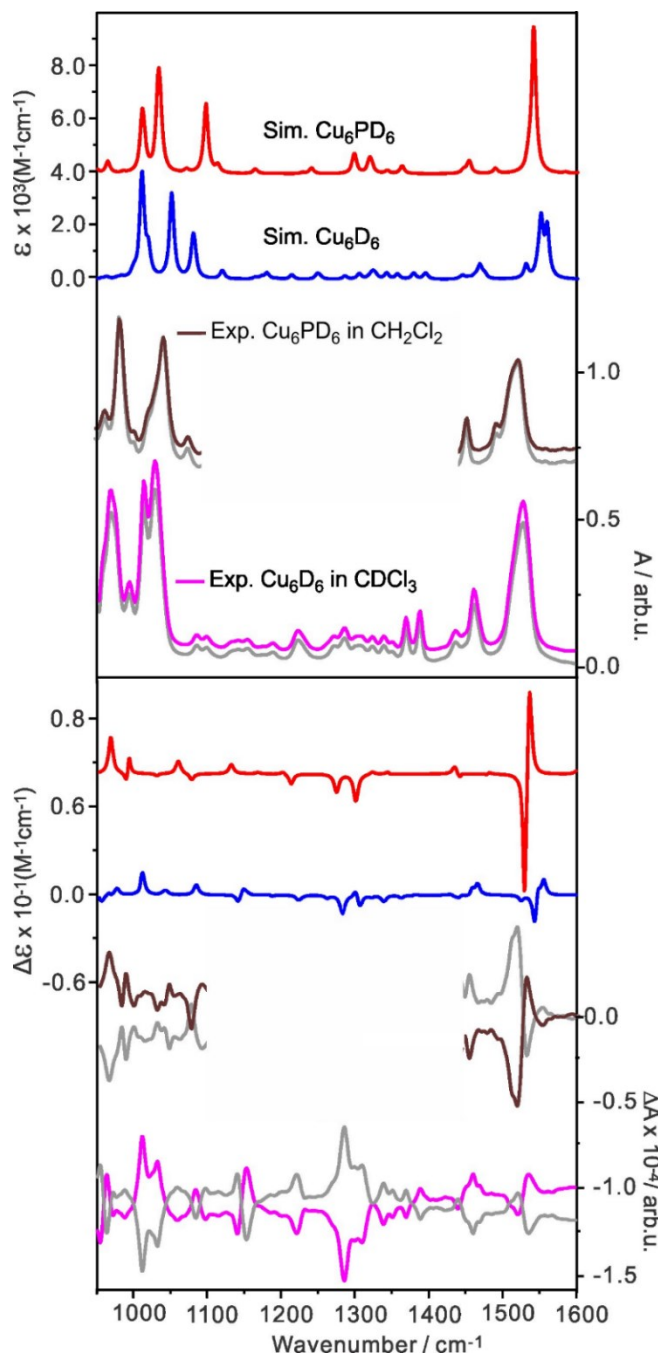


Figure A5. Comparison of the simulated and the experimental IR and VCD spectra of Cu_6PD_6 and Cu_6D_6 . The corresponding experimental IR and VCD spectra of Cu_6PL_6 and Cu_6L_6 are given in grey colour. The geometry optimizations and the IR and VCD simulations were carried out at the B3PW91-D3BJ/6-31G(d) (LanL2DZ for Cu) level.

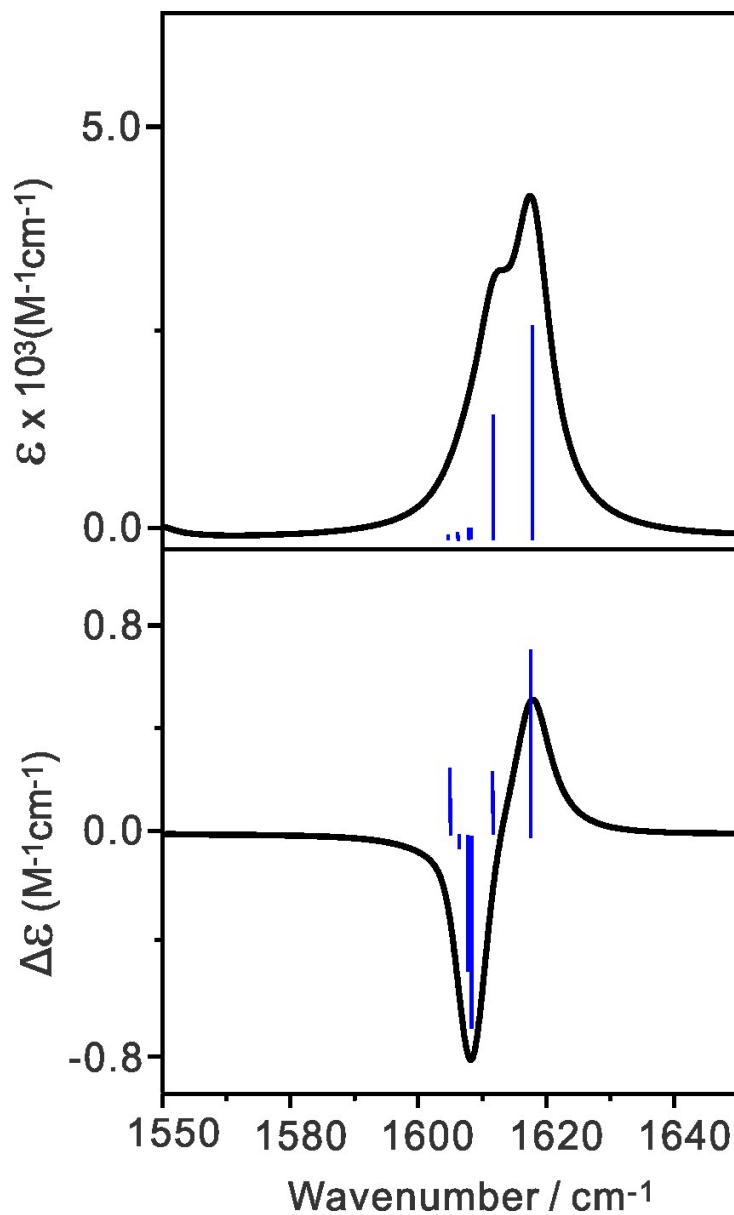


Figure A6. The zoom-in exciton section showing the exciton coupling of the bisignate bands of the six C=N stretching modes which are presented by the blue sticks. It is interesting to note that drastically different IR and VCD intensities of these modes. Some have greatly enhanced g factors.

Appendix B: Supporting Information for Chapter 4

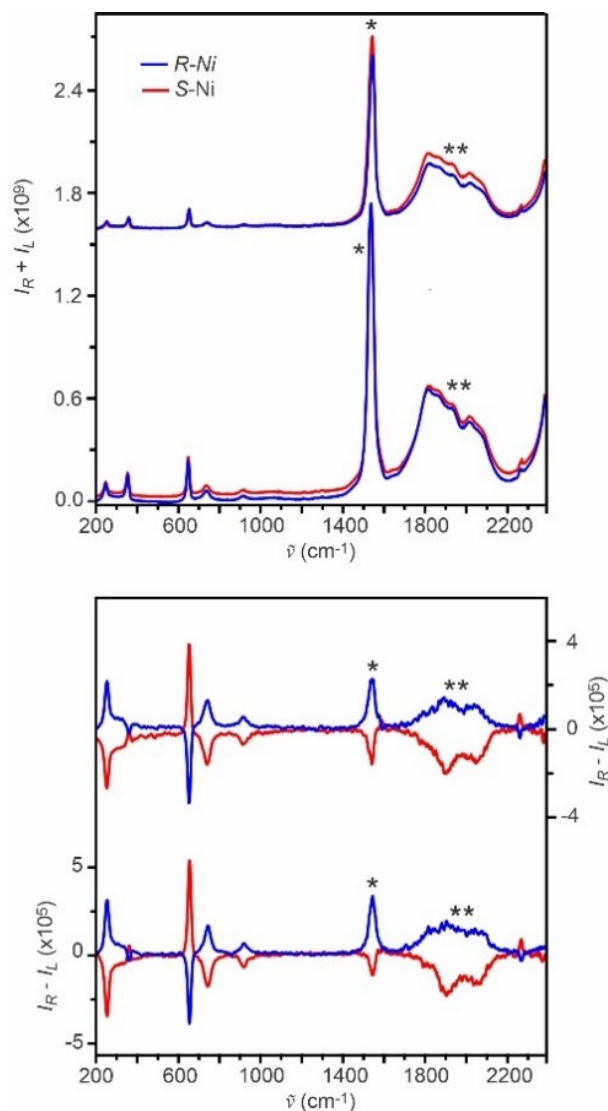


Figure B1. $I_R + I_L$ (top) and $I_R - I_L$ (bottom) spectra of the racemic $\text{Eu}(\text{FOD})_3$ and the chiral Ni complex solutions with a constant concentration of racemic $\text{Eu}(\text{FOD})_3$ (19.1 mM) in CDCl_3 with the standard one-cell experimental setup. The concentrations of S - or R -Ni are 7.6 mM (top) and 3.8 mM (bottom). Please see the main text for discussion on the intensities of the Eu species (marked by asterisks).

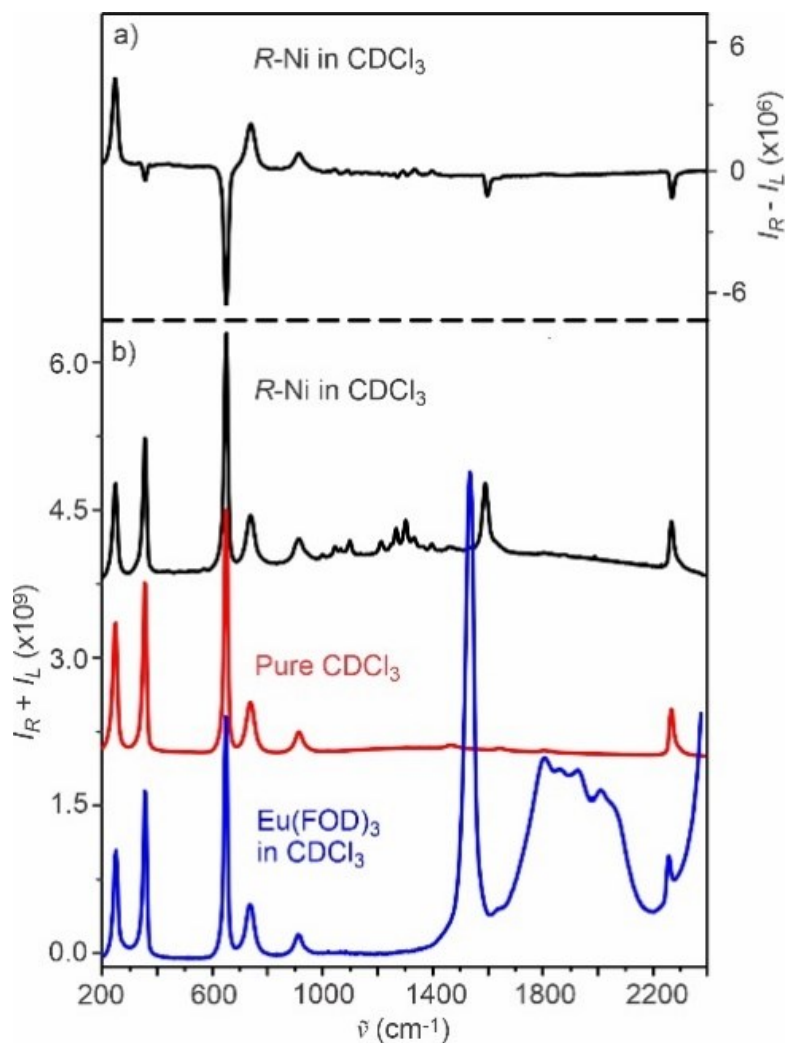


Figure B2. These are the standard one-cell experimental data. Top: $I_R - I_L$ (top) spectrum of $R\text{-Ni}$ (8.3 mM) in CDCl_3 . Bottom: $I_R + I_L$ spectra of $R\text{-Ni}$ (8.3 mM) in CDCl_3 , pure CDCl_3 , and $\text{Eu}(\text{FOD})_3$ (4.6 mM) in CDCl_3 . From the $I_R + I_L$ spectra, one can see no visible change to the band positions of CDCl_3 .

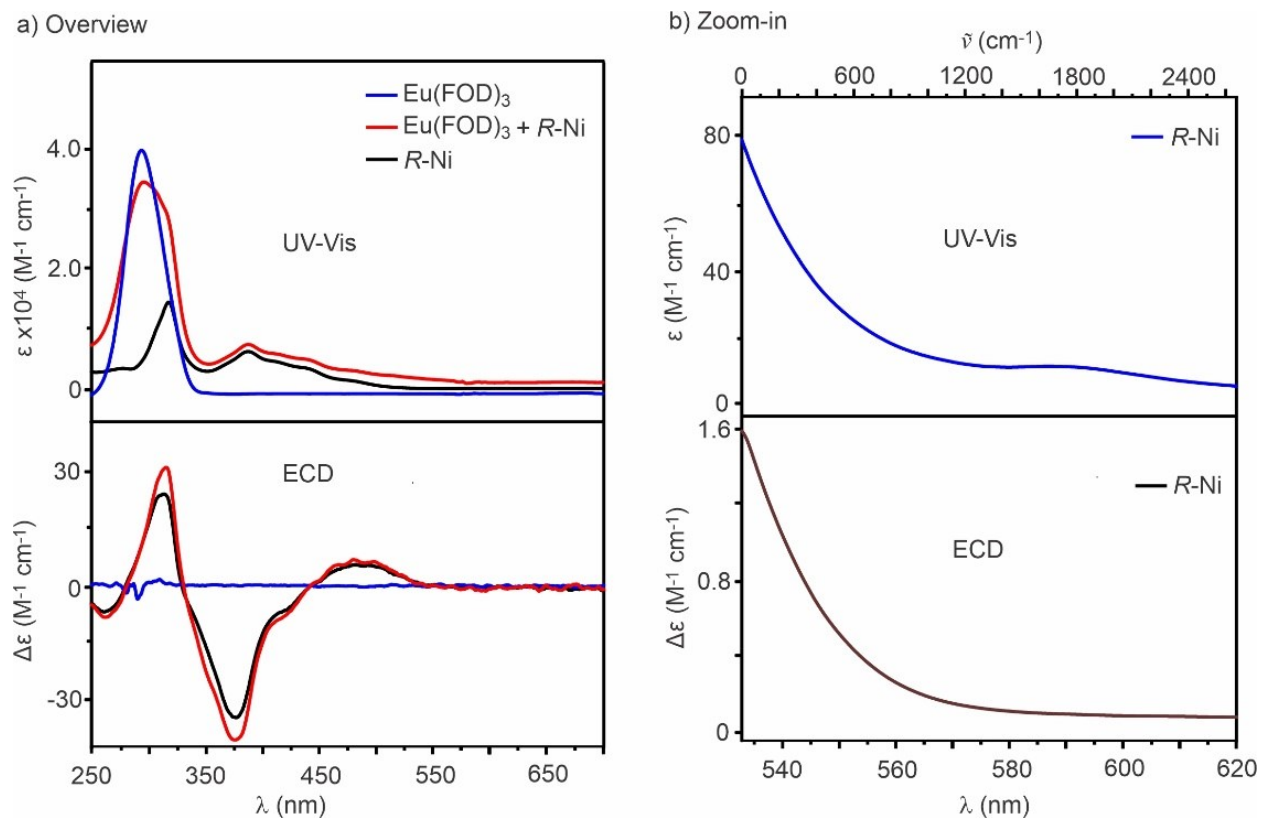


Figure B3. a) UV-Vis (top) and ECD (bottom) spectra of racemic Eu(FOD)₃ (0.77 mM, blue), *R*-Ni (0.31 mM, black), and a mixture (red) of Eu(FOD)₃ and *R*-Ni (0.38 mM, 0.16 mM, red) in CDCl₃. The path length used is 1 mm. The intensities for only *R*-Ni and only Eu(FOD)₃ solutions were scaled by a factor of 0.5 for easy comparison. b) The UV-Vis (blue) and ECD (black) spectra from 532 nm to 620 nm of *R*-Ni (9.2 mM) in CDCl₃, corresponding to the relevant Raman range from 0-2668 cm⁻¹ (see the Raman axis at the top). The path length used is 10 mm.

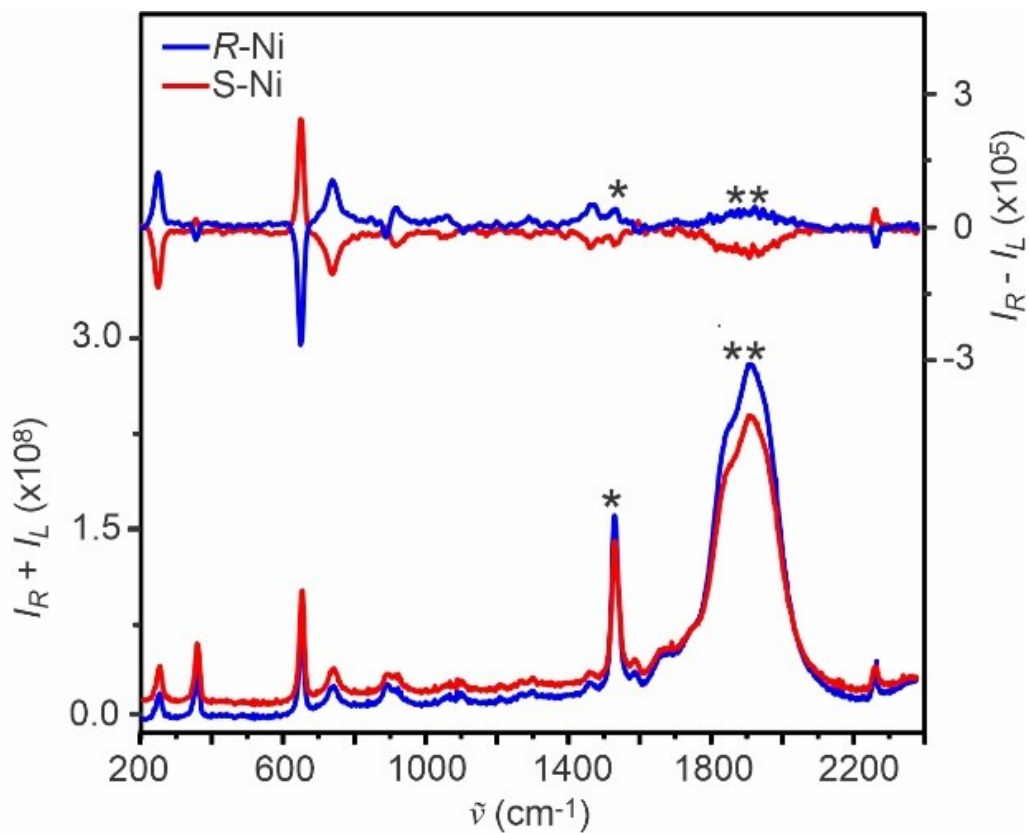


Figure B4. Two-cell $I_R + I_L$ (top) and $I_R - I_L$ (bottom) spectra of the achiral EuCl_3 solutions with a concentration of 7.6 mM of S- and R-Ni in CDCl_3 in Cell 1. The concentration of a chiral EuCl_3 in ethanol in Cell 2 is 38 mM. Asterisk * and ** indicates the sharp Eu band at $\sim 1524 \text{ cm}^{-1}$ and the broad Eu features in the $1800\text{--}2200 \text{ cm}^{-1}$ region.

Table B 1. The experimental dissymmetric $g_{\text{dis}} = (I_R - I_L) / (I_R + I_L)$ factors of the vibrational bands of *R*-Ni and Eu(FOD)₃ in CDCl₃ with the one-cell setup.

Vibrational Bands ν (cm ⁻¹)	Assigned Species	Experimental ($g_{\text{dis}} * 10^{-3}$) ¹				
		Concentrations in mM of Eu(FOD) ₃ : <i>R</i> -Ni				
		0 : 7.6	4.9 : 7.6	9.5 : 7.6	19.1 : 7.6	19.1 : 3.8
1582	<i>R</i> -Ni	-0.96	NA ²	NA ²	-0.54 ²	NA ²
1531	Eu(FOD) ₃	---	0.20	0.19	0.21	0.17
1893	Eu(FOD) ₃	---	0.38	0.38	0.40	0.30
2008	Eu(FOD) ₃	---	0.38	0.45	0.50	0.30
246	CDCl ₃	4.67	5.36	4.96	5.67	3.40
351	CDCl ₃	-0.67	-0.75	-0.70	-0.86	-0.41
647	CDCl ₃	-3.15	-3.50	-2.90	-3.90	-1.80
735	CDCl ₃	3.46	4.27	4.00	.48	2.56
907	CDCl ₃	3.25	2.81	2.84	2.81	1.71
2257	CDCl ₃	-2.21	-2.34	-2.19	-1.95	-0.95

¹ The estimated error is $\sim 0.02 * 10^{-3}$ based on the three repeated experiments.

² It is very difficult to calculate the CID value of *R*-Ni in the mixed solutions with Eu(FOD)₃ because the strong Eu(FOD)₃ luminescence band overlaps severely with the Ni Raman band. This value is given to demonstrate the correct sign and rough magnitude.

Table B2. The experimental dissymmetric $g_{\text{dis}} = (I_R - I_L) / (I_R + I_L)$ factors of the vibrational bands of *R*-Ni in CDCl₃ (Cell 1) and Eu(FOD)₃ and EuCl₃ in ethanol (Cell 2) with the two-cell setup.

Vibrational Bands ν (cm ⁻¹)	Assigned Species	Experimental ($g_{\text{dis}} * 10^{-3}$) ¹					
		Conc. (mM) of Eu(FOD) ₃ : <i>R</i> -Ni				Conc.(mM) of EuCl ₃ : <i>R</i> -Ni	
		4.9 : 7.6	9.5 : 7.6	19.1 : 7.6	19.1 : 3.8		38.1 : 7.6
Cell 1							
1582	<i>R</i> -Ni	NA ²	NA ²	NA ²	NA ²		-0.52 ²
246	CDCl ₃	4.98	5.32	5.24	3.45		5.68
351	CDCl ₃	-0.77	-0.92	-0.85	-0.48		-1.19
647	CDCl ₃	-3.06	-3.43	-3.11	-1.61		-3.43
735	CDCl ₃	0.53	0.46	0.47	0.25		0.54
907	CDCl ₃	2.50	2.89	2.66	1.48		2.26
2257	CDCl ₃	-3.42	-3.70	-3.19	-1.89		-3.13
Cell 2							
1531	Eu(FOD) ₃	0.19	0.18	0.19	0.10		---
1893	Eu(FOD) ₃	0.10	0.09	0.08	0.04		---
1524	EuCl ₃	---	---	---	---		0.20
1908	EuCl ₃	---	---	---	---		0.14
885	Ethanol	-1.33	-1.30	-1.18	-0.70		-1.16
1054	Ethanol	1.77	1.87	1.70	0.84		1.75
1095	Ethanol	-1.40	-1.53	-1.45	-0.77		-1.50
1279	Ethanol	2.07	2.75	3.20	1.51		3.30
1457	Ethanol	2.80	2.30	2.90	1.76		2.89

¹ The estimated error is $0.02 * 10^{-3}$ based on the three repeated experiments for most data except those related to ethanol which have an estimated error of $0.06 * 10^{-3}$ because of the lower signal-to-noise ratios of the ethanol bands.

² Not available because of the severe overlap between the strong Eu(FOD)₃ luminescence band and the Ni Raman band. This value with EuCl₃ is given to demonstrate the correct sign and rough magnitude.

Table B3. Comparison of the experimental and simulated dissymmetric $g_{\text{dis}} = (I_R - I_L)/(I_R + I_L)$ factors of *R*-Ni and CDCl₃ in Cell 1 and Eu(FOD)₃, EuCl₃ and ethanol in Cell 2 with the two-cell experimental setup.¹

Cell 1: <i>R</i> -Ni in CDCl ₃ and Cell 2: Eu(FOD) ₃ in ethanol				Cell 1: <i>R</i> -Ni in CDCl ₃ and Cell 2: EuCl ₃ in ethanol			
Vibrational Bands ν (cm ⁻¹)	Assigned Species	Experimental $g_{\text{dis}} * 10^{-3}$	Simulated $g_{\text{dis}} * 10^{-3}$	Vibrational Bands ν (cm ⁻¹)	Assigned Species	Experimental $g_{\text{dis}} * 10^{-3}$	Simulated $g_{\text{dis}} * 10^{-3}$
Cell 1				Cell 1			
1582	<i>R</i> -Ni	-0.57	-0.47	1582	<i>R</i> -Ni	-0.53	-0.67
246	CDCl ₃	5.24	5.31	246	CDCl ₃	5.68	5.47
351	CDCl ₃	-0.85	-0.78	351	CDCl ₃	-1.19	-1.31
647	CDCl ₃	-3.11	-2.97	647	CDCl ₃	-3.43	-3.15
735	CDCl ₃	0.47	0.42	735	CDCl ₃	0.54	0.52
907	CDCl ₃	1.48	1.53	907	CDCl ₃	2.26	2.05
2257	CDCl ₃	-3.19	-3.22	2257	CDCl ₃	-3.13	-3.23
Cell 2				Cell 2			
1531	Eu(FOD) ₃	0.19	0.20	1524	EuCl ₃	0.20	0.22
1803	Eu(FOD) ₃	0.08	0.10	1903	EuCl ₃	0.14	0.11
885	Ethanol	-1.18	-1.13	885	Ethanol	-1.16	-1.17
1054	Ethanol	1.70	1.66	1054	Ethanol	1.75	1.56
1095	Ethanol	-1.45	-1.25	1095	Ethanol	-1.50	-1.44
1279	Ethanol	3.20	3.35	1279	Ethanol	3.30	3.27
1457	Ethanol	2.90	2.81	1457	Ethanol	2.89	2.99

¹ The estimated error is $0.02 * 10^{-3}$ based on the three repeated experiments for most data except those related to ethanol which have an estimated error of $0.06 * 10^{-3}$ because of the lower signal-to-noise ratios of the ethanol bands.

Appendix C: Supporting Information for Chapter 5

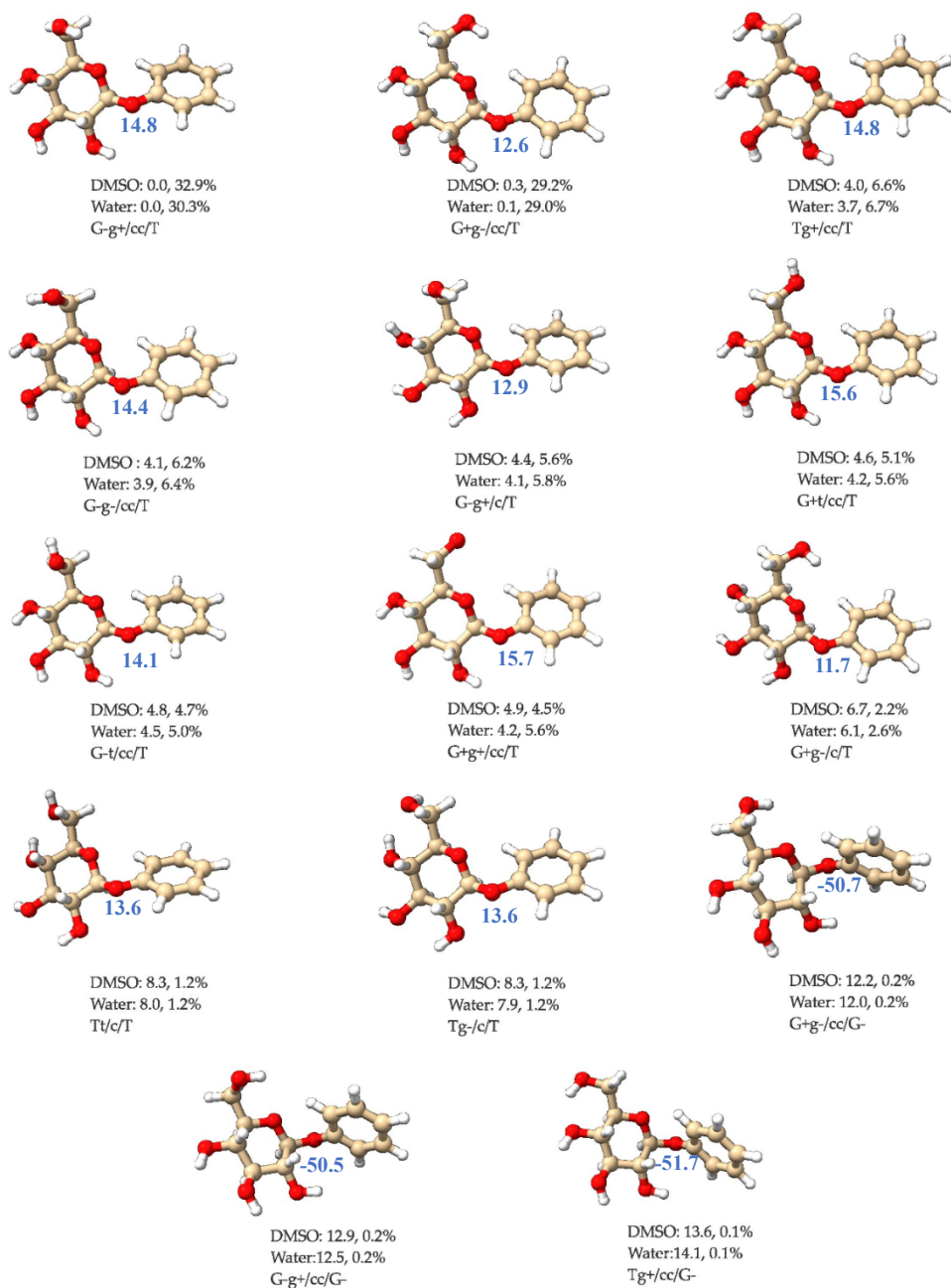


Figure C1. The C1-O1-C7-C12 dihedral angle values which correspond to the tilting of the phenyl plane are given in blue (in unit of degree) for each of the 14 most stable conformers of ph- β -glu at the B3LYP-D3BJ/def2-TZVPD level with the PCM of DMSO.

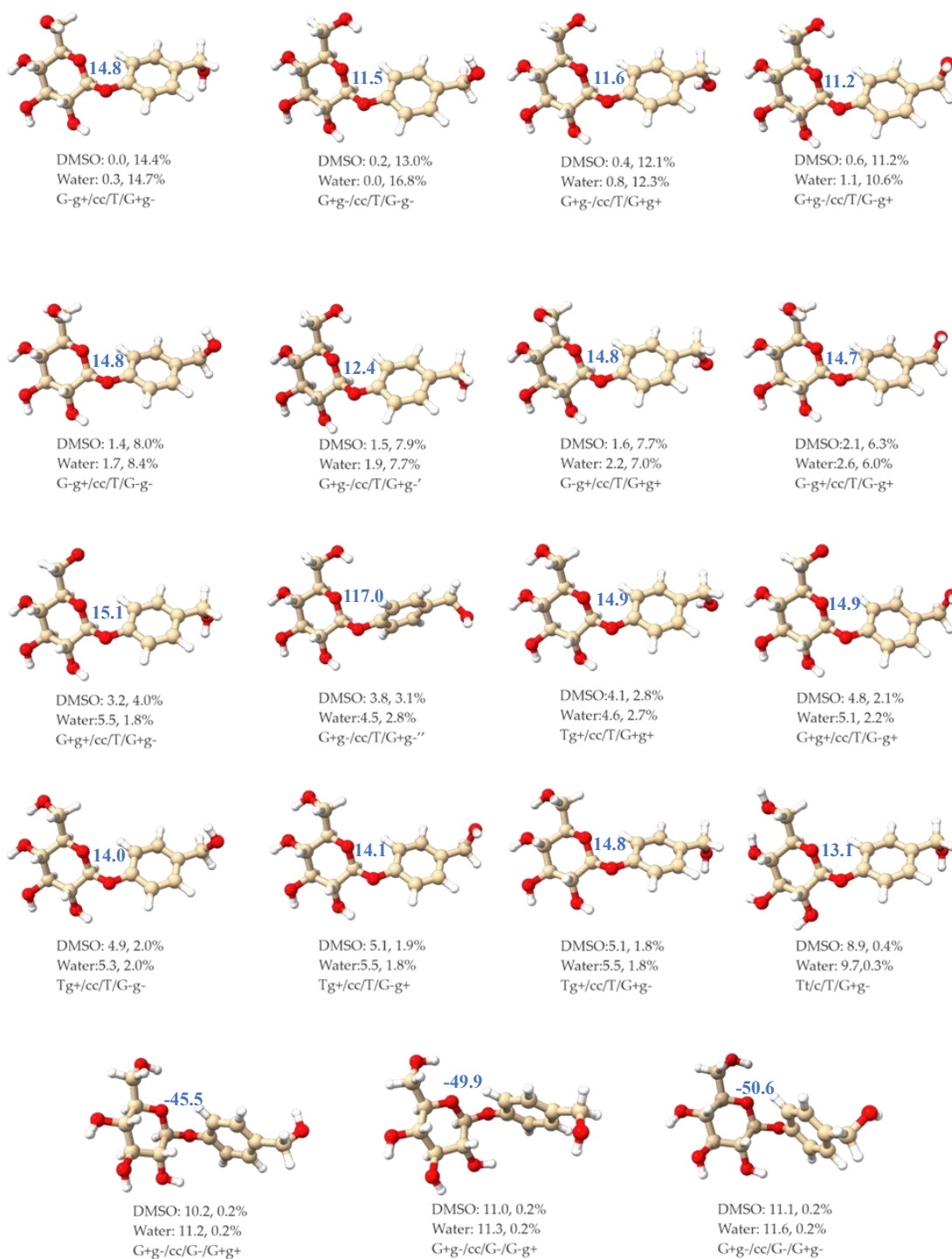


Figure C2. The C1-O1-C7-C12 dihedral angle values which correspond to the tilting of the phenyl plane are given in blue (in unit of degree) for each of the 19 most stable conformers of gastrodin at the B3LYP-D3BJ/def2-TZVPD level with the PCM of DMSO.

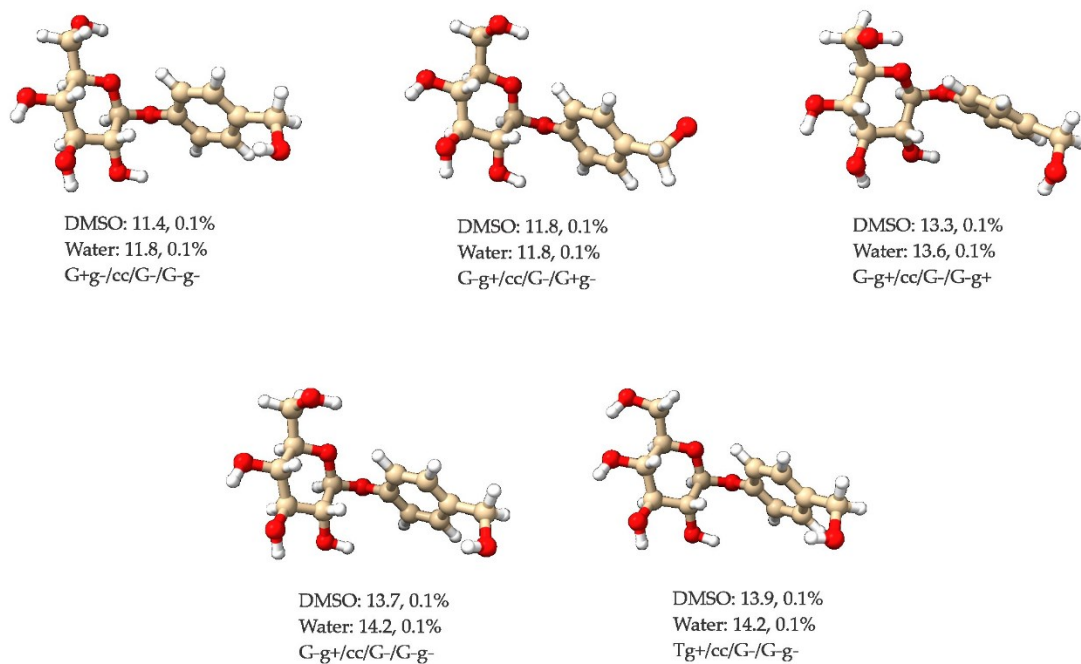


Figure C3. Geometries of the five less stable conformers of gastrodin with the Boltzmann population factors $\leq 0.1\%$ at the B3LYP-D3BJ/def2-TZVPD level with the PCM of DMSO or Water. The relative free energies in kJ mol⁻¹ and the percentage Boltzmann factors at 298 K are also given for both solvents.

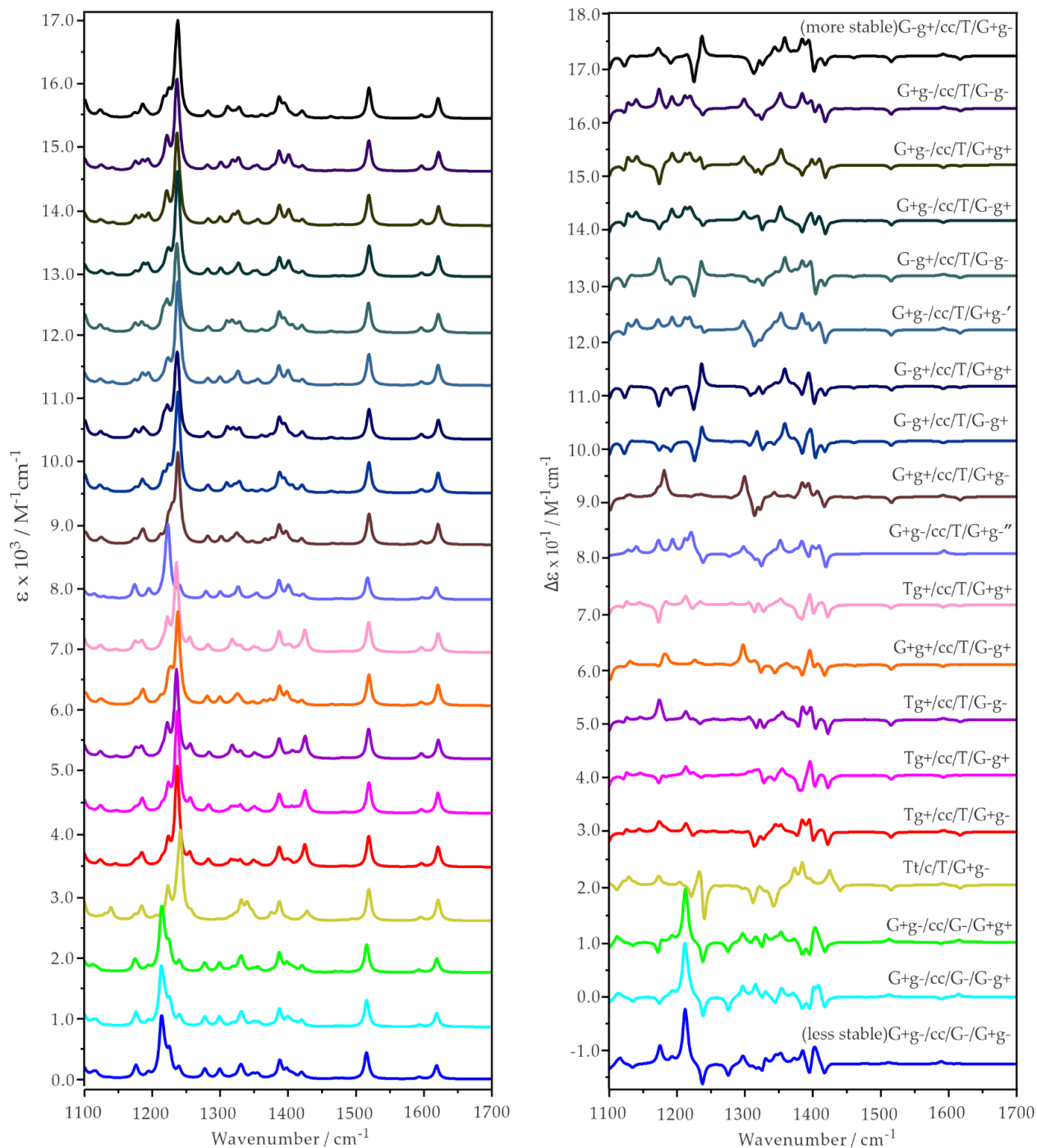


Figure C4. The simulated individual IR and VCD spectra of the 19 most stable gastrodin conformers with the Boltzmann population factors greater than 0.1% at the B3LYP-D3BJ/def2-TZVPD level with the PCM of DMSO.

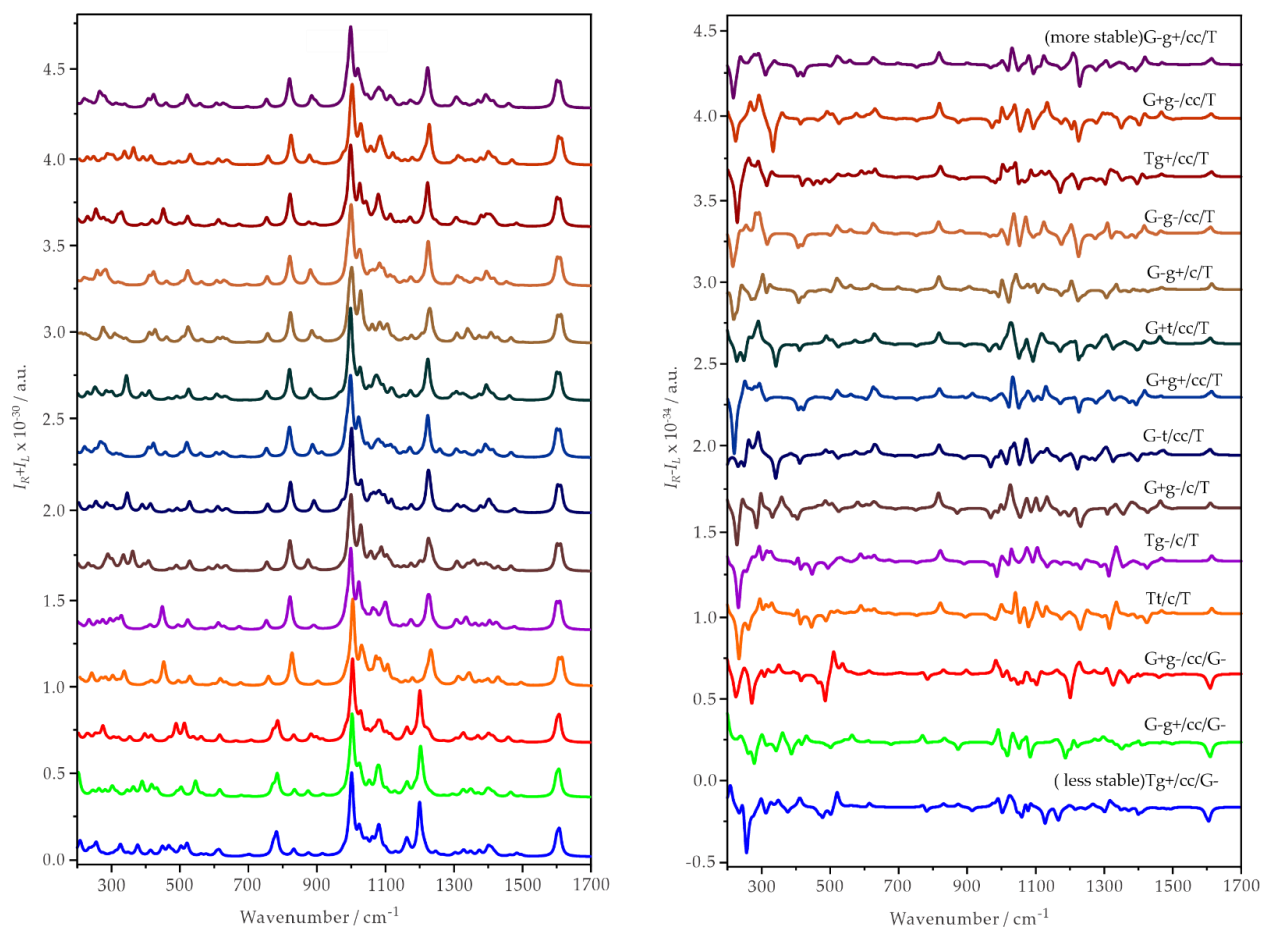


Figure C5. The simulated individual Raman and ROA spectra of the 14 most stable ph- β -glu conformers at the B3LYP- D3BJ/def2-TZVPD level with the PCM of water.

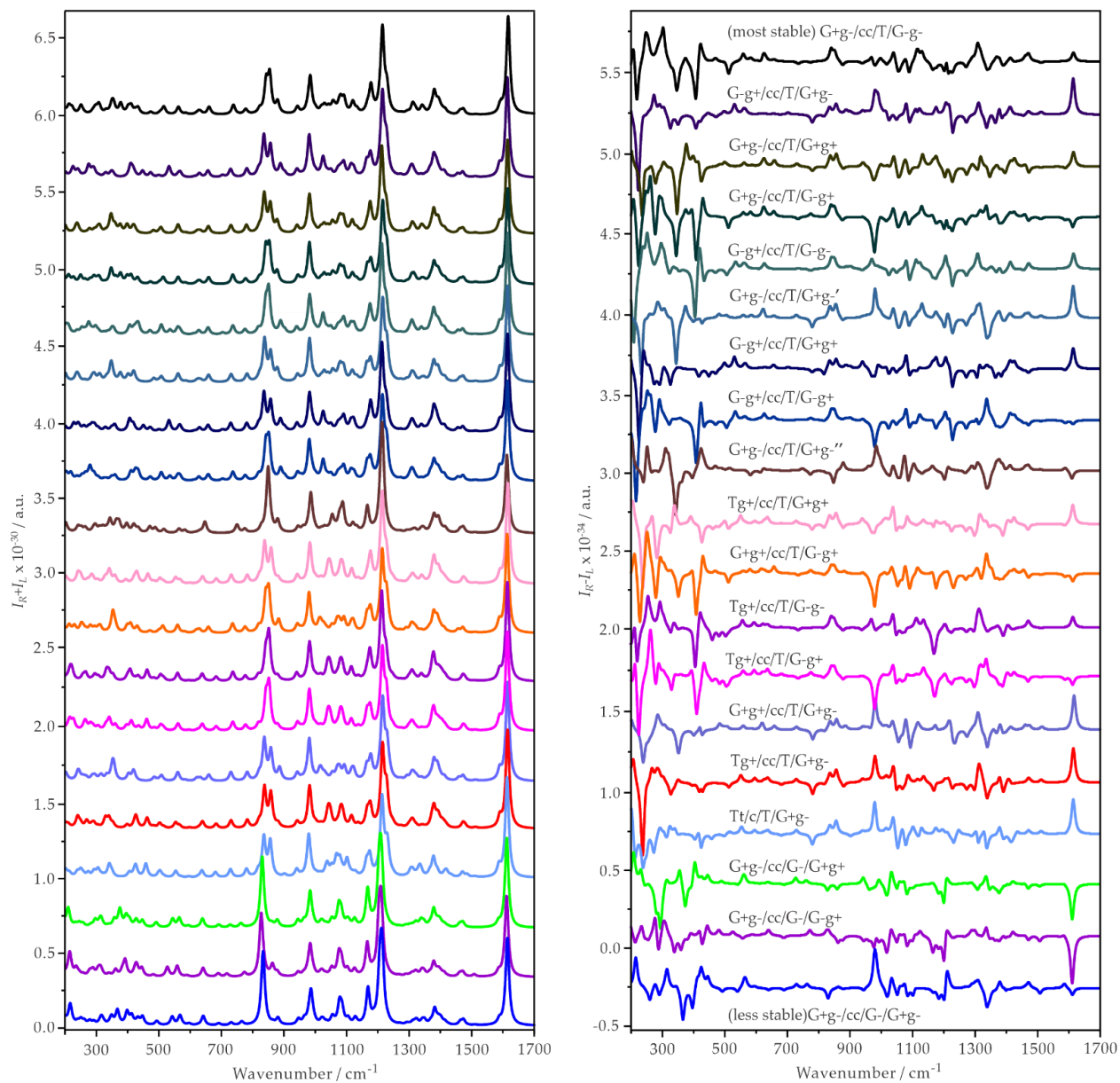


Figure C6. The simulated individual Raman and ROA spectra of the 19 most stable gastrodin conformers with the Boltzmann population factors greater than 0.1% at the B3LYP-D3BJ/def2-TZVPD level with the PCM of water.

Table C 1. The parameters of four main conformers of ph β -glu at the B3LYP-D3BJ/def2-TZVPD level in Water.

Structural parameters	G-g+/cc/T	G+g-/cc/T	Tg+/cc/T	G-g-/cc/T
r(H ₂ -O ₁)/Å	2.584	2.591	2.584	2.583
r(H ₃ -O ₂) /Å	2.532	2.542	2.554	2.544
r(H ₄ -O ₃) /Å	2.424	2.420	2.474	2.420
r(H ₆ -O ₄ /O ₅) /Å	2.426	2.408	1.993	3.067
θ (C ₂ -C ₁ -O ₁ -C ₇)/°	160.0	161.2	160.0	160.1
θ (C ₃ -C ₂ -O ₂ -H ₂) /°	-172.4	-172.1	-172.2	-172.4
θ (C ₄ -C ₃ -O ₃ -H ₃) /°	176.5	175.5	176.1	176.3
θ (C ₅ -C ₄ -O ₄ -H ₄) /°	173.0	171.9	179.6	172.6
θ (O ₅ -C ₅ -C ₆ -O ₆) /°	-60.3	61.7	169.8	-66.3
θ (C ₅ -C ₆ -O ₆ -H ₆) /°	57.3	-56.5	48.2	-82.2
θ (C ₁ -O ₁ -C ₇ -C ₁₂) /°	14.9	12.7	14.9	14.5

Table C2. The parameters of four main conformers of gastrodin at the B3LYP-D3BJ/def2-TZVPD level in Water.

Structural parameters	G-g+/cc/T/G+g-	G+g-/cc/T/G-g-	G+g-/cc/T/G+g+	G+g-/cc/T/G-g+
r(H ₂ -O ₁)/Å	2.587	2.595	2.594	2.596
r(H ₃ -O ₂) /Å	2.531	2.542	2.541	2.541
r(H ₄ -O ₃) /Å	2.422	2.417	2.418	2.416
r(H ₆ -O ₅) /Å	2.425	2.416	2.413	2.411
r(H ₁₂ -O ₅) /Å	2.546	2.577	2.576	2.577
θ (C ₂ -C ₁ -O ₁ -C ₇)/°	160.3	161.6	161.5	161.6
θ (C ₃ -C ₂ -O ₂ -H ₂) /°	-172.2	-171.9	-171.9	-171.8
θ (C ₄ -C ₃ -O ₃ -H ₃) /°	176.5	175.5	175.6	175.5
θ (C ₅ -C ₄ -O ₄ -H ₄) /°	172.9	171.7	171.9	171.7
θ (O ₅ -C ₅ -C ₆ -O ₆) /°	-60.3	61.8	61.9	61.8
θ (C ₅ -C ₆ -O ₆ -H ₆) /°	57.4	-57.0	-56.8	-57.0
θ (C ₁ -O ₁ -C ₇ -C ₁₂) /°	14.5	11.5	11.5	11.3
θ (C ₉ -C ₁₀ -C ₁₃ -O ₇) /°	100.2	-74.1	74.9	-100.6
θ (C ₁₀ -C ₁₃ -O ₇ -H ₇) /°	-56.8	-56.6	56.6	56.9

Appendix D: Supporting Information for Chapter 6

Sample Name	rr-co-salen sigma	Position	-1	Instrument Name	oaTOF6220	User Name	ami
Inj Vol	5	InjPosition		SampleType	Sample	IRM Calibration Status	Success
Data Filename	23030301.d	ACQ Method		Comment	M. Alshalalfeh, Xu	Acquired Time	3/3/2023 4:49:36 PM

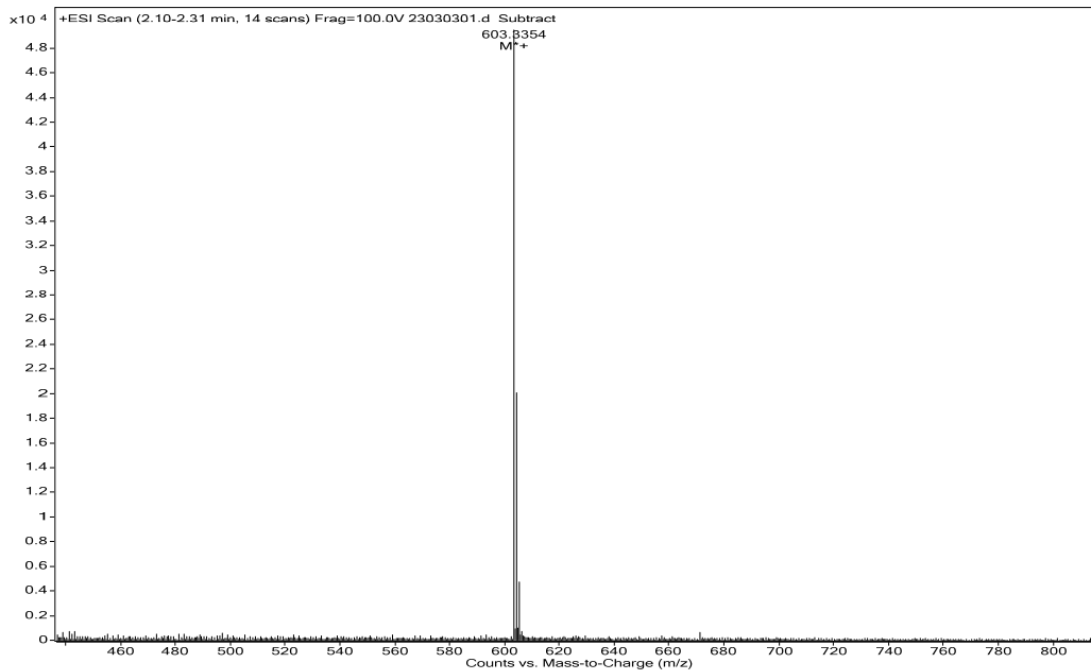


Figure D1. Experimental mass spectrum of (R,R)-Co(II)-salen-chxn.

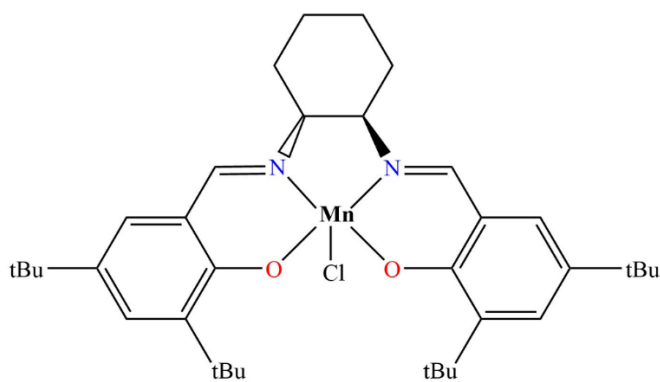


Figure D2. The molecular formula of the R,R-Mn-Cl(III)-salen-chxn complex, (R,R)-(+)-N,N'-Bis(3,5-di-tert-butylsalicylidene)-1,2-cyclohexanediaminomanganese(III) chloride. Here tBu indicates the tertbutyl group.

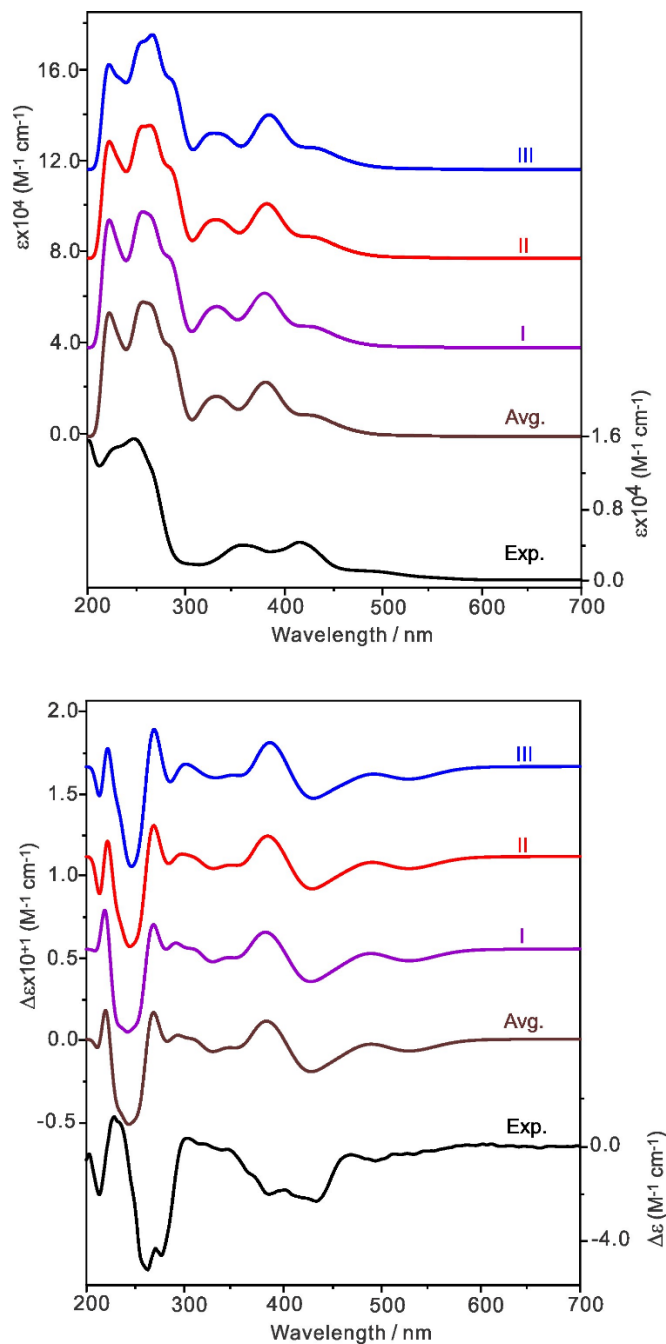


Figure D3. The simulated individual and Boltzmann average UV-Vis (top) and ECD (bottom) spectra of Co(II)-salen-chxn (low spin with spin multiplicity of 2) using the B3LYP-D3BJ/6-311++G(d,p)/PCM(acetonitrile) level of theory. The first 250 electronic states were included in the calculations at the level of theory indicated. For the Averaged spectra, we used the same Boltzmann weights derived from the IR and VCD calculations.

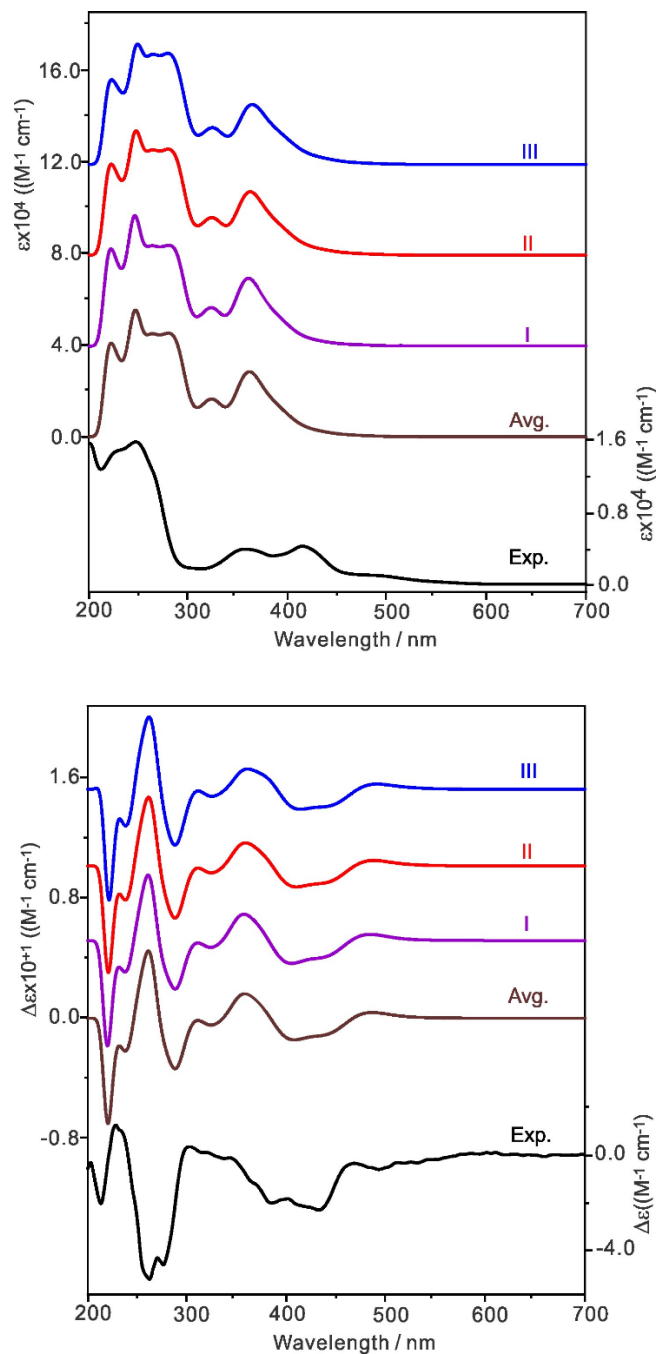


Figure D4. The simulated individual and Boltzmann average UV-Vis (top) and ECD (bottom) spectra of Co(II)-salen-chxn (high spin, with spin multiplicity of 4) using the B3LYP-D3BJ/6-311++G(d,p)/PCM(acetonitrile) level of theory. The first 250 electronic states were included in the calculations at the level of theory indicated. For the Averaged spectra, we used the same Boltzmann weights derived from the IR and VCD calculations.